TECHNISCHE UNIVERSITÄT DRESDEN

Fakultät Mathematik und Naturwissenschaften
Fachrichtung Physik
Institut für Angewandte Photophysik

Molecular Doping of Organic Semiconductors

A Conductivity and Seebeck Study

Dissertation

zur Erlangung des akademischen Grades
Doctor rerum naturalium

vorgelegt von
Torben Menke

Dresden 2013

Eingereicht am 26. März 2013
1. Gutachter: Prof. Dr. Karl Leo
2. Gutachter: Prof. Dr. Elizabeth von Hauff
Verteidigt am 19. Juli 2013
Veröffentlicht im Verlag Dr Hut, München unter der ISBN 978-3-8439-1177-1

för miene leiben Öllern

Abstract

This work aims at improving the understanding of the fundamental physics behind molecular doping of organic semiconductors, being a requirement for efficient devices like organic light-emitting diodes (OLED) and organic photovoltaic cells (OPV). The underlying physics is studied by electrical conductivity and thermoelectrical Seebeck measurements and the influences of doping concentration and temperature are investigated. Thin doped layers are prepared in vacuum by thermal co-evaporation of host and dopant molecules and measured in-situ.

The fullerene C_{60}, known for its high electron mobility, is chosen as host for five different n-dopants. Two strongly ionizing air-sensitive molecules ($Cr_2(hpp)_4$ and $W_2(hpp)_4$) and three air-stable precursor compounds (AOB, DMBI-POH and *o*-MeO-DMBI-I) which form the active dopants upon deposition are studied to compare their doping mechanism. High conductivities are achieved, with a maximum of $10.9\,{}^{S}/_{cm}$. Investigating the sample degradation by air-exposure, a method for regeneration is proposed, which allows for device processing steps under ambient conditions, greatly enhancing device fabrication possibilities.

Various material combinations for p-doping are compared to study the influence of the molecular energy levels of host (MeO-TPD and BF-DPB) and dopant (F_6-TCNNQ and $C_{60}F_{36}$). Corrections for the only estimated literature values for the dopant levels are proposed. Furthermore, the model system of similar-sized host pentacene and dopant F_4-TCNQ is studied and compared to theoretical predictions.

Finally, a model is developed that allows for estimating charge carrier mobility, density of free charge carriers, doping efficiency, as well as the transport level position from combining conductivity and Seebeck data.

Kurzfassung

Diese Arbeit untersucht organische Halbleiter und den Einfluss von molekularer Dotierung auf deren elektrische Eigenschaften, mit dem Ziel effizientere Bauelemente wie organische Leuchtdioden oder Solarzellen zu ermöglichen. Mittels Leitfähigkeitsuntersuchungen sowie thermoelektrischen Seebeck-Messungen werden die Einflüsse der Dotierkonzentration sowie der Temperatur auf die elektrischen Eigenschaften dünner dotierter Schichten analysiert. Das Abscheiden der Schichten durch Koverdampfen im Vakuum ermöglicht eine in-situ Analyse.

Das Fulleren C_{60}, bekannt für besonders hohe Elektronenbeweglichkeit, wird als Wirt für fünf verschieden n-Dotanden, zwei extrem stark ionisierende luftreaktive ($Cr_2(hpp)_4$ und $W_2(hpp)_4$) sowie drei luftstabile (AOB, DMBI-POH und *o*-MeO-DMBI-I), verwendet. Dies ermöglicht Schlüsse auf die unterschiedlichen zugrunde liegenden Dotiermechanismen und das Erreichen von Leitfähigkeiten von bis zu 10.9 $^{S}/_{cm}$. Für einen der luftreaktiven Dotanden wird die Probendegradation an Luft untersucht und eine Regenerationsmethode aufgezeigt, die Prozessierungsschritte in Luft erlaubt und somit entscheidend für zukünftige Bauelementfertigung sein könnte.

Verschiedene p-dotierte Materialkombinationen werden untersucht, um den Einfluss der molekularen Energieniveaus von Wirt (MeO-TPD und BF-DPB) und Dotand (F_6-TCNNQ und $C_{60}F_{36}$) auf die Dotierung zu studieren. Dies ermöglicht Schlussfolgerungen auf die in der Literatur bisher nur abgeschätzten Energieniveaus dieser Dotanden. Ferner werden die Eigenschaften des bereits theoretisch modellierten Paares Pentacen und F_4-TCNQ mit den Vorhersagen verglichen und die Abweichungen diskutiert.

Abschießend wird ein Modell entwickelt, das die Abschätzung von Dotiereffizienz, Ladungsträgerkonzentration, Ladungsträgerbeweglichkeit sowie der Position des Transportniveaus aus Leitfähigkeits- und Seebeck-Messungen erlaubt.

Contents

List of Publications

Articles

1. Max L. Tietze, Florian Wölzl, Torben Menke, Axel Fischer, Moritz K. Riede, Karl Leo & Björn Lüssem, *Self-passivation of molecular n-type doping during air-exposure using a highly efficient air-instable dopant*, accepted by Physica Status Solidi A (2013) http://dx.doi.org/10.1002/pssa.201330049

2. Torben Menke, Pen Wei, Debdutta Ray, Hans Kleemann, Benjamin D. Naab, Zhenan Bao, Karl Leo & Moritz K. Riede, *A comparison of two air-stable molecular n-dopants for C_{60}*, Organic Electronics 13, 3319–3325 (2012) http://dx.doi.org/10.1016/j.orgel.2012.09.024

3. Torben Menke, Debdutta Ray, Jan Meiss, Karl Leo & Moritz K. Riede, *In-situ conductivity and Seebeck measurements of highly efficient n-dopants in fullerene C_{60}*, Applied Physics Letters 100, 093304 (2012) http://dx.doi.org/10.1063/1.3689778

4. Pen Wei, Torben Menke, Benjamin D. Naab, Karl Leo, Moritz K. Riede & Zhenan Bao, *2-(2-methoxyphenyl)-1,3-dimethyl-1H-benzoimidazol-3-ium iodide as a new air-stable n-type dopant for vacuum processed organic semiconductor thin films*, Journal of the American Chemical Society 134, 3999-4002 (2012) http://dx.doi.org/10.1021/ja211382x

5. Hans Kleemann, Alexander A. Zakhidov, Merve Anderson, Torben Menke, Karl Leo & Björn Lüssem, *Direct structuring of C_{60} thin film transistors by photolithography under ambient conditions*, Organic Electronics 13, 506-513 (2012) http://dx.doi.org/10.1016/j.orgel.2011.12.009

6. Jan Meiss, Torben Menke, Karl Leo, Christian Uhrich, Wolf-Michael Gnehr, Stefan Sonntag, Martin Pfeiffer & Moritz K. Riede, *Highly efficient semitransparent tandem organic solar cells with complementary absorber materials*, Applied Physics Letters 99, 043301 (2011) http://dx.doi.org/10.1063/1.3610551

7. Suren A. Gevorgyan, Martin Hermenau, Torben Menke, et al., *An inter-laboratory stability study of roll-to-roll coated flexible polymer solar*

modules, Solar Energy Materials and Solar Cells 95, 1398-1416 (2011) http://dx.doi.org/10.1016/j.solmat.2011.01.010

8. Jan Meiss, Steffen Pfuetzner, Markus Hummert, Torben Menke, Karl Leo & Moritz K. Riede, *ITO-free, semitransparent small-molecule organic solar cells with dibenzoperiflanthene as absorber*, Proc. EU PVSEC 25 mixi, 303-305 (2010) http://dx.doi.org/10.4229/25thEUPVSEC2010-1CO.10.6

9. Gerwin Chilla, Tobias Kipp, Torben Menke, Detlef Heitmann, Marija Nikolic, Andreas Frömsdorf, Andreas Kornowski, Stephan Förster & Horst Weller, *Direct observation of confined acoustic phonons in the photoluminescence spectra of a single CdSe-CdS-ZnS core-shell-shell nanocrystal*, Physical Review Letters 100, 57403-57404 (2008) http://dx.doi.org/10.1103/PhysRevLett.100.057403

Conference Contributions

1. Torben Menke, Pen Wei, Debdutta Ray, Zhenan Bao, Karl Leo & Moritz K. Riede, *Seebeck measurements on two air-stable n-dopants for C_{60}*
   MRS Spring Meeting 2012, San Francisco, (Talk)

2. Torben Menke, Pen Wei, Debdutta Ray, Zhenan Bao, Karl Leo & Moritz K. Riede, *Seebeck measurements on two air-stable n-dopants for C_{60}*
   76. Jahrestagung der DPG, Berlin, (Talk)

3. Torben Menke, Pen Wei, Debdutta Ray, Zhenan Bao, Karl Leo & Moritz K. Riede, *Seebeck measurements on two air-stable n-dopants for C_{60}*
   11^{th} European Conference on Molecular Electronics 2011, Barcelona, (Talk)

4. Torben Menke, Pen Wei, Debdutta Ray, Jan Meiss, Zhenan Bao, Karl Leo & Moritz K. Riede, *Investigating the effect of molecular doping on the energy levels using Seebeck measurements*
   75. Jahrestagung der DPG, Dresden, (Poster)

5. Torben Menke, Selina Olthof, Pen Wei, Zhenan Bao, Karl Leo & Moritz K. Riede, *Investigating the effect of doping on the energy levels using Seebeck measurements*
   Plastic Electronics 2010, Dresden, (Talk)

6. Torben Menke, Gerwin Chilla, Marija Nikolic, Andreas Frömsdorf, Tobias Kipp, Detlef Heitmann, Horst Weller & Stephan Förster, *Photoluminescence spectroscopy of CdSe/CdS(/ZnS) quantum dots*
   71. Jahrestagung der DPG, Dresden, (Poster)

Nomenclature

Table 0.1: *Physical constants*

e	elementary electric charge constant	$1.602\,167\,487(40)\cdot10^{-19}$ C [Moh08]
k_B	Boltzmann constant	$1.380\,650\,4(24)\cdot10^{-23}$ J/K [Moh08]
		$= 8.617\,343(15)\cdot10^{-5}$ eV/K [Moh08]
N_{Avo}	Avogadro constant	$6.022\,141\,79(30)\cdot10^{23}$ mol^{-1} [Moh08]

Table 0.2: *Abbreviations*

a.u.	arbitrary unit
AFM	atomic force microscope
CAS	Chemical Abstracts Service
CSC	conventional (inorganic) semiconductor
CV	cyclic voltammetry
e	electron
EA	electron affinity
h	hole
HOMO	highest occupied molecular orbital
IAPP	Institut für Angewandte Photophysik der TU Dresden
IE	ionization energy
IPES	inverse photoemission spectroscopy
LUMO	lowest unoccupied molecular orbital
OFET	organic field-effect transistor
OLED	organic light-emitting diode
OPV	organic photovoltaic cell
OSC	organic semiconductor
rms	root-mean-square
SC	semiconductor
SMU	source measure unit
UPS	ultraviolet photoelectron spectroscopy

Table 0.3: *Investigated molecules, details can be found in section 3.2 and in table 3.2 on page 50.*

AOB	3,6-bis(dimethylamino)acridine
BF-DPB	N,N'-Bis(9,9-dimethyl-fluoren-2-yl)-N,N'-diphenyl-benzidine
C_{60}	fullerene consisting of 60 carbon atoms
$C_{60}F_{36}$	fluorinated derivative of the fullerene C_{60}
$Cr_2(hpp)_4$	tetrakis(1,3,4,6,7,8-hexahydro-2H-pyrimido[1,2-a]pyrimidinato)-dichromium (II)
DMBI-POH	2-(1,3-dimethyl-1*H*-benzoimidazol-3-ium-2-yl)phenolatehydrate
F_4-TCNQ	tetrafluoro-tetracyanoquinodimethane
F_6-TCNNQ	1,3,4,5,7,8-hexafluorotetracyanonaphthoquinodimethane
MeO-TPD	N,N,N',N'-tetrakis 4-methoxyphenyl-benzidine
o-MeO-DMBI-I	2-(2-methoxyphenyl)-1,3-dimethyl-1*H*-benzoimidazol-3-ium iodide
pentacene	pentacene
$W_2(hpp)_4$	tetrakis(1,3,4,6,7,8-hexahydro-2H-pyrimido[1,2-a]pyrimidinato)-ditungsten (II)

Table 0.4: *Symbols*

	Densities	
DOS	density of states	(2.1)
n	density of free charge carriers	(2.1)
n_e	density of free electrons	
n_h	density of free holes	
n_i	intrinsic charge carrier density	(2.10)
n_D	density of dopant molecules	
n_H	density of host molecules	
n_{Mol}	total density of molecules	
N_A	concentration of acceptors	
N_A^-	concentration of ionized acceptors	(2.12)
N_C	effective density of states in the conduction band	
N_D	concentration of donors	
N_D^+	concentration of ionized donors	(2.12)
N_V	effective density of states in the valence band	
	Energies	
E_A	acceptor energy level	
$E_{act,\sigma}$	activation energy of the conductivity $\sigma(T)$	(2.25)
E_C	conduction energy: minimum of conduction band	
E_D	donor energy level	
E_F	chemical potential / Fermi level	(2.3)
E_{gap}	band gap $= E_C - E_V$	
E_G	position of the maximum of Gaussian distribution	(2.26)
σ_G	standard deviation of Gaussian distribution	(2.26)
E_S	Seebeck energy $= E_F - E_{Tr}$	(2.66)
E_{Tr}	transport level	(2.62)
E_V	valence energy: maximum of valence band	

	Other Symbols	
A	cross-section	(2.22)
C	doping concentration (in molar ratio MR)	(2.42)
d_{c}	distance between parallel contacts	(2.22)
ε	dielectric constant	
$\mathscr{E}$	electric field	(2.21)
f_{B}	Boltzmann distribution function	(2.4)
f_{FD}	Fermi-Dirac distribution function	(2.3)
g_{A}	ground state degeneracy of the accepter level	(2.12)
g_{D}	ground state degeneracy of the donor level	(2.11)
h_{l}	layer thickness	(2.22)
η_{dop}	doping efficiency	(2.44)
I	electric current	
j	current density	
l_{c}	contact length	(2.22)
M	molar mass	
μ	mobility	(2.24)
pKa	acid dissociation constant	
P	pressure	
Π	Peltier coefficient	(2.52)
R	electric resistance	
R_{rms}	root-mean-square roughness (AFM)	
ρ	density of a material	
S	Seebeck coefficient	(2.46)
σ	conductivity	(2.22)
t	time	
τ	characteristic time constant	(4.2)
T	temperature	
T_{d}	temperature difference during Seebeck measurements	
T_{dep}	material deposition temperature	
T_{g}	glass transition temperature	
T_{m}	mean temperature during Seebeck measurements	
T_{sub}	substrate temperature	
v_{d}	drift velocity	(2.20)
V	electric voltage	
V_{S}	thermoelectric/Seebeck voltage	(2.47)
χ	maximal relative change of σ	(4.2)

Chapter 1

Introduction

The second half of the 20th century was characterized by the advance of semiconductor electronics that led to the invention of computers, affecting most parts of today's daily life. Most commonly the semiconductor material silicon is used, being the second most abundant element in the Earth's crust and having already been used for fabrication of ordinary glass for centuries. One of the key elements that enabled the breakthrough of semiconductor technology is doping, i.e. the introduction of electron donating or accepting impurities that allow for controlling of the majority charge carriers. Doping enables the design of p-n-junctions, being the building block for most electronic devices, from transistors to light-emitting diodes and photovoltaic cells. Furthermore, it allows for adjusting the conductivity over orders of magnitude by increasing the charge carrier density and therefore tuning charge injection, extraction and transport properties.

Recently, semiconductors composed of chemically synthesized organic (i.e. hydrocarbon-based) molecules increasingly gained attention, since organic dyes with delocalized π-systems have promising properties for optoelectronic devices. The major drawback of organic semiconductors is their rather low charge carrier mobility, being several orders of magnitude below the values of typical conventional semiconductors. This is due to the weak interaction between adjacent organic molecules in a layer that leads to a slower charge-transfer between the molecules, compared to the almost unhindered band transport in a crystalline inorganic semiconductor formed by covalently bound atoms. But, whereas a limited variety of conventional (inorganic) semiconductor materials is available, the toolbox of organic chemistry allows to design and synthesize molecules with desired properties.

The optoelectronic properties of organic semiconductors led to the development of organic light-emitting diodes (OLED) and organic photovoltaic cells (OPV), converting

electricity to light and vice versa. The lower refractive index of organic semiconductors compared to conventional semiconductors allows for good light in- and outcoupling. In the last 15 years, the development of both technologies was accompanied by an exponentially increasing number of publications over time that drove exponentially increasing record efficiencies, as shown in figure 1.1. In contrast to conventional electronics, both types of devices, OLEDs and OPV, can in principle be fabricated on foils allowing for flexible lightweight devices and large device areas, which opens new areas of applications. The main drawback is that device lifetime is limited by reactions with water and oxygen, requiring exceptionally good encapsulation. Device thicknesses in the range of just hundred nanometers and low fabrication temperatures with typical substrate temperatures below 100 °C lead to very low material and energy consumption and hence promise low production costs.

OLEDs are developed for lighting as well as for display applications. OLED lighting competes with fluorescent lighting as well as inorganic light-emitting diode (LED) technology. While LEDs are usually point light sources, OLEDs are natural area emitters of diffuse light and allow for new design options like transparent lighting panels. At the time of writing, first products are commercially available. OLEDs for display applications have already proven their potential and successfully emerged into markets where they are competing with conventional liquid crystal display (LCD) technology. Key advantages of OLED displays are higher contrast, potentially low power consumption, smaller thickness and larger viewing angle, mostly enabled by the direct emission of light with the desired color instead of a combination of white backlight and color filters like in LCDs.

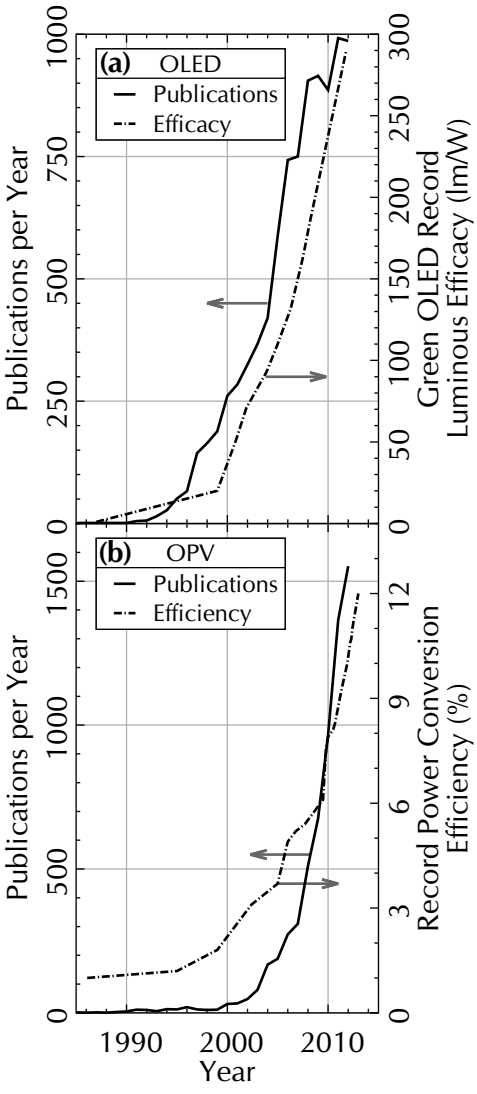

Figure 1.1: *(a) OLED and (b) OPV publications per year and laboratory "hero" performance.* [OW,ISI]

Organic semiconductor-based photovoltaics is a promising candidate for providing future electricity supply. Besides silicon-based photovoltaics, it seems to be the only non-concentrated technology with sufficient raw material available for a TW-scale production [Fel08], required for a significant share of worldwide supply of sustainable electricity. While for silicon-based photovoltaics the record efficiencies stagnated in recent years and only the production costs could be dramatically reduced, in the last 15 years exponentially increasing OPV record efficiencies have been reported, as shown in figure 1.1 (b). At the time of writing, a record power conversion efficiency of 12 % [Hel13] is published which is below the record for polycrystalline silicon cells (20.4 %) [Gre13]

but already above the value for amorphous silicon (10.1 %) [Gre13]. In contrast to inorganic cells, the efficiency is stable between room temperature and elevated operating temperature and a better low-light performance is reported [Rie11b,Hel13]. The major drawback for polycrystalline silicon-based photovoltaic modules is the rather long energy payback time (e.g. $\approx$ 2 years when installed in Germany [Fra13]). Roll-to-roll processing of OPV modules on flexible substrates might allow for a high production throughput and hence, together with low material consumption and low fabrication temperatures, enable short energy payback time and low cost [Anc12]. Furthermore, the narrow absorption bands of organic semiconductors allow for fabrication of color-tunable semi-transparent cells as well as for efficiency-optimized tandem or triple cells [Rie11b,Hel13].

Two classes of organic semiconductors are typically distinguished: polymers and small molecules. Polymers are large molecules consisting of repeating structural units and are typically deposited by wet chemical methods like coating or printing from solution. They show higher charge carrier mobilities than small molecules due to their intra-molecular transport, but chain length dispersity and solvent contamination hamper reproducibility. Small molecules are compounds of rather low molar mass, often allowing for purification and deposition by thermal evaporation, typically in vacuum. Charge carrier mobilities are usually lower than in polymers and the initial cost for large scale production by vacuum deposition tends to be larger compared to solution processing of polymers. However, the thermal evaporation process allows for freely designable multilayer devices, which is hardly possible for polymers, due to the interaction of solvents with layers already deposited and the lack of orthogonal solvents.

Organic semiconductors can be doped by co-depositing electron donating or accepting atoms or molecules along with the host material. Doping of organic semiconductors has been shown to improve device performance significantly [Wal07,Lüs13], but contrary to conventional semiconductors, the underlying physics is far from being completely understood. It is the aim of this thesis to contribute to the understanding of the fundamental physics of doping of organic semiconductors by studying the molecular doping in vacuum deposited layers of organic small molecules.

This thesis is structured into nine chapters. Following this introduction, chapter 2 provides the theoretical background and reviews relevant literature for the studies presented in the subsequent chapters. In chapter 3, the experimental techniques as well as the developed setup are explained in detail. Furthermore, the investigated organic compounds are introduced and their key properties along a draft historical background are summarized. The presentation of the results starts in chapter 4 with investigations of the fullerene C_{60} n-doped by the two novel dopants $Cr_2(hpp)_4$ and $W_2(hpp)_4$ of extremely low ionization energies and which hence are reactive to air. The degradation induced by air-exposure of doped layers is studied and a regeneration treatment is presented. In chapter 5, C_{60} is n-doped by air-stable precursor compounds (AOB, DMBI-POH and *o*-MeO-DMBI-I) that form the active dopant compound during deposition. This transformation is investigated more closely for the two novel DMBI derivatives. Following the studies of n-doping, in chapter 6 two amorphous hosts (MeO-TPD and BF-DPB) are p-doped by two different dopants (F_6-TCNNQ and

$C_{60}F_{36}$) and the influence of the molecular energy levels on the doping is analyzed. Afterwards, in chapter 7 the model system of the polycrystalline host pentacene p-doped by the similar-sized dopant F_4-TCNQ is investigated and the data are compared to theoretical predictions for this combination. Finally, in chapter 8 a model is developed that allows to derive lower limits for the charge carrier mobility, the density of free charge carriers as well as the doping efficiency from conductivity data and furthermore allows to narrow down the energetic position of the transport level level when combined with Seebeck data. Concluding, the findings of this thesis are summarized in chapter 9 and directions for future studies are outlined.

Chapter 2

Fundamentals of Organic Semiconductors

In this chapter, the basics of semiconductor physics are summarized, as they are required for understanding the results presented in this work. Initially the key properties of conventional (inorganic) semiconductors (CSCs) are considered. In a second step, organic semiconductors (OSCs) are introduced and differences to conventional semiconductors are outlined. Finally, the Seebeck effect is discussed and correlations to semiconductor properties are derived.

2.1 Conventional Semiconductors

This section introduces the fundamentals of conventional semiconductors, in particular the differences between intrinsic and doped semiconductors are highlighted. More detailed information can be found in textbooks [Sze81,Thu11,End92].

2.1.1 Intrinsic Semiconductors

A semiconductor (SC) is called intrinsic if it is pure and free of impurities. A conventional inorganic semiconductor material, like silicon (Si) or gallium arsenide (GaAs), consists of covalently bound atoms forming a crystalline lattice structure. The discrete energy levels of a single atom are affected by the interaction of the periodically arranged neighboring atoms and a band structure of allowed and forbidden energy eigenstates for electrons is formed.

The population of electrons in the bands depends on the temperature T. Semiconductors have the special property that at $T \to 0\,\mathrm{K}$ every band is either completely occupied or empty. Occupied bands are those lying deepest in energy and the highest occupied band is called valence band, whereas the lowest unoccupied band is called conduction band. The second important property of semiconductors is the presence of a forbidden energetic region between the occupied and the empty bands. As only incompletely filled bands can contribute to transport, at $T \to 0\,\mathrm{K}$ charge transport is impossible (unless the material is illuminated or charges are injected).

In the following, the lowest allowed energy of the conduction band will be called the conduction energy E_C and the highest allowed energy of the valence band the valence energy E_V. The energetic gap between conduction and valence band and hence the difference between E_V and E_C is called bandgap E_gap, being a key property of a semiconductor and is usually in the range of 0.5 eV to 2 eV. At room temperature, the typical semiconductors Si and GaAS have bandgaps of 1.12 and 1.42 eV [Sze81], respectively.

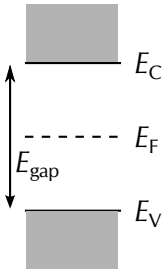

With increasing temperature, an increasing number of electrons from the valence band reaches the conduction band due to their thermal energy, leaving unoccupied states in the valence band, the so-called holes, behind. Holes can be described in a similar manner to electrons and in the following, the indices “e” and “h” will are used for addressing parameters of electrons and holes, respectively. The density of free electrons in the conduction band n_e depends on the density of available states $DOS(E)$ in the conduction band and the occupation probability distribution $f(E,T)$, which accounts for the temperature:

$$n_\mathrm{e} = \int_{-\infty}^{\infty} DOS(E) \cdot f(E,T)\, dE\ . \tag{2.1}$$

Its energy-resolved derivative is called the differential electron density $n'(E)$:

$$n'_e(E) = DOS(E) \cdot f(E,T) \,. \tag{2.2}$$

Electrons are fermions[‡] and therefore each state can only be occupied by one particle. Hence, the occupation probability f is given by the Fermi-Dirac distribution function (compare figure 2.1 (a)):

$$f_{FD}(E,T) = \frac{1}{1+\exp\left(\frac{E-E_F}{k_B T}\right)} \,. \tag{2.3}$$

Here, k_B is Boltzmann's[§] constant and at $T = 25\,°C$ the product $k_B T = 25.7\,meV$. E_F is the electro-chemical potential which is temperature-dependent as well. For $T \to 0\,K$, the Fermi-Dirac distribution function becomes a step function and the occupation probability is zero for all states with an energy above the chemical potential ($f_{FD}(E,T) = 0$ for $E > E_F$ at $T \to 0\,K$). The highest occupied energy state at 0 K is called Fermi *energy*. At higher temperature, the chemical potential is called Fermi *level* and is temperature-dependent. In the following, only the term Fermi level will be used, since all temperatures discussed are well above 0 K. The Fermi level is the energy correlated to an occupation probability of 50 % ($f_{FD}(E_F,T) = 0.5$). In case of intrinsic semiconductors discussed so far, the value of E_F is close to the middle of the bandgap, compare equation (2.17) below.

The Fermi-Dirac distribution function can be approximated by the Boltzmann distribution function for $E - E_F \gg k_B T$

$$f_B(E,T) = \exp\left(-\frac{E-E_F}{k_B T}\right) \,. \tag{2.4}$$

Figure 2.1 (b) compares the two functions and it can be seen that at $E = E_F$ the value of $f_B(E)$ is twice the value of $f_{FD}(E)$. At higher energies the error is strongly decreasing e.g. already at $E = E_F + 3\,k_B T$, the overestimation is as small as $\approx 5\,\%$. A general expression for the overestimation of $f_{FD}(E)$ by using $f_B(E)$ can be written as

$$\frac{f_{FD}(E)}{f_B(E)} - 1 = \exp\left(-\frac{E-E_F}{k_B T}\right) = f_B(E) \,, \tag{2.5}$$

which interestingly is identical to the Boltzmann distribution function itself.

The density of states of an intrinsic conventional semiconductor is zero in the energy gap between valence and conduction band and non-zero in the bands. Close to the minimum of the conduction band it can be approximated by a square root proportionality to the energy above E_C [Sze81] :

$$DOS(E) \propto \sqrt{E - E_C} \qquad \text{for } E > E_C \,. \tag{2.6}$$

[‡] after Italian scientist Enrico Fermi [Fer26] (1901–1954)

[§] after Austrian scientist Ludwig Eduard Boltzmann (1844–1906)

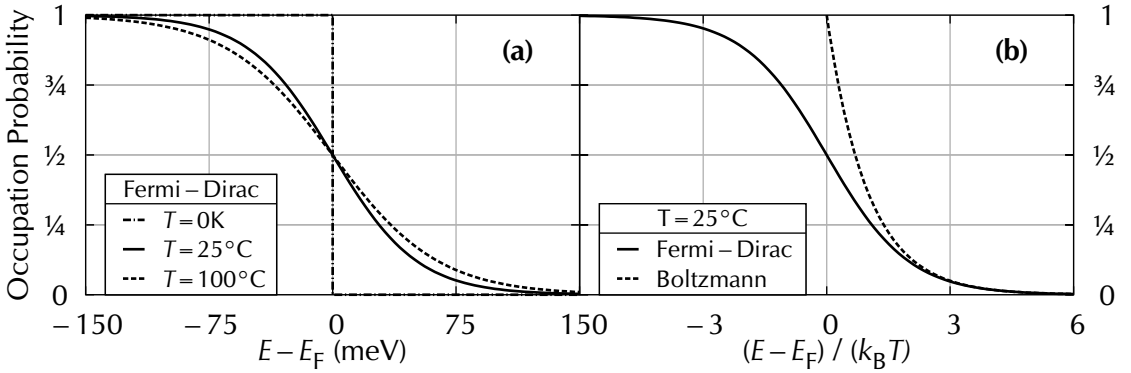

Figure 2.1: *(a) Fermi-Dirac distribution function $f_{FD}(E)$ for the occupation probability at $T = 25\,°C$, 0 K and 100 °C. (b) Comparison of Fermi-Dirac $f_{FD}(E)$ and Boltzmann distribution function $f_B(E)$ for $T = 25\,°C$ ($k_B T = 25.7\,meV$).*

Using this density of states and the Boltzmann approximation for the Fermi-Dirac distribution function f_{FD}, equation (2.1) can be solved analytically to

$$n_{\mathrm{e}} = N_{\mathrm{C}} \exp\left(-\frac{E_{\mathrm{C}} - E_{\mathrm{F}}}{k_{\mathrm{B}} T}\right) . \tag{2.7}$$

Analogously to electrons, the density of free holes n_{h} in the valence band can be derived, resulting in

$$n_{\mathrm{h}} = N_{\mathrm{V}} \exp\left(-\frac{E_{\mathrm{F}} - E_{\mathrm{V}}}{k_{\mathrm{B}} T}\right) . \tag{2.8}$$

The prefactors N_{C} and N_{V} are the so-called effective density of states in the conduction and valence band, both being proportional to $(k_{\mathrm{B}} T)^{3/2}$ and of the unit $^1/_{\mathrm{cm}^3}$.

The above equations are only valid in thermal equilibrium and have to be modified if an external bias voltage or illumination is applied to the system. Exemplary, the absorption of a photon would lead to an increase of both, n_{e} and n_{h}, making it impossible to describe the system with one Fermi level. Instead, separate quasi-Fermi levels for electrons and holes have to be introduced if thermal relaxation inside the bands is much faster than relaxation from band to band.

In an uncharged and undisturbed intrinsic semiconductor at a given temperature, the number of electrons in the conduction band equals the number of holes in the valence band (neutrality condition). This density is called the intrinsic charge carrier density n_{i}

$$n_{\mathrm{e}} = n_{\mathrm{h}} = n_{\mathrm{i}} . \tag{2.9}$$

It is important to note that the square of n_{i}

$$n_{\mathrm{i}}^2 = n_{\mathrm{e}} \cdot n_{\mathrm{h}} = N_{\mathrm{C}} N_{\mathrm{V}} \exp\left(-\frac{E_{\mathrm{gap}}}{k_{\mathrm{B}} T}\right) , \tag{2.10}$$

is independent of the Fermi level E_{F} and can be calculated from N_{V}, N_{C}, and the bandgap E_{gap}. Equation (2.10) is the law of mass action, known from basic chemistry.

2.1.2 Doped Semiconductors

In order to increase the number of free charge carriers $n_{e/h}$ of a semiconductor, suitable impurities of other elements can be introduced. In a so-called doped semiconductor, some of the atoms in the lattice structure are replaced by atoms of a different material, having one valence electron more or one valence electron less than the host element. These impurities are called dopants.

In case of a dopant with one additional valence electron, this electron is only weakly bound inside the lattice of the host material, as no partner for a covalent bond is available. Hence, only little thermal energy is needed for this electron to reach the conduction band and thus to increase the density of free electrons n_e. Such dopants are called donors or n-dopants as they donate their negatively charged valence electron to the host material.

The same principle works in an analogous manner for dopant atoms that have one valence electron less than the host. These dopants are called acceptors or p-dopants since a valence electron of the surrounding host atoms is taken and a positively charged hole is created on the host.

Silicon, for example, is typically n-doped using phosphorus (P) as donor or p-doped using boron (B) as acceptor with typical dopant concentrations in the range of a few parts per million (ppm).

In the following, N_D and N_A are the absolute values of the dopant concentration of donors and acceptors in the host material, usually given in the unit $^1/_{cm^3}$. The energy levels of the dopants are located in the bandgap of the host. While the donor level E_D is near the conduction band (below E_C), the acceptor level E_A is near the valence band (above E_V).

2.1.2.1 Ionization of Dopants

Thermal energy is needed for the ionization of dopants and thus generation of free charges for the conduction or valence band. Two classes of dopants can be distinguished: dopants with either a *deep* or a *shallow* level with respect to the host material. Shallow dopants have an energy level than close to the band edge that thermal energy is sufficient to ionize (most of) them. Deep dopants on the other hand, have energy levels several $k_B T$ away from the band edge, so that ionization is less probable. Generally, the density of ionized donors N_D^+ and ionized acceptors N_A^- are [Sho50]

$$N_D^+ = N_D \left(1 - \frac{1}{1 + \frac{1}{g_D} \exp\left(E_D - E_F\right) k_B T} \right) \tag{2.11}$$

$$N_A^- = N_A \left(\frac{1}{1 + g_A \exp\left(E_A - E_F\right) k_B T} \right) , \tag{2.12}$$

with g_A and g_D being the ground state degeneracy of the donor and acceptor levels. Typically the degeneracy of these levels is $g = 2$ as each level can be occupied by two

electrons of opposite spin ($\pm 1/2$). Additional degeneracy can be introduced by the host material. For Si and GaAs, the valence band is twofold degenerate and thus they have two hole levels each being twofold spin degenerate, leading to a value of $g_A = 4$ in these materials. The temperature regime, where the thermal energy is sufficient to ionize almost all dopants ($N_D^+ \approx N_D$ and $N_A^- \approx N_A$) is called the saturation range. The ratio of the density of free charge carriers $n_{e/h}$ to the density of dopants can be defined as doping efficiency η_{dop} (for $N_D \gg n_i$):

$$\eta_{dop} = \frac{n_e}{N_D} \quad \text{or} \quad \eta_{dop} = \frac{n_h}{N_A} \,. \tag{2.13}$$

The law of mass action ($n_i^2 = n_e \cdot n_h$, equation (2.10)) is valid for doped semiconductors as well. In contrast to intrinsic SCs, for doped SCs the density of free electrons in the conduction band n_e does not equal the density of free holes in the valence band n_h. Hence, the neutrality condition for doped SCs has to include the ionized dopants as well:

$$n_e + N_A^- = n_h + N_D^+ \tag{2.14}$$

$$\begin{aligned} &\Rightarrow N_C \exp\left(-\frac{E_C - E_F}{k_B T}\right) + N_A \left(\frac{1}{1 + g_A \exp\left(E_A - E_F\right) k_B T}\right) \\ &= N_V \exp\left(-\frac{E_F - E_V}{k_B T}\right) + N_D \left(1 - \frac{1}{1 + \frac{1}{g_D} \exp\left(E_D - E_F\right) k_B T}\right) \,, \end{aligned} \tag{2.15}$$

(Boltzmann approximation used).

If, for example in an n-doped SC, only donors and no acceptors ($N_A = 0$, $N_D > 0$) are present, the neutrality condition (2.14) and the law of mass action (2.10) can be used to derive an expression for the density of free electrons in the condition band n_e [Thu11]:

$$\begin{aligned} n_e &= n_h + N_D^+ \quad \text{and} \quad n_h = \frac{n_i^2}{n_e} \quad \Rightarrow \quad n_e^2 - n_e N_D^+ - n_i^2 = 0 \\ n_e &= \frac{N_D^+}{2} + \sqrt{\left(\frac{N_D^+}{2}\right)^2 + n_i^2} \,. \end{aligned} \tag{2.16}$$

This clearly shows the two sources for the density of free electrons in the conduction band: the excited electrons from the valence band and those from the ionized donors. An analogous trend can be found for acceptor-only doping and n_h.

2.1.2.2 Fermi Level Position

For an intrinsic semiconductor, the Fermi level E_F is located close to the middle of the bandgap:

$$E_F = \frac{E_C + E_V}{2} + \frac{k_B T}{2} \cdot \ln\left(\frac{N_V}{N_C}\right) \,. \tag{2.17}$$

Introducing dopants leads to a shift of E_F. In case of n-doping, the Fermi level moves towards the conduction band, whereas for p-doping, it moves towards the valence band. By solving the neutrality condition (2.15), the value of E_F can be calculated, keeping in mind that all four terms (n_e, n_h, N_D^+, N_A^-) depend on E_F.

In case of shallow dopants or at elevated temperatures, when most dopants are ionized, the position of E_F is given by:

$$E_F = E_C - \frac{k_B T}{2} \cdot \ln\left(\frac{N_C}{N_D}\right) \qquad \text{for n-doping} \qquad (2.18)$$

$$E_F = E_V + \frac{k_B T}{2} \cdot \ln\left(\frac{N_V}{N_A}\right) \qquad \text{for p-doping} \qquad (2.19)$$

The influence of E_F on the Fermi-Dirac distribution function f_{FD} and hence on the density of free electrons n_e, being the integrated product of f_{FD} and the density of states DOS, is displayed in figure 2.2. It is drawn for the case of n-doping, hence E_F shifts towards E_C. Two Fermi-Dirac distribution functions with different values of E_F, corresponding to different doping concentrations, are drawn in part (a). E_{F1} is chosen to be 200 meV below E_C, E_{F2} is 50 meV larger and hence 150 meV below E_C. In part (b) of the figure, the DOS is sketched, showing a square root dependency on the energy above the conduction band minimum E_C, compare equation (2.6). Finally, the products of density of states and the two different Fermi-Dirac distribution functions are drawn in part (c). These products correspond to the differential density of free electrons $n_e'(E)$, as shown by equation (2.2). Therefore, the areas under the curves are the total densities of free electrons n_{e1} and n_{e2}, respectively, compare equation (2.1) on page 6. For the chosen values of E_{F1} and E_{F2}, the density of free electrons n_{e2} is 7 times larger than n_{e1}, which displays the strong influence of the Fermi level position

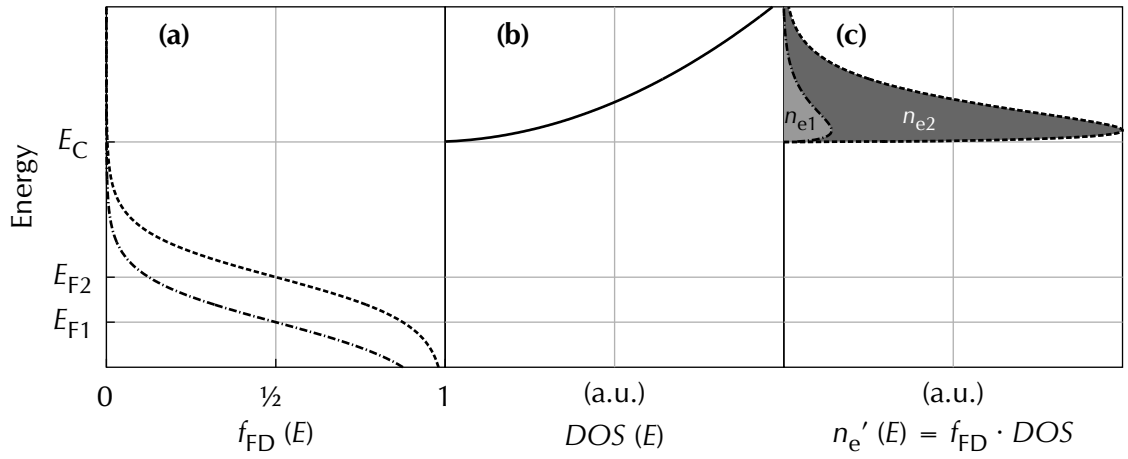

Figure 2.2: *Influence of Fermi level E_F on Fermi-Dirac distribution function $f_{FD}(E)$ and density of free electrons n_e for n-doping: (a) $f_{FD}(E)$ for two different positions of E_F below the conduction energy E_C, $E_{F1} = E_C - 200\,meV$ and $E_{F2} = E_C - 150\,meV$ (b) density of states $DOS(E)$ (c) product of $f_{FD}(E)$ and $DOS(E)$, displaying the strong influence of E_F on the density of free electrons n_e corresponding to the area under the curve.*

on the density of free electrons. An analogous picture can be drawn for p-doping, where E_F shifts towards the E_V and increases the density of free holes n_h.

Extremely high doping concentrations result in the Fermi level approaching the band edge. At a difference less than $2\,k_B T$, the semiconductor properties are vanishing and metallic behavior is observed. Furthermore, the Boltzmann approximation for the Fermi-Dirac distribution function is not valid for these so-called degenerate semiconductors and the equations can only be solved numerically.

2.1.3 Charge Carrier Transport

Free charges (holes in the valence band and electrons in the conduction band) are in constant motion due to their thermal energy. Besides this random thermal movement, an ordered/directed transport is possible under two conditions: Diffusion transport due to a gradient in the density of free charge carriers and hence E_F in the material and drift transport due to the presence of an electrical field.

Diffusion transport is the thermally driven motion of charges from regions of higher to regions of lower charge carrier concentration. Hence, diffusion transport takes place if a gradient in the density of free charge carriers is present in the material. Fluctuations of the charge carrier concentration can be generated for example by different temperatures in the material (compare section 2.3.1) or by local excess carrier generation.

Drift transport is the directed motion of charges, driven by the presence of an electric field $\mathscr{E}$. Each electron carries one negative elementary electric charge $-e$, whereas a hole (being an unoccupied electron state) carries $+e$. An electric field leads to a Coulomb[‡] force accelerating electrons and holes in opposite directions.

The mean drift velocity v_d of the charges in direction of the force is proportional to the electric field $\mathscr{E}$. The proportionality factor of the unit $\mathrm{cm^2/Vs}$ is called the mobility μ and is usually different for electrons and holes:

$$v_d^e = \mu_e \cdot \mathscr{E} \qquad\qquad v_d^h = \mu_h \cdot \mathscr{E}\ . \tag{2.20}$$

In a general case, e.g. for non-isotropic materials, the mobility is a tensor and equation (2.20) must be read vectorially. The mobility of charges in a semiconductor depends on many parameters, e.g. morphology, density of free charge carriers, electric field and temperature. At low temperatures, the mobility is limited by scattering at ionized impurities, due to the low energy and hence low velocity of the charge carriers. Therefore, a decrease in temperature usually leads to a decrease in mobility. At high temperatures on the other hand, the charge carrier motion is disturbed by lattice vibrations, so-called phonons, leading to a decreasing mobility as well. In the temperature region between these two regimes, typically around room temperature, the mobility has a maximum.

[‡] after French scientist Charles Augustin de Coulomb [Cou85] (1736–1806)

As the electric field $\mathscr{E}$ is defined as the gradient of the electric potential V, a field across a material can be generated by applying different electrical potentials to either side of the material. Applying a voltage V between two parallel sheet contacts of distance d_c the resulting electric field $\mathscr{E}$ is

$$\mathscr{E} = \frac{dV}{dx} = \frac{V}{d_c} \,. \tag{2.21}$$

The drift of charges towards the contacts sum up to a current flow I through the material, following Ohm's[‡] law. In case of a material cross-section A, Ohm's law can be written as

$$I = \frac{1}{R} \cdot V = \frac{A\sigma}{d_c} \cdot V \Rightarrow \sigma = \frac{I}{V} \cdot \frac{d_c}{A} \,, \tag{2.22}$$

with the conductivity σ of the material defining its resistance $R = {}^{d_c}/_{A\sigma}$. The typical unit used for the conductivity of semiconductors is ${}^{S}/_{cm} = {}^{1}/_{\Omega\,cm}$. Applying a voltage V and measuring the current response I, the conductivity of the material can be calculated using equation (2.22).

Instead of the total current I, the geometry independent current density $j = {}^{I}/_{A}$ is used to compare different measurements. The current density can be written as the sum of electron and hole contributions, each being the product of the density of free charge carriers and their mean velocity:

$$j = e n_e v_d^e + e n_h v_d^h \,. \tag{2.23}$$

Combining equations (2.20)-(2.23), the conductivity of a semiconductor can be written as

$$\sigma = e \cdot n_e \cdot \mu_e + e \cdot n_h \cdot \mu_h \,. \tag{2.24}$$

[‡]after German scientist Georg Simon Ohm [Ohm27] (1789–1854)

2.2 Organic Semiconductors

In this section, molecular organic semiconductors (OSCs) are introduced and the main differences to conventional semiconductors (CSCs) are discussed. For more general properties of organic semiconductors, the reader is referred to the textbooks [Pop99,Sch05].

Organic, i.e. hydrocarbon-based, chemistry allows for the synthesis of a large variety of molecules. Despite most of the organic molecules being electrical isolators, in the last century semiconducting [Bol63], metallic [Fer73,Col73] and even superconducting [Jér80] organic molecules have been discovered. As shown in figure 1.1 on page 2, in recent years, the topic of conducting organic compounds gained more and more attention and in 2000, Heeger, MacDiarmid, and Shirakawa were awarded with the Nobel Prize in chemistry for their work on highly conducting conjugated polymers [Nor00]. Since this thesis focuses on semiconductor physics, only this class of materials will be discussed in the following.

When atoms form molecules, the atomic orbitals (being solutions to the Schrödinger[‡] equation and describing the probability of an electron to be located in a specific spatial region) are combined to molecular orbitals, whereby the number of molecular valence orbitals equaling the total number of atomic valence orbitals prior to the formation of the molecule. Since electrons are fermions and hence are subject to the Pauli[§] exclusion principle, each orbital can only be occupied by two electrons of opposite spin. Orbitals are populated by electrons according to their energy levels.

Carbon, being the building block of organic molecules, has six electrons: two core electrons and four valence electrons. The first and second s-orbitals are populated each by two electrons and the remaining two electrons are located in two of three degenerate 2p-orbitals. This configuration is abbreviated as $1s^2 2s^2 2p^2$. Whereas s-orbitals are symmetric around the nucleus, the three 2p-orbitals are dumbbell-shaped [Upp74], as drawn in figure 2.3 (a). Upon formation of molecules, for carbon atoms it is energetically favorable that the valence orbitals rearrange and form hybrid orbitals. Depending on the number of contributing atomic p-orbitals these hybrids are called sp, sp^2 or sp^3. In case of sp^2 configuration, the four valence electrons populate three degenerate hybrid sp^2-orbitals and one remaining p-orbital. The sp^2-orbitals align in one plane, perpendicular to the remaining p-orbital. Adjacent carbon atoms form covalent σ-bonds with their hybrid orbitals, which are located between the atoms. The remaining p-orbitals form a second so-called π-bond parallel to the plane of the sp^2-orbitals, as sketched in figure 2.3 (a). This π-bond leads to delocalization of the π-electrons, which can extend over many atoms, as drawn in figure 2.3 (b) for the case of six carbon atoms forming a benzene ring. Hence, the electrons in the delocalized π-system are no longer constrained to single atoms and owing to this delocalization, electron transport through the molecule is significantly improved. Inter-molecular electron transport is enabled via interactions between the

[‡] after Austrian scientist Erwin Rudolf Josef Alexander Schrödinger [Sch26] (1887–1961)

[§] after Austrian scientist Wolfgang Pauli [Pau25] (1887–1961)

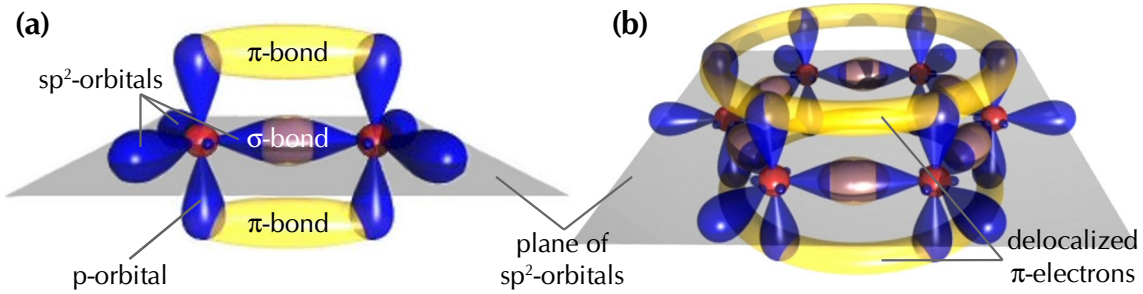

Figure 2.3: *(a) Orbitals and bonds for two sp^2-hybridised carbon atoms, as in ethylene. (b) Delocalized π-electron-system in a benzene ring consisting of six sp^2-hybridised carbon atoms. Images taken from reference [OW] and modified.*

π-systems of adjacent molecules and tunneling of electrons, so-called hopping. For more information on the fundamental physics of molecules, the reader is referred to the textbooks [Hak06,Dem09].

The energetic difference between the highest occupied and the lowest unoccupied π-orbital is smaller compared to the hybrid sp^2-orbitals. Thus, in a molecule with delocalized π-system, the highest occupied molecular orbital (HOMO) and the lowest unoccupied molecular orbital (LUMO) are typically delocalized π-orbitals. Since the energetic difference between HOMO and LUMO typically decreases with increasing the delocalization over more atoms, the design of molecules with desired energy levels is possible. If the energetic difference between HOMO and LUMO is small enough, the molecule can show semiconducting properties. Consequently, the HOMO level of a molecular semiconductor can roughly be compared to the valence band minimum of a conventional semiconductor and analogously the LUMO level to the conduction band minimum.

Organic semiconductors can be divided into two major categories: small molecules and polymers. Semiconducting small molecules include aromatic hydrocarbon compounds like anthracene and pentacene; as well as pyrenes, perylens, oligothiophenes and phtalocyanines. Polymeric organic semiconductors include aromatic compounds like polythiophenes, polyacetylene and their derivatives. While layers of small molecular semiconductors are usually deposited by thermal evaporation in vacuum, the heavier polymers are commonly processed from solution. In this work, only thermally deposited small molecules are investigated.

The main difference between OSCs and CSCs is that instead of covalently bound atoms, the molecules interact via the weaker van der Waals[‡] forces. As a result, OSCs are usually amorphous or polycrystalline and have lower dielectric constants in the order of $\varepsilon \approx 3$ to 5 compared to CSCs with $\varepsilon \approx 10$ to 15 [Rie11a]. The lower ε results in a lower shielding of charges and thus to a stronger Coulomb interaction between them, compared to CSCs.

One advantage of the weak van der Waals interaction between the molecules and the disordered structure of OSCs is that they are less sensitive to impurities and struc-

[‡]after Dutch scientist Johannes Diderik van der Waals [Waa73] (1837–1923)

tural defects than CSCs. They can inherit impurity levels of up to a fraction of percent and still work well[Rie11a], whereas such high concentrations would render CSCs completely useless. As a consequence, intentional doping concentrations have to be considerably higher for OSCs, which is discussed in section 2.2.3.

2.2.1 Charge Carrier Transport

Due to the weak inter-molecular interaction, non-crystalline OSCs usually do not form a band structure of allowed and forbidden energy regions (compare section 2.1.1). Instead, the charge transport occurs via hopping processes from one molecule to the other. One characteristic attribute for hopping transport is its temperature dependence. While for CSCs the mobility decreases at elevated temperatures due to scattering of the charges at lattice vibrations (compare section 2.1.3), for OSCs the hopping probability and hence the mobility increase with temperature. Usually, the conductivity σ is found to be thermally activated as

$$\sigma(T) = \sigma_0 \exp\left(-\frac{E_{\mathrm{act},\sigma}}{k_\mathrm{B} T}\right), \tag{2.25}$$

where k_B is Boltzmann's constant, σ_0 is interpreted as theoretical maximum of the conductivity and $E_{\mathrm{act},\sigma}$ is the activation energy of the conductivity.

The temperature dependence of the mobility may differ from a simple activated case to a model where hopping along a manifold of states is assumed[Bäs82,Vis98]. Besides the temperature, the mobility is influenced by the density of free charge carriers and applied external fields as well, but this interaction is not completely understood at present. For further information on charge transport in organic molecules, the reader is referred to the review articles[Tes09,Tro11]. An overview about traps in organic semiconductors is given in reference[Sch04].

2.2.2 Density of States

The density of states of organic semiconductors has a different distribution than for conventional semiconductors. While for CSCs a square root shaped *DOS* can be approximated near the band edges, compare section 2.1, for OSCs usually a Gaussian[‡] distribution is assumed[Sch03,Tie12], which accounts for the energetic broadening of molecular energy levels due to the disorder as well as intra- and inter-molecular interactions and orientations. The *DOS* of OSCs can be modeled by the following equation, which is drawn in figure 2.4:

$$DOS(E) = \frac{n_\mathrm{H}}{\sqrt{2\pi}\,\sigma_\mathrm{G}} \exp\left(-\frac{(E - E_\mathrm{G})^2}{2\sigma_\mathrm{G}^2}\right). \tag{2.26}$$

[‡]after German scientist Johann Carl Friedrich Gauß (1777–1855)

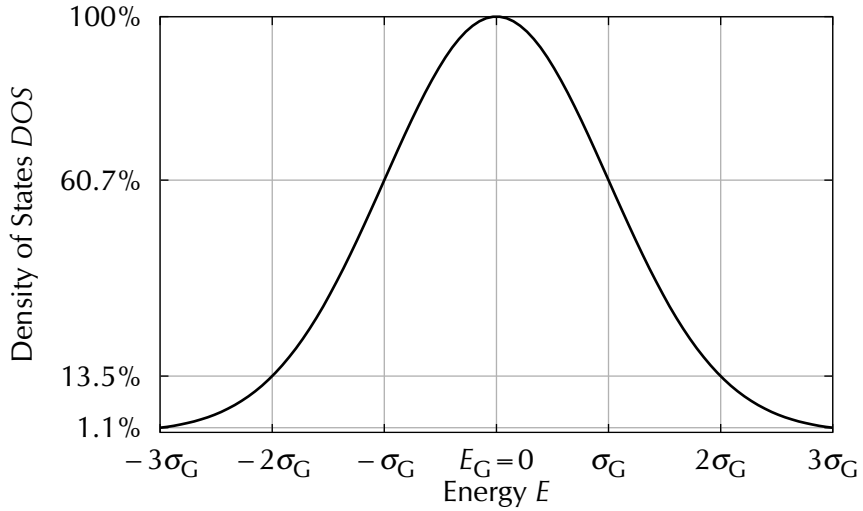

Figure 2.4: *Sketch of a normalized Gaussian distributed density of states, following equation (2.26) and arbitrary positioned at $E_G = 0$.*

Here, E_G is the position of the maximum of the distribution and σ_G is the standard deviation, being a measure for the width of the Gaussian distribution. At $E = E_\mathrm{G} \pm \sqrt{2}\,\sigma_\mathrm{G}$ the distribution is reduced to the maximum divided by Euler's[‡] number. As each molecule is assumed to be able to contribute one state, integration of $DOS(E)$ over all energies yields the total density of (host) molecules n_H.

Similar to a square root shaped density of states, for a Gaussian shaped *DOS* it is possible to solve equation (2.1) on page 6 for the density of free charge carriers $n_\mathrm{e/h}$ analytically, when using the Boltzmann approximation for the Fermi-Dirac distribution function [Tie12]. For clarity, additional steps not included in the original publication are shown here, as well as the adoption of this approach for electrons instead of holes:

$$n_\mathrm{e} = \int_{-\infty}^{+\infty} \overbrace{\frac{n_\mathrm{H}}{\sqrt{2\pi}\,\sigma_\mathrm{G}} \exp\left(-\frac{(E-E_\mathrm{G})^2}{2\sigma_\mathrm{G}^2}\right)}^{DOS(E)} \cdot \overbrace{\exp\left(-\frac{E-E_\mathrm{F}}{k_\mathrm{B}T}\right)}^{f_\mathrm{B}(E)} dE \tag{2.27}$$

with $x := E - E_\mathrm{G}$, $C_1 := \frac{n_\mathrm{H}}{\sqrt{2\pi}\sigma_\mathrm{G}}$ and $C_2 := \frac{\sigma_\mathrm{G}^2}{k_\mathrm{B}T}$ this becomes

$$n_\mathrm{e} = C_1 \int_{-\infty}^{+\infty} dx \exp\left(-\frac{1}{2\sigma_\mathrm{G}^2}\left(x^2 + 2xC_2 + 2C_2\left(E_\mathrm{G} - E_\mathrm{F}\right)\right)\right) \tag{2.28}$$

[‡]after Swiss scientist Leonhard Euler (1707–1783)

with $\left(x+C_2\right)^2 = x^2 + 2xC_2 + C_2^2$ this simplifies to

$$n_e = C_1 \int_{-\infty}^{+\infty} dx \exp\left(-\frac{1}{2\sigma_G^2}\left(\left(x+C_2\right)^2 - C_2^2 + 2C_2\left(E_G - E_F\right)\right)\right) \tag{2.29}$$

$$= C_1 \exp\left(-\frac{-C_2^2 + 2C_2\left(E_G - E_F\right)}{2\sigma_G^2}\right) \int_{-\infty}^{+\infty} dx \exp\left(-\frac{(x+C_2)^2}{2\sigma_G^2}\right) \tag{2.30}$$

$$= C_1 \exp\left(+\frac{\sigma_G^2}{2(k_B T)^2} - \frac{E_G - E_F}{k_B T}\right) \int_{-\infty}^{+\infty} dx \quad \underbrace{\exp\left(-\frac{\left(x + \frac{\sigma_G^2}{k_B T}\right)^2}{2\sigma_G^2}\right)}_{\text{= definition of Gaussian, compare (2.26)}} \tag{2.31}$$

$$= n_H \frac{1}{\sqrt{2\pi}\sigma_G} \exp\left(+\frac{\sigma_G^2}{2(k_B T)^2} - \frac{E_G - E_F}{k_B T}\right) \quad \cdot \sqrt{2\pi}\,\sigma_G \tag{2.32}$$

$$n_e = n_H \exp\left(-\frac{\left(E_G - \frac{\sigma_G^2}{2k_B T}\right) - E_F}{k_B T}\right). \tag{2.33}$$

An analogous calculation [May10] can be performed for p-doping to obtain the density of free holes n_h, when a corresponding density of states is used, (having its maximum below E_F)

$$n_h = n_H \exp\left(-\frac{E_F - \left(E_G + \frac{\sigma_G^2}{2k_B T}\right)}{k_B T}\right). \tag{2.34}$$

These terms are similar to the equations for CSCs:

$$n_e = N_C \exp\left(-\frac{E_C - E_F}{k_B T}\right) \qquad (2.7) \qquad\qquad n_h = N_V \exp\left(-\frac{E_F - E_V}{k_B T}\right). \qquad (2.8)$$

In case of a Gaussian distributed density of states, the prefactors N_C and N_V are replaced by the density of molecules n_H and the energy level of the conduction band is replaced by a term that depends on the position of the maximum E_G and the width σ_G of the Gaussian distribution.

If E_F is close to E_G and hence f_B is strongly overlapping with the density of states, the Boltzmann approximation is not valid. Here, the Fermi-Dirac distribution function $f_{FD}(E)$ has to be used and the integral (2.1) solved numerically. Both functions, f_{FD} and f_B, are drawn in figure 2.5 together with a Gaussian *DOS*, where E_F is arbitrary placed at a distance of $4 \cdot \sigma_G$ from the E_G. The product of distribution function and *DOS* is the differential density of free electrons $n_e'(E)$ and is shown as inset. The area under that curve corresponds to density of free electrons n_e, analogously to figure 2.2 on page 11. It can clearly be seen that using f_B, n_e would be overestimated as the contribution for $E < E_F$ is strongly overrated. Therefore, in the following all calculations of $n_{e/h}$ are performed numerically, using f_{FD}.

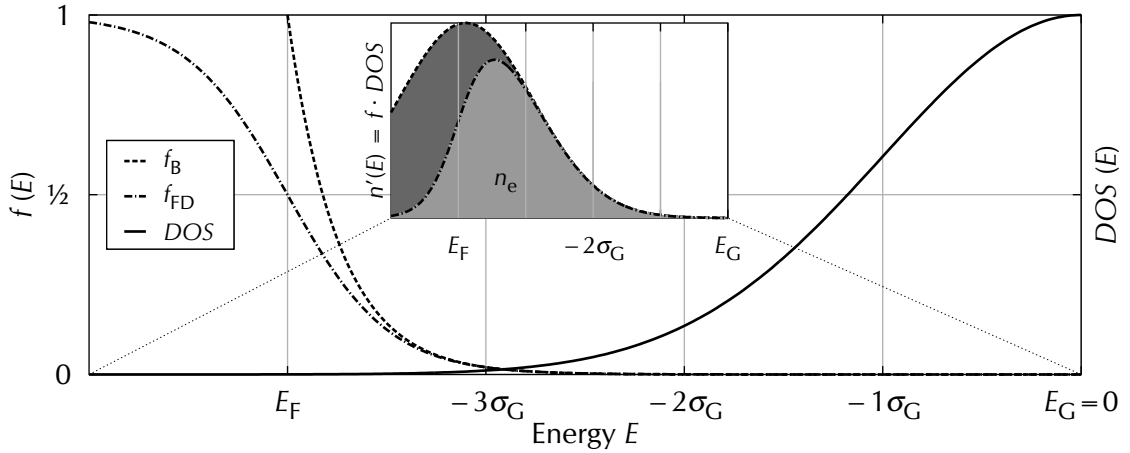

Figure 2.5: *Comparing the influence of Boltzmann f_B and Fermi-Dirac f_{FD} distribution functions on the density of free electrons n_e for the case of E_F close to E_G, here at a distance of $4\sigma_G$. Inset: product of DOS and f, being the differential density of free electrons $n'_e(E)$, calculated for f_{FD} (light gray) and overestimation via f_B (dark gray). Parameters: $\sigma_G = 100\,meV$, $E_F = Eg - 4 \cdot \sigma_G$, $T = 25\,°C$.*

2.2.3 Doping of Organic Semiconductors

Doping of conventional semiconductors was the key element that led to the breakthrough of semiconductor technology, as it allows for control of the majority charge carriers and hence the design of p-n-junctions, the building block for most modern electronic devices. Furthermore, doping allows for adjusting the conductivity as well as the position of the Fermi level position in a layer, enhancing device design freedom and performance. Similar to conventional semiconductors, it is possible to dope organic semiconductors by adding electron acceptors or electron donors to the layer, which drastically increases the density of free charge carriers. Hence, doping of organic semiconductors raises the conductivity by several orders of magnitude and furthermore allows to overcome contact limitations between metal contacts and organic layers and thus improves charge injection and extraction, which are crucial for efficient devices. Besides increasing the density of free charge carriers, doping can also effect the charge carrier mobility by either filling of traps or by generation of additional traps [Sch04,Ark05b]. In the following, a brief overview about history and different approaches for doping of organic layers is given. For more details, the reader is referred to the textbook chapters [Rie11a,Lüs12,Leo13] and the review articles [Wal07,Lüs13].

2.2.3.1 History of Doping Experiments

First attempts of p-doping of organic semiconductors have been reported as early as 1954 when Akamatu et al. [Aka54] used the halogen bromine as acceptor in perylenes. Later, extensive studies on p-doping using halogen gases have been performed [Cur62,Yam79]. Oxygen-exposure can lead to p-doping as well [Vät96,Ham93]. Suc-

cessful n-doping has first been reported [Ram90,Had91] in 1990, when alkali metals like cesium were used as donors and have recently been theoretically described [Mit12a].

A common problem of using atoms to dope an OSC is the diffusion of atoms through the device that leads to a lowering of device efficiency and lifetimes [Wal07]. This issue can be overcome by using larger or heavier compounds, like organic molecules. A molecular n-dopant donates an electron from its HOMO to the LUMO of the host material, whereas a molecular p-dopant accepts an electron from the HOMO of the host into its LUMO, creating a hole at the host. Thus, for successful doping suitable energy levels of host and dopant are required.

The first successful p-doping of an OSC using an organic dopant has been shown by Kearns et al. [Kea60] in 1960. Molecular p-dopants are strong electron accepting molecules with a deep lying LUMO level. They typically contain fluorine, the most electronegative element in the periodic table. In recent years, heavy metal oxides like MoO_3 or WO_3 have gained attention as these molecules have been reported to be less diffusive [Cha06] and are able to dope materials with HOMO levels as deep as 6 eV [Mey09,Krö09].

It took 40 more years until the first organic n-dopant has been reported by Nollau et al. [Nol00] in 2000. The reason is that n-dopants need to have shallow HOMO levels (with respect to the vacuum level) in order to donate an electron into the LUMO of the host. Therefore, they are highly reactive materials that are usually unstable in air and hence require handling in an inert atmosphere.

The n-dopants reactivity to air can be alleviated by using stable precursor compounds which form the active dopant compound in-situ during depositing of the doped layer in vacuum. This approach has been first presented by Werner et al. [Wer03b] using the cationic salt pyronin B chloride which upon vacuum deposition separates from its chloride anion. Recently, a different approach has been presented by Guo et al. [Guo12], who used dimers that were cleaved during deposition, yielding the advantage of less unintended side products that could interfere with the doping process.

2.2.3.2 Doping Mechanisms

Doping is usually described as a two-step process. First, the dopant is ionized, transferring an electron (or hole) to the host and leaving a hole (electron) on the dopant molecule behind. Afterwards, the electron (hole) has to dissociate against the Coulomb attraction of the hole (electron) left on the dopant. This principle holds for conventional and organic semiconductors.

In case of molecular doping of an organic host, a suitable dopant molecule is required for the first step. The ionization energy (IE) corresponds to the difference between the HOMO and the vacuum level, compare figure 2.6 (a), and is a measure of the energy it takes to remove the least bound electron from the molecule. On the other hand, the difference between the LUMO and the vacuum level is referred to as electron affinity (EA). A molecule with a low IE is likely to donate electrons and can therefore be used as n-dopant, whereas p-dopants typically have high EA to allow for electron accepting,

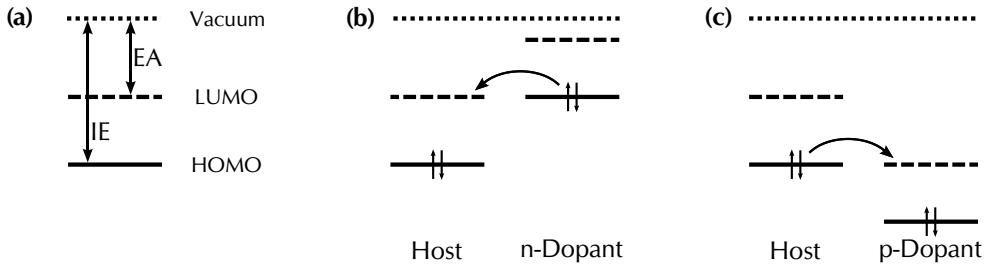

Figure 2.6: *Sketch of doping principle for OSCs. (a) Relation of HOMO and LUMO to vacuum level via ionization energy (IE) and electron affinity (EA). (b) n-doping: an electron is transfered from the HOMO of the dopant to the LUMO of the host. (c) p-doping: an electron is transfered from the HOMO of the host to the LUMO of the dopant, generating a hole at the host.*

as sketched in figure 2.6 (b) and (c). The IE can be measured using ultraviolet photoelectron spectroscopy (UPS) in vacuum with a typical accuracy of $\pm 0.13\,\mathrm{eV}$ [Olt10]. The EA on the other hand can be studied by inverse photoemission spectroscopy (IPES) in vacuum, which due to a smaller cross-section has a lower accuracy, typically around $\pm 0.30\,\mathrm{eV}$. Recently, a high resolution IPES setup has been presented [Yos12] that uses electrons of kinetic energies below $4\,\mathrm{eV}$ and is a promising method for measuring the EA with higher accuracy. Soluble compounds can be probed by the wet chemical method of cyclic voltammetry (CV), which allows for an estimation of HOMO and LUMO levels, but as the energy levels usually differ between solutions and deposited layers, for the samples investigated in this thesis, values determined by UPS and IPES are preferred. As it is difficult to measure the molecular energy levels of dopants deposited into a layer of host molecules, today it is not clear if the energy levels of the dopants are affected by the surrounding host molecules. Therefore, in this work the energy levels of dopant molecules deposited into layers of hosts molecules are assumed to remain at the levels determined for pure dopant layers. Besides suitable energy levels, overlap of orbitals between host and dopant, as well as morphological properties are essential for charge-transfer.

The second step of doping, the dissociation of the generated charge pair, is easier to achieve for CSCs, as their dielectric constants ($\varepsilon \approx 10$ to 15) are higher than for OSCs ($\varepsilon \approx 3$ to 5) [Rie11a]. Therefore, the Coulomb interaction between charges is much stronger in case of OSCs, requiring a larger distance between the charges to overcome the attraction.

Mityashin et al. [Mit12b] calculated the potential landscape around an ionized dopant for the model system of pentacene doped by F_4-TCNQ[‡], as these molecules have a similar size as well as suitable energy levels. Varying the concentration of dopants in the system, they found that a certain minimum concentration of dopants is required in order to change the potential landscape sufficiently to allow for dissociation and hence generation of free charges. This finding is different to CSCs, where no fundamental lower limit of doping concentration is known. Their results explain the much higher doping concentrations needed for OSCs, compared to CSCs.

[‡]compare section 3.2 for details on the materials

Salzmann et al.[Sal12] introduced an alternative model for the doping process of OSCs, suggesting the formation of a hybrid of host and dopant by a hybridization of their orbitals. They conclude that due to an offset of the energy levels of host and hybrid state, only a fraction of the hybrids can be ionized at finite temperature and thus the maximum density of free charge carriers is limited.

2.2.3.3 Units of Doping Concentration

While in CSCs typically doping concentrations are in the part per million (ppm) range, for OSCs much higher concentrations, typically in the range of several percent are required. The reasons are the disordered structure that leads to the lower charge carrier mobilities and the high density of traps, which has to be overcome by doping, as well as the above discussed required change in potential landscape. In OSCs, the doping concentration C is usually expressed either in terms of weight (e.g. wt%) or in terms of molecule numbers (e.g. mol%). Using terms of weight is more technically oriented, as during sample fabrication typically the weight of the materials is directly controlled. Expressing C in terms of numbers of molecules, on the other hand, is physically easier to interpret but requires the knowledge of the molar mass M of each compound, which for proprietary materials or compounds that transform during deposition may not be available. As the structures of all materials used in this thesis are known, the doping concentration can be expressed in terms of numbers of molecules. Thereby, it is assumed that the dopant molecules substitute host molecules and therefore adopt the density of the host. The unit molar ratio (MR), being the ratio of dopant to host molecules, is a relevant figure for quantitative evaluations and hence chosen as unit for all doping concentrations in the following:

$$C \text{ in MR} = \frac{n_\mathrm{D}}{n_\mathrm{H}} , \tag{2.35}$$

with density of host molecules n_H and density of dopant molecules n_D. Besides MR, in literature frequently the unit molar percent (mol%) is found, being defined as the relative number/density of dopant molecules to the total number/density of molecules

$$\text{mol\%} = 100\% \cdot \frac{n_\mathrm{D}}{n_\mathrm{H} + n_\mathrm{D}} . \tag{2.36}$$

Analogously to mol%, the unit weight percent (wt%) is defined as ratio of the mass of dopant material to the total mass

$$\text{wt\%} = 100\% \cdot \frac{m_\mathrm{D}}{m_\mathrm{H} + m_\mathrm{D}} . \tag{2.37}$$

Conversion between the different units can be performed via

$$\text{MR} = \frac{\text{mol\%}}{100\% - \text{mol\%}} \qquad \text{mol\%} = 100\% \cdot \frac{\text{MR}}{\text{MR} + 1} \tag{2.38}$$

$$\text{MR} = \frac{M_\mathrm{H}}{M_\mathrm{D}} \cdot \frac{\text{wt\%}}{100\% - \text{wt\%}} \qquad \text{wt\%} = 100\% \cdot \left(1 + \frac{M_\mathrm{H}}{M_\mathrm{D}} \cdot \frac{1}{\text{MR}}\right)^{-1} \tag{2.39}$$

with the molar masses of host and dopant, M_H and M_D, respectively.

2.2.3.4 Calculating Molecular Densities

In an undoped layer, the density of molecules n_{Mol} can be calculated from the molar mass M and the density ρ of the material, using the Avogadro[‡] constant N_{Avo}:

$$n_{\mathrm{Mol}} = \frac{N_{\mathrm{Avo}} \cdot \rho}{M} \ . \tag{2.40}$$

In a doped layer, n_{Mol} is the sum of partial densities of host n_{H} and dopant n_{D} molecules. Assuming dopant molecules to neatly replace host molecules one by one, the total density of molecules n_{Mol} is unchanged upon doping. Expressing the doping concentration C in terms of molar ratio MR, the following expressions for n_{H} and n_{D} can be derived:

$$n_{\mathrm{Mol}} = n_{\mathrm{H}} + n_{\mathrm{D}} \tag{2.41}$$

$$C = \frac{n_{\mathrm{D}}}{n_{\mathrm{H}}} \tag{2.42}$$

$$n_{\mathrm{H}} = \frac{n_{\mathrm{Mol}}}{1+C} \qquad \text{and} \qquad n_{\mathrm{D}} = \frac{n_{\mathrm{Mol}} \cdot C}{1+C} \ . \tag{2.43}$$

For dopant densities much greater than the intrinsic charge carrier density n_{i}, the doping efficiency η_{dop} is defined as the ratio of the density of free charge carriers (electrons or holes) $n_{\mathrm{e/h}}$ to the density of dopant molecules n_{D}, analogously to equation (2.13) for CSCs:

$$\eta_{\mathrm{dop}} = \frac{n_{\mathrm{e/h}}}{n_{\mathrm{D}}} = n_{\mathrm{e/h}} \cdot \frac{1+C}{n_{\mathrm{Mol}} \cdot C} \tag{2.44}$$

$$\Rightarrow n_{\mathrm{e/h}} = \eta_{\mathrm{dop}} \cdot n_{\mathrm{Mol}} \cdot \frac{C}{1+C} \ . \tag{2.45}$$

[‡]after Italian scientist Lorenzo Romano Amedeo Carlo Avogadro, Conte di Quaregna e Cerreto (1776–1856)

2.3 Seebeck Effect

The Seebeck effect is of great interest for semiconductor physics, as it allows for determination of the type of the majority charge carriers as well as the relative position of the Fermi level with respect to the transport level.

2.3.1 Phenomenological Description

In 1821, the Estonian-German physicist Thomas Johann Seebeck discovered [See23] that a magnetic force arises when junctions of two different metal wires are heated to different temperatures. He detected the force by a compass needle and therefore named his finding the *thermomagnetic* effect. Seebeck interpreted this effect to be the origin of the earth's magnetic field, due to the veins of metals and ores in the ground [See23]. Nowadays we know that his conclusion is wrong since the earth's magnetic field is explained by the motion of molten iron alloys in the earth's core. Furthermore, today it is proven that in Seebeck's discovery not a magnetic force is generated in the first place, but a voltage gradient that drives charges along the wires, which leads to the magnetic field he detected. Hence, his discovery is now called *thermoelectric* or Seebeck effect. This effect is observed for both, metals and semiconductors, but not for superconducting materials (at temperatures below their critical temperature), as a resistance free material cannot hold a voltage gradient.

Phenomenologically, the Seebeck effect can be understood as follows: In a metal or semiconductor, the energetic distribution of the free charge carriers is shifted to higher energy states upon heating (compare section 2.1). Thus, if one side of the material is hotter than the other, the charge carriers on the hotter side have higher energies on average. This leads to a displacement diffusion current (compare section 2.1.3) towards the cold side, resulting in a charging of the two sides of the material. With increasing charge accumulation at the sides, an electric field opposite to the diffusion current builds up, limiting the total voltage being generated. If electrons are the dominating charge carriers, the cold side will be charged negatively, whereas for hole dominated materials the cold side is charged positively. Therefore, the Seebeck effect can be used to identify the type of dominating charge carriers in the material.

Different devices employ the Seebeck effect. Examples are a prominent class of thermometers, the thermocouples (used in our setup to measure the temperatures of the material sources, as discussed in section 3.1.1), as well as thermoelectric generators, which generate electricity from temperature gradients. Future applications in space flight might be possible, as the large temperature difference between space and the inside of the shuttle are beneficial for this kind of power supply. Recently, Kraemer et al. published [Kra11] a design for a solar driven thermoelectric generator as alternative to photovoltaic cells with a peak efficiency of 4.6 %. Requirements for materials for thermoelectric generators are a strong Seebeck effect and high electrical conductivity combined with low thermal conductivity. Insects utilize the Seebeck effect is as well: The cuticle of hornets for example, has been reported [Shi81,Bar09] to show positive

and negative values, for the yellow-colored and brown-colored cuticle, respectively. It is speculated that the hornets use this for temperature detection. Recently, the spin Seebeck effect has been reported, which should allow for spin-voltage generators, being crucial for driving spintronic devices[Uch08].

2.3.2 Definition and Measurement of the Seebeck Coefficient

If two sides of a material are held at different temperatures, a voltage V is generated, which is proportional to the temperature difference ΔT for small ΔT. The proportionality is given by a material property called Seebeck coefficient S, which is defined for spatial steps of infinitesimally small temperature differences along the material, as

$$S(T_\mathrm{m}) := \lim_{\Delta T \to 0} \frac{\Delta V}{\Delta T} \,. \tag{2.46}$$

The total voltage difference V_S between the ends of the material is given by the path integral along the material[Wag07]:

$$V_\mathrm{S} = \int_{x_1}^{x_2} S(T)\, \partial_x T \; dx = \int_{T_1}^{T_2} S(T)\, \partial_x T \; dT \,. \tag{2.47}$$

Choosing $T_2 - T_1$ to be small enough that the Seebeck coefficient $S(T)$ can be considered constant in the range of T_1 to T_2 and additionally assuming a linear temperature gradient, equation (2.47) can be simplified to

$$V_\mathrm{S} = S \int_{T_1}^{T_2} \partial_x T \; dT = S \cdot (T_2 - T_1) \,. \tag{2.48}$$

In general, the Seebeck coefficient is temperature-dependent and will therefore be written as $S(T_\mathrm{m})$ in the following, with T_m being the mean temperature of T_1 and T_2 and the applied temperature difference is $T_\mathrm{d} = T_2 - T_1$.

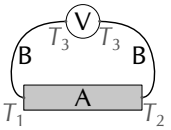

In order to measure the thermoelectric voltage V_S along a material A (with a Seebeck coefficient S_A), two points with temperatures T_1 and T_2 have to be connected by wires of a material B (with Seebeck coefficient S_B) to a voltmeter that is at a temperature T_3. It is conventional to contact the *high* input of the voltmeter to the *cold* side. Consequently, a positive sign of the voltage is obtained if holes are the dominating charge carriers. The total measured thermoelectric voltage is the sum of the individual contributions:

$$\begin{aligned} V_\mathrm{S} &= S_\mathrm{B} \cdot (T_3 - T_1) + S_\mathrm{A} \cdot (T_1 - T_2) + S_\mathrm{B} \cdot (T_2 - T_3) \\ &= (S_\mathrm{A} - S_\mathrm{B}) \cdot (T_1 - T_2) \,, \end{aligned} \tag{2.49}$$

which is independent of the temperature T_3 at the voltmeter, but affected by the Seebeck coefficients of the connecting wires S_B.

The Seebeck coefficients of semiconductors are in the range of several hundred to thousand $\mu\mathrm{V/K}$, whereas for metals only few $\mu\mathrm{V/K}$ are measured ($S_\mathrm{SC} \gg S_\mathrm{metal}$). Copper,

for example, has $S \approx 2\,^{\mu V}/_{K}$ at room temperature [Dem04]. Hence, if a metal is used to contact a voltmeter to the ends of an investigated semiconductor, the contribution of the wires in equation (2.49) can be neglected and the Seebeck coefficient is

$$S_A \approx \frac{V_S}{T_1 - T_2} \,. \tag{2.50}$$

2.3.3 Correlation to Semiconductor Energy Levels

2.3.3.1 Conventional Semiconductors

In 1971 Fritzsche published a correlation of the Seebeck coefficient and the energy levels of a semiconductor [Fri71]. He started with the Peltier‡ coefficient Π, which correlates to the Seebeck coefficient via the Thomson§ relation

$$\Pi = S \cdot T \,. \tag{2.51}$$

Π, on the other hand, is defined as the energy carried by the electrons per unit charge, whereas the energy is measured with respect to the Fermi level E_F. The contribution of each electron to Π is proportional to its relative contribution to the total conductivity, so Π can be written as [Fri71]

$$\Pi = -\frac{1}{e} \int_{-\infty}^{+\infty} (E - E_F) \, \frac{\sigma'(E)}{\sigma} \, dE \,, \tag{2.52}$$

with the differential conductivity $\sigma'(E)$ that can be defined by equations (2.24) and (2.2), introducing the energetic distribution of the mobility $\mu(E)$:

$$\sigma'(E)dE = e \cdot n'(E) \cdot \mu(E) \, dE = e \cdot DOS(E) \cdot f_{FD}(E) \cdot \mu(E) \, dE \,. \tag{2.53}$$

Integration gives the total conductivity

$$\sigma(E) = \int_{-\infty}^{+\infty} \sigma'(E) dE \,. \tag{2.54}$$

Using equation (2.51), the Seebeck coefficient can be written as

$$S = \frac{\Pi}{T} = -\frac{k_B}{e} \int_{-\infty}^{+\infty} \frac{E - E_F}{k_B T} \cdot \frac{\sigma'(E)}{\sigma} \, dE \,. \tag{2.55}$$

Fritzsche found that in case of one band only conduction with no states below the conduction band edge E_C (electron (e) conduction) or above the valence band edge E_V (hole (h) conduction), equation (2.55) can be simplified to

$$S = -\frac{k_B}{e} \left(\frac{E_C - E_F}{k_B T} + A_C \right) \qquad \text{for e-conduction} \tag{2.56}$$

$$S = +\frac{k_B}{e} \left(\frac{E_F - E_V}{k_B T} + A_V \right) \,. \qquad \text{for h-conduction} \tag{2.57}$$

‡after French scientist Jean Charles Athanase Peltier [Pel34] (1785–1845)

§after British scientist William Thomson, later 1st Lord Kelvin (1824–1907)

The terms A_C and A_V in the order of 1 account for the energetic dependency of the density of states $DOS(E)$ and the mobility $\mu(E)$ above E_C or below E_V. If the Fermi level is at a large distance to the corresponding band edge ($E_C - E_F \gg k_B T$ or $E_F - E_V \gg k_B T$), A_C and A_V can be neglected. This leads to a simplified version of the equations above:

$$S = -\frac{E_C - E_F}{e\,T} \qquad \text{for e-conduction} \tag{2.58}$$

$$S = +\frac{E_F - E_V}{e\,T}\ . \qquad \text{for h-conduction} \tag{2.59}$$

In conclusion, the sign of the Seebeck coefficient S identifies whether electrons or holes are the dominating charge carriers, whereas the value of S is correlated to the difference between the Fermi level and the corresponding band edge, E_C or E_V. In the following, the term Seebeck energy E_S will be used for this difference, which has a negative value for electron conduction and a positive value for hole conduction:

$$E_S := E_F - E_C \quad \text{or} \quad E_S := E_F - E_V\ . \tag{2.60}$$

Equations (2.58) and (2.59) can hence be simplified to

$$S = \frac{E_S}{e\,T} \quad \Rightarrow \quad E_S = S \cdot e \cdot T\ . \tag{2.61}$$

This relation allows for the direct correlation of thermoelectric measurements and the relative position of the Fermi level, using the same equation for both, electron and hole conduction. Therefore, Seebeck measurements are an important tool to investigate doped semiconductors.

One interesting phenomenon is that at high doping concentrations and low temperatures, a sign change of S can occur, as first reported by Geballe et al.[Geb55] for n- and p-doped silicon. The reason is that the role of host and dopant is exchanged and conduction along the ionized dopants, instead of along the host material, becomes the dominating transport mechanism.

2.3.3.2 Organic Semiconductors

In organic semiconductors where no band structure is present, Fritzsche's equations (2.56) and (2.57) are not valid. For this case, Schmechel derived a similar expression[Sch03]. He described the density of states $DOS(E)$ of an amorphous sample by a single Gaussian distribution, as defined by equation (2.26) on page 16. This distribution was assumed to include all electronic states of host and dopant (if the sample is doped).

Schmechel defined a transport level E_{Tr} as the averaged energy of the charge carriers contributing to the conductivity, weighted by the conductivity distribution

$$E_{Tr} := \frac{\int_{-\infty}^{+\infty} E\ \sigma'(E)\ dE}{\int_{-\infty}^{+\infty} \sigma'(E)\ dE} = \frac{1}{\sigma}\int_{-\infty}^{+\infty} E\ \sigma'(E)\ dE\ . \tag{2.62}$$

This quantity is used to simplify equation (2.55) for the Seebeck coefficient

$$S = -\frac{1}{e\,T} \int_{-\infty}^{+\infty} (E - E_\mathrm{F}) \, \frac{\sigma'(E)}{\sigma} \, dE$$

$$= -\frac{1}{e\,T} \left(E_\mathrm{Tr} - \frac{E_\mathrm{F}}{\sigma} \int_{-\infty}^{+\infty} \sigma'(E) \, dE \right) \tag{2.63}$$

$$S = \frac{E_\mathrm{F} - E_\mathrm{Tr}}{e\,T} \, . \tag{2.64}$$

The expression (2.64) is similar to the equations (2.56) and (2.57) derived by Fritzsche. Here, the terms A_C and A_V are missing and the band edges E_C and E_V are replaced by the transport level E_Tr. If E_S is again introduced, in this case as the difference between Fermi level and *transport* level

$$E_\mathrm{S} := E_\mathrm{F} - E_\mathrm{Tr} \, , \tag{2.65}$$

one obtains the same equation as for conventional semiconductors (CSCs)

$$S = \frac{E_\mathrm{S}}{e\,T} \quad \Rightarrow \quad E_\mathrm{S} = e \cdot T \cdot S \, . \tag{2.66}$$

The field-dependency of the Seebeck coefficient of high mobility organic compounds was studied and found to be similar to conventional semiconductors [Per08]. Recently, the conductivity and the Seebeck coefficient of a single molecular junction was successfully measured simultaneously [Wid12] which allowed an insight into the fundamental physics of single molecules.

2.4 Correlation of Seebeck Coefficient and Charge Carrier Density

2.4.1 Conventional Semiconductors

In section 2.1, a correlation of the density of free charge carriers and the energy levels is calculated for conventional semiconductors using the Boltzmann approximation[‡], leading to the following equations for electrons and holes

$$n_e = N_C \exp\left(-\frac{E_C - E_F}{k_B T}\right) \tag{2.7}$$

$$n_h = N_V \exp\left(-\frac{E_F - E_V}{k_B T}\right). \tag{2.8}$$

Fritzsche's findings for the correlation of the Seebeck coefficient and the energy levels (in case of a one band only transport) are discussed in section 2.3.3.1. If the Fermi level is far away from the corresponding band edge, the simple relation of equation (2.61) is obtained

$$S = \frac{E_S}{e\,T} \tag{2.61}$$

$$\text{with} \quad E_S := E_F - E_C \quad \text{or} \quad E_S := E_F - E_V\,. \tag{2.60}$$

Substituting this equation (2.61) into the equations (2.7) and (2.8), one obtains

$$n_e = N_C \exp\left(-\frac{-E_S}{k_B T}\right) \tag{2.67}$$

$$n_h = N_V \exp\left(-\frac{+E_S}{k_B T}\right). \tag{2.68}$$

As S, and hence E_S, is negative for electron conducting materials, the argument of the exponential function in both equations is negative, e.g. a greater value of the Seebeck coefficient $|S|$, and hence $|E_S|$, is directly correlated to a smaller density of free charge carriers $n_{e/h}$. In these equations, the temperature dependence of $n_{e/h}$ is given by the temperature dependencies of the prefactors N_C or N_V and of the Fermi level E_F, contributing to S and hence E_S.

A sketch of the energy levels E_F, E_C and E_S is presented in figure 2.7 (a) on page 31, for the case of n-doping with $|E_S| = 200\,\text{meV}$. Analogously to figure 2.2 on page 11, the Fermi-Dirac distribution function $f_{FD}(E)$ and the square root shaped $DOS(E)$ are drawn in order to derive their product, the differential density of free electrons $n'_e(E)$, which is shown in a normalized scale as well. Integrating $n'_e(E)$ over all energies yields the total density of free electrons n_e, corresponding to the area under the curve. It can be seen that at energies $E < E_C$, there is no contribution to n_e, as the DOS is zero. The strongest contribution to n_e is at energies above but close to E_C. An analogous picture can be drawn for p-doping, where E_S corresponds to the difference between E_F and the valence energy E_V and the density of free holes n_h is derived the same way.

[‡]requiring $E_C - E_F \gg k_B T$ or $E_F - E_V \gg k_B T$

2.4.2 Organic Semiconductors

In section 2.2, a calculation of the density of free charge carriers for OSCs with a Gaussian distributed density of states is shown, resulting in the following equations, where again the Boltzmann approximation is used to solve the integration analytically:

$$n_\mathrm{e} = n_\mathrm{H} \exp\left(-\frac{E_\mathrm{G} - E_\mathrm{F} - \frac{\sigma_\mathrm{G}^2}{2k_\mathrm{B}T}}{k_\mathrm{B}T} \right) \tag{2.33}$$

$$n_\mathrm{h} = n_\mathrm{H} \exp\left(-\frac{E_\mathrm{F} - E_\mathrm{G} - \frac{\sigma_\mathrm{G}^2}{2k_\mathrm{B}T}}{k_\mathrm{B}T} \right) . \tag{2.34}$$

In section 2.3.3.2, the correlation between the Seebeck coefficient and the difference between Fermi level E_F and transport level E_Tr is derived for OSCs to:

$$S = \frac{E_\mathrm{S}}{e\,T} \tag{2.66}$$

$$\text{with} \quad E_\mathrm{S} := E_\mathrm{F} - E_\mathrm{Tr} \Rightarrow E_\mathrm{F} = E_\mathrm{S} + E_\mathrm{Tr} \, . \tag{2.65}$$

This allows for deriving a relation of the Seebeck coefficient to the density of free charge carriers by combining above equations, while setting the origin of the energy scale to $E_\mathrm{G} = 0$:

$$n_\mathrm{e} = n_\mathrm{H} \cdot \exp\left(-\frac{-(E_\mathrm{S} + E_\mathrm{Tr}) - \frac{\sigma_\mathrm{G}^2}{2k_\mathrm{B}T}}{k_\mathrm{B}T} \right) \tag{2.69}$$

$$n_\mathrm{h} = n_\mathrm{H} \cdot \exp\left(-\frac{E_\mathrm{S} + E_\mathrm{Tr} - \frac{\sigma_\mathrm{G}^2}{2k_\mathrm{B}T}}{k_\mathrm{B}T} \right) . \tag{2.70}$$

Note that in equation (2.69), both E_S and E_Tr have negative values due to electron conduction. Therefore, equations (2.69) and (2.70) show formally the same dependency on E_S as derived for CSCs (compare (2.67) and (2.68)):

$$n_\mathrm{e,h} \propto n_\mathrm{H} \cdot \exp\left(-\frac{|E_\mathrm{S}|}{k_\mathrm{B}T} \right) . \tag{2.71}$$

The above discussed energy levels are plotted in figure 2.7 (b), for the case of n-doping and choosing $|E_\mathrm{S}| = 200\,\mathrm{meV}$, $\sigma_\mathrm{G} = 100\,\mathrm{meV}$ and $E_\mathrm{Tr} = -2\,\sigma_\mathrm{G}$. Again, the Fermi-Dirac distribution function $f_\mathrm{FD}(E)$ and the normalized density of states $DOS(E)$ are drawn in order to derive their product, the differential density of free electrons $n'_\mathrm{e}(E)$, which is shown in a normalized scale as well. Integrating $n'_\mathrm{e}(E)$ over all energies yields the total density of free electrons n_e, corresponding to the filled area under the curve.

Comparing $n'_\mathrm{e}(E)$ for organic and conventional SCs, a completely different shape is found. While for CSCs the maximum is close to the conduction energy $E_\mathrm{C} = E_\mathrm{F} + |Es|$,

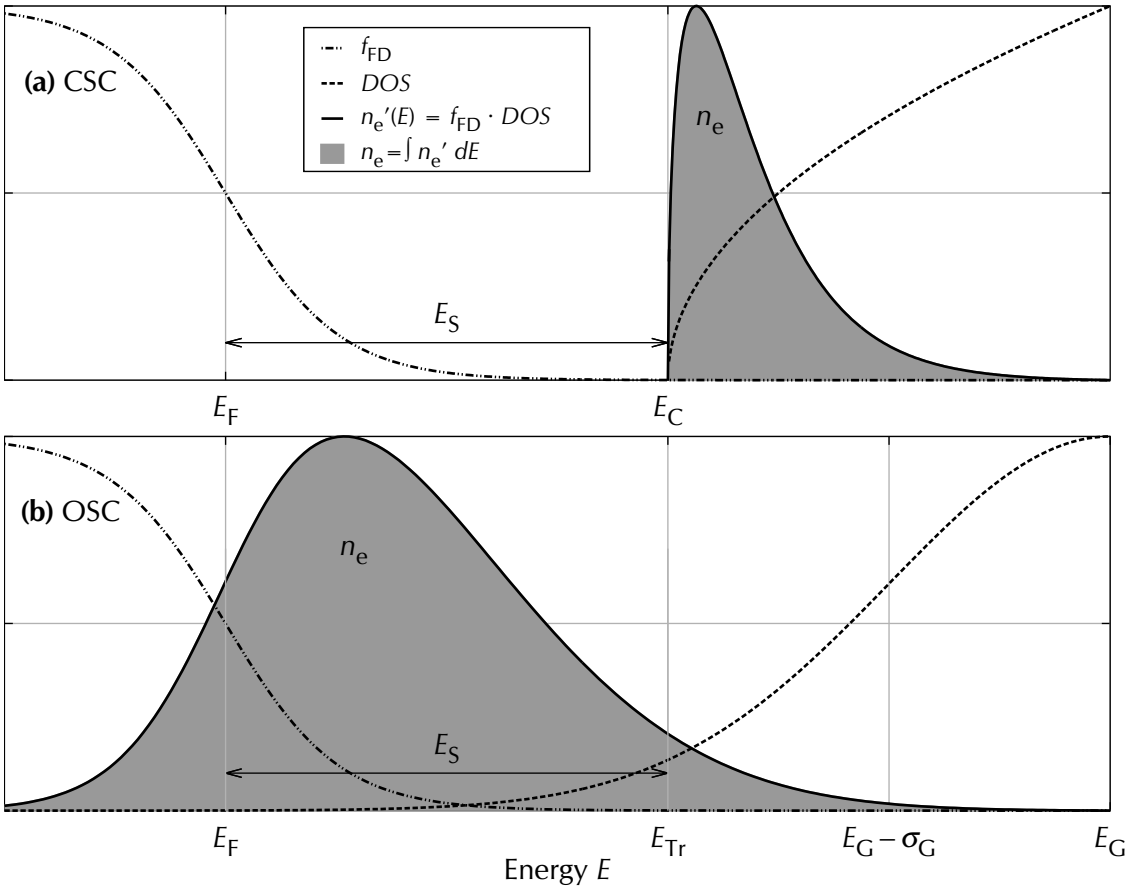

Figure 2.7: *Energy levels, Fermi-Dirac distribution function $f_{FD}(E)$, normalized density of states $DOS(E)$ as well as their normalized product, the differential density of free electrons $n_e'(E) = f_{FD}(E) \cdot DOS(E)$ for n-doped (a) conventional and (b) organic semiconductors. The area under $n_e'(E)$ corresponds to the total density of free electrons n_e. Parameters: $T = 25\,°C$, $|E_S| = 200\,meV$, $\sigma_G = 100\,meV$, $E_{Tr} = -2\,\sigma_G$.*

for OSCs the maximum is between E_F and E_{Tr}. For a different set of parameters, the maximum can even be shifted below E_F, showing that it is important to use the Fermi-Dirac distribution function instead of the approximation via the Boltzmann distribution function. Still the trends expected from the analytical calculations using the Boltzmann approximation hold, as a decreasing value of E_S is related to a gain in n_e, due to a larger overlap of the DOS and the f_{FD}, as expected from conventional semiconductors.

2.4.3 Temperature Dependencies

The temperature dependencies of the conductivity σ and the density of free charge carriers $n_{e/h}$ can be compared to draw conclusions for the temperature dependence of the mobility $\mu(T)$. In the following, hole only conduction is assumed, but the same

argumentation holds for electron conduction. Starting from equation (2.24)

$$\sigma(T) = e \cdot n_{\mathrm{h}}(T) \cdot \mu_{\mathrm{h}}(T)\,,$$

and substituting the equation (2.25) for the temperature activation of σ and the above derived correlation of n_{h} and E_{S} (2.70)

$$\sigma(T) \propto \exp\left(-\frac{E_{\mathrm{act},\sigma}}{k_{\mathrm{B}}T}\right) \tag{2.25}$$

$$n_{\mathrm{h}}(T) \propto \exp\left(-\frac{E_{\mathrm{S}}(T)}{k_{\mathrm{B}}T}\right) \cdot \exp\left(-\frac{E_{\mathrm{Tr}} - \frac{\sigma_{\mathrm{G}}^2}{2k_{\mathrm{B}}T}}{k_{\mathrm{B}}T}\right)\,, \tag{2.70}$$

the temperature dependencies of the mobility is estimated to

$$\Rightarrow \mu_{\mathrm{h}}(T) \propto \exp\left(-\frac{E_{\mathrm{act},\sigma} - E_{\mathrm{S}}(T)}{k_{\mathrm{B}}T}\right) \cdot \exp\left(+\frac{E_{\mathrm{Tr}} - \frac{\sigma_{\mathrm{G}}^2}{2k_{\mathrm{B}}T}}{k_{\mathrm{B}}T}\right)\,. \tag{2.72}$$

As the Boltzmann approximation is used to derive equation (2.70) and furthermore the temperature dependence of the conductivity might differ from the simple case, given in equation (2.25), the temperature dependence of the mobility might deviate from the simple model derived here. More complex models can be found in the literature [Bäs82,Vis98], but these require profound knowledge of the underlying mechanism, which are still under scientific debate. Therefore, rather the above presented model is used to explain trends of the data presented in the subsequent chapters.

Chapter 3

Experimental

This chapter presents the experimental setup and introduces the investigated materials. In section 3.1, changes and improvements to the setup performed during this thesis are highlighted and the resolution limit is estimated. Section 3.2 gives an overview of all investigate materials and summarizes their key parameters.

3.1 Seebeck Setup

3.1.1 Technical Details

Most samples investigated in this thesis are fabricated and measured in-situ in the same vacuum chamber. This chamber had been originally designed by Wolfgang Böhm [Böh95] to be suitable for in-situ Seebeck measurements and has been used and modified by several people in this institute [Bey97,Pfe99,Plö99,Män04a,Blo01,Nol02,Wer03a,Li05,Har08].

During this thesis, several major changes to the setup are performed that improved the measurement accuracy and reproducibility. The old rotary vane pre-pump of the vacuum chamber is replaced by an oil-free scroll pump (Anest Iwata ISP 250), in order to avoid contamination of the samples by oil vapor, which is essential for reproducible experiments. Furthermore, the new pump increased the evacuation speed. This scroll pump in combination with a turbo pump (Leybold TurboVac 151) is used to evacuate the vacuum chamber of $\approx 15\,\mathrm{L}$ volume. 12 hours after sample insertion a base pressure of $3{\cdot}10^{-5}\,\mathrm{Pa}$ ($= 3{\cdot}10^{-7}\,\mathrm{mbar}$) suitable for sample fabrication is reached. Pumping for several days, a pressure of $5{\cdot}10^{-6}\,\mathrm{Pa}$ can be reached. Sensing of the pressure is performed by two vacuum sensors, Leybold TR 211 for the range of $10^{5}\,\mathrm{Pa}$ to $0.1\,\mathrm{Pa}$ and Leybold PR 37 for $0.1\,\mathrm{Pa}$ to $10^{-8}\,\mathrm{Pa}$. Both sensors are connected to a controller unit (Combivac CM 31).

The structure of the vacuum chamber is sketched in figure 3.1 (a). At the bottom there are flanges for up to three material sources (CreaPhys DE-FR/2.2) which evaporate organic material onto a substrate placed at the top of the chamber. The deposition rates are detected separately for each material by rate monitors positioned above the sources.

In each material source the organic material is filled into a crucible, which in vacuum can be heated to the materials' sublimation temperature via a copper coil, surrounding the crucible. A type K thermocouple temperature sensor (employing the Seebeck effect of a chromel[‡]–alumel[§] junction) is placed at the bottom of the crucible and connected to a PID controller (Eurotherm 2208e) that controls the heating current through the copper coil. In this work, always two sources are used in parallel that allow for co-deposition of host and dopant material, compare figure 3.1 (a). The material consumption of the setup is quite low, as 100 mg of an organic host material typically is sufficient to produce 10 samples of 30 nm to 40 nm layer thickness.

During deposition, the evaporation rates of host and dopant, and thus the doping concentration, are monitored independently using two quartz crystal monitors, positioned above the material sources, compare figure 3.1 (a), and connected to two rate monitors (Sycon STM-100/MF). When material is deposited onto these quartz crystals, their resonance frequency changes. By detecting this change, the mass increase is measured, which can be related to a layer thickness via the material's density. For

[‡]Chromel: Alloy of approximately 90 % nickel and 10 % chromium

[§]Alumel: Alloy of approximately 95 % nickel, 2 % manganese, 2 % aluminium and 1 % silicon

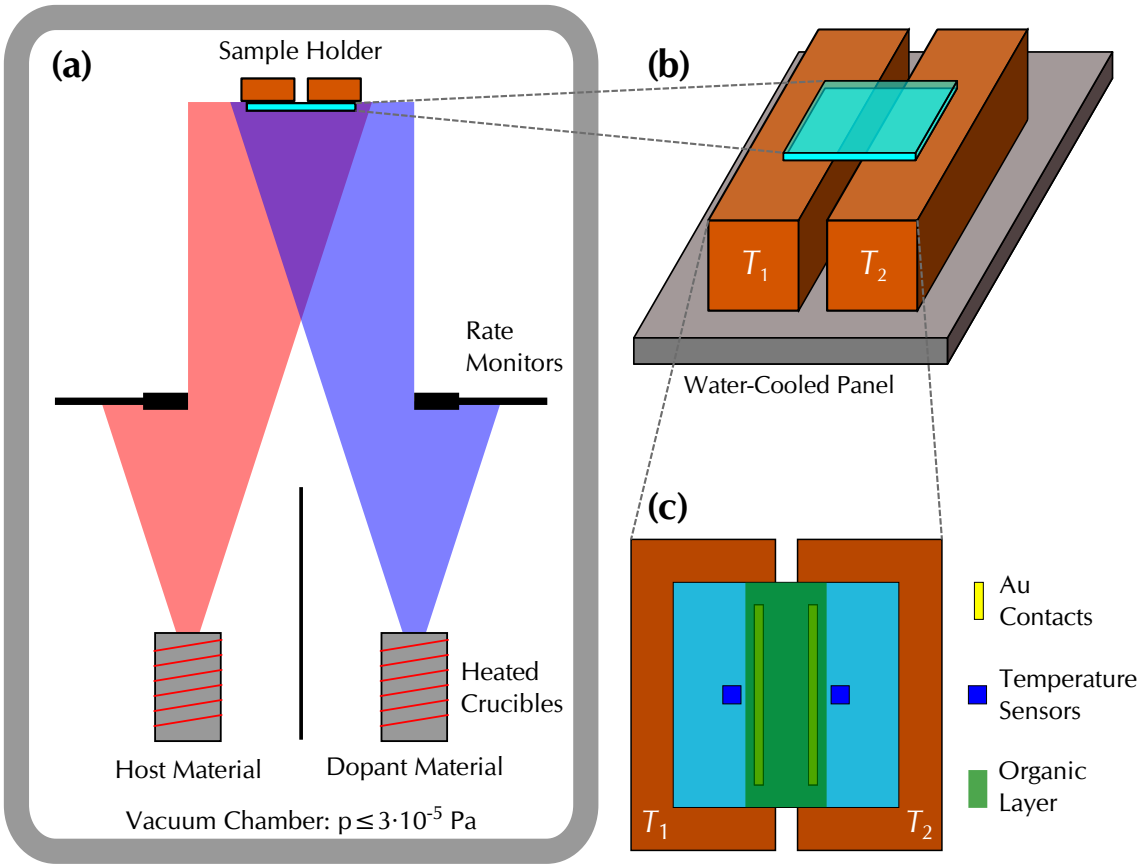

Figure 3.1: *Experimental setup: Sketches of (a) vacuum chamber during co-deposition with substrate at the top; (b) sample holder with substrate mounted onto electrically heated copper blocks which are water-cooled from the backside and placed at the top of (a); (c) sample layout and measurement geometry.*

each material, the geometrical correlation between the position of the corresponding quartz crystal and the sample position is measured, as the materials usually differ in angular dependency of deposition rate. This is done by placing a third quartz crystal at the position of the sample and comparing its detected mass increase with the mass increase measured by the other monitoring quartzes. Water-cooling is applied to the rate monitor of the host material, to compensate for heating during deposition of host material onto the crystal. It turned out that for the high sensitivity of the dopant source required by the low dopant deposition rates, temperature fluctuations of the cooling water led to fake rates displayed by the rate monitor. Therefore, no water-cooling is applied for the dopant rate monitor, which is possible due to the low deposition rates of the dopants and hence low heat transport to the sensor. The lowest controllable doping concentration of this setup is in the range of 0.5 wt% (compare section 2.2.3.3 for definitions of different units for the doping concentration).

The key component of the setup is the sample holder, as it allows for temperature-dependent conductivity and Seebeck measurements. In this work, the sample holder is redesigned to improve the measurement resolution. The sample holder consists of two copper blocks on which the sample's substrate is mounted and positioned above

the material sources. These copper blocks can be heated independently via electric heaters placed inside them and thus allow for applying different temperatures at each side of the sample, compare figure 3.1 (b) and (c). The copper blocks are mounted onto a water-cooled panel, to allow faster cooling and stable temperature control close to room temperature.

This setup allows for substrate temperatures in the range of $T_{\mathrm{sub}} = 20\,^{\circ}\mathrm{C}$ to $120\,^{\circ}\mathrm{C}$. By replacing the cooling water with liquid nitrogen, the range was extended down to $T_{\mathrm{sub}} = -120\,^{\circ}\mathrm{C}$. As the temperature control turned to be too unstable for reliable Seebeck measurements, liquid nitrogen cooling is not used for the data presented in this thesis, but might in future be used for low temperature conductivity investigations.

As the sample holder is mounted onto the top flange of the vacuum chamber, the substrate has to be mounted in ambient atmosphere. The substrate is glued onto the copper blocks by liquid silver ink, which is heated and dried prior to insertion of the sample holder into the vacuum chamber. During evacuation of the vacuum chamber and prior to layer deposition, the substrate is heated to $T_{\mathrm{sub}} = 120\,^{\circ}\mathrm{C}$ to remove particles condensed onto the substrate.

The substrates used are square sheets of glass with a size of 25 mm × 25 mm and 1 mm thickness. They are pre-structured with two parallel gold contacts with $d_{\mathrm{c}} = 5\,\mathrm{mm}$ inter-finger distance, $l_{\mathrm{c}} = 20\,\mathrm{mm}$ length and a thickness of 40 nm, compare figure 3.1 (c). Gold is chosen as it does not oxidize in air and is known for having good injection properties suitable for many organic materials[Kit11]. Below the gold, 3 nm of chromium is deposited as a coupling agent between glass and gold. A source measure unit (SMU) that is able to measure a current while applying a voltage and vice versa, is connected to the gold contacts.

A new high resolution source measure unit (Keithley SMU 236) is used to increase the resolution of voltage and current measurement. In order to employ the full potential of this device and to allow for voltage measurements in the mV-regime, the electrical shielding, grounding and wiring of the setup are completely upgraded. The former BNC coaxial cables for the electrical measurements are replaced by twofold shielded triaxial cables. The length of all cables are reduced to minimize electrical disturbances. Note: It is conventional for Seebeck measurements to contact the *high* input of the SMU to the *cold* side of the sample, as this leads to a positive sign of the thermovoltage if holes are the dominating charge carriers, compare section 2.3.2.

The temperature of the sample is measured at thermally equivalent positions to the contacts, insulated from the organic layer, compare figure 3.1 (c). The previously used sensors of type K thermocouples, are replaced by platinum resistance based sensors (Pt1000), as they provide higher accuracy and mechanical stability. Sensors of accuracy class B/5 were chosen that had been verified at $T = 0\,^{\circ}\mathrm{C}$ and $100\,^{\circ}\mathrm{C}$. The nominal accuracy is $\pm 0.06\,\mathrm{K}$ at $T = 0\,^{\circ}\mathrm{C}$ and $\pm 0.16\,\mathrm{K}$ at $T = 100\,^{\circ}\mathrm{C}$. As these resistance based sensors have $1000\,\Omega$ at $T = 0\,^{\circ}\mathrm{C}$, the influence of the cables between sensor and controller can be neglected. The sensors are glued onto the substrate by liquid silver ink during mounting of the substrate on the sample holder. A two channel PID controller (Eurotherm 3504N) is used to read the sensors and to control two power supplies

(Elektro-Automatik EA-PS 3032-10) for heating the copper blocks. The model Eurotherm 3508N that was tried first turned out to strongly interfere with the voltage measurement, as it introduced an AC voltage of 3 MHz with 3.5 V peak to peak amplitude onto the sample holder inside the vacuum chamber. This happened because the first measurement channel of the device misses a galvanic isolation. Therefore, the model 3504N with two galvanically isolated channel modules was installed instead.

During this thesis, all measurement devices (SMU, 3 PID controllers, 2 pressure sensors and 2 rate monitors) were attached to and controlled by a computer and the corresponding software was developed. A graphical user interface[‡] for the sample deposition process allowed for precise control of the deposition rates and hence the homogeneity. Logging of all important parameters during the fabrication process turned out to be very helpful for diagnostics. Furthermore, the computer control enables automation and remote control of measurements, allowing for longer measurement time and more stable temperature control without electrical disturbances by people operating the setup. This enhanced the accuracy (see section 3.1.5 below) and reproducibility of the measurements which are the basis for the data presented in this thesis. As a side effect, it increases the measurement comfort and saves a lot of time for the operator.

3.1.2 Sample Preparation

Molecular doping is performed by co-evaporation of host and dopant material, as shown in figure 3.1 (a). Thereby, it is assumed that each dopant molecule substitutes a host molecule and therefore adopts the density of the host material. The doping concentration C is typically expressed in terms of weight (e.g. wt%) for proprietary materials, whereas for known structures it can be converted into physically more relevant terms of molecule numbers. In this thesis, the latter is used, as all material structures are published and the unit molar ratio (MR) is chosen, as defined as section 2.2.3.3. A conversion between wt% and MR for the materials used in this thesis is given in table 3.1 on page 49, which is calculated via equation (2.39) on page 22.

The substrate temperature during material deposition is controlled to $T_{\mathrm{sub}} = 25\,^{\circ}\mathrm{C}$ in order to ensure the same layer growth condition for all samples. Most samples investigated in this thesis are deposited at slow rates of $0.01\,^{\mathrm{nm}}/_{\mathrm{s}}$ to $0.02\,^{\mathrm{nm}}/_{\mathrm{s}}$, to allow for precise control of the rates and hence the homogeneity of the doping concentration throughout the layer. The layer thickness of most samples is chosen to $h_{\mathrm{l}} = 30\,\mathrm{nm}$, as this thickness is a compromise between material consumption and layer homogeneity. As the gold contacts on the substrate are produced at a height of 40 nm, no geometrical injection problems are expected for this layer thickness.

During sample fabrication the rate monitors of host and dopant materials are continuously logged by a computer, allowing to monitor the homogeneity of the doping concentration by comparing the amount of material deposited. Ideally, the amount of deposited dopant material increases linearly with the amount of deposited host

[‡]written in Python and QT

material and hence total layer thickness, corresponding to a constant doping ratio. As a second measurement of the homogeneity, the conductivity of the deposited layer is continuously probed by applying a voltage of $V = 10\,\mathrm{V}$ and measuring the current. The layer thickness is calculated as the sum of thicknesses measured by host and dopant rate monitors, assuming the dopant molecules to adopt the density of the host molecules.

3.1.3 Monitoring the Layer Growth

Figure 3.2 shows the current flow through a layer as well as the amount of dopant material deposited versus the total layer thickness during fabrication of a typical sample. The doping concentration is the same throughout this sample as the amount of dopant material increases linearly with the layer thickness. The current measured during fabrication, depicted on the left axis in figure 3.2, shows a typical behavior, similar for all samples: During deposition of the first nanometer, no current above detection limit could be detected. Between 1 nm and 3 nm, there is a rapid increase over several orders of magnitude, as highlighted by the inset of figure 3.2. After 15 nm, the current increase is linear with increasing layer thickness.

This trend can be understood from the fact that the materials do not grow monolayer by monolayer, but in a disordered island-like growth. Therefore, it takes a certain minimum amount of material until first continuous pathways between the electrodes are formed. After deposition of more material, the first completely closed layer is formed. The linear increase after approximately 15 nm suggests that the surface roughness stays at a constant level and that the thickness of the closed layer increases linearly with the amount of material.

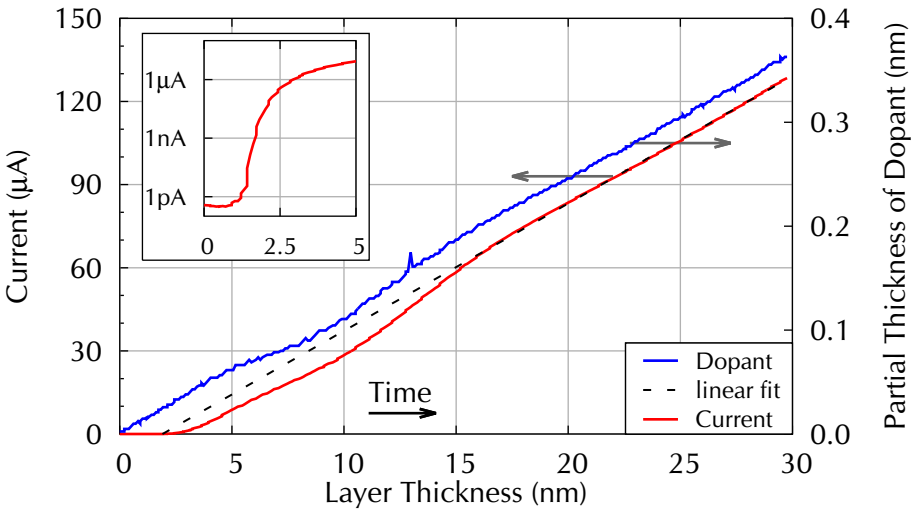

Figure 3.2: *Current (left axis) and amount of dopant material deposited (right axis) during co-deposition of host and dopant. Sample: $C = 0.022\,MR$ of $Cr_2(hpp)_4$ in C_{60}, compare section 3.2 for details on the materials. Inset: Onset of current flow in logarithmic scale.*

In this regime, the data are fitted linearly (dashed line) and extrapolated to an interception with the x-axis, which is found at approximately 2 nm. This suggests that a part of the deposited material forms surface structures that do not contribute to the lateral conductivity. Therefore, the thickness of closed layers is expected to be less than the nominal value, calculated from the rate monitors. The interception depends on the materials used, as well as on the homogeneity of the doping concentration throughout the layer and for most samples it is found to be in the order of 4 nm.

Combining the measured current and nominal layer thickness, the conductivity during deposition can be derived, as shown in figure 3.3. In case of the sample discussed above, for low thicknesses up to 16 nm, the calculated value of the conductivity increases strongly with the layer thickness. This can be explained by an overestimation of the thickness of closed layers as discussed above. Most samples investigated reach saturation at 10 nm to 15 nm. The higher value for this sample is attributed to a variation of doping concentration around a thickness of 10 nm, visible as a slight kink in the plotted amount of dopant material.

Assuming that the thickness of the closed layer is 2 nm less than the nominal thickness, as indicated by the interception of the extrapolated fit line with the x-axis in figure 3.2, a closed layer conductivity can be estimated using this reduced thickness. The estimated closed layer conductivity is larger than the conductivity derived using the nominal thickness, as can be seen in figure 3.3. This estimated conductivity might be more realistic, as the sample roughness is taken into account. Nevertheless, as the homogeneity of the doping and the roughness of the samples might be altered by the following measurements (e.g. by heating) and be different for different samples, it is decided to use for all samples the nominal thickness instead of an estimated one in the following. The underestimation of the conductivity at a sample with 30 nm nominal thickness and closed layer thickness of 2 nm less, would be 6.7 %. Ideally this underestimation would be the same for all samples and can therefore be neglected when comparing the samples.

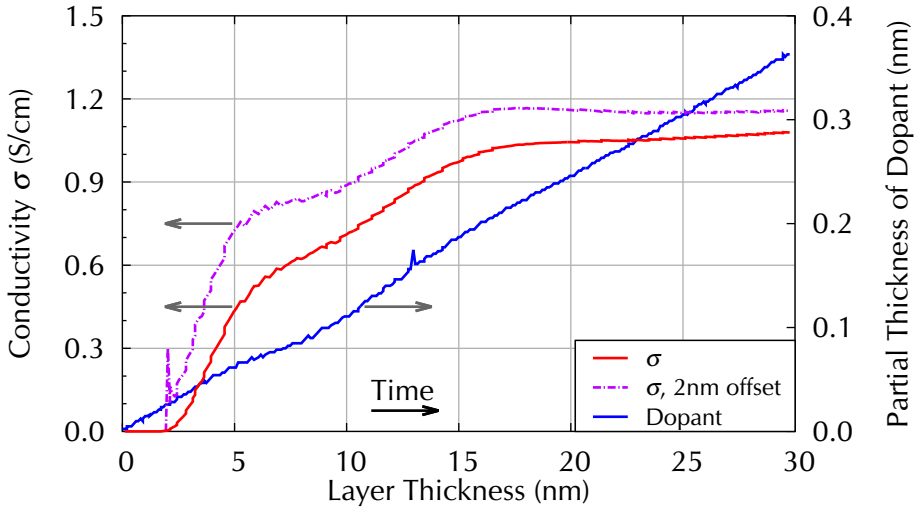

Figure 3.3: *Conductivity vs. layer thickness for a sample of $C = 0.022\,MR$ of $Cr_2(hpp)_4$ in C_{60}.*

3.1.4 Measurement Routine

After sample fabrication, prior to the Seebeck and conductivity measurements, for each sample the current–voltage relation is probed to ensure ohmic injection. With a step size of 1 V the voltage is varied between −10 V and 10 V. A linear and symmetric correlation is found for all samples investigated in this thesis, suggesting ohmic injection from the contacts into the layer for the conductivity measurement at $V = 1\,\mathrm{V}$.

The setup allows for temperature-dependent conductivity and Seebeck measurements though varying the temperature of the two copper blocks and hence of the contacts on the sample. At each mean temperature T_m, the conductivity is probed first. Afterwards, the Seebeck coefficient (compare section 2.3.2) is measured. Finally, the conductivity is probed again to check if the layer was affected by the temperature. This procedure is repeated for different mean temperatures T_m.

The conductivity at a temperature T is determined by heating both contacts to $T_1 = T_2 = T$, compare figure 3.1 on page 35 (c), and applying a voltage V while measuring the current flow I through the layer. Knowing the layer thickness h_l and the contact geometry (distance d_c and length l_c) the conductivity is calculated using equation (2.22) on page 13:

$$\sigma = \frac{I}{V} \cdot \frac{d_\mathrm{c}}{l_\mathrm{c} \cdot h_\mathrm{l}} \,. \tag{2.22}$$

A low voltage of $V = 1\,\mathrm{V}$ is used to prevent heating and charging of the layer. This voltage is applied for 10 seconds before the current measurement is started. During 2 minutes the measured currents are averaged to compensate for noise. After the current measurement, the opposite voltage of $V = -1\,\mathrm{V}$ is applied for 20 seconds, to reduce charging effects of the layer and ensure reproducible conditions for the next measurement.

The Seebeck measurement at a mean temperature T_m is performed by applying a temperature difference T_d to the contacts and hence inducing a temperature gradient on the sample and measuring the generated thermovoltage V_S. The contacts are heated to $T_1 = T_\mathrm{m} + \frac{T_\mathrm{d}}{2}$ and $T_2 = T_\mathrm{m} - \frac{T_\mathrm{d}}{2}$, respectively. All Seebeck measurements are performed with a temperature difference of $T_\mathrm{d} = 5\,\mathrm{K}$, as this value has been successfully used in earlier works using the same setup. V_S is measured continuously for 20 minutes for most samples and data of the last 15 minutes are averaged. Each measurement of the thermovoltage is followed by a measurement at swapped temperatures to exclude systematic errors. The resulting Seebeck coefficient $S = \frac{V_\mathrm{S}}{T_\mathrm{d}}$, compare equation (2.50) on page 26, is the average of the two measurements

$$S = \frac{S_+ + S_-}{2} \,. \tag{3.1}$$

As a stable temperature is the key to reliable Seebeck measurements, strict waiting conditions are introduced in the measurement routine that are required to be fulfilled for at least 2 minutes before the Seebeck measurement is started. Firstly, the

temperature measured at each of the two sensors has to be as close as 0.2 K to the set-point. Secondly, the slope of the change of the temperatures has to be below 0.2 $^{K}/_{min}$. Finally, the current measured at $V = 0\,V$ is required to be below 0.2 pA. The last condition is introduced to ensure that charges, which might have build up in the layer during conductivity measurements, are removed and do not affect the Seebeck measurements. The same requirements are used for conductivity measurements, but the minimal waiting time is reduced to 1 minute, as these measurements are less sensitive towards small variations of the temperature.

3.1.5 Electrical Resolution Limit

The Keithley SMU 236 has a scale step of 0.01 pA in the smallest measurement range. In its data sheet, an accuracy of $\pm(0.3\,\% + 0.1\,pA)$ for new devices is given. It is found that the device displays an offset of 0.4 pA at $V = 10\,V$ at open circuit conditions prior to sample deposition in the vacuum chamber. Therefore, it is assumed that 1 pA is the lowest reliably measured current. Applying $V = 1\,V$ to a sample, as used for the conductivity measurements, this leads to a resolution limit of $10^{12}\,\Omega$ or $\sigma = 8.3{\cdot}10^{-8}\,^{S}/_{cm}$ for a 30 nm thick layer in the given sample geometry, compare figure 3.1 (c). This limit could in principle be pushed down to $\sigma = 2.3{\cdot}10^{-10}\,^{S}/_{cm}$ by applying the maximum voltage of the SMU of $V = 110\,V$ and using a layer thickness of 100 nm. As the conductivities of undoped organic semiconductors are typically even lower, it is not possible to measure such layers in the given sample geometry. An optimized sample geometry for conductivity measurements of low conductivities should have a large ratio of contact length l_c to contact distance d_c, which can be achieved by serpentine shaped contacts, similar to typical (O)FET structures for material research. This however would make Seebeck measurements impossible, as no constant temperature gradient can be applied between serpentine shaped contacts.

Seebeck measurements are also limited by the resolution of the current measurement, as internally the device performs a measurement of a voltage by measuring the current flow through an internal resistor. Thus, for thermovoltage V_S (Seebeck) measurements a lower limit of the layer conductivity can roughly be estimated, assuming that the conductivity of the layer limits the current generated by the temperature gradient. Using the typical temperature gradient of $T_d = 5\,K$ to investigate a doped sample of $S = 700\,^{\mu V}/_{K}$, a value of $V_S = 3.5\,mV$ is expected. Together with the above derived minimal detectable current of 1 pA this leads to a requirement for the conductivity to be at least $\sigma = 2.4{\cdot}10^{-5}\,^{S}/_{cm}$ for the given sample geometry. This rather high limit is reduced by averaging two measurements of opposite temperature gradient T_d, as this cancels out constant device offsets. Furthermore, by averaging the measured thermovoltages for several minutes, the accuracy is increased further, but systematic errors persist. It is therefore estimated that the minimal current for Seebeck measurements is in the range of 0.1 pA, leading to a lower limit of $\sigma = 2.4{\cdot}10^{-6}\,^{S}/_{cm}$. This value is in agreement with the limit found in the data, compare section 6.2.2, where for samples of lower conductivities it was not possible to perform reliable Seebeck measurements.

3.1.6 Leakage Current

Applying a voltage of $V = 10\,\mathrm{V}$ to the contacts of the glass substrate prior to layer deposition in vacuum, a leakage current between 0.3 pA and 1.0 pA is detected at a substrate temperature of $T_{\mathrm{sub}} = 25\,^{\circ}\mathrm{C}$. This current is found to increase with T_{sub} and hence is not a measurement artifact of the source measure unit. As scratching the glass surface had no effect on the current, contamination of the substrate surface during metal contact preparation or by condensation can be excluded. It has been reported that most glasses are not perfect isolators, but show an ionic conductivity [Ing89]. Therefore, it must be assumed that a current flows through the glass into the copper sample holder and on the other side back through the glass. This allows for conversion of a current into a conductivity using equation (2.22) on page 13 with a contact distance of 2 mm, being twice the glass thickness, and neglecting the contribution of the highly conducting metal sample holder.

Figure 3.4 shows the current at temperatures between $T_{\mathrm{sub}} = 25\,^{\circ}\mathrm{C}$ and 110 °C in an Arrhenius‡ plot, displaying the current and the corresponding conductivity in a logarithmic scale against the inverse of the temperature. In this temperature range the observed glass conductivity ranges from $8{\cdot}10^{-14}\,\mathrm{S/cm}$ to $5{\cdot}10^{-11}\,\mathrm{S/cm}$. At temperatures above 50 °C a linear correlation between the logarithm of the current and the inverse of the temperature is found, as highlighted by the dashed fit line. At lower temperatures the resolution of the SMU affects the measurement and leads to a deviation from the linear trend.

The temperature dependence indicates a thermally activated transport, as expected for ionic glass conductivity [Ing89] and allows for deriving a thermal activation energy

‡after Swedish scientist Svante August Arrhenius [Arr84] (1859–1927)

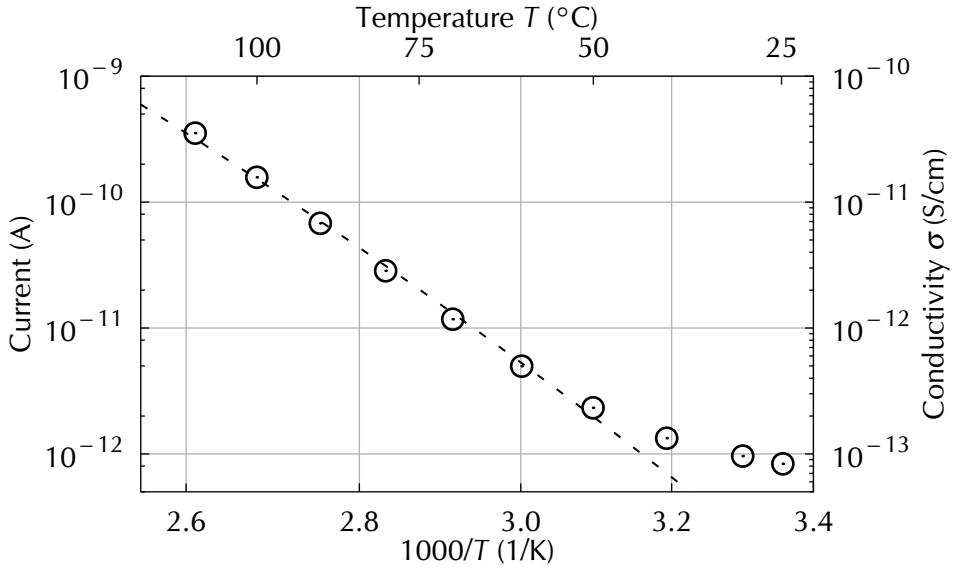

Figure 3.4: *Leakage current at $V = 10\,\mathrm{V}$ prior to layer deposition. The dashed line corresponds to a linear fit.*

of the conductivity $E_{\mathrm{act},\sigma}$, using equation (2.25) on page 16. Different glass substrates are found to vary in $E_{\mathrm{act},\sigma}$, with a mean value of $E_{\mathrm{act},\sigma} = 926\,\mathrm{meV}$. A measurement of a glass substrate on a heating plate in air showed a continuation of this tendency up to 300 °C.

These findings show that leakage currents through the glass substrate can be neglected at temperatures below 50 °C. At higher temperatures and measured currents in the sub-nA regime, leakage currents might influence the measurement. In the used sample geometry a current of 0.1 nA at $V = 10\,\mathrm{V}$ through a 30 nm thick layer corresponds to a conductivity of $8.3{\cdot}10^{-7}\,\mathrm{S/cm}$. Consequently, as a rule of thumb samples of conductivities below $10^{-6}\,\mathrm{S/cm}$ at $T = 50\,°\mathrm{C}$ are not measured reliably at elevated temperatures.

3.2 Materials

In this section, the organic materials investigated during this thesis are briefly introduced. Their structures are presented in figure 3.5 and their key properties are summarized in table 3.2 on page 50. A conversion between the doping concentration expressed in molar ratio (MR) and in weight% (wt%) for typical values is given in table 3.1 on page 49. Most materials were purified by vacuum sublimation prior to sample fabrication.

3.2.1 Host Materials

Fullerene C_{60}

Fullerenes are spherical or ellipsoid molecules containing only carbon atoms, similar to graphene. They are named after the American architect Richard Buckminster Fuller, known for his geodesic domes. First theoretical predictions of this class of molecules have been published in 1970 by Osawa [Osa70,Osa93], 15 years before the first successful synthesis of the approximately spherical C_{60} molecule [Kro85] which has been awarded with the Nobel Prize in chemistry in 1996. For further information about the electrical and optical properties of fullerenes, the reader is referred to reference [Mak01].

C_{60}, the fullerene consisting of sixty spherically aligned carbon atoms is a semiconductor with a remarkably high electron mobility of up to $\mu = 4.9\,{}^{\mathrm{cm}^2}/_{\mathrm{Vs}}$ [Ita06]‡. Therefore, it is commonly used in electron transport layers of organic photovoltaic cells (OPV) and hence an interesting subject for studying n-doped layers. C_{60} molecules with their spherical shape and diameter of approximately 7 Å preferably align in a face-centered cubic (fcc) polycrystalline structure [Pei93]. Air-exposure of vacuum deposited undoped or doped C_{60} layers has been reported to result in a decrease of conductivity, attributed to oxygen absorption [Ham93,Fuj94]. A much smaller decrease has been observed for exposure to N_2 [Fuj94]. Its electron affinity EA of (4.0 ± 0.3) eV [Zha09] requires n-dopants with an ionization energy IE in a similar range or even below, to allow for electron transfer and doping. Interestingly, it was shown that C_{60} molecules in the solid state are rotating rapidly and nearly isotropically [Tyc91]. Recently, the presence of fullerenes has been detected in outer space [Cam10,Loh23]. The C_{60} used in this work has been purchased from CreaPhys GmbH, Germany, purified by vacuum gradient sublimation and was used as received.

MeO-TPD

MeO-TPD (N,N,N',N'-tetrakis 4-methoxyphenyl-benzidine) has been first synthesized in 1998 [The98] as a novel hole transport material for organic light-emitting diodes (OLEDs). It forms amorphous layers [Pfe03] with hole mobilities in the range of $\mu = 2.3{\cdot}10^{-5}\,{}^{\mathrm{cm}^2}/_{\mathrm{Vs}}$§. MeO-TPD has a low ionization en-

‡measured in an organic field-effect transistor (OFET) geometry on top of a pentacene monolayer
§measured by Moritz Philipp Hein (IAPP) in an OFET geometry on SiO_2 substrate

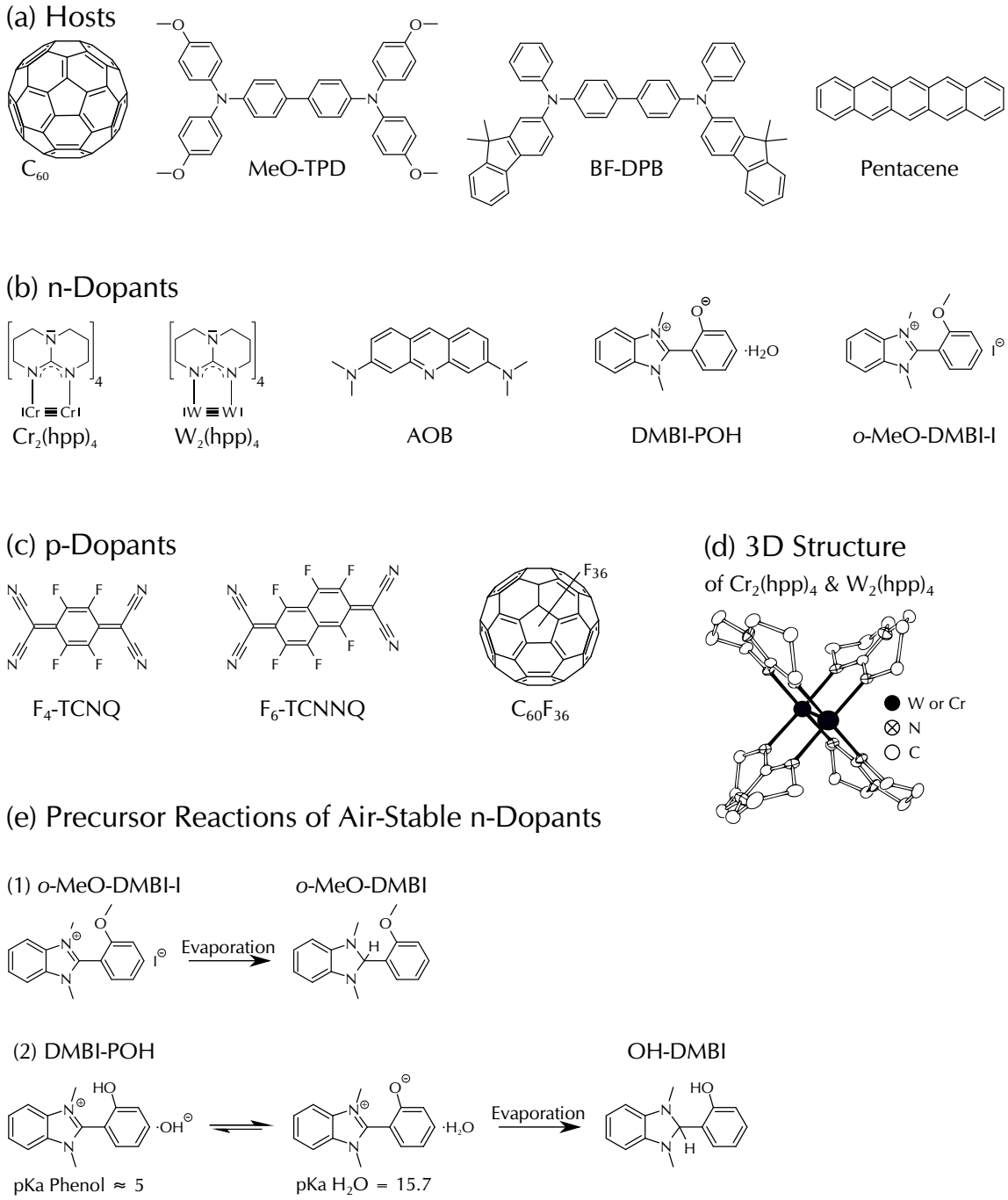

Figure 3.5: *(a)-(c) Structures of the host and dopant compounds investigated in this work. (d) 3-dimensional structure of $Cr_2(hpp)_4$ and $W_2(hpp)_4$, reproduced after [Cot03]. (e1) Proposed reaction for formation of the neutral dopant compound o-MeO-DMBI from the air-stable precursor o-MeO-DMBI-I. (e2) Resonant structure of DMBI-POH and proposed reaction for formation of the neutral dopant OH-DMBI.*

ergy of IE = (5.10 ± 0.13) eV[Olt09,Tie12] and a wide bandgap in the range of $E_{gap} = 3.2\,eV$[He04a]. Theoretical studies found the second highest occupied molecular orbital (HOMO-1) to be only 0.4 eV below the HOMO[Mat10]. The material has been successfully used in OLEDs[He04b] and organic photovoltaic cells (OPV)[Dre04], but due to a rather low glass transition temperature of only $T_g = 67\,°C$[The98], devices incorporating this material cannot withstand elevated temperatures. Nevertheless, in this thesis it is chosen as one of the host materials for p-doped layers, due to its relevance for research and its rather low ionization energy. MeO-TPD has been bought from Sensient Technologies Corporation, USA, and was purified twice by vacuum gradient sublimation.

BF-DPB

BF-DPB (N,N'-Bis(9,9-dimethyl-fluoren-2-yl)-N,N'-diphenyl-benzidine) is the second hole transport material investigated in this thesis. This material has been first presented in 2001[Has01] for the use in OLED hole transport layers. BF-DPB has the same backbone as MeO-TPD, but different side groups that lead to a 0.13 eV larger ionization energy of IE = (5.23 ± 0.13) eV[Mee11]. Due to the structural similarity to MeO-TPD, BF-DPB is expected to form amorphous layers as well. Tests showed that BF-DPB is thermally more stable than MeO-TPD. Hole mobilities in the range of $\mu = 5.7{\cdot}10^{-5}\,cm^2/Vs$‡ have been measured, which are twice as high as for MeO-TPD. BF-DPB has been bought from Sensient Technologies Corporation, USA, and was purified by vacuum gradient sublimation.

Pentacene

Pentacene is a planar polycyclic aromatic hydrocarbon molecule consisting of five linearly fused benzene rings, leading to a high conjugation and semiconductor properties. This molecule has a length in the range of 14 Å, twice as long as the diameter of C_{60} molecules. The first synthesis has been described over 100 years ago[Mil12]. Pentacene has been one of the first conjugated organic oligomers used as p-type semiconductor and is still used as reference for all newly developed organic semiconductors[Mur07]. The crystalline structure[Ha09] with rather large crystallite size[Kle12a] leads to high carrier mobilities above $1\,cm^2/Vs$[Mur07]§. Pentacene is prominent for application in organic field-effect transistors (OFETs), as complementary to C_{60} with a similar mobility, pentacene is stable to air-exposure, allowing for lithographic processing steps[Ste06]. Due to degradation under UV light, pentacene cannot be used in photovoltaic cells. Pentacene has a low ionization energy in the range of IE = 4.90 eV[Sal12] to 5.15 eV[Fuk06]. In 2009 high resolution atomic force microscopy (AFM) investigations of single molecules of pentacene on Cu(111) have been presented[Gro09], impressively resolving the atomic positions and bonds. Pentacene has been bought from Sensient Technologies Corporation, USA, and was purified three times by vacuum gradient sublimation.

‡measured by Moritz Philipp Hein (IAPP) in an OFET geometry on SiO_2 substrate
§measured in an OFET geometry

3.2.2 n-Dopants

$Cr_2(hpp)_4$ and $W_2(hpp)_4$

The n-dopants $Cr_2(hpp)_4$ and $W_2(hpp)_4$ are dimetal complexes of chromium or tungsten with the anion of 1,3,4,6,7,8-hexahydro-2H-pyrimido[1,2-a]pyrimidine (hpp). These compounds were first presented by Cotton et al.[Cot02,Cot05] in 2002, and their use in OLEDs has been reported[Wer05,Wel09]. Both materials exhibit an extremely low ionization energy (IE). Using ultraviolet photoelectron spectroscopy (UPS) Selina Olthof (IAPP) measured[‡] the IEs of pure $Cr_2(hpp)_4$ and $W_2(hpp)_4$ films to (3.95 ± 0.13) eV and (2.68 ± 0.13) eV, respectively[Men12a]. The IE of $W_2(hpp)_4$ is even shallower than for cesium (IE = 3.9 eV), the least electronegative stable element. As these compounds easily oxidize in air, they have to be handled in an inert gas atmosphere or vacuum. Both dopants have been purchased from Novaled AG, Germany, and were used as received.

AOB

Acridine orange base (AOB, 3,6-bis(dimethylamino)acridine) is a fluorescent cationic dye used frequently in biology to distinguish DNA and RNA and to detect microbial content of soil and water. Its application as air-stable n-dopant for C_{60} has been first presented in 2006[Li06], where its doping mechanism has been explained as follows: During vacuum co-deposition of AOB and C_{60}, a dyad of a positively charged acridine dye and a C_{60} anion radical, connected by a C–N chemical bond, is formed and acts as dopant. It has been shown that this process can be accelerated by illumination during deposition. Today, AOB is known for being diffusive and to contaminate vacuum chambers, therefore, it is hardly used in devices any more. AOB has been purchased from Sigma-Aldrich Co. LLC, Germany, and was purified twice by vacuum gradient sublimation.

DMBI Derivatives: DMBI-POH and *o*-MeO-DMBI-I

The investigation of DMBI (1*H*-benzoimidazole) derivatives for the use as n-dopants was started by Peng Wei and Benjamin D. Naab from Professor Zhenan Bao's group at Stanford University, USA. They first published the application of N-DMBI[§] to dope PCBM[¶] via solution processing[Wei10]. During this thesis, in a cooperation with Professor Bao's group DMBI-POH (2-(1,3-dimethyl-1*H*-benzoimidazol-3-ium-2-yl)phenolatehydrate) and *o*-MeO-DMBI-I (2-(2-methoxyphenyl)-1,3-dimethyl-1*H*-benzoimidazol-3-ium iodide) have been investigated for the use as air-stable n-dopants for vacuum co-deposition.

Studies of *o*-MeO-DMBI-I by various techniques suggest that during co-deposition, a reduction reaction takes place that generates the active doping compound, likely

[‡]UPS spectra measured using a Specs Phoibos 100 setup at a base pressure below 10^{-8} Pa. Details about the setup can be found in reference[Olt10].

[§]N-DMBI is (4-(1,3-dimethyl-2,3-dihydro-1*H*-benzoimidazol-2-yl)phenyl)dimethylamine

[¶]PCBM is [6,6]-phenyl-C_{61}-butyric acid methyl ester

o-MeO-DMBI, as shown in figure 3.5 (e1). It seems evident that heating leads to the formation of its neutral compound as the active dopant, together with the concomitant loss of the iodide ion. Hence, for calculation of the molar doping concentration of samples doped by *o*-MeO-DMBI-I, the molar mass of *o*-MeO-DMBI has to be used, compare table 3.2 on page 50. Details of the doping mechanism are presented in section 5.5. *o*-MeO-DMBI-I has been synthesized at Stanford University, USA, and was used as received.

DMBI-POH has been purchased as OH-DMBI (2-(1,3-dimethyl-2,3-dihydro-1*H*-benzoimidazol-2-yl)phenol) from Sigma-Aldrich Co. LLC., USA and was used as received. A conversion under ambient conditions to a resonant structure was detected by the cooperation partners at Stanford University. The resonant structure was characterized as shown in figure 3.5 (e2) by ^{1}H-NMR and elemental analysis. By examining the acid dissociation constants (pKa) of these two resonant structures, it is evident that the equilibrium should favor the phenolate hydrate structure of DMBI-POH.

Similar to *o*-MeO-DMBI-I, DMBI-POH is expected to form its neutral compound, OH-DMBI (2-(1,3-dimethyl-2,3-dihydro-1*H*-benzoimidazol-2-yl)phenol), as the active n-type dopant. A reduction reaction during co-deposition is possible, similar to the one of *o*-MeO-DMBI-I due to their structural similarity, especially with DMBI-POH's resonant structure with an OH^- anion. The structure of OH-DMBI is shown in figure 3.5 (e2). Therefore, in order to calculate the molar doping concentration of samples doped by DMBI-POH, the molar mass of OH-DMBI has to be used, compare table 3.2 on page 50.

3.2.3 p-Dopants

Typical molecular p-dopants are strongly electron attracting compounds, usually containing fluorine atoms. In this thesis, three different p-dopants have been used.

F_4-TCNQ

F_4-TCNQ (tetrafluoro-tetracyanoquinodimethane), has been first synthesized by Wheland et al.[Whe75] and has been used as p-dopant for many years[Blo98,Pfe98], having an electron affinity of EA = 5.25 eV[Gao01]. Unfortunately, this light compound has been found to be highly diffusive having a low sticking coefficient[Koe10]. This led to device degradation and contamination of vacuum chambers. F_4-TCNQ has been purchased from abcr GmbH & Co. KG, Germany, and was used as received.

F_6-TCNNQ

F_6-TCNNQ (1,3,4,5,7,8-hexafluorotetracyanonaphthoquinodimethane) is a close relative to the prominent molecular p-dopant F_4-TCNQ, with a second aromatic ring, leading to an increase of molar mass by ⅓ and a 20 K higher deposition temperature T_{dep}, compare table 3.2. It has been presented by Koech et al.[Koe10] to replace the volatile F_4-TCNQ and its electron affinity has been estimated to EA = 5.0 eV[Tie12]

which allows successfully doping of different host materials [Tie12,Kle12a]. F_6-TCNNQ has been purchased from Novaled AG, Germany, and was used as received.

$C_{60}F_{36}$

$C_{60}F_{36}$, a fluorinated derivative of the fullerene C_{60} was first synthesized in 1991 [Sel91]. The utilization of this heavy compound as p-dopant has been demonstrated in 2011, where its electron affinity has been estimated to EA = 5.38 eV [Mee11]. Despite its molar mass being almost twice as heavy as C_{60} and its diameter of around 10.5 Å being 50 % larger, the deposition temperature of $C_{60}F_{36}$ is 235 K lower, but above the values for the other two investigated p-dopants. $C_{60}F_{36}$ has been purchased from MTR Ltd, USA, and was used as received.

Table 3.1: *Conversion between two typical units for the doping concentration: molar ratio (MR) and weight percentage (wt%) for used material combinations, using equation (2.39) on page 22. The lowest controllable doping concentration of this setup is in the range of 0.5 wt%.*

		wt% to MR		MR to wt%	
Host	Dopant	1 wt%	10 wt%	0.01 MR	0.10 MR
C_{60}	$Cr_2(hpp)_4$	0.0111	0.1219	0.90%	8.35%
C_{60}	$W_2(hpp)_4$	0.0079	0.0870	1.26%	11.33%
C_{60}	AOB	0.0274	0.3018	0.37%	3.55%
C_{60}	OH-DMBI	0.0303	0.3332	0.33%	3.23%
C_{60}	*o*-MeO-DMBI	0.0286	0.3149	0.35%	3.41%
MeO-TPD	F_6-TCNNQ	0.0170	0.1867	0.59%	5.62%
MeO-TPD	$C_{60}F_{36}$	0.0044	0.0482	2.26%	18.75%
BF-DPB	F_6-TCNNQ	0.0201	0.2212	0.50%	4.78%
BF-DPB	$C_{60}F_{36}$	0.0052	0.0570	1.91%	16.31%
pentacene	F_4-TCNQ	0.0102	0.1120	0.98%	9.03%

Table 3.2: *Material parameters. T_{dep} is the temperature at which typically a deposition rate was detected. Accuracies for the IE (usually measured by UPS) are in the range of ±0.13 eV, whereas for the EA (usually measured by IPES) larger errors of ±0.30 eV are common.*

Name	Molar Mass M $^{g}/_{mol}$	Density ρ $^{g}/_{cm^3}$	T_{dep} °C	Supplier	CAS Number	IE eV	EA eV
Host Materials							
C_{60}	720.6	1.630	410	CreaPhys	99685-96-8	6.35 [Zha09] – 6.45 [Aka08]	3.9 [Olt12] – 4.5 [Aka08]
MeO-TPD	608.7	1.463	170	Sensient	122738-21-0	5.10 eV [Olt09,Tie12]	1.9 eV [He04a]
BF-DPB	720.9	1.210	200	Sensient	361486-60-4	5.23 eV [Mee11]	
pentacene	278.4	1.320	160	Sensient	135-48-8	4.90 [Sal12] – 5.15 [Fuk06]	2.7 [Cha09]
n-Dopants							
$Cr_2(hpp)_4$	656.8		115	Novaled	200943-63-1	3.95 [Men12a]	
$W_2(hpp)_4$	920.4		190	Novaled	463931-34-2	2.86 [Men12a]	
AOB	265.4		70	Sigma-Aldrich	494-38-2		
DMBI-POH	256.3		110	Sigma-Aldrich			
OH-DMBI	240.3		–		3652-93-5		
o-MeO-DMBI-I	380.2		185	Stanford Uni.	201416-21-9		
o-MeO-DMBI	254.3		–				
p-Dopants							
F_4-TCNQ	276.1		100	abcr	29261-33-4	8.34 [Gao01]	5.25 [Gao01] (IPES)
F_6-TCNNQ	362.2		120	Novaled	912482-15-6		5.00 [Tie12] (CV)
$C_{60}F_{36}$	1404.6		175	MTR	1190690-26-6	8.38 [Mee11]	5.38 [Mee11] (est.)

Chapter 4

Air-Sensitive n-Dopants in C_{60}

This first results chapter studies the properties of n-doped C_{60} layers incorporating two different n-dopants, $Cr_2(hpp)_4$ or $W_2(hpp)_4$. Both dopants are compounds with extremely low ionization energies and thus not stable in air. First, in section 4.1 the conductivity of differently doped samples, measured directly after sample preparation is probed. A change over time is observed and modeled theoretically. Afterwards, a thermal annealing step is performed to ensure stable measurement conditions and the influence of the doping concentration is analyzed. Finally, temperature-dependent conductivity measurements are discussed, which indicate a thermally activated hopping process and therefore allow to derive an activation energy of the conductivity. In section 4.2, thermoelectric (Seebeck) measurements are presented and the influence of temperature and doping concentration is discussed. The results are compared to the activation energy of the conductivity and conclusions for the mobility are drawn. Section 4.3 presents atomic force microscopy (AFM) studies, probing the surface roughness of differently doped samples for indications of clustering or agglomeration of dopants. Finally, in section 4.4 degradation studies of the effect of air-exposure on the n-doped samples are discussed and a regeneration treatment is presented. This chapter ends with a summary in section 4.5.

Doping of conventional semiconductors was the key element that led to the breakthrough of semiconductor technology, as it allows for control of the majority charge carriers and hence the design of p-n-junctions, being the building block for most electronic devices. In this chapter, n-doping of the high mobility electron transport material C_{60}, frequently used in organic photovoltaic cells (OPV), is studied by using two novel n-dopants, $Cr_2(hpp)_4$ and $W_2(hpp)_4$, having extremely low ionization energies of IE $= (3.95 \pm 0.13)$ eV and (2.68 ± 0.13) eV, respectively. As the IEs of both dopant compounds are determined to be lower than the electron affinity of C_{60} with EA $= (4.0 \pm 0.3)$ eV [Zha09], efficient charge-transfer and therefore effective doping is expected. This fact is especially the case for $W_2(hpp)_4$, as its IE is even shallower than the IE of the efficient molecular dopant decamethylcobaltocene[‡]. Further details about the materials are summarized in the materials section 3.2. A selection of the results presented here is published in reference [Men12a].

Samples of 30 nm thick doped layers are prepared and investigated in vacuum according to sections 3.1.2 and 3.1.4. The base pressure during sample procession for the $Cr_2(hpp)_4$ samples was $P \approx 3{\cdot}10^{-5}$ Pa ($= 3{\cdot}10^{-7}$ mbar). Due to technical problems, for the samples using $W_2(hpp)_4$, the pressure was one order of magnitude higher, around $P \approx 3{\cdot}10^{-4}$ Pa.

4.1 Conductivity

Conductivity measurements are the first method of choice for studying doping. Therefore, in the following the conductivities σ of layers of C_{60} n-doped by various doping concentrations C of $Cr_2(hpp)_4$ or $W_2(hpp)_4$ are presented. As a linear and symmetric current-voltage relation is measured for all samples, and the reported contact resistance between gold and C_{60} is low [Kit11], the charge injection can be neglected. The conductivity data, measured directly after fabrication of the samples at $T = 25\,^{\circ}$C is shown in figure 4.1.

Even for the lowest doping concentration, the conductivity of the doped layers is several orders of magnitude higher than for undoped C_{60}, which has been reported to be in the order of $\sigma = 2{\cdot}10^{-8}\,\mathrm{S/cm}$ [Li06] and which would be below the resolution limit of the setup of $\sigma = 8.3{\cdot}10^{-8}\,\mathrm{S/cm}$ as discussed in section 3.1.5. A linear increase of $\sigma(C)$ is observed for both dopants, covering three orders of magnitude. A detailed discussion of the dependence of σ on C is performed in section 4.1.2, as it is later found that a thermal annealing step is necessary in order to ensure reproducible and stable measurement conditions for later measurements. The maximum conductivity measured directly after sample fabrications is $\sigma = 7.35\,\mathrm{S/cm}$ for $C = 0.210$ MR of $Cr_2(hpp)_4$ and $\sigma = 4.97\,\mathrm{S/cm}$ for $C = 0.150$ MR of $W_2(hpp)_4$. At even higher doping concentrations the conductivity decreases, which is attributed to high percentages of dopant molecules disturbing the morphology of the host material, hindering the charge carrier transport.

[‡]Decamethylcobaltocene is also known as DMC or $CoCp^*_2$, IE $= 3.30$ eV [Cha08]

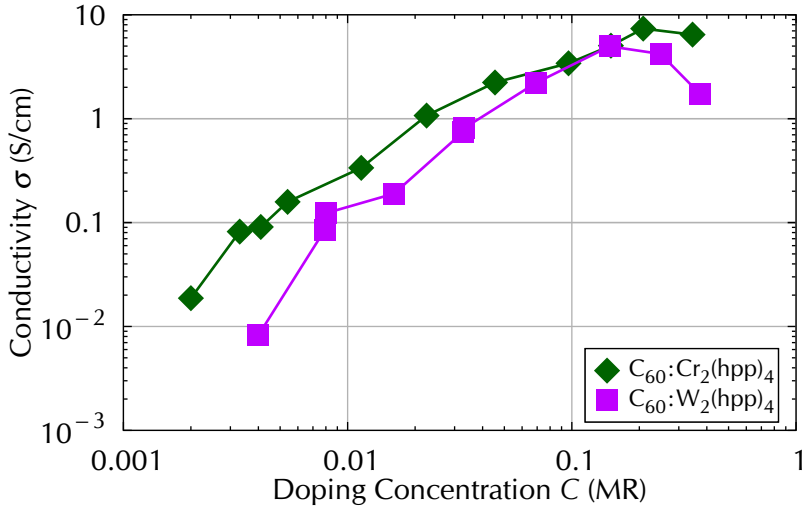

Figure 4.1: *As-prepared conductivity σ vs. doping concentration C of samples of C_{60} n-doped by $Cr_2(hpp)_4$ or $W_2(hpp)_4$, measured at $T = 25\,^{\circ}C$. Compare to undoped C_{60} with $\sigma \approx 2{\cdot}10^{-8}\,{}^{S}/_{cm}$* [Li06].

C_{60} is known for its high electron mobility, compared to other OSCs, which results in such high conductivities. In comparison, the typical OLED electron transport material BPhen[‡], for example, reaches conductivities of less than $\sigma = 10^{-6}\,{}^{S}/_{cm}$ when doped by Cs_2CO_3 [Par08].

4.1.1 Conductivity Changes after Preparation

Prior to further measurements, the conductivity of each sample is continuously probed in-situ for 1 hour at a temperature of $T = 25\,^{\circ}C$. Interestingly, a change of σ is observed for all samples. While for high C a drop of σ is detected, a gain is found for low C. Figure 4.2 compares the normalized changes in σ of a weakly (a) and a strongly (b) doped sample of $Cr_2(hpp)_4$.

The data can be described by employing a simple model using a differential equation describing population growth for the case of constant generation rate (c_1) and population dependent extinction rate ($c_2 \cdot \sigma(t)$):

$$\frac{d\sigma(t)}{dt} = c_1 - c_2 \cdot \sigma(t)\,, \tag{4.1}$$

which can be solved to

$$\frac{\sigma(t)}{\sigma_0} = 1 + \chi\left(1 - \exp\left(-\frac{t}{\tau}\right)\right)\,, \tag{4.2}$$

where σ_0 is the initial conductivity and χ is the maximal relative change, reached after a time $t \gg \tau$, with τ being a time constant describing the speed of the change.

[‡]BPhen is 4,7-diphenyl-1,10-phenanthroline

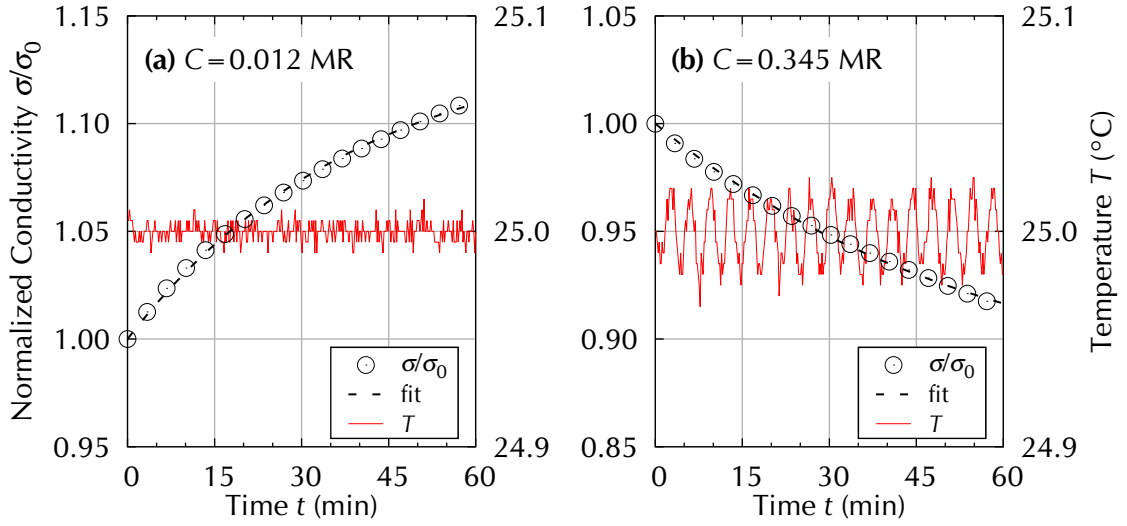

Figure 4.2: *Conductivity changes of samples of C_{60} doped by $Cr_2(hpp)_4$ during the first hour after deposition, continuously measuring in-situ at $T = 25\,°C$. The doping concentrations are (a) $C = 0.012\,MR$ and (b) $C = 0.345\,MR$. A fit (dashed line) is performed using equation (4.2).*

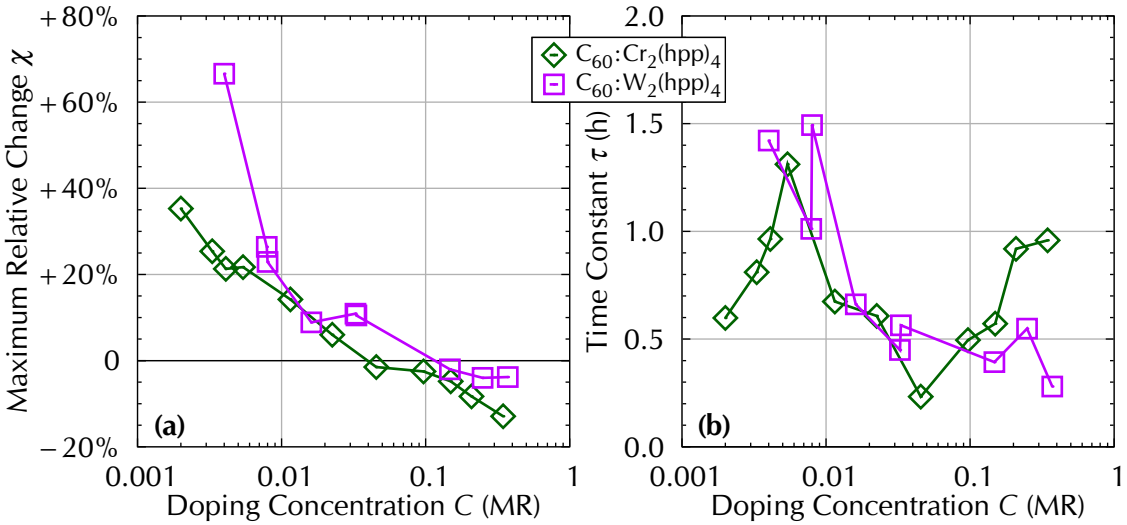

Figure 4.3: *Fitting parameters of conductivity change during the first hour after sample preparation according to equation (4.2): (a) maximal relative change χ reached after $t \gg \tau$ (b) time constant τ describing the speed of the change.*

The value of χ is positive for increasing and negative for decreasing conductivity over time. As the dashed fitting lines in figure 4.2 show, the model describes the data well. Applying this model to the continuous measurements for each sample, the parameters χ and τ can be derived, which are summarized in figure 4.3.

Both dopants show the same tendency: At low C, the in-situ conductivity significantly increases during the first hour after sample preparation. Hence, the fitting parameter χ is positive for these samples, as figure 4.3 (a) shows. With increasing C, the magnitude of the change χ is reduced, reaching negative values for high $C > 0.040\,MR$. Interestingly, for the samples of the highest conductivities measured directly after

sample preparation, a value of $\chi \approx 0$ is observed, showing that the conductivity stays almost constant.

The time constant τ seems to decrease with rising C for the $W_2(hpp)_4$ samples, whereas for $Cr_2(hpp)_4$ no clear trend is observed. For all samples, τ varies between 0.25 and 1.5 hours, meaning that for some samples the speed of change is 6 times faster than for others. The sample preparation conditions (rate, homogeneity, pressure, etc.) might have an effect on τ, but so far no simple relation could be found. Thus, an interplay of these parameters might control τ.

In order to verify whether the current flow though the layer is the origin for the change in conductivity, a control measurement is performed on one sample of $C = 0.033\,\mathrm{MR}$ of $W_2(hpp)_4$, where instead of continuously measuring, σ is probed only for 20 s every 20 minutes. The result is identical, suggesting that the current flow is not the cause of this phenomenon.

4.1.2 Relation of Conductivity to Doping Concentration

In order to investigate the effect of the change in conductivity in more detail and to ensure stable measurement conditions, the samples are thermally annealed prior to further measurements, as proposed by Nollau et al.[Nol00]. They are slowly heated from $T = 25\,^\circ\mathrm{C}$ to $100\,^\circ\mathrm{C}$ and kept at this temperature for 20 minutes. Afterwards, the conductivity is found to be constant over time, and the temperature-dependent measurement routine, described in section 3.1.4, is started at $T = 30\,^\circ\mathrm{C}$.

The conductivity probed at $T = 30\,^\circ\mathrm{C}$ after thermal annealing is compared to the initial conductivity measured directly after deposition of the layers (at $T = 25\,^\circ\mathrm{C}$). Figure 4.4 shows that the same trend is observed for both dopants: While at low doping concentrations thermal annealing leads to a gain in σ, at high C a lowering is found. Highly doped samples of $Cr_2(hpp)_4$ show a much more pronounced effect than samples of $W_2(hpp)_4$.

The change induced by the thermal annealing is in agreement with the tendency observed during the one hour measurement directly after sample deposition, presented in the last section. This agreement suggests that the annealing accelerates the process responsible for the change of the conductivity after deposition. Only two samples are inconsistent with this trend: The samples of $C = 0.045\,\mathrm{MR}$ and $0.097\,\mathrm{MR}$ of $Cr_2(hpp)_4$ show a small reduction in σ during the first hour after fabrication at $T = 25\,^\circ\mathrm{C}$, but a gain after thermal annealing. This gain is larger than the expected effect of the 5 K higher temperature for the measurement after annealing.

Three different phenomena might be responsible for the changes in conductivity with time and temperature. Firstly, residual quantities of gases like O_2 and moisture, being present in the vacuum chamber, might react with the n-doped layers, binding electrons and hence reducing the conductivity. Thermal annealing can remove these products from the layer, enhancing the conductivity[Fuj94]. Secondly, in the regime

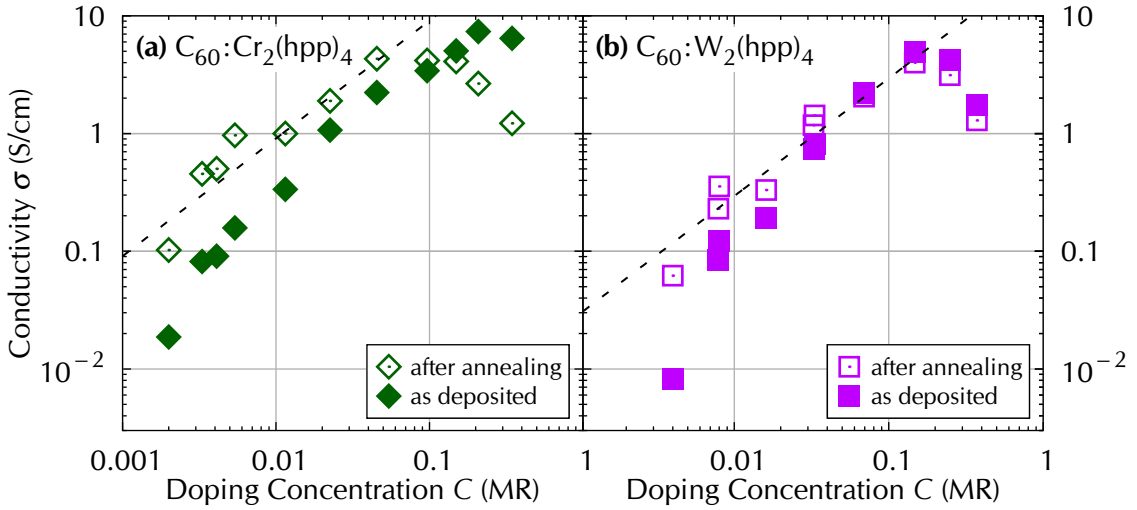

Figure 4.4: *Conductivity before (filled symbols, at $T = 25\,°C$) and after (empty symbols, at $T = 30\,°C$) thermal annealing (at $T = 100\,°C$) for C_{60} doped by (a) $Cr_2(hpp)_4$ and (b) $W_2(hpp)_4$. The dashed lines represent a slope of 1.0.*

of low doping concentration, slow and small rearrangement of the molecules introduced by interactions between host and dopant molecules might lead to an increasing doping efficiency and thus conductivity over time. This effect might be accelerated by thermal annealing. Thirdly, in the regime of high doping concentration, a phase separation and demixing of host and dopant can occur, leading to a reduced conductivity due to shielding of dopants and hence a reduced number of free charges. This rather slow process can be accelerated by heating, as it has been shown for organic photovoltaic cells, where phase separation in the active layer improves the exciton separation by formation of a bulk heterojunction [Sue04].

After the thermal annealing step, the maximum conductivity measured at $T = 30\,°C$ is $\sigma = 4.3\,^{S}/_{cm}$ at $C = 0.045\,MR$ of $Cr_2(hpp)_4$, and $\sigma = 4.0\,^{S}/_{cm}$ at $0.147\,MR$ of $W_2(hpp)_4$. As indicated by the dashed lines in figure 4.4 (a) and (b), possessing a slope of 1.0, the conductivity has a linear relation to the doping concentration. Hence, each additional dopant molecule contributes by the same amount to the total conductivity. This trend is not always the case, as other studies on organic dopants have shown [Män01,Gre04].

A stronger slope might be present in the region of lowest doping concentrations for both dopants. This tendency is in agreement with the results Olthof et al. [Olt12] have reported for the material system of C_{60} doped by $[RuCp^*(mes)]_2$[‡]. A superlinear increase of $\sigma(C)$ below $0.001\,MR$ was observed, which they attributed to filling of trap states. Here, the doping concentration is higher, but filling of trap states might also be responsible for the rather low conductivities of the lowest doped samples.

At very large doping concentrations $C > 0.100\,MR$, this linear relation does not hold any more as both sample series show a drop of σ. A possible explanation could be a drop in the electron mobility due to a disturbance of the morphology [Kle12a] when more than 10 dopant molecules per 100 host molecules are introduced into the layer.

[‡] $[RuCp^*(mes)]_2$ is ruthenium(pentamethylcyclopentadienyl)(1,3,5,-trimethylbenzene)

As the dopant molecules have different properties than the host molecules, a substitution of molecules leads to a change in the electronic landscape in the layer[Mit12b]. If deposited dopant molecules preferable align to dopant molecules already present in the layer, at high C a clustering can happen, leading to a phase separation of host and dopant materials, as discussed above. For doped layers, a phase separation would result in a reduced doping efficiency as some of the dopant molecules are shielded from the host molecules and thus are not able to donate an electron[Mit12b]. In order to check for possible changes of the layer morphology induced by doping, atomic force microscopy (AFM) measurements are performed using an AIST-NT Combiscope AFM. The measurements are presented in section 4.3 and show a rising roughness with C in the medium doping regime. Interestingly, at high C smooth surfaces are found again. This counter-intuitive trend might be a measurement artifact, since the measurements are performed in air.

In contrast to what is expected from the ionization energies (IEs), using $Cr_2(hpp)_4$ leads to a more efficient doping of C_{60} compared to $W_2(hpp)_4$. Assuming that there is no change of molecular levels on formation of ions, this observation might be explained by morphological effects, or by $W_2(hpp)_4$ reacting more strongly with oxygen contaminations being present in the vacuum chamber.

In order to check if the above mentioned higher pressure during sample procession of $W_2(hpp)_4$ samples had an influence on σ, a sample of $C = 0.033\,\mathrm{MR}$ of $W_2(hpp)_4$ is produced at the same pressure as the $Cr_2(hpp)_4$ samples, after solving the technical problems. This sample showed after thermal annealing an almost equal conductivity to the earlier $W_2(hpp)_4$ samples of similar doping concentration. Again, the conductivity is lower than of a corresponding sample of $Cr_2(hpp)_4$. Hence, the effect of the elevated base pressure seems not to be crucial.

4.1.3 Temperature Dependence of the Conductivity

Measuring the conductivity (after thermal annealing) at different temperatures, a reversible gain of σ with temperature is observed. Figure 4.5 shows the data of all samples in Arrhenius plots, displaying the conductivity in a logarithmic scale against the reciprocal of the temperature T^{-1}. An exceptionally good agreement with a linear relation is found for all samples, corresponding to an exponential relation of σ to T^{-1}, consistent with earlier studies on doped organic layers[Fuj94,Pfe98]. Thus, this data can be fitted in good agreement with a thermally activated transport relation using equation (2.25) on page 16. Hence, most likely hopping transport is dominant in these samples and therefore an activation energy of the conductivity $E_{\mathrm{act},\sigma}$ can be derived.

The resulting $E_{\mathrm{act},\sigma}$ of the differently doped samples range from $E_{\mathrm{act},\sigma} = 54\,\mathrm{meV}$ to 160 meV and are shown in figure 4.6. All obtained values are well below the previously reported value for undoped C_{60} of around 640 meV[Li06]. At low C, the $E_{\mathrm{act},\sigma}$ is lower for samples of $Cr_2(hpp)_4$ than for $W_2(hpp)_4$, whereas for $C > 0.020\,\mathrm{MR}$, the values for both dopants match clearly within experimental scattering. Up to

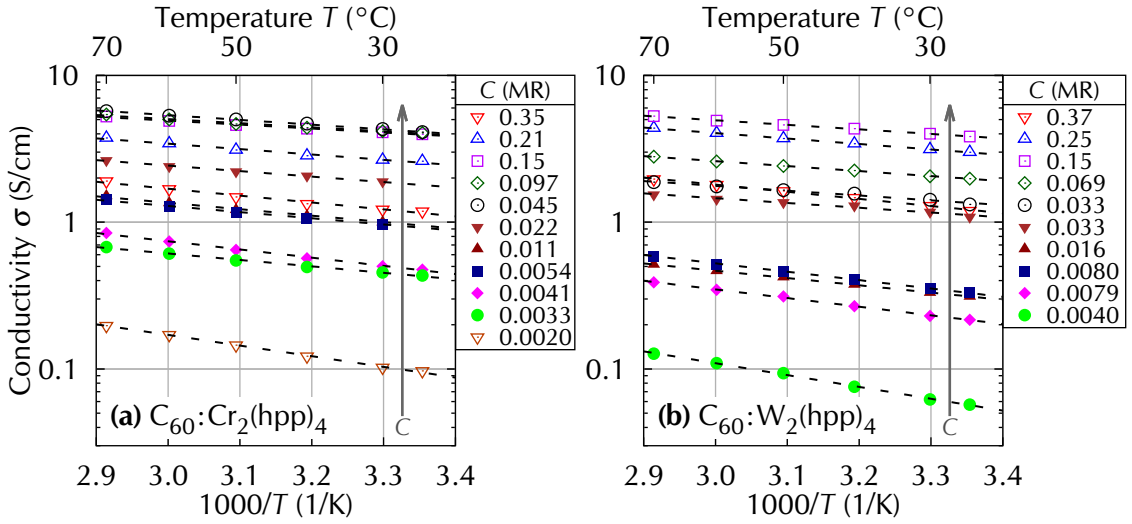

Figure 4.5: *Temperature dependence of the conductivity $\sigma(T)$ of samples of C_{60} doped by (a) $Cr_2(hpp)_4$ and (b) $W_2(hpp)_4$. Lines are fits using equation (2.25) on page 16.*

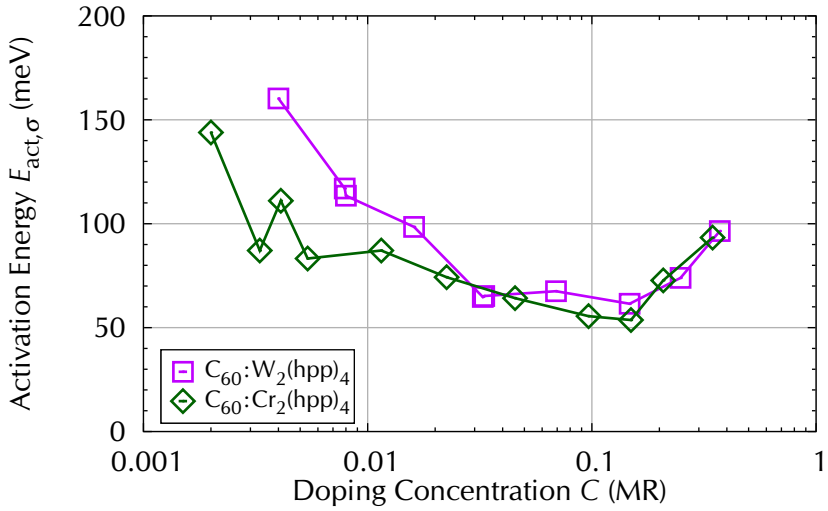

Figure 4.6: *Activation energy of the conductivity $E_{act,\sigma}$, derived from the temperature dependence of the conductivity $\sigma(T)$ in the range of $T = 30\,°C$ to $70\,°C$, shown above in figure 4.5, using equation (2.25) on page 16.*

$C = 0.100\,\mathrm{MR}$, a decrease of $E_{\mathrm{act},\sigma}$ with increasing C is found, as expected from earlier experiments [Pfe98,Li06]. Highly doped samples show a different behavior of rising $E_{\mathrm{act},\sigma}$ with doping concentration.

The drop of $E_{\mathrm{act},\sigma}$ with increasing C is attributed to a shift of the Fermi level towards the transport level of C_{60}. This shift leads to a reduction of the temperature dependence of the density of free electrons $n_e(T)$, which according to (2.24) contributes to the conductivity as

$$\sigma(T) = e \cdot n_e(T) \cdot \mu_e(T)\,. \tag{2.24}$$

A minimum of $E_{\mathrm{act},\sigma}$ at $C \approx 0.100\,\mathrm{MR}$ suggests a pinning of E_F and hence a saturation of the doping efficiency. The increase of $E_{\mathrm{act},\sigma}$ at $C > 0.100\,\mathrm{MR}$ might be attributed

to a rise of the temperature dependence of the electron mobility $\mu_e(T)$, probably caused by a disturbance of the morphology of the host material by the large percentage of dopant molecules. Studies on pentacene, which forms polycrystalline layers as well, have shown that an increasing amount of dopants leads to a disturbance of the morphology and a decreasing crystallite size[Kle12a]. The observed rising $E_{act,\sigma}$ is in agreement with the reduced conductivity at $C > 0.100$ MR, as shown in figure 4.4.

4.2 Thermoelectric Measurements

4.2.1 Temperature Dependence of the Seebeck Coefficient

Along with the conductivity measurements, thermoelectric (Seebeck) measurements are performed. The measured Seebeck coefficients S for C_{60} doped by $Cr_2(hpp)_4$ or $W_2(hpp)_4$ are presented in figure 4.7 (a) and (c). They are negative in sign, thus, for all samples, electrons are the dominating charge carrier species and hole conduction

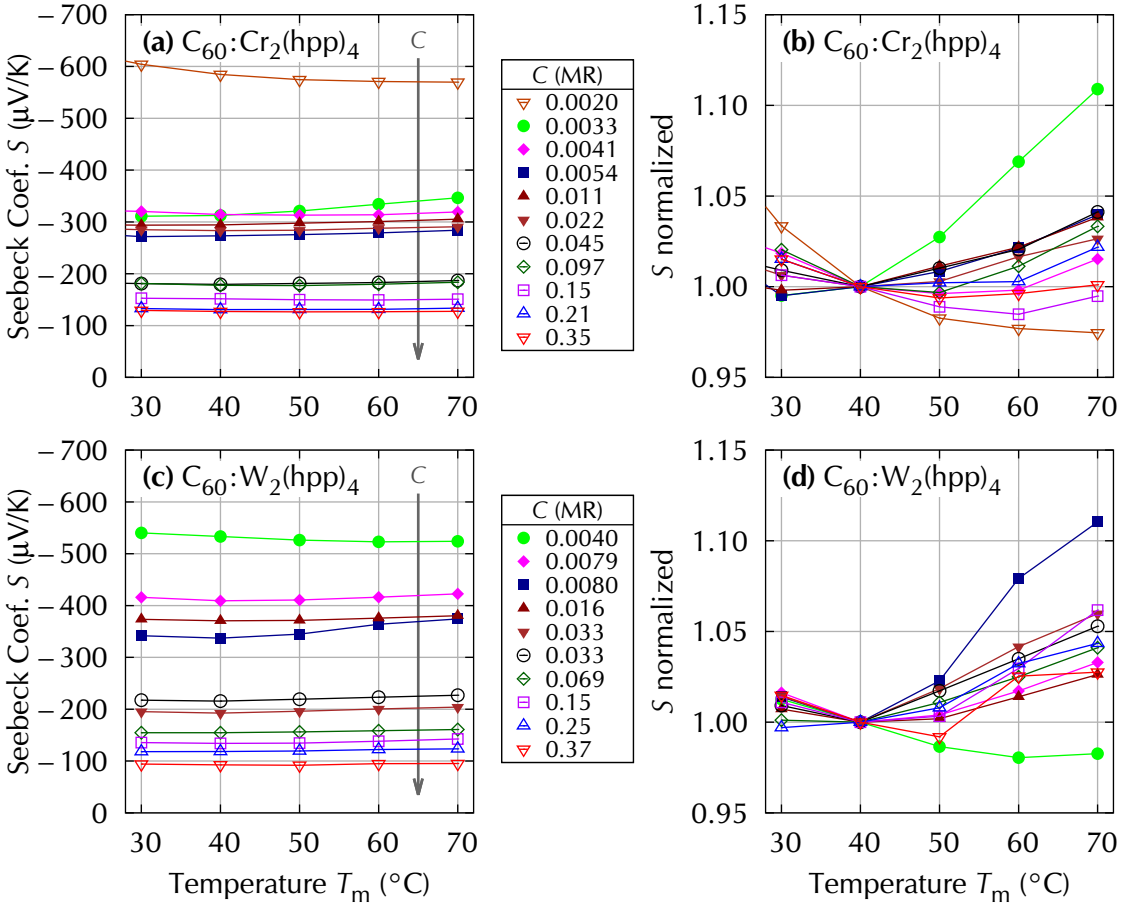

Figure 4.7: *Temperature dependence of the Seebeck coefficient S for C_{60} doped by $Cr_2(hpp)_4$ and $W_2(hpp)_4$ in (a) and (c). At the right side, in (b) and (d) the relative changes of S are shown, normalized to the $T_m = 40\,°C$ measurements.*

along the dopant molecules is not observed. The values for S range from $-90\,\mu V/K$ to $-600\,\mu V/K$ and a lowering of $|S|$ with rising C is detected.

In order to investigate the influence of the mean temperature T_m, the relative changes of S, normalized to the measurements at $T_m = 40\,°C$, are shown in figure 4.7 (b) and (d) for $Cr_2(hpp)_4$ and $W_2(hpp)_4$, respectively. $T_m = 40\,°C$ is chosen, as it is a device-relevant temperature and more stable to control than $T_m = 30\,°C$. In the investigated temperature range of $T_m = 30\,°C$ to $70\,°C$, the S of most of the $Cr_2(hpp)_4$ samples scatters around relative changes of $-0.5\,\%$ to $+5\,\%$. The two lowest doped samples of $C = 0.0020\,MR$ and $0.0033\,MR$ are an exception with changes of $-3\,\%$ and $+11\,\%$ at $T_m = 70\,°C$. In case of using $W_2(hpp)_4$, most samples show a gain in the order of $4\,\% \pm 2\,\%$, with again two weakly doped samples showing stronger changes.

Summarizing, a small upward trend of S between $2\,\%$ and $6\,\%$ is measured for most samples with no direct relation to the doping concentration. It is not clear why weakly doped samples differ from the general trend. Since the influence of the doping concentration on S is much more pronounced than the effect of the temperature, a comparison of differently doped samples is performed in the next section.

4.2.2 Relation of Seebeck Coefficient to Doping Concentration

In figure 4.8, the Seebeck coefficients S at $T_m = 40\,°C$ are compared for different doping concentrations. A decrease of $|S|$ with increasing C is found for both dopants, ranging from $-585\,\mu V/K$ to $-93\,\mu V/K$. By using equation (2.66) on page 28, the energetic difference E_S between the Fermi level E_F and the transport level E_{Tr} is derived:

$$E_S = S \cdot e \cdot T \quad \text{with} \quad E_S := E_F - E_{Tr}\,. \tag{2.66}$$

This quantity is shown as the right hand axis in figure 4.8. A maximum of $E_S = -183\,meV$ is measured for $C = 0.002\,MR$ of $Cr_2(hpp)_4$. For $W_2(hpp)_4$, the

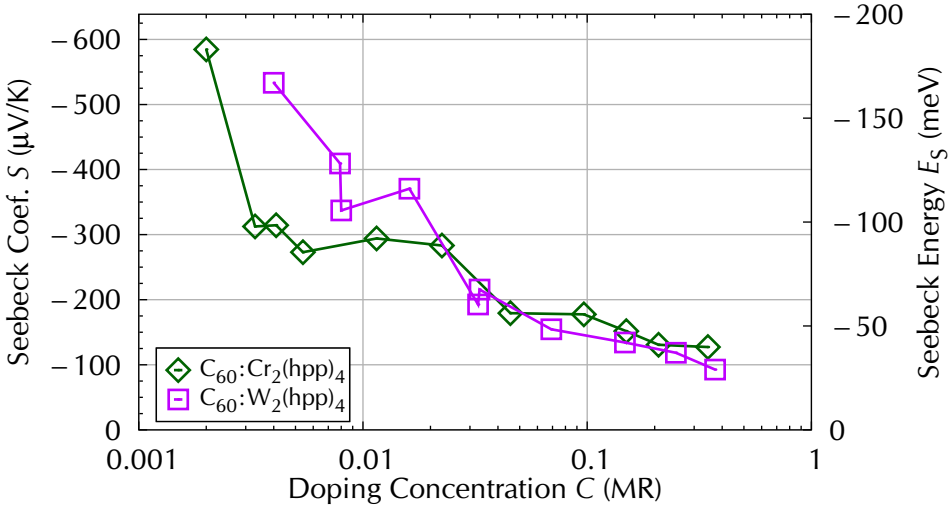

Figure 4.8: *Seebeck coefficient S and derived Seebeck energy E_S at $T_m = 40\,°C$.*

largest E_S of $-167\,\mathrm{meV}$ is measured for the lowest concentration ($C = 0.004\,\mathrm{MR}$) as well.

Following the trend of S, the value of E_S drops with rising C for both dopants, showing a shift of the Fermi level E_F towards the transport level E_{Tr}. A similar tendency has been reported earlier for other material systems [Nol00]. A value of $E_S < 50\,\mathrm{meV}$ is found at high C for both dopants, which indicates that E_F is energetically close to E_{Tr} at a difference below $2\,k_B T$. In such a case, E_F can get pinned close to E_{Tr} which will result in a saturation of E_S, compare degenerate doping in section 2.1.2.2. While for conventional semiconductors the Seebeck coefficient at very high doping concentrations has been reported to increase again [Ike10], this behavior is not observed in this data.

Using the Boltzmann approximation, the density of free electrons $n_e(T)$ is found to be related to E_S via equation (2.71) on page 30:

$$n_e(T) \propto \exp\left(-\frac{|E_S(T)|}{k_B T}\right).$$

Hence, a decreasing value of E_S is attributed to an increasing density of free electrons. In case of highly doped samples, $|E_S|$ is in the order of $2\,k_B T$ and therefore the Boltzmann approximation is not valid, but still a lowering of $|E_S|$ is correlated to a drop of n_e, as discussed in section 2.4.3.

It can be summarized that the Seebeck coefficient tends towards saturation at high doping concentrations of each dopant, $Cr_2(hpp)_4$ and $W_2(hpp)_4$. This saturation is explained by pinning of the Fermi level close to the transport level at these high doping concentrations.

4.2.3 Comparison of Seebeck Energy and Activation Energy

In figure 4.9 (a) and (b), the Seebeck energy E_S (energetic difference between Fermi level E_F and transport level E_{Tr}) and the activation energy of the conductivity $E_{act,\sigma}$, are illustrated for samples doped by $Cr_2(hpp)_4$ and $W_2(hpp)_4$, respectively. A good agreement of the two energies is observed for $C < 0.100\,\mathrm{MR}$ of each dopant. At higher doping concentrations, an increasing difference is measured, due to a rise in $E_{act,\sigma}$, as discussed in section 4.1.3. If the mobility $\mu(T)$ has an Arrhenius-like temperature dependence, the difference between $E_{act,\sigma}$ and E_S is attributed to an activation of the mobility, as discussed in section 2.4.3.

Considering the continuing decrease in the Seebeck coefficient even after $C = 0.100\,\mathrm{MR}$, the final gain of $E_{act,\sigma}$ and drop of conductivity at high doping concentrations must be due to changes of the value of the mobility in the layer. At these high C, a disturbance of the morphology by the large number of dopant molecules is expected, negatively affecting the mobility. This agrees with the results of Harada et al. [Har07] who showed that the OFET-mobility of AOB-doped C_{60} decreases upon doping. In the following section, AFM studies of the surface roughness are presented to check for the influence of doping on the morphology.

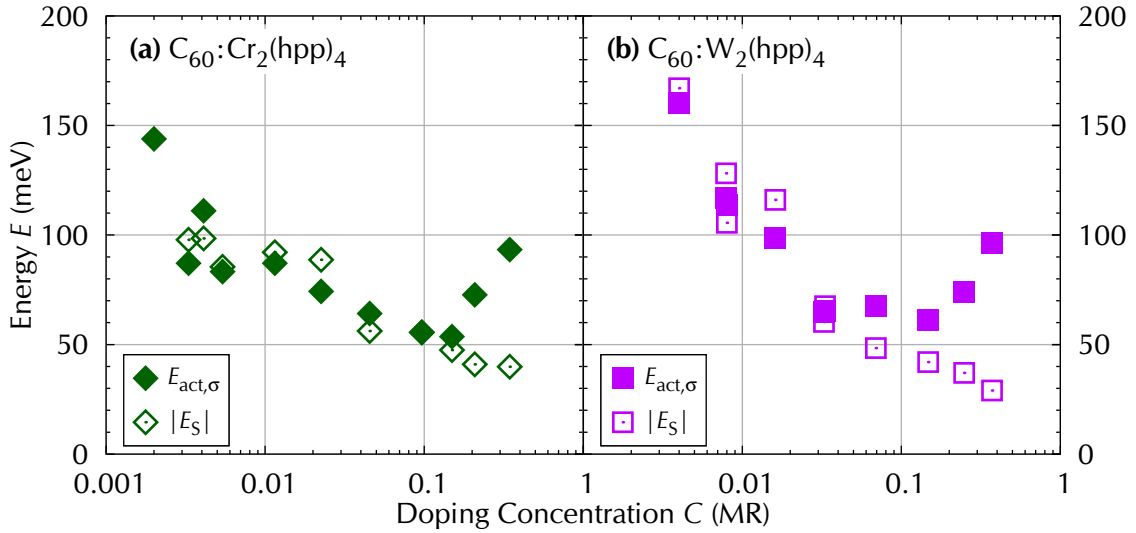

Figure 4.9: *Comparison of Seebeck energy E_S and activation energy of the conductivity $E_{act,\sigma}$. E_S is measured at $T_m = 40\,°C$, $E_{act,\sigma}$ is fitted from conductivity data in the range of $T = 30\,°C$ to $70\,°C$.*

However, the temperature dependence of the mobility may differ from a simple activated case to a model where hopping along a manifold of states is assumed [Bäs82,Vis98]. In order to differentiate, it would be necessary to measure the mobility independently, for example by temperature-dependent Hall effect or time of flight (TOF) measurements. Using OFET measurements to derive the mobility of doped layers is delicate, since doping leads to a strong contribution of bulk current to the drain current making the mobility analysis based on the gradual channel approximation ambiguous. Furthermore, the high applied field results in a high occupation of the density of states and hence to different conditions compared to the conductivity and Seebeck measurements.

4.3 Morphology

In order to check for an influence of the presence of dopant molecules on the morphology of the layers, atomic force microscopy (AFM) measurements are performed on the surfaces of a selection of the same samples electrically investigated and discussed above. After the electrical measurements, the samples are removed from the vacuum chamber and stored in air for several hours before and during the AFM measurements. Therefore, the results might differ from freshly prepared samples, measured in an inert atmosphere.

The topographies of selected samples are illustrated in figure 4.10, each scanned on an area of $2\,\mu m \times 2\,\mu m$. As a figure of merit, the root-mean-square surface roughness R_{rms} is written onto the images and plotted against the doping concentration in figure 4.11. Most samples show a smooth surface formation with $R_{rms} < 1\,nm$. This roughness value is in the order of less than 3.3 % of the nominal layer thickness of

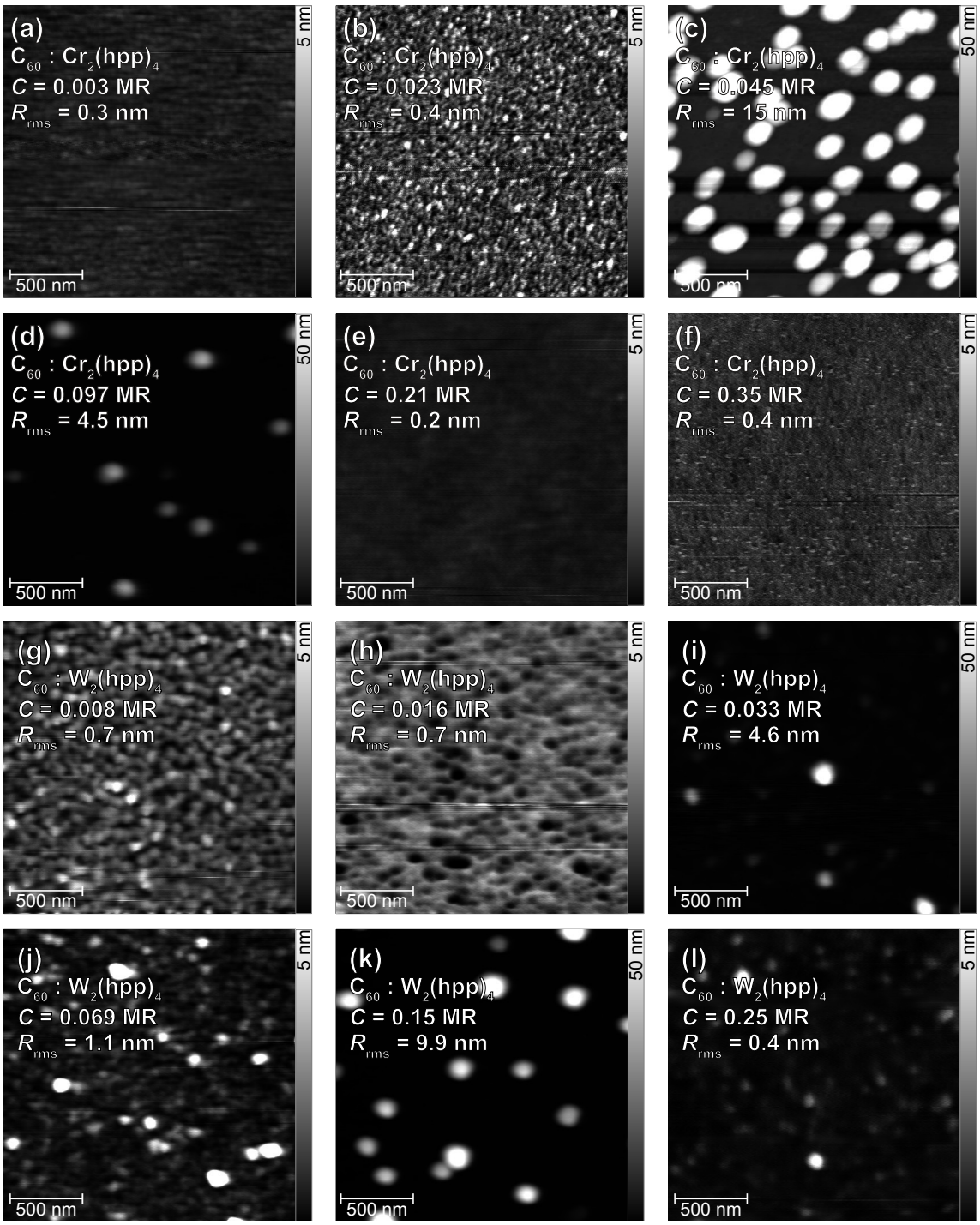

Figure 4.10: *AFM images of a selection of samples. (a-f): C_{60} doped by $Cr_2(hpp)_4$, (g-l): C_{60} doped by $W_2(hpp)_4$. Note the different height scales. Parameters: 2 µm × 2 µm scan area, 30 nm layer thickness, measurements performed in air after electrical investigations and thermal annealing.*

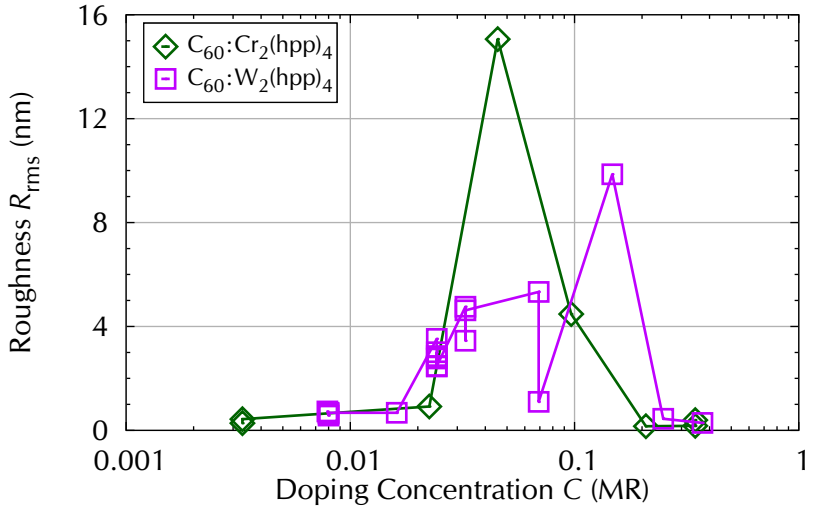

Figure 4.11: *AFM root-mean-square surface roughness R_{rms} of all measured samples, scanned on an area of 2 µm × 2 µm, as shown in figure 4.10.*

30 nm. Interestingly, for both dopants the samples in the medium doping regime of $C = 0.020$ MR to 0.200 MR have rough surfaces with large spikes of more than twice the nominal thickness of the layer. This might be an indication for aggregation of dopants. However, as AFM can neither resolve material content nor the depth profile, further studies with different techniques would be necessary to verify this. Possible candidates are X-ray diffraction or refraction, preferable in an inert atmosphere that could provide information about the crystallinity of the layers.

Surprisingly, highly doped samples of $C > 0.200$ MR for both dopants showed smooth surfaces, even smoother than weakly doped samples. Due to the fact that the measurements are performed in air, this might be a measurement artifact. As ionized dopants could generate a dipole moment on the surface, it is probable that a hydrogen film is formed on the surface, shielding the real topography of the deposited layer. In order to verify this, AFM measurements in vacuum or an inert atmosphere would be necessary, preferable with a thermal annealing of the samples prior to the measurement to remove condensed particles from the surface.

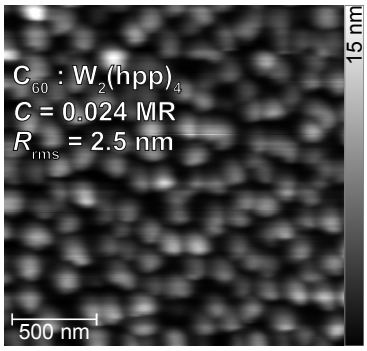

Figure 4.12: *AFM image of an unheated sample of C_{60} doped by $C = 0.024$ MR W_2(hpp)$_4$.*

One freshly prepared non-annealed sample of C_{60} doped by $C = 0.024$ MR of W_2(hpp)$_4$ is investigated and its topography is illustrated in figure 4.12. As the surface of this sample is rough as well with $R_{rms} = 2.5$ nm, it seems evident that the roughness is not an artifact of the thermal annealing procedure.

4.4 Degradation

As the used n-dopants $Cr_2(hpp)_4$ and $W_2(hpp)_4$ have low ionization energies and are hence prone to be highly reactive to air, the influence of air on doped layers of these compounds is studied in this section. A selection of the results presented here can be found in reference [Tie13]. $W_2(hpp)_4$ is chosen, as this dopant has the lower ionization energy (IE) and is therefore expected to show a faster reaction with air, compared to $Cr_2(hpp)_4$. A 30 nm thick layer of C_{60} doped by $C = 0.033$ MR of $W_2(hpp)_4$ is fabricated and measured in an analogous way to previous samples. Directly after fabrication, the conductivity is $\sigma = 2.27\,^{S}/_{cm}$. Following a thermal annealing step, conductivity and Seebeck measurements at different temperatures in the range of 25 °C to 100 °C are performed. After the measurements, the sample is thermally annealed again for 1 hour at an elevated temperature of 120 °C. Afterwards, a reduced conductivity of $1.88\,^{S}/_{cm}$ is measured at 25 °C.

After closing the valve and switching off the vacuum pumps, slowly N_2 gas is injected into the vacuum chamber and the conductivity is continuously probed for 88 minutes. A lowering by more than one order of magnitude is detected, as shown in figure 4.13. Next, the vacuum chamber is opened and the sample is placed in air for 16 minutes, while still continuously probing the conductivity. A rapid drop by three orders of magnitude, down to a value of $\sigma = 1.7{\cdot}10^{-5}\,^{S}/_{cm}$ is observed, showing that air strongly interacts with the n-doped layer. As it is unlikely that the sample reacted with N_2, it is suggested that the degradation in N_2 atmosphere is due to air, entering the chamber through the weak valve separating the vacuum chamber from the disabled pumps.

Such a decrease of conductivity by oxygen-exposure has been reported for metal-doped C_{60} and attributed to the formation of deep oxygen-related electron traps [Fuj94] which were further identified to the formation of oxygen-bridges at single and between adjacent C_{60} molecules [Tse10]. Furthermore, the charge carrier mobility in

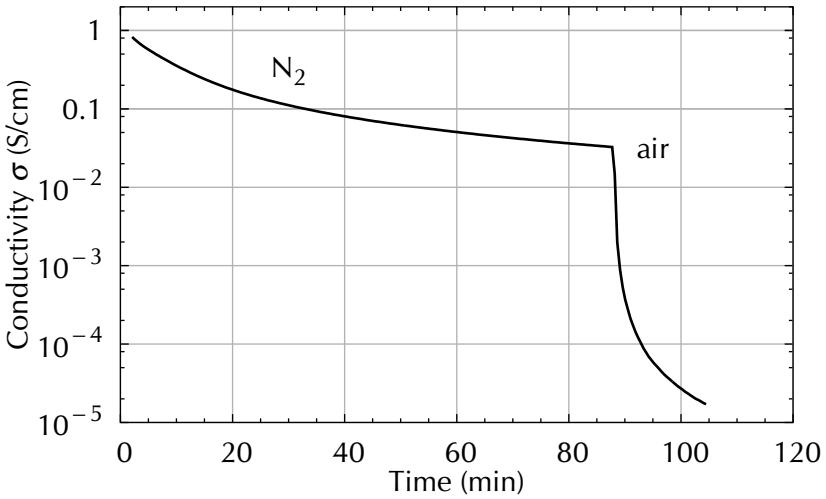

Figure 4.13: *Conductivity during exposure to N_2 (88 minutes) and to air (16 minutes).*

intrinsic C_{60} has been observed to drop under air-exposure by several orders of magnitude [Kön99]. Therefore, the vanishing conductivity might not necessarily be correlated to an oxidation and decomposition of $W_2(hpp)_4$ molecules under air-exposure.

After this measurement, the sample is stored again in the vacuum chamber and the pumps are connected and switched on again, evacuating the chamber for several hours. Monitoring the conductivity, an increase up to a value of $\sigma = 2.1{\cdot}10^{-3}\,\mathrm{S/cm}$ is observed at a pressure of $2{\cdot}10^{-5}$ Pa, shown in figure 4.14 (a). Hence, 0.1% of the initial conductivity is restored by the vacuum, indicating that the molecular n-doping is still partly intact.

An additional, much stronger restoring of the conductivity is achieved by slowly heating the sample in vacuum up to 120 °C, in steps of 5 K and 20 minutes at each temperature. As shown in figure 4.14 (b), the conductivity rises significantly with temperature. Cooling the sample back down to 25 °C, the conductivity stayed at a level of $\sigma = 0.44\,\mathrm{S/cm}$. Applying several longer cycles of heating to 120 °C and cooling down to 25 °C a saturation at $\sigma = 0.60\,\mathrm{S/cm}$ is found.

In conclusion, the initial conductivity of $\sigma = 1.88\,\mathrm{S/cm}$ (100 %) decreased to $\sigma = 1.7{\cdot}10^{-5}\,\mathrm{S/cm}$ (≈ 0.001 %) after 16 minutes in air. By vacuum treatment $\sigma = 2.1{\cdot}10^{-3}\,\mathrm{S/cm}$ (≈ 0.1 %) and by heat treatment $\sigma = 0.60\,\mathrm{S/cm}$ (≈ 32 %) are restored.

The annealing and removal of oxygen- and hydrogen-related electron traps in pure C_{60} has already been investigated by the thermally stimulated current (TSC) technique and validated by an enhanced OFET-mobility of four orders of magnitude when thermally annealed after air-exposure [Mat07]. Since for the above discussed sample more than 30 % of the initial conductivity is restored by vacuum and heat treatment, it is concluded that the n-doping stays at least partly intact during the air-exposure and is only compensated by oxygen-related traps and p-doping effects.

The same sample is later exposed to air for 3 hours to check for the longtime effects. Again, a drop in conductivity is measured, down to a value of $\sigma = 6.6{\cdot}10^{-7}\,\mathrm{S/cm}$. Re-evacuating the vacuum chamber leads to $\sigma = 2.3{\cdot}10^{-5}\,\mathrm{S/cm}$ and heat treatment to $\sigma = 0.03\,\mathrm{S/cm}$. Thus, the much longer air-exposure reduces the final conductivity by

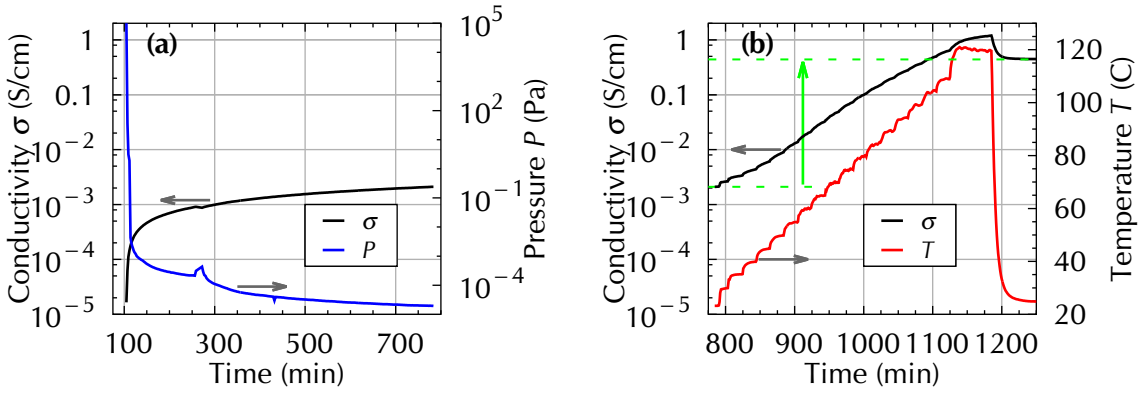

Figure 4.14: *Conductivity regeneration by (a) vacuum and (b) in-situ heat treatment.*

an additional factor of 20. The final value is still above the conductivity of a freshly fabricated and thermally annealed sample of C_{60} doped by $C = 0.014\,\mathrm{MR}$ of the air-stable precursor n-dopant AOB that will be presented and discussed in the following chapter. However, it seems evident that the longer exposure degrades more $W_2(hpp)_4$ molecules within the C_{60} layer.

Besides the conductivity, the Seebeck energy E_S and the activation energy of the conductivity $E_{act,\sigma}$ are measured after vacuum and heat treatment. A summary is given in table 4.1. The initial conductivity dropped by a factor of 3 after 16 minutes in air and by an additional factor of 20 after 3 hours in air. 16 minutes in air increased $|E_S|$ by 8.8 meV to 82.3 meV (+12 %) and $E_{act,\sigma}$ by 3.8 meV to 103.4 meV (+4 %). The second exposure of 3 hours in air leads to a gain of $|E_S|$ by another 28.0 meV (+34 %) and of $E_{act,\sigma}$ by 43.1 meV (+42 %).

The rise in $|E_S|$ corresponds to an increased difference between the Fermi level E_F and the transport level E_{Tr} and hence to a smaller density of free electrons n_e. However, after 3 hours of air-exposure the observed $|E_S|$ of the investigated sample of $C = 0.033\,\mathrm{MR}$ of $W_2(hpp)_4$ is still lower than the corresponding value of an unexposed sample with a tenth of the doping concentration: $|E_S| = 167\,\mathrm{meV}$ at $C = 0.004\,\mathrm{MR}$. This comparison clearly shows that for the air-exposed sample, at least 10 % of the $W_2(hpp)_4$ molecules survive the contact with air and are still providing molecular n-doping. As the measured Seebeck coefficients S are still negative, compensating p-doping of C_{60} by oxygen can be excluded. While the E_S is already strongly affected by 16 minutes of air-exposure, the $E_{act,\sigma}$ only significantly increases after the 3 hours exposure. This suggests a slow but strong change of the charge carrier mobility due to a sustainable formation of electron traps, whereas in case of short exposure most of the induced electron traps can be removed by thermal annealing in vacuum. Furthermore, the larger amount of degradation products that are expected to be present in the layer after 3 hours of air-exposure could act as additional trap states and hence raise $E_{act,\sigma}$.

Table 4.1: *Overview of the effect on air-exposure on the observables conductivity σ, Seebeck coefficient S, Seebeck energy E_S and activation energy of the conductivity $E_{act,\sigma}$. All measurements performed on the same sample of $C = 0.033\,\mathrm{MR}$ $W_2(hpp)_4$.*

measurement after	σ $^{S}/_{cm}$	S $^{\mu V}/_{K}$	$\lvert E_S \rvert$ meV	$E_{act,\sigma}$ meV
	($T = 25\,^\circ\mathrm{C}$)	($T_m = 40\,^\circ\mathrm{C}$)		($T = 25$ to $70\,^\circ\mathrm{C}$)
sample preparation	2.27			
annealing at 70 °C	2.90	−226.1	67.7	77.8
several loops 25 °C to 100 °C	1.78	−234.8	73.5	99.6
60 min at 120 °C	1.88			
16 min in air	$1.7{\cdot}10^{-5}$			
th. annealed in vacuum	0.60	−262.8	82.3	103.4
180 min in air	$6.6{\cdot}10^{-7}$			
th. annealed in vacuum	0.03	−352.2	110.3	146.5

Further studies of the degradation mechanism of pure $W_2(hpp)_4$ as well as of layers of C_{60} doped by $W_2(hpp)_4$ employing the techniques of ultraviolet photoelectron spectroscopy (UPS), X-ray photoelectron spectroscopy (XPS) as well as laser desorption/ionization time of flight mass spectrometry (LDI-TOF-MS) revealed that the majority of the dopant molecules immediately decomposes after air-exposure [Tie13]. However, the remaining $W_2(hpp)_4$ molecules stay intact and slowly degrade with an exponential decay time of ≈ 13 minutes. These findings are attributed to a rise of the IE of $W_2(hpp)_4$ upon charge-transfer, resulting in a protection against oxidation in air. Consequently, the observed recovery of the conductivity is interpreted as a self-passivation of the molecular n-doping. Such a passivation mechanism of n-doped layers enables processing steps under ambient conditions, greatly enhancing device fabrication possibilities [Kle12b].

4.5 Conclusion

It is found that both dopants, $Cr_2(hpp)_4$ and $W_2(hpp)_4$, are well suited to n-doped C_{60}. Extremely high conductivities of up to $\sigma = 7\,^{S}/_{cm}$ are measured, with $Cr_2(hpp)_4$ leading to larger values than $W_2(hpp)_4$. Continuously probing the conductivity for 1 hour after sample preparation, an increase for low and a decrease for high doping concentrations is observed. In order to ensure comparable measurement conditions, the samples are thermally annealed prior to the electrical investigations. Afterwards, for both dopants a linear relation of $\sigma(C)$ is measured, until at high C a drop in σ is detected. This reduction is attributed either to a disturbance of the morphology by the large amount of dopants in the layer and hence a drop of the mobility or to a reduced doping efficiency due to clustering of dopants. Seebeck data showed that S decreases further at high C and hence the density of free electrons increases, which suggests that the doping efficiency is not decreasing and the drop in conductivity is due to a reduced mobility.

Such high conductivities are relevant for device applications, since they enable good charge injection and extraction from the contacts, hence reducing ohmic losses and increasing device performance [Blo98]. Furthermore, the substitution of the metal contacts by highly conducting doped organic layers would allow for pure organic devices [Sch13]. Additionally, in organic tandem photovoltaic cells, a highly conducting recombination and spacer layer between the two subcells is crucial for device performance [Rie11b,Mei11].

Varying the temperature, the conductivity is found to be in good agreement with a thermally activated hopping transport and an activation energy of the conductivity $E_{act,\sigma}$ is derived. $E_{act,\sigma}$ decreases with C for low and moderate C of both dopants, attributed to a shift of the Fermi level towards the transport level. At high C, the $E_{act,\sigma}$ increases, indicating a disturbance of the morphology of the host material by the large percentage of dopant molecules, in agreement with the conductivity data.

Thermoelectric measurements prove that for all samples electrons are the dominating charge carriers and allow for deriving the energetic difference E_S between Fermi level

and transport level. This difference is reduced with raising doping concentration, as expected from the trend of $E_{\mathrm{act},\sigma}$. As E_S does not increase at high C, the observed rise of $E_{\mathrm{act},\sigma}$ and the reduced σ are attributed to changes in the mobility.

AFM studies of the surface roughness yield a rising surface roughness with doping concentration in the low and medium doping regime. At high C, the surfaces are found to be very smooth, which is attributed to a hydrogen film on the surface, attracted by the strongly ionizing dopants and shielding the real topography. Hence, AFM is not a suitable technique to study the morphology of doped layers, as only the surface is probed and material content cannot be resolved.

Air-exposure of n-doped layers is found to lead to fast degradation of the conductivity. However, a large fraction of the initial conductivity can be restored by vacuum and heat treatment. This finding could allow for device processing steps under ambient conditions, greatly enhancing device fabrication possibilities.

Overall it is shown that both dopants are exceptionally well suited for n-doping C_{60}. Recently, $W_2(hpp)_4$ was successfully deployed in devices[Sch12,Fis12]. It would be interesting to study these dopants in hosts of lower electron affinity to investigate the influence of the molecules' energy levels. First measurements of successfully n-doping ZnPc[‡] by $W_2(hpp)_4$[Bur13] are promising.

[‡]ZnPc is zinc phthalocyanine, EA = 3.34 eV[Gao01]

Chapter 5

Air-Stable n-Dopants in C_{60}

In this chapter, the doping mechanisms of two air-stable precursor n-dopants, AOB and DMBI-POH, are studied and compared to the air-sensitive dopants discussed in the previous chapter. Air-stable n-dopants are much easier to handle and thereby are promising candidates for replacing air-sensitive n-dopants in the future. In section 5.1, the conductivity of differently doped samples is investigated. Directly after sample preparation, a strong gain over time is detected. Following a thermal annealing step, samples doped by AOB yield a linear, samples of DMBI-POH a superlinear relation of conductivity to doping concentration and possible explanations are discussed. Temperature-dependent measurements are again indicating a thermally activated hopping process, allowing for deriving an activation energy of the conductivity. The second section 5.2 presents thermoelectric (Seebeck) investigations for a variation of the temperature and the doping concentration. The results are compared to the activation energy of the conductivity and conclusions for the mobility are drawn. Section 5.3 presents atomic force microscopy (AFM) studies, probing the surface roughness of differently doped samples for indications of clustering or agglomeration of dopants. The findings are summarized in section 5.4. Finally, in section 5.5, DMBI-POH is compared to a closely related compound, o-MeO-DMBI-I, and a similar doping mechanism for both is proposed.

In the previous chapter, two typical n-dopants with extremely low ionization energies are investigated. As such n-dopants are usually unstable in air, handling in an inert atmosphere is required, complicating the fabrication process. In this chapter, the two n-dopants AOB and DMBI-POH which are air-stable prior to deposition are investigated. Both dopants are salt precursor compounds and form the active dopant compound in-situ during material deposition, as discussed in section 3.2.2, where the materials' properties are summarized as well. Again, C_{60} is used as host material and the same set of experiments is also performed on the air-stable dopants. A selection of the results presented here is published in reference [Men12b].

In general, it is expected that not all deposited air-stable precursor molecules undergo the transformation to the active dopant compounds, hence the doping efficiency of this class of dopants is likely to be lower compared to air-sensitive dopants, where the source material is already the active dopant compound.

Sample preparation and measurements are performed in vacuum, as discussed in sections 3.1.2 and 3.1.4. To ensure optimal preparation conditions for AOB, the chamber is illuminated using a halogen lamp, as proposed by Li et al. [Li06]. For calculating the doping concentration of DMBI-POH samples, the molar mass of OH-DMBI (240.3 $^{g}/_{mol}$) is used, as this material is expected to be formed during deposition, as discussed in section 3.2.2 and later supported by section 5.5.1.

As only small quantities of the rather expensive material DMBI-POH were available, thinner layers of 20 nm thickness are produced for samples of high doping concentration $C > 0.200$ MR instead of the usual 30 nm. This different layer thickness does not influence the thermoelectric properties and has only little influence on the conductivity via the surface roughness, as discussed in section 3.1.3.

5.1 Conductivity

The conductivities of layers of C_{60} doped by various doping concentrations of AOB or DMBI-POH are shown in figure 5.1. Measurements are performed directly after fabrication of the samples at $T = 25\,°C$. As a linear and symmetric current-voltage relation is measured for all samples, and the literature value for the contact resistance between gold and C_{60} is low [Kit11], the charge injection can be neglected. Both materials efficiently dope C_{60} as the conductivity of the doped layers is several orders of magnitude higher than for undoped C_{60}, which has been reported to be in the order of $\sigma = 2{\cdot}10^{-8}\,{}^{S}/_{cm}$ [Li06] and which would be below the resolution limit of the Seebeck setup of $\sigma = 8.3{\cdot}10^{-8}\,{}^{S}/_{cm}$ as discussed in section 3.1.5. The conductivity can be tuned by doping over two orders of magnitude for each dopant. At high C, DMBI-POH samples reach $\sigma > 1\,{}^{S}/_{cm}$, whereas for AOB the σ is approximately 100 fold lower at each C. Samples doped by DMBI-POH show a saturation at $C > 0.100$ MR, whereas for AOB samples no distinct saturation is visible. This observation is in contrast to the results determined for high doping concentrations of the air-sensitive dopants $Cr_2(hpp)_4$ and $W_2(hpp)_4$ (compare figure 4.1 on page 53), as high C of these materials lead to a decrease in σ. The result is even more surprising, since higher doping

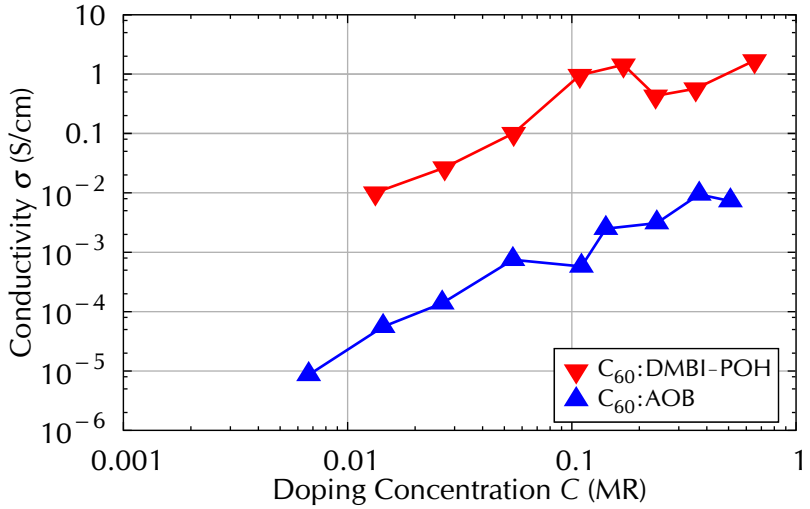

Figure 5.1: *As-prepared conductivity σ vs. doping concentration C of samples of C_{60} doped by AOB or DMBI-POH, measured at $T = 25\,°C$. Compare to undoped C_{60} with $\sigma \approx 2{\cdot}10^{-8}\,{}^{S}/_{cm}$ [Li06].*

concentration of $C = 0.650\,\mathrm{MR}$ and $C = 0.510\,\mathrm{MR}$ are used for DMBI-POH and AOB, respectively. This finding suggests that the lighter dopants AOB and DMBI-POH do not disturb the morphology of C_{60} as strongly as the heavier and strongly electronegative dopants $Cr_2(hpp)_4$ and $W_2(hpp)_4$. The relation between conductivity and doping concentration is discussed in more detail in section 5.1.2. First, the change in conductivity directly after sample preparation and the influence of thermal annealing are discussed.

5.1.1 Conductivity Changes after Preparation

As for most sets of materials, prior to further measurements, the conductivity of each sample is continuously probed for 1 hour at a fixed temperature of $T = 25\,°C$. A strong increase of conductivity with time is detected for both dopants at all doping concentrations. In order to quantify the change in σ, the data are fitted according to equation (4.2) on page 53. The resulting fitting parameters are shown in figure 5.2.

The fitted maximal relative change χ is much larger for samples doped by AOB than for DMBI-POH, with a maximum of $\chi = +350\,\%$ for $C = 0.026\,\mathrm{MR}$ of AOB, compared to $\chi = +76\,\%$ at a similar doping concentration of $C = 0.027\,\mathrm{MR}$ of DMBI-POH. The change χ detected for both materials is stronger than for $Cr_2(hpp)_4$ and $W_2(hpp)_4$. Furthermore, whereas for $Cr_2(hpp)_4$ and $W_2(hpp)_4$ a decrease of σ at $C > 0.040\,\mathrm{MR}$ is found, all samples doped by the two air-stable dopants show an increase of σ during the first hour after deposition.

As it has been reported [Li06] that illumination during deposition can accelerate/enhance the doping process for AOB, it is possible that in this case during sample fabrication the illumination intensity was too low, or that AOB generally needs more time to deploy its full doping capability and therefore shows a much stronger

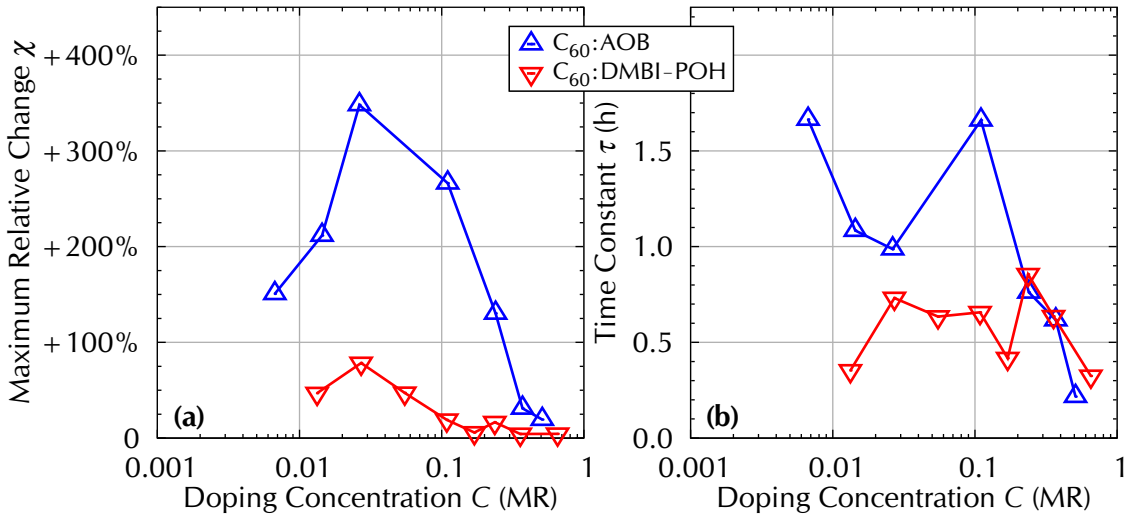

Figure 5.2: *Fitting parameters of conductivity change during the first hour after sample preparation, according to equation (4.2) on page 53: (a) maximal relative change χ reached after $t \gg \tau$ (b) time constant τ describing the speed of the change.*

change after preparation than DMBI-POH. The positive change observed for all doping concentrations of both materials might be due to a molecular rearrangement, as the dopants are much smaller than C_{60} and might be able to diffuse until they find a suitable host molecule to donate their electron to.

The time constant τ is smaller for almost all DMBI-POH samples than for the AOB samples, corresponding to a faster approach of saturation. While the values of the DMBI-POH samples scatter around $\tau = 0.6 \pm 0.3$ hours, for AOB τ drops with rising doping concentration from 1.7 hours at $C = 0.007\,\mathrm{MR}$ to 0.2 hours at $C = 0.510\,\mathrm{MR}$. The reason for this difference is not clear at present.

5.1.2 Relation of Conductivity to Doping Concentration

As discussed in section 4.1.2, all samples are thermally annealed prior to further measurements, in order to ensure stable measurement conditions. They are slowly heated from $T = 25\,^{\circ}\mathrm{C}$ to $100\,^{\circ}\mathrm{C}$ and kept at this temperature for 60 minutes. Afterwards, the samples are slowly cooled down and the measurement routine (compare section 3.1.4) is started with a conductivity measurement at $T = 25\,^{\circ}\mathrm{C}$, where no further change of σ over time is detected.

In figure 5.3, the conductivity after thermal annealing is compared to the conductivity measured directly after sample preparation (compare figure 5.1), both measured at $T = 25\,^{\circ}\mathrm{C}$. After annealing, a strong increase by two to three orders of magnitude is observed for the AOB samples, demonstrating that illumination alone is not sufficient to deploy the full doping capability of AOB. The conductivity of the DMBI-POH samples increases to a lesser extent, by a factor of about 10. Thermal annealing seems to accelerate the effect responsible for the change of conductivity during the first

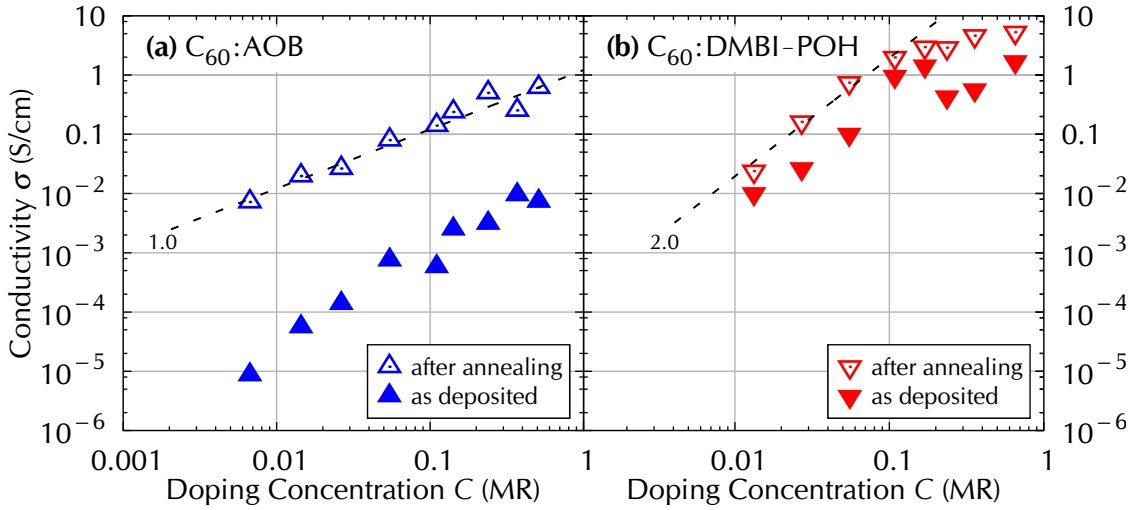

Figure 5.3: *Conductivity before (filled symbols) and after (empty symbols) thermal annealing (at $T = 100\,°C$) for C_{60} doped by (a) AOB and (b) DMBI-POH. The dashed lines represent a slope of 1.0 for AOB and a slope of 2.0 for DMBI-POH.*

hour after sample preparation. This observation is consistent with the results for the air-sensitive dopants $Cr_2(hpp)_4$ and $W_2(hpp)_4$, compare section 4.1.2.

For the air-sensitive dopants, three different contributions to the change of conductivity are discussed in the previous chapter: Firstly, residual quantities of O_2 and moisture, present in the vacuum chamber, could react with the n-doped layers and reduce the conductivity. Thermal annealing might remove these impurities and hence increase the conductivity. Secondly, small rearrangements of the molecules could lead to an increase in conductivity. Thirdly, a phase separation and demixing of host and dopant at high doping concentration may reduce the conductivity due to shielding of dopants. As the observed changes of the conductivity are all positive and much stronger than for the air-sensitive dopants, the changes are most likely due to a major additional contribution. Most probably, the transformation which forms the active dopant compounds from the air-stable precursor molecules is not completed by all molecules during sample deposition. Instead, the process continues afterwards and can be accelerated by heating the doped layer.

After the thermal annealing step, an increasing conductivity with doping concentration is measured for both dopants. For AOB, a linear correlation between doping concentration and conductivity, highlighted by the dashed line of slope 1.0 in figure 5.3 (a), is found for over two orders of magnitude with no saturation visible in the data. Thus, each additional dopant molecule contributes identically to the increase of σ. At the highest $C = 0.510\,\mathrm{MR}$ of AOB, $\sigma = 0.6\,{}^{\mathrm{S}}/_{\mathrm{cm}}$ is measured at $T = 25\,°C$. This value is higher than the previously reported data [Li06], which is due to the higher doping concentration and optimized preparation conditions, e.g. illumination during evaporation and the thermal annealing step.

The conductivity of almost all DMBI-POH samples is one order of magnitude higher than for AOB at corresponding doping concentrations, when measured at $T = 25\,°C$

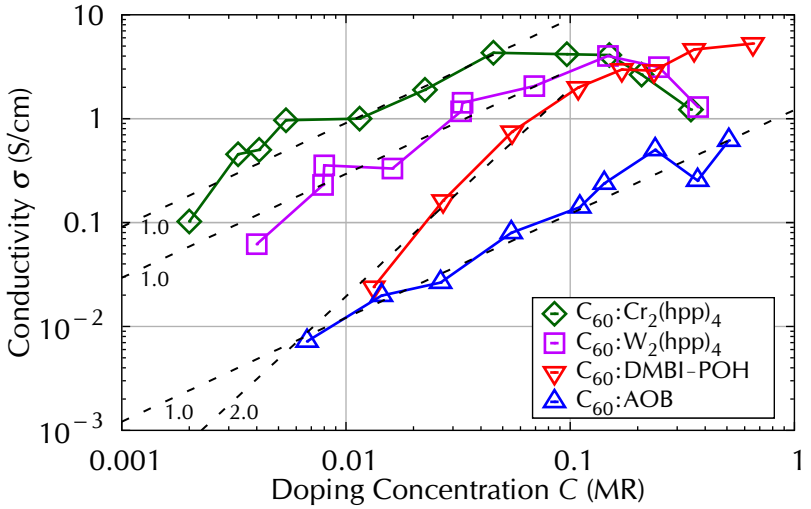

Figure 5.4: *Comparing the conductivity after thermal annealing of samples of C_{60} doped by air-stable (AOB and DMBI-POH, $T = 25\,°C$) and air-sensitive ($Cr_2(hpp)_4$ and $W_2(hpp)_4$, $T = 30\,°C$) dopants. The dashed lines of slopes 1.0 and 2.0 are guides to the eye.*

after the thermal annealing. A highest value of $\sigma = 5.3\,{}^{S}/_{cm}$ is found at $C = 0.650\,\text{MR}$, which is even $1\,{}^{S}/_{cm}$ higher than the record conductivity for the air-sensitive dopants (after thermal annealing), summarized in figure 5.4. The DMBI-POH samples show a different tendency than the samples doped by AOB, as for low C the σ increases superlinearly with C at a slope of 2.0, highlighted by the dashed line in figure 5.3 (b). At $C > 0.150\,\text{MR}$ the slope is reduced, first to a value in the range of 1.0 and later a saturation is detected. The reduced slope for $C > 0.150\,\text{MR}$ of DMBI-POH, might be attributed to aggregation of dopant molecules, leading to a decreasing doping efficiency[Mit12b], or to a disturbance of the morphology resulting in a lower mobility[Kle12a]. In section 5.3, AFM studies on doped layers are presented, showing peaks arising from the layer for $C > 0.150\,\text{MR}$, which makes both explanations plausible.

In agreement with AOB, samples doped by the air-sensitive dopants $Cr_2(hpp)_4$ and $W_2(hpp)_4$ show a linear relation of σ to C as summarized in figure 5.4. The superlinear increase for DMBI-POH suggests that there may be a difference in the doping or transport mechanism when C_{60} is doped by DMBI-POH. A conductivity slope of more than 1.0 has been reported as well as predicted by various groups and models, as discussed below.

Our collaborators from Stanford University observed a similar slope in the range of 2.0 for PCBM[‡] doped by the neutral dopant N-DMBI[§] which is closely related to DMBI-POH[Wei10]. Gregg et al.[Gre04] expected a superlinear relation for all excitonic semiconductors, due to a decrease of exciton binding energy with increasing doping concentration. Männig et al.[Män01] interpreted a superlinear increase of the conductivity upon doping as indication for shallow states in combination with percolative transport and a sublinear increase as indication for deep donors states. Both of these

[‡]PCBM is [6,6]-phenyl-C_{61}-butyric acid methyl ester
[§]N-DMBI is (4-(1,3-dimethyl-2,3-dihydro-1*H*-benzoimidazol-2-yl)phenyl)dimethylamine

models can be used to explain the mechanism of doping of C_{60} with DMBI-POH but they are at odds with the observations for the other three n-dopants (AOB, $Cr_2(hpp)_4$ and $W_2(hpp)_4$). However, the fact that the conductivity increase is not superlinear for the other dopants does not invalidate these models.

According to Arkhipov et al.[Ark05b], doping generates deep Coulombic traps in disordered organic semiconductors, which can reduce the mobility with increasing doping concentration. These traps may be generated by changes of the energy levels due to the presence of ionized dopants or could be created by disturbances in the morphology. OH-DMBI, being the active dopant compound formed from DMBI-POH is the smallest of the investigated n-dopants (with a diameter of ≈1.0 nm, compare figure 3.5 on page 45), thus it may cause small morphological disturbances of the C_{60} host molecules, leading to a superlinear increase of σ at $C < 0.100\,\mathrm{MR}$. To validate this hypothesis, morphological analysis of the molecular arrangement by techniques like X-ray diffraction or refraction should be performed. Since AOB is the least efficient dopant (with respect to the conductivity), it might have a deeper donor state compared to DMBI-POH resulting in generation of trap states and hence a decreasing mobility with rising doping concentration. The presence of traps could be investigated e.g. by methods like impedance spectroscopy (IS)[Bur12] or thermally stimulated current (TSC)-based methods like charge-based deep level transient spectroscopy (Q-DLTS)[Gau01]. This however is beyond the scope of this thesis.

A deep donor state for AOB agrees with the results of Harada et al.[Har07] who demonstrated that the OFET-mobility of AOB-doped C_{60} decreases upon doping. Increasing C from 0.010 MR to 0.075 MR, the mobility dropped by a factor of three, which corresponds to a slope of -0.5 in a logarithmic scale. The decreasing mobility was attributed to a scattering of charge carriers at ionized impurities, introduced by doping. Even if the density of free electrons n_e increased superlinearly with C for AOB samples as well, a decreasing mobility would lead to a reduced slope of $\sigma(C)$.

Olthof et al.[Olt12] have reported for the material system of C_{60} doped by $[RuCp^*(mes)]_2$[‡] that at $C < 0.001\,\mathrm{MR}$, a superlinear slope of $\sigma(C)$ is attributed to filling of trap states. As the doping concentrations investigated in this thesis are above 0.001 MR, filling of host material trap states is not likely to be responsible for the superlinear slope. Olthof et al. furthermore reported on a gain in mobility upon doping, which they again attributed to filling of trap states. As they have assumed a concentration-independent doping efficiency of $\eta_{dop} = 100\,\%$ to calculate the density of free electrons n_e from C, their approach is contrary to the model of a threshold doping concentration presented by Mityashin et al.[Mit12b], as discussed in section 2.2.3.2. Up to now, it is not clear which model is correct for the material system presented here.

Another considerable reason leading to a superlinear increase of conductivity for DMBI-POH compared to AOB would be that as in these systems charge carriers are transported along a manifold of states distributed in energy and space, a charge carrier density-dependent mobility is expected. Upon increasing the charge carrier den-

[‡] $[RuCp^*(mes)]_2$ is ruthenium(pentamethylcyclopentadienyl)(1,3,5,-trimethylbenzene)

sity, the mobility may increase if the low-lying localized states are filled, leading to a transport dominantly along the denser part of the density of states. This phenomenon is observed in OFETs where these states are filled by the gate bias. It is possible that for efficient doping a similar effect may be present. In such a case the conductivity increases superlinearly with C. However, dopants such as $Cr_2(hpp)_4$ and $W_2(hpp)_4$, which lead in C_{60} to conductivities similar to DMBI-POH, as summarized in figure 5.4, do not show such a behavior, suggesting that this phenomenon may not be dominant in this system.

5.1.3 Temperature Dependence of the Conductivity

In analogy to the samples of C_{60} doped by the air-sensitive dopants in the previous chapters, the conductivity after thermal annealing is probed at different temperatures between $T = 25\,°C$ and $100\,°C$ and is found to rise with temperature. Figure 5.5 displays the measured data of all samples in Arrhenius plots. A linear relation is found, in agreement with the results for the air-sensitive dopants and the literature, indicating a thermally activated transport mechanism for which again an activation energy of the conductivity $E_{act,\sigma}$ can be derived employing equation (2.25) on page 16.

The resulting values of the differently doped samples range from $E_{act,\sigma} = 63\,meV$ for low to 241 meV for high doping concentrations and are illustrated in figure 5.6. They are well below the previously reported value for undoped C_{60} of around 640 meV[Li06]. The $E_{act,\sigma}$ is higher for the AOB samples than for the DMBI-POH ones, excluding the lowest doped DMBI-POH sample. While for the AOB samples $E_{act,\sigma}$ slowly drops with rising doping concentration, the DMBI-POH samples yield a much stronger decrease and a saturation at $E_{act,\sigma} \approx 75\,meV$ at $C > 0.150\,MR$. At the same doping concentration, a reduction of the superlinear slope of $\sigma(C)$ is observed in figure 5.3 on page 75.

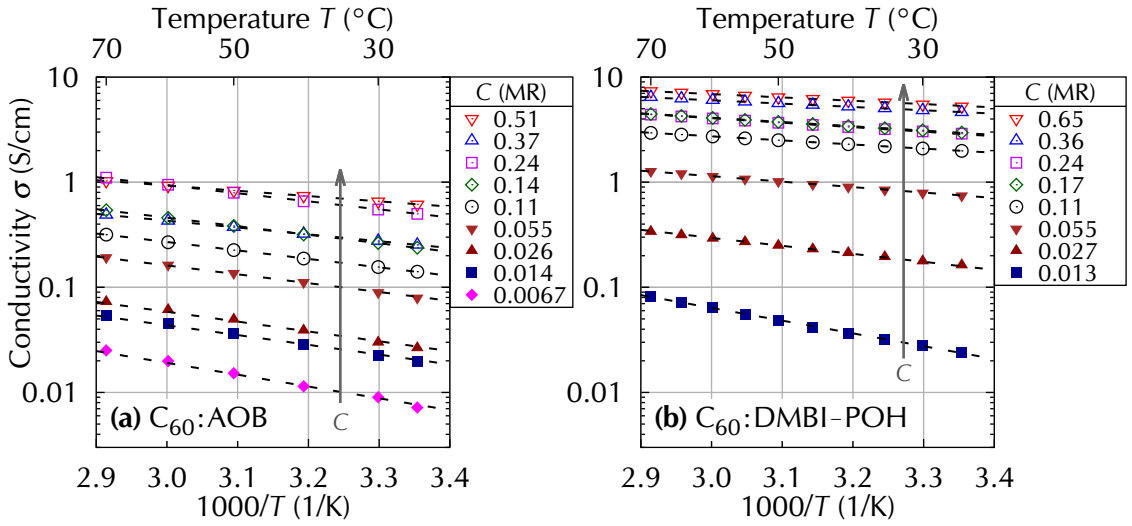

Figure 5.5: *Temperature dependence of the conductivity of C_{60} doped by (a) AOB and (b) DMBI-POH. Lines are fits using equation (2.25) on page 16.*

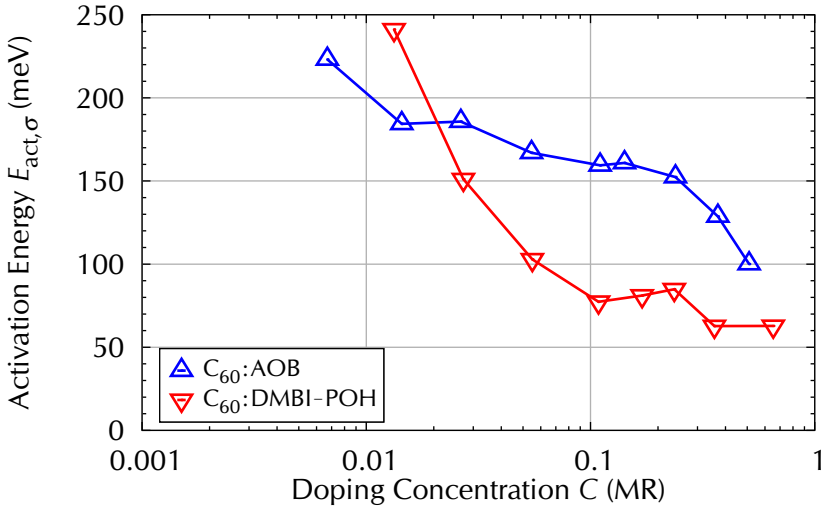

Figure 5.6: *Activation energy of the conductivity $E_{act,\sigma}$, derived from the temperature dependence of the conductivity $\sigma(T)$ in the range of $T = 25\,°C$ to $100\,°C$ shown in figure 5.5, using equation (2.25) on page 16.*

As discussed in section 4.1.3, the drop of $E_{act,\sigma}$ with increasing doping concentration is attributed to a shift of the Fermi level E_F towards the transport level E_{Tr} of C_{60}. This shift leads to a reduction of the temperature dependence of the density of free electrons $n_e(T)$.

At high doping concentrations of AOB, a rapid drop of $E_{act,\sigma}$ is observed. This may be attributed to the fact that at high C, AOB (which is not as efficient as DMBI-POH) is able to fill up the deeper states of the density of states and to contribute more to the shift of the E_F. Such a process is similar to what is known as compensation in classic semiconductor theory. When compensation is the dominant effect, E_F is pinned to the dopant level. If compensation is no longer the main effect, E_F shifts towards the conduction band minimum E_C (for n-doping). A higher dopant level of DMBI-POH would lead to a more efficient filling of the energetically lower lying low-mobility states of the hosts density of states, thus generating an overall higher mobility along with a lower $E_{act,\sigma}$.

In case of C_{60} n-doped by the air-sensitive dopants $Cr_2(hpp)_4$ and $W_2(hpp)_4$, at high doping concentrations an increase of $E_{act,\sigma}$ along with a decrease of σ is found. This behavior is not observed for the lighter dopants AOB and DMBI-POH, even though the doping concentrations are higher. Since this effect is attributed to a disturbance of the morphology of the host material by the large percentage of dopant molecules, AOB and DMBI-POH are understood to lead to less disturbance, which might be attributed to their smaller size. AFM investigations, presented in section 5.3, show that with rising doping concentration more and more artifacts are arising on the samples' surfaces for C_{60} doped by each of the two air-stable dopants. These artifacts are an indication for agglomeration of dopants or charge-transfer complexes.

5.2 Thermoelectric Measurements

5.2.1 Temperature Dependence of the Seebeck Coefficient

Along with the conductivity investigations, thermoelectric (Seebeck) studies are performed. The probed Seebeck coefficients S for layers of C_{60} doped by AOB or DMBI-POH are presented in figure 5.7 (a) and (c). As expected, they are negative in sign, thus, for all samples, electrons are the dominating charge carrier species and hole conduction along the dopant molecules is not observed. The resulting values range from $S = -120\,\mu V/K$ to $-580\,\mu V/K$ and a decrease of $|S|$ with increasing C is detected, similar to the results for the air-sensitive dopants in section 4.2.

In order to investigate the influence of the mean temperature T_m, the relative changes of S, normalized to the measurements at $T_m = 40\,°C$, are depicted in figure 5.7 (b) and (d). A temperature of 40 °C is chosen, as it is a device-relevant temperature and allows for more stable temperature control than $T_m = 30\,°C$. In the investigated range of $T_m = 30\,°C$ to 100 °C all DMBI-POH samples except the two lowest doped

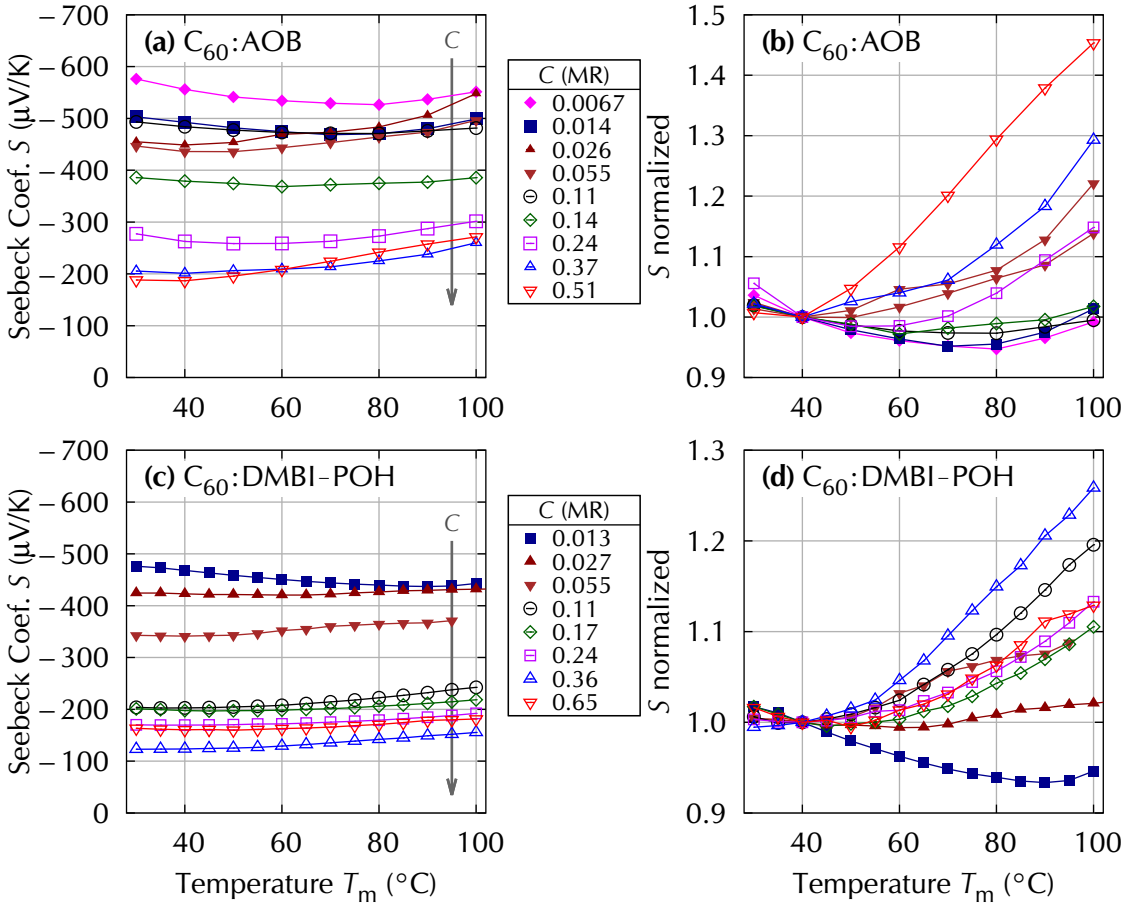

Figure 5.7: *Temperature dependence of the Seebeck coefficient S for C_{60} doped by AOB and DMBI-POH in (a) and (c). At the right side, in (b) and (d), the relative changes of S are illustrated, normalized to the $T_m = 40\,°C$ measurements.*

ones show a strong gain of $|S|$ with T, in the order of +10 % to +25 % (compare figure 5.7 (d)). There is no clear relation between doping concentration and the magnitude of increase present in the data. In case of doping by AOB, even stronger increases by up to +45 % are recorded, but on the other hand four of the nine samples yield a more or less temperature-independent S. Thus, there is again no clear trend visible.

As the temperature dependence of S for samples doped by the air-sensitive dopants $Cr_2(hpp)_4$ and $W_2(hpp)_4$, discussed in section 4.2.1, is measured in a smaller temperature range of $T_m = 30\,°C$ to $70\,°C$, the 4 dopants can only be compared in this range, where the relative changes are similar. It is not clear up to now why for AOB and DMBI-POH the strongest change is recorded at high doping concentrations, whereas for $Cr_2(hpp)_4$ and $W_2(hpp)_4$ the weakly doped samples show the strongest change.

5.2.2 Relation of Seebeck Coefficient to Doping Concentration

Comparing the Seebeck coefficients at $T_m = 40\,°C$ for different doping concentrations, a reduction of $|S|$ with rising C is found for both dopants, ranging from $S = -714\,\mu V/K$ to $-124\,\mu V/K$, as illustrated in figure 5.8. Using equation (2.66) on page 28, again the energetic difference E_S between the Fermi level E_F and the transport level E_{Tr} can be derived:

$$E_S = S \cdot e \cdot T \quad \text{with} \quad E_S := E_F - E_{Tr}\,. \tag{2.66}$$

This quantity is drawn as the right hand axis in figure 5.8. A maximum of $E_S = -183\,meV$ is measured for the lowest doping concentration of $C = 0.0067\,MR$ of AOB. Analogously, for DMBI-POH the largest $E_S = -147\,meV$ is measured for the lowest doping concentration of $C = 0.013\,MR$.

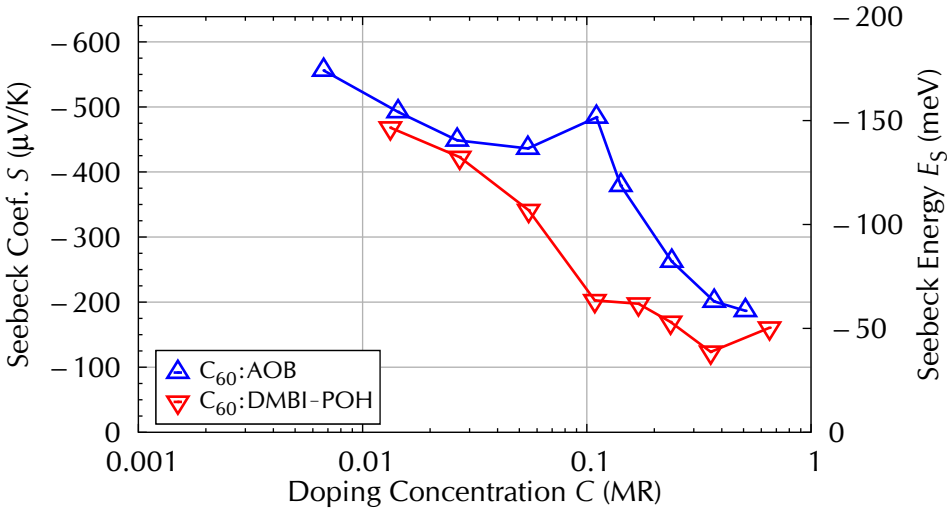

Figure 5.8: *Seebeck coefficient S and derived Seebeck energy E_S at $T_m = 40\,°C$.*

Following the trend of S, the value of E_S drops with rising C for both dopants, which corresponds to a shift of the Fermi level E_F towards the transport level E_{Tr} and thus an increasing charge carrier density n_e, which is in agreement with the observations of the air-sensitive dopants. At high doping concentrations, a value of $E_S < 65\,\text{meV}$ is derived for both dopants. This saturation value is somewhat higher than observed for the air-sensitive dopants, where $E_S < 50\,\text{meV}$ was found in section 4.2.2. Again, the saturation can be explained by a pinning of E_F close to E_{Tr} via degenerate doping.

5.2.3 Comparison of Seebeck Energy and Activation Energy

In figure 5.9, the Seebeck energy E_S is compared to the previously discussed activation energy of the conductivity $E_{act,\sigma}$, for AOB and DMBI-POH in part (a) and (b), respectively. The DMBI-POH samples show for almost all doping concentrations a reasonable agreement of the two energies, whereas for all AOB samples a difference of $E_{act,\sigma} \approx E_S + 50\,\text{meV}$ is observed.

If the temperature dependence is Arrhenius-like, the difference between $E_{act,\sigma}$ and E_S for the AOB samples is attributed to an activation of the mobility, as discussed in section 4.2.3. For the air-sensitive dopants, a discrepancy between $E_{act,\sigma}$ and E_S is observed only at high C, which is attributed to a disturbance of the morphology by the large number of dopant molecules. Such a temperature-activated mobility is another indication that AOB introduces deep lying trap states. However, the temperature dependence of the mobility may differ from a simple activated case, as discussed in section 4.2.3.

Harada et al.[Har07] have reported a temperature-independent OFET-mobility for C_{60} doped by $C = 0.010\,\text{MR}$ to $0.075\,\text{MR}$ of AOB in the range of $T = 30\,°\text{C}$ to $100\,°\text{C}$. The

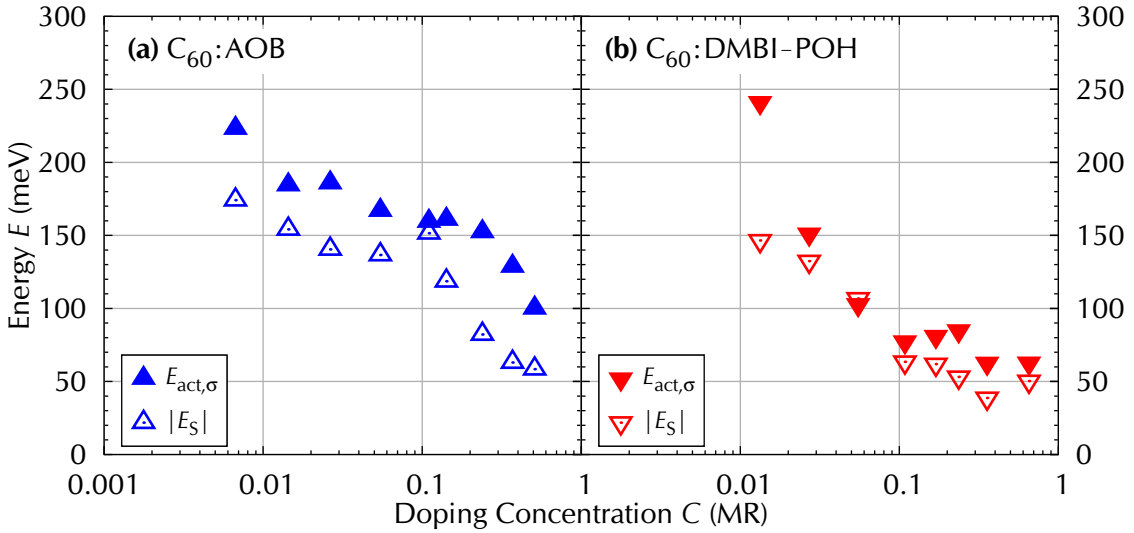

Figure 5.9: *Comparison of Seebeck energy E_S and activation energy of the conductivity $E_{act,\sigma}$. E_S is measured at $T_m = 40\,°\text{C}$, $E_{act,\sigma}$ is fitted from the conductivity data presented in figure 5.5 in the range of $T = 25\,°\text{C}$ to $100\,°\text{C}$.*

reason for the difference in results might be the filling of the trap states by electrons accumulated within the OFET channel region by applying a gate-source potential. However, as discussed in section 4.2.3, the high applied fields required for OFET experiments are expected to affect the occupation of the density of states and thus the resulting mobility.

5.3 Morphology

Atomic force microscopy (AFM) investigations are performed on the same samples electrically investigated and discussed above to check for an influence of the presence of dopant molecules on the morphology of the layers. As AFM studies could only be performed in air, after the electrical investigations the samples are removed from the vacuum chamber and the Seebeck setup and stored in air for several hours before and during the AFM measurement. Therefore, the results might differ from freshly prepared samples, investigated in an inert atmosphere. The topographies of selected samples are depicted in figure 5.10, each scanned on an area of $5\,\mu m \times 5\,\mu m$. As a figure of merit, the root-mean-square surface roughness R_{rms} is written onto the images and summarized against the doping concentration in figure 5.11. The different layer thicknesses of the samples (mostly 20 nm for DMBI-POH and 30 nm for AOB samples, as discussed earlier), make the absolute numbers of the R_{rms} not directly comparable, but the trends are reliable. Due to a larger scan area of $5\,\mu m \times 5\,\mu m$, compared to $2\,\mu m \times 2\,\mu m$ used for the measurements on the air-sensitive dopants, the R_{rms} values are not directly comparable to these values either.

At low to medium doping concentrations, a smooth surface is detected for both dopants, in agreement with the findings for the air-sensitive dopants. With rising doping concentration the roughness increases for both dopants and artifacts become visible on the surface. A similar trend is observed for both dopants: At $C = 0.240\,MR$ many small spikes are present, whereas at higher doping concentrations fewer but much larger spikes are found, which lead to a saturation of the R_{rms} value. The largest artifacts are observed for the DMBI-POH samples with peaks of up to 75 nm reaching out of a layer with a nominal thickness of 20 nm. These artifacts are an indication for agglomeration of dopants or charge-transfer complexes. Compared to the air-sensitive dopants, the increase of the roughness occurs at higher doping concentrations, which can be explained by the smaller weight and size of the air-stable compounds. The rough surfaces found for $C > 0.100\,MR$ suggest that for devices where smooth layers are required in order to prevent shortcuts, lower doping concentrations should be used. It is not clear if the surface structures are generated by the thermal annealing step, as only annealed samples are investigated.

Contrary to these results, the investigations of the air-sensitive dopants yield smooth surfaces at high doping concentrations, which is interpreted as a measurement artifact due to the presence of a hydrogen film on the surface, attracted by the ionized dopants. As the topography is visible here, it is suggested that these dopants do not react as strongly with the ambient.

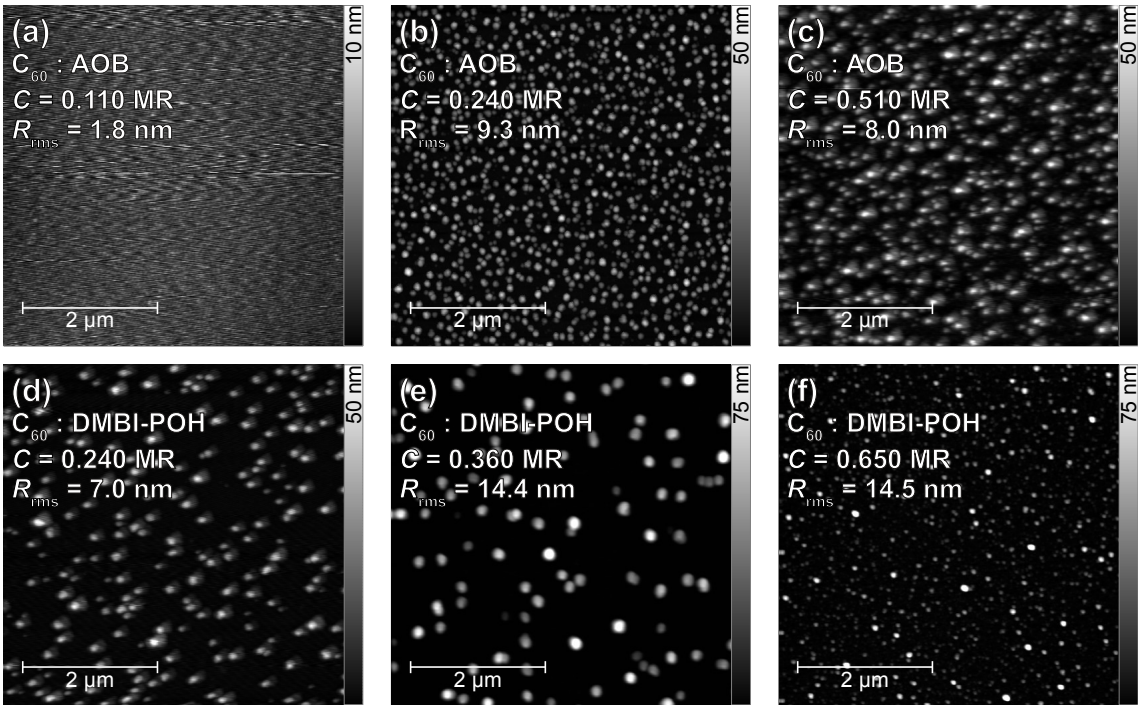

Figure 5.10: *AFM images of a selection of Seebeck samples. (a-c): C_{60} doped by AOB, (d-f): C_{60} doped by DMBI-POH. Note the different height scales. Parameters: 5 µm × 5 µm scan area, 30 nm layer thickness for AOB samples and 20 nm for DMBI-POH, measurements performed in air after electrical investigations and thermal annealing.*

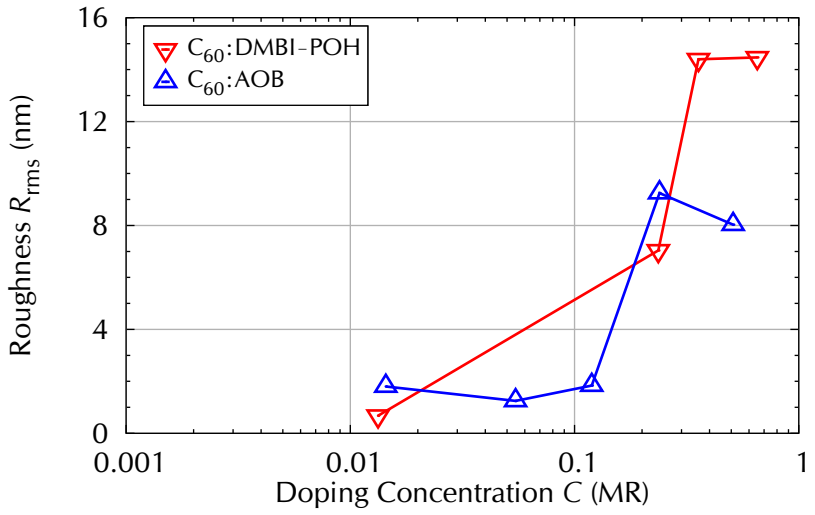

Figure 5.11: *AFM root-mean-square surface roughness R_{rms} of all studied samples, scanned on an area of 5 µm × 5 µm, as depicted in figure 5.10.*

5.4 Conclusion for AOB and DMBI-POH

Despite the expectation of a lower doping efficiency for the air-stable dopants compared to the air-sensitive dopants, due to the required transformation to form the active dopant compounds from the air-stable precursor, doping C_{60} by DMBI-POH leads to comparable results to $Cr_2(hpp)_4$ and $W_2(hpp)_4$, whereas AOB yields lower values. Even the values achieved using AOB should be sufficient for device application in photovoltaic cells, as C_{60} has a high charge carrier mobility. All doped C_{60} layers are stable up to $T = 100\,°C$, being above the evaporation temperature of the AOB precursor compound. A strong increase of conductivity over time is observed for AOB samples directly after sample processing, suggesting that the doping process is not completed during the deposition. Thermal annealing greatly enhances the conductivity of AOB samples and is required to ensure stable measurement conditions. A less pronounced effect is observed for DMBI-POH, yielding already high conductivities directly after sample fabrication. After annealing, DMBI-POH generates one order of magnitude higher conductivities in doped layers, with a maximum of $\sigma = 5.3\,{}^{S}/_{cm}$, comparable to the values for the air-sensitive dopants $Cr_2(hpp)_4$ and $W_2(hpp)_4$.

While for AOB layers, as well as for the air-sensitive compounds, a linear relation of $\sigma(C)$, a superlinear relation is found for DMBI-POH. This could either be due to a difference in the doping mechanism or to a difference in the transport properties of the doped system.

With increasing doping concentration, the activation energy of the conductivity for both dopants drops significantly. The Seebeck studies show the same tendency for the energetic difference between the Fermi level and the transport level. For AOB, the magnitude of this difference is smaller than the activation energy of the conductivity. It is concluded that the mobility in the AOB layers is thermally activated and that the IE of AOB is expected to be larger than the IE of OH-DMBI, being the proposed active dopant formed from DMBI-POH.

AFM surface scans yield a strong gain in surface roughness for $C > 0.100\,\mathrm{MR}$ of both dopants. This suggests that for devices, where smooth layers are required in order to prevent shortcuts, lower doping concentrations should be used.

Overall, the dopant DMBI-POH yields a better doping efficiency compared to AOB. The achieved conductivities are comparable to the results obtained for the air-sensitive dopants $Cr_2(hpp)_4$ and $W_2(hpp)_4$, making DMBI-POH a promising candidate for application in future devices, especially as DMBI-POH is air-stable prior to processing.

In the next section, DMBI-POH is compared to a closely related novel dopant, namely *o*-MeO-DMBI-I.

5.5 *o*-MeO-DMBI-I

Based on the experience with the commercially available n-dopant compounds N-DMBI and DMBI-POH, our cooperation partners Peng Wei and Benjamin D. Naab from Professor Zhenan Bao's group of Stanford University started designing and synthesizing new dopants. One promising material they developed is *o*-MeO-DMBI-I. Its structure is similar to DMBI-POH, as illustrated in figure 3.5 (b) on page 45 and its key parameters are presented in section 3.2.2. This material is stable during vacuum deposition, and first experiments performed in Stanford indicated excellent doping performance comparable to DMBI-POH. Consequently, further investigations were started in Dresden. A selection of the results presented here is published in reference [Wei12].

Obvious differences compared to DMBI-POH are that *o*-MeO-DMBI-I is a white crystalline powder, whereas DMBI-POH is a yellow fuzzy structured material. The deposition temperature of *o*-MeO-DMBI-I is found to be around $T_{\mathrm{dep}} = 185\,^{\circ}\mathrm{C}$, being 75 K higher than for DMBI-POH (compare table 3.2). This allows more stable temperature control during layer deposition. The similarity of the chemical structures of both compounds suggests a similar doping mechanism.

5.5.1 Doping Mechanism

A sudden increase of base pressure in the vacuum chamber by more than one order of magnitude is detected as soon as the deposition of *o*-MeO-DMBI-I starts. At $T = 100\,^{\circ}\mathrm{C}$ the base pressure is $7.3{\cdot}10^{-6}$ Pa with no detectable deposition rate, whereas at $T = 185\,^{\circ}\mathrm{C}$ during layer deposition a pressure of $1.6{\cdot}10^{-4}$ Pa is observed. The pressure remains at this level until the temperature is decreased to a level where the deposition stopped. In order to investigate these observations, a mass spectrometer (Pfeiffer QMG220) is installed at the vacuum chamber.

In figure 5.12, a wide mass spectrum scan from 0 u to 300 u performed at a rate of $2\,{}^{\mathrm{s}}/_{\mathrm{u}}$ is presented, which is probed at a dopant source temperature of 185 °C. Two dominant peaks around 127 u and 142 u are present, each having several side peaks. The relative heights of the peaks are found to vary between different measurements, probably related to changes in pressure during the long scan time. The left inset of figure 5.12 is a zoom into the area of these two main peaks, displaying the substructure. The peak at 127 u is assigned to ionized iodine I^- (126.9 u), the smaller one next to it to HI (127.9 u). Iodine has a boiling point of 184.3 °C at atmospheric pressure, hence the freed iodine is expected to turn into the gas phase at 185 °C in vacuum. The second large peak around 142 u is attributed to CH_3I (141.9 u). These findings suggest that the material *o*-MeO-DMBI-I loses its iodine atom upon deposition, forming *o*-MeO-DMBI as active dopant compound.

A high resolution mass spectrum obtained at a 10× slower scan speed of $20\,{}^{\mathrm{s}}/_{\mathrm{u}}$, presented as right inset of figure 5.12, resolved a peak at 254.3 u that nicely fits to the expected dopant compound *o*-MeO-DMBI and is above the value expected for I_2 at

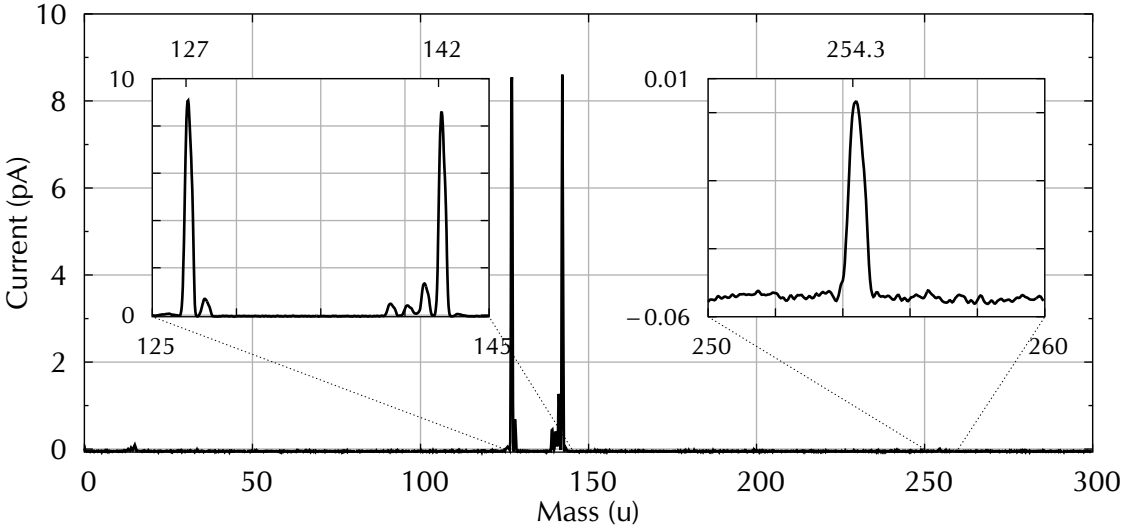

Figure 5.12: *Mass spectrum obtained during o-MeO-DMBI-I deposition at a material temperature of around 185 °C at $P = 1.6{\cdot}10^{-4}$ Pa, probed at a scan speed of 2 s/u. Left inset: zoomed region of main structure. Right inset: high resolution measurement at 20 s/u.*

253.8 u. As no mass peak for a neutral radical at 253.3 u is observed, it is hypothesized that the doping mechanism is the following: *o*-MeO-DMBI-I is reduced during evaporation under high vacuum to form *o*-MeO-DMBI (compare figure 3.5 (e1) on page 45), which then transfers an electron to a C_{60} molecule. Therefore, in order to calculate the doping concentration of samples doped by *o*-MeO-DMBI-I, the molar mass of *o*-MeO-DMBI ($M = 254.3\,\mathrm{g/mol}$) has to be used.

Further investigations on the doping mechanism were performed by our partners at Stanford University. X-ray photoelectron spectroscopy (XPS) measurements on pure *o*-MeO-DMBI-I layers fabricated by vacuum deposition yielded no iodide peak, indicating that *o*-MeO-DMBI-I is reduced and lost I^- during the evaporation. Furthermore, this suggests that the lost I^- does not contaminate the deposited layers. [Wei12]

Due to the structural similarity of *o*-MeO-DMBI-I and DMBI-POH (compare figure 3.5 (b) on page 45) it is expected that DMBI-POH undergoes a similar transition to form the active dopant compound OH-DMBI during deposition of the material. The proposed reaction is illustrated in figure 3.5 (e2). Thus, in order to calculate the doping concentration of samples doped by DMBI-POH, the molar mass of OH-DMBI ($M = 240.3\,\mathrm{g/mol}$) has to be used.

5.5.2 Comparison to DMBI-POH

Figure 5.13 compares the conductivities of C_{60} layers doped by *o*-MeO-DMBI-I to the data for DMBI-POH, presented in section 5.1.2. For the new compound *o*-MeO-DMBI-I, the conductivity after thermal annealing (empty symbols) is in the same range as for the DMBI-POH samples. The lowest doped sample of $C = 0.027$ MR

of *o*-MeO-DMBI-I has an almost identical value of $\sigma = 0.174\,^{S}/_{cm}$ to the corresponding sample of DMBI-POH with $\sigma = 0.162\,^{S}/_{cm}$ at $C = 0.027$ MR. A maximum of $\sigma = 10.9\,^{S}/_{cm}$ is measured for $C = 0.310$ MR, being more than twice as high as the record value observed for DMBI-POH as well as for $Cr_2(hpp)_4$ and $W_2(hpp)_4$. At even higher doping concentrations of *o*-MeO-DMBI-I, the conductivity decreases, in contrast to DMBI-POH, where a saturation is observed. The relation of the conductivity to the doping concentration follows the same trend for both materials. Samples doped by *o*-MeO-DMBI-I show as well a superlinear increase of $\sigma(C)$, as the dashed line in figure 5.13, possessing a slope of 2.0, indicates. Reproducibility is proven by two samples of $C = 0.246$ MR of *o*-MeO-DMBI-I showing almost identical values.

The most interesting difference between the two dopants is that for the new compound, the thermal annealing after preparation has only little effect on the conductivity. While for most DMBI-POH samples a gain on almost one order of magnitude is found, the strongest change observed for the *o*-MeO-DMBI-I samples is an increase by a factor of 3.6, found for the lowest doped sample. Hence, for *o*-MeO-DMBI-I thermal annealing is not necessary to achieve high conductivities.

Surprisingly, reproducing the samples in our group's multi chamber vacuum tool was not successful. The conductivities of 5 samples with doping concentrations from $C = 0.150$ MR up to 0.700 MR were between $0.03\,^{S}/_{cm}$ and $0.3\,^{S}/_{cm}$ with no clear relation between σ and C. Thermal annealing made it possible to reach comparable conductivities to the samples fabricated in the Seebeck setup. The main differences between the chambers is that in the multi chamber tool, the base pressure is one order of magnitude lower, in the range of $8{\cdot}10^{-7}$ Pa. During deposition a pressure in the range of $2{\cdot}10^{-6}$ Pa is measured, being almost a factor of 100 lower than the increased pressure recorded during fabrication in the Seebeck setup. Hence, most probably the

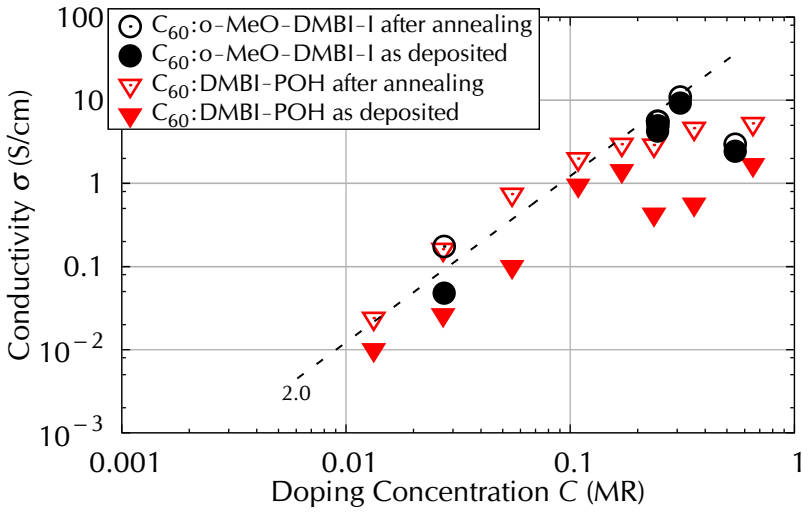

Figure 5.13: *Conductivity of C_{60} doped by o-MeO-DMBI-I and DMBI-POH, before (filled symbols) and after (empty symbols) thermal annealing (at $T = 100\,°C$), measured at $T = 25\,°C$. Note the two samples of identical $C = 0.246$ MR of o-MeO-DMBI-I proving the reproducibility. The dashed line represents a slope of 2.0.*

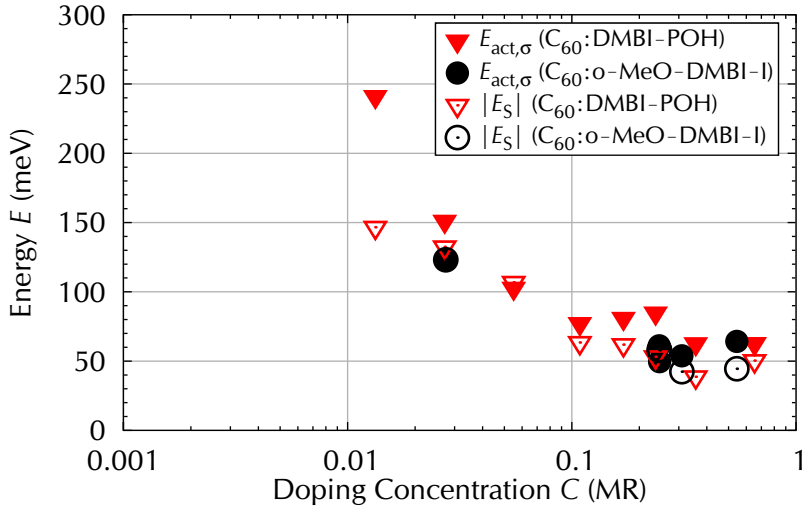

Figure 5.14: *Comparing Seebeck energy E_S (empty symbols) and activation energy of the conductivity $E_{act,\sigma}$ (filled symbols) of C_{60} doped by o-MeO-DMBI-I and DMBI-POH. E_S is measured at $T_m = 40\,°C$, $E_{act,\sigma}$ is derived from the range of $T = 25\,°C$ to $100\,°C$.*

Seebeck chamber with the worse base pressure has more leakage gas flow through the chamber towards the pumps. It might be possible that this material flow transports the iodine gas (produced by formation of *o*-MeO-DMBI from *o*-MeO-DMBI-I) away from the deposited layer, whereas in the multi chamber tool iodine might reach the substrate, leading to a reformation of *o*-MeO-DMBI-I. Another difference of the multi chamber tool compared to the Seebeck setup is a different pressure sensor that generates an electric arc, illuminating the chamber and maybe affecting the materials during deposition. However, deactivating the sensor had no affect on the samples.

Temperature-dependent conductivity and Seebeck measurements are performed on the *o*-MeO-DMBI-I samples as well. A comparison to DMBI-POH is shown in figure 5.14. Seebeck measurements (empty symbols) of the two compounds are in reasonable agreement, leading to the assumption that the doping efficiency of *o*-MeO-DMBI-I is comparable to DMBI-POH. The activation energy of the conductivity $E_{act,\sigma}$ (filled symbols) is somewhat lower for most *o*-MeO-DMBI-I samples and closer to E_S, indicating a smaller contribution of the mobility to $E_{act,\sigma}$.

In conclusion, there are several indications for *o*-MeO-DMBI-I and DMBI-POH having a similar doping mechanism. Comparable values of σ, E_S and $E_{act,\sigma}$, as well as a superlinear increase of $\sigma(C)$ are observed. The high maximum of $\sigma = 10.9\,{}^{S}/_{cm}$ for *o*-MeO-DMBI-I is the record value measured for all material combinations during this thesis. Its deposition temperature in the range of $T_{dep} = 185\,°C$ makes the rate better controllable than for DMBI-POH, which is deposited as $T_{dep} = 110\,°C$. Furthermore, for this compound thermal annealing is not necessary to achieve high conductivities, at least not in the Seebeck setup. Hence, *o*-MeO-DMBI-I is a promising new dopant that should be tested in devices.

Chapter 6

p-Dopants in Amorphous Hosts

After investigating n-doping in the last two chapters, this chapter investigates p-doped material systems. Two hosts and two dopants are chosen in order to study the influence of the molecular energy levels. While the host material used for the n-doping experiments is the exceptionally well conducting polycrystalline C_{60}, the two hosts studied in this chapter are more typical amorphous organic semiconductors with approximately five orders of magnitude lower mobilities. In section 6.1, the conductivity of differently doped samples is studied. Afterwards, it is investigated how the conductivity is influenced by the temperature, which again supports a thermally activated hopping process and therefore allows to derive an activation energy of the conductivity. Section 6.2 presents thermoelectric (Seebeck) investigations for a variation of the temperature and the doping concentration. The results are compared to the activation energy of the conductivity and conclusions for the mobility are drawn. In section 6.3, the thermal stability is investigated and finally, in section 6.4, the results are summarized.

One major difference of p-doping to n-doping is that p-doped layers are usually degrading more slowly under air-exposure or under contact with residual quantities of O_2 present in the vacuum chamber. The reason is that oxygen leads to a p-doping as well [Ham93] and hence to traps in n-doped layers.

Four different material combinations are investigated in this chapter. As host materials, MeO-TPD and BF-DPB are chosen which have been both used in OLEDs [Rei09] and OPV [Män04b,Her12]. The host materials are selected to have slightly different ionization energies, in particular IE = 5.07 eV for MeO-TPD [Tie12] and 5.23 eV for BF-DPB [Mee11]. Two different p-dopants, F_6-TCNNQ and $C_{60}F_{36}$, are studied, having estimated electron affinities of EA ≈ 5.00 eV for F_6-TCNNQ [Tie12,Wel09] and (5.38 ± 0.30) eV for $C_{60}F_{36}$ [Mee11]. Since different techniques for the estimations have been used and the errors are rather large, the true values may differ. From the measured values of the hosts' IEs and the estimated values of the dopants' EAs, the doping is expected to be more efficient for $C_{60}F_{36}$, whereas for F_6-TCNNQ very low doping efficiency is expected. However, energy levels are merely a rough guide to predict the doping effectiveness, as microscopic details like spatial arrangements of orbitals play an important role as well. While the two hosts are of similar weight, the dopant $C_{60}F_{36}$ is almost 4 times as heavy as F_6-TCNNQ. Further details about the materials are summarized in the materials section 3.2.

6.1 Conductivity

The first method of choice to study the doping is the investigation of the conductivity. In comparison to the exceptionally well electron conducting C_{60}, used as host in the last two chapters, both investigated hole transporters are expected to show several orders of magnitude lower conductivities. This expectation is based on the fact that C_{60} molecules have a spherical shape and therefore align in an ordered face-centered cubic (fcc) polycrystalline structure [Pei93] that allows for high charge carrier mobilities, whereas both hole transporting materials are expected to form amorphous layers with much lower mobilities, as discussed in section 3.2.1. OFET-mobility experiments‡ yield similar carrier mobilities for both hole transport materials of $\mu = 2.3{\cdot}10^{-5}\,\mathrm{cm^2/Vs}$ for MeO-TPD and $\mu = 5.7{\cdot}10^{-5}\,\mathrm{cm^2/Vs}$ for BF-DPB. These values are five orders of magnitude lower than record values for C_{60} [Ita06].

6.1.1 Relation of Conductivity to Doping Concentration

The conductivities of samples of MeO-TPD and BF-DPB, doped by different doping concentrations of F_6-TCNNQ or $C_{60}F_{36}$ are presented in figure 6.1 (a), measured directly after sample fabrication at $T = 25\,°\mathrm{C}$. As a linear and symmetric current-voltage

‡measured by Moritz Philipp Hein (IAPP) in an OFET geometry on SiO_2 substrate

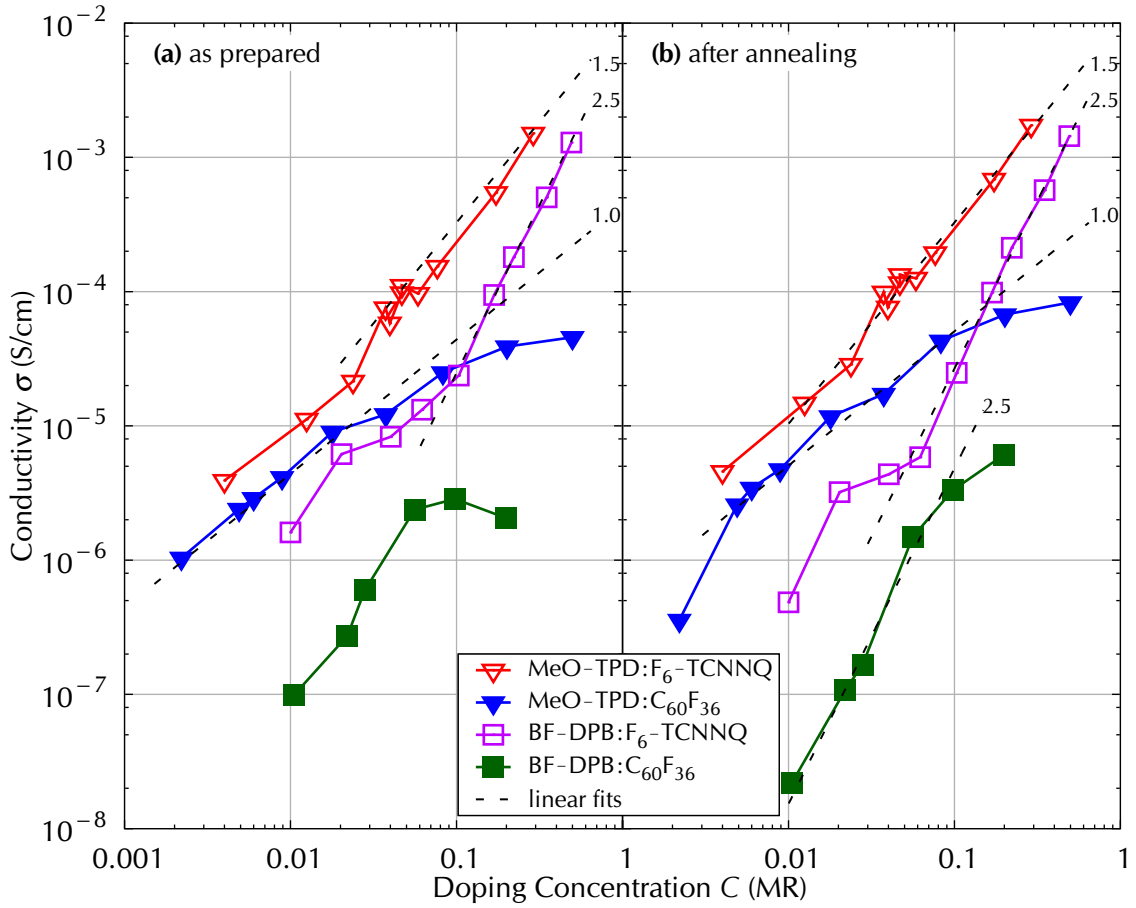

Figure 6.1: *Conductivity σ vs. doping concentration C for samples of MeO-TPD (triangles) and BF-DPB (squares) doped by F_6-TCNNQ (empty symbols) and $C_{60}F_{36}$ (filled symbols). (a) As-prepared, measured at $T = 25\,°C$ and (b) after thermal annealing for 1 hour at $T = 45\,°C$ (MeO-TPD) or $70\,°C$ (BF-DPB), probed at $T = 30\,°C$. Dashed lines with slopes of 1.0, 1.5 and 2.5 are guides to the eye.*

relation is detected for all samples, the contact resistance and consequently the injection are negligible. It can be seen that each dopant is able to dope both host materials, and the conductivity can be tuned over several orders of magnitude.

As discussed in the previous chapters, the samples are thermally annealed prior to further investigations, to ensure stable measurement conditions. Only moderate temperatures are applied for samples of MeO-TPD, since is has a low glass transition temperature in the range of $T_g = 67\,°C$, as discussed in section 3.2.1. The samples are slowly heated from $T = 25\,°C$ to $45\,°C$ for MeO-TPD or to $70\,°C$ for BF-DPB and kept at this temperature for 60 minutes. Afterwards, the samples are slowly cooled down and the measurement routine (compare section 3.1.4) starts with a conductivity experiment at $T = 30\,°C$. This data, depicted in figure 6.1 (b) shows that for most samples, the annealing has only minor influence on the conductivity.

Samples of MeO-TPD doped by F_6-TCNNQ yield the highest conductivity σ at each doping concentration C. A linear relation of $\sigma(C)$ is found for low C, whereas for

$C > 0.030\,\mathrm{MR}$ up to the highest prepared doping concentration of $C = 0.290\,\mathrm{MR}$ a superlinear slope of 1.5 is determined, indicated by the dashed lines in figure 6.1. No saturation at high doping concentrations is observed, in contrast to the n-doping experiments of chapters 4 and 5. The highest measured conductivity is $\sigma = 1.73{\cdot}10^{-3}\,\mathrm{S/cm}$ at $C = 0.290\,\mathrm{MR}$. Thermal annealing at $T = 45\,^{\circ}\mathrm{C}$ hardly has an influence on the samples of this material combination.

Doping MeO-TPD by $C_{60}F_{36}$ instead, results for $C < 0.100\,\mathrm{MR}$ in the second highest conductivity value at each doping concentration. At low doping concentrations, a linear relation of $\sigma(C)$ is found, indicated by the dashed line of slope 1.0, and at $C > 0.030\,\mathrm{MR}$ the slope is reduced. The highest detected conductivity is $\sigma = 8.31{\cdot}10^{-5}\,\mathrm{S/cm}$ at $C = 0.500\,\mathrm{MR}$. Thermal annealing at $T = 45\,^{\circ}\mathrm{C}$ increases σ for most samples, only the lowest doped sample has a reduced value after annealing, despite measuring at 5 K higher temperature.

BF-DPB doped by F_6-TCNNQ yields for $C < 0.100\,\mathrm{MR}$ lower conductivities than both MeO-TPD combinations. At $C > 0.060\,\mathrm{MR}$ a superlinear increase with a slope of 2.5 is determined without a saturation visible at high doping concentrations. The highest detected conductivity is $\sigma = 1.44{\cdot}10^{-3}\,\mathrm{S/cm}$ at $C = 0.490\,\mathrm{MR}$, being close to the maximum measured for MeO-TPD doped by the same dopant, but at an almost twice as high C. Thermal treatment reduces σ for weakly doped samples, whereas highly doped samples are almost unaffected.

Doping BF-DPB by $C_{60}F_{36}$ gives the lowest conductivities, with mostly one order of magnitude lower values compared to the same host doped by F_6-TCNNQ. Starting from a value of $\sigma = 2.2{\cdot}10^{-8}\,\mathrm{S/cm}$ at $C = 0.011\,\mathrm{MR}$, which is below the estimated resolution limit of the setup (compare section 3.1.5), σ rises superlinearly with C as well with a slope of 2.5 and reaches $\sigma = 6.10{\cdot}10^{-6}\,\mathrm{S/cm}$ at $C = 0.200\,\mathrm{MR}$. Again, thermal treatment lowers the σ for weakly, but raises σ for highly doped samples.

Comparing the hosts, samples of MeO-TPD yield higher conductivities than samples of BF-DPB for the same dopant. As for both hosts similar OFET-mobilities have been measured ($\mu = 2.3{\cdot}10^{-5}\,\mathrm{cm^2/Vs}$ for MeO-TPD and $\mu = 5.7{\cdot}10^{-5}\,\mathrm{cm^2/Vs}$ for BF-DPB), the difference in σ must be due to the density of free holes n_h. This finding is in agreement with MeO-TPD having a lower ionization energy than BF-DPB (compare section 3.2.1), which is expected to lead to MeO-TPD being easier to dope by p-dopants, and thus allowing for a higher doping efficiency. Both series that use BF-DPB as host show the same strong slope of 2.5, indicating that either the doping efficiency or the mobility rises strongly upon increasing doping concentration.

Comparing the dopants, it is found that for samples doped by the larger and 4 times heavier $C_{60}F_{36}$, the slope of the conductivity decreases at high C, whereas for the lighter F_6-TCNNQ instead the superlinear relation of $\sigma(C)$ continues at high C with no saturation in the investigated doping regime. The absence of a saturation when doping by F_6-TCNNQ is attributed to the fact that both hosts, MeO-TPD and BF-DPB, form amorphous layers that are less sensitive to impurities than the polycrystalline C_{60} layers, investigated in the previous chapters 4 and 5. The decreasing slope at high concentrations of $C_{60}F_{36}$ is attributed to a disturbance of the microstructure by

the heavy dopant, since at the same molecular doping ratio (MR), using $C_{60}F_{36}$ leads to a 4 times higher dopant mass deposited into the layer. Different slopes of $\sigma(C)$ are discussed in detail in section 5.1.2 for C_{60} doped by AOB (linear) and DMBI-POH (superlinear). Here, for the F_6-TCNNQ-doped samples, the trend is different, as for low C a linear slope is found and only at high concentrations the slope increases. The thermal annealing effects the conductivity of samples doped by $C_{60}F_{36}$ stronger than samples of F_6-TCNNQ, suggesting that the thermal energy allows for rearrangement of the heavier molecules.

The conductivity data follows the opposite trend as expected from the energy levels given in literature. Doping by F_6-TCNNQ is more efficient than doping by $C_{60}F_{36}$ for both hosts, which suggests that the roughly estimated EAs of the dopants are incorrect, since the measurements of the hosts IEs are more accurate. As F_6-TCNNQ is able to dope BF-DPB (IE = 5.23 eV) well the real EA of F_6-TCNNQ is expected to be larger than this value. This statement is supported by the closely related dopant F_4-TCNQ having an EA = 5.25 eV[Gao01], measured by inverse photoemission spectroscopy (IPES). Cyclic voltammetry (CV) measurements on F_4-TCNQ and F_6-TCNNQ yield similar values for the EA of both compounds[Wel09], hence it is expected that the real EA of F_6-TCNNQ is in the range of EA = 5.25 eV, which is above the estimated literature value of EA ≈ 5.00 eV[Tie12].

As $C_{60}F_{36}$ does not dope BF-DPB with its IE= 5.23 eV well, the real EA of $C_{60}F_{36}$ is expected to be smaller than this value. Furthermore, the saturation of σ at high C of $C_{60}F_{36}$ in both hosts indicates the EA of $C_{60}F_{36}$ might even be smaller than or in the range of the IE of MeO-TPD (IE= 5.07 eV). Due to inter- and intra-molecular interactions, the IE and EA are no sharp levels but distributed in energy. Consequently, $C_{60}F_{36}$ is able to dope some of the host molecules, despite its EA being expected to be low compared to the IE of both hosts. At high C, most of the host molecules with sufficient small IE are already doped and additional dopants find no suitable hosts and the conductivity saturates. This model is supported by the data, since for BF-DPB as host (with the larger IE) the saturation of σ occurs at lower C than for MeO-TPD.

6.1.2 Temperature Dependence of the Conductivity

The conductivity increases with temperature for all samples, similar to the case of the n-doped samples discussed in the previous chapters. Figure 6.2 presents the experimental data of all samples in Arrhenius plots. Due to the low glass transition temperature of MeO-TPD ($T_g = 67\,°C$), the samples with MeO-TPD as host material are only investigated in the range of $T = 25\,°C$ to $45\,°C$, see figure 6.2 parts (a) and (b). The samples comprising BF-DPB on the other hand, are successfully investigated up to $T = 70\,°C$, some samples even up to $80\,°C$, compare figure 6.2 parts (c) and (d). Since the detected temperature-dependent leakage currents through the glass substrate (as discussed in section 3.1.6) are in a similar range to the measured currents, an estimation of their contribution to the conductivity of a 30 nm thick layer at $V = 1\,V$ is performed and included into figure 6.2. It can be seen in figure 6.2 (d)

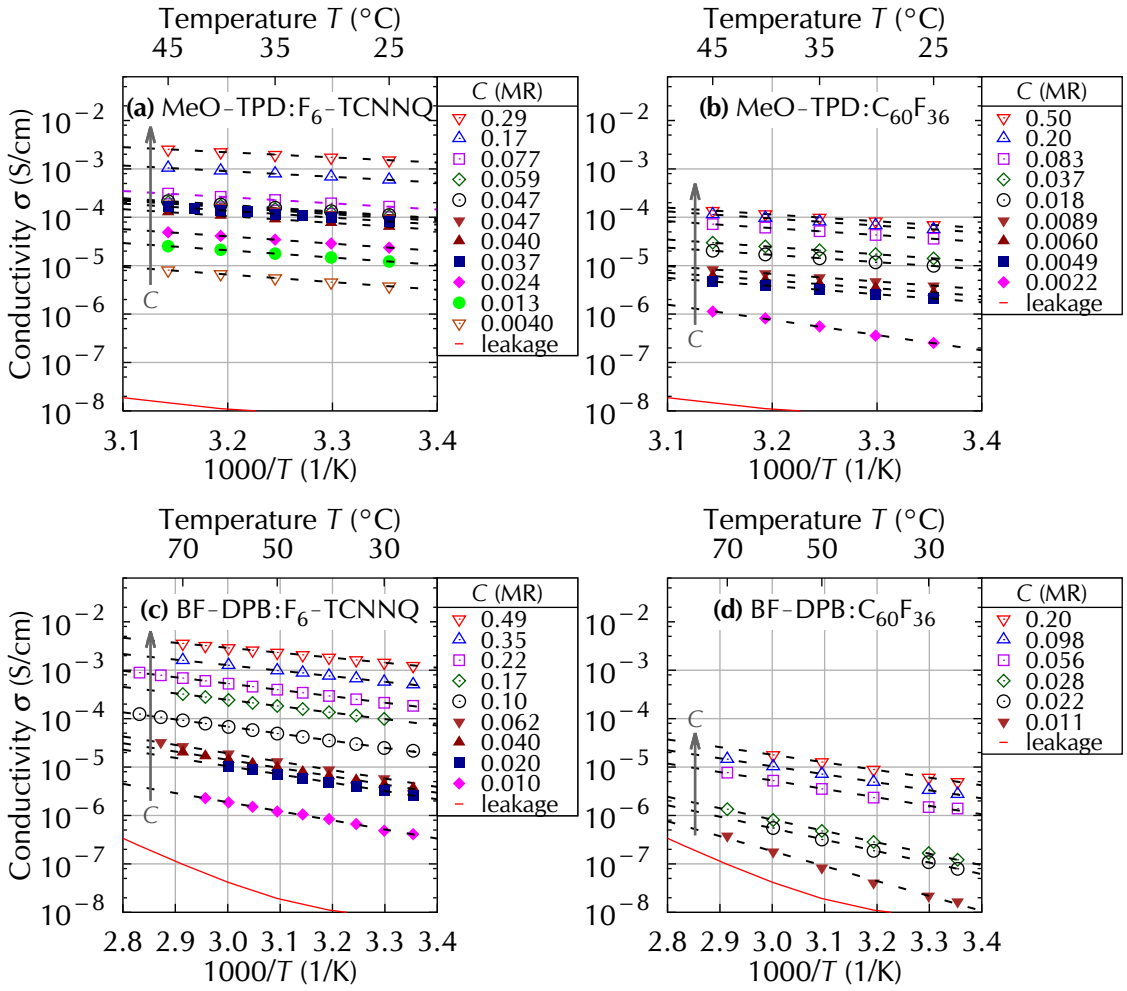

Figure 6.2: *Temperature dependence of the conductivity for four different material combinations. Lines are fits using equation (2.25) on page 16. The contribution of the leakage current through the glass substrate is estimated for a 30 nm thick layer using the data of figure 3.4 on page 42.*

that for the three lowest doping concentrations of $C_{60}F_{36}$ in BF-DPB the contribution of the leakage currents cannot be neglected.

A linear relation of inverse temperature to conductivity is found in the Arrhenius plots. Therefore, again a thermally activated transport mechanism is concluded, allowing to derive an activation energy of the conductivity $E_{\mathrm{act},\sigma}$ via equation (2.25) on page 16. This property is plotted in figure 6.3 against the doping concentration for all four material systems, excluding the three samples of the lowest doping concentrations of $C_{60}F_{36}$ in BF-DPB due to the relatively strong contribution of the leakage currents.

The resulting values of the different samples range from $E_{\mathrm{act},\sigma} = 204\,\mathrm{meV}$ to 374 meV, being much higher than observed for the n-doped samples of the previous chapters, where most values are found to be in the range of $E_{\mathrm{act},\sigma} = 50\,\mathrm{meV}$ to 175 meV. An almost linear reduction of $E_{\mathrm{act},\sigma}$ with rising doping concentration in this semi-logarithmic scale is present for all four material combinations, with no saturation visible.

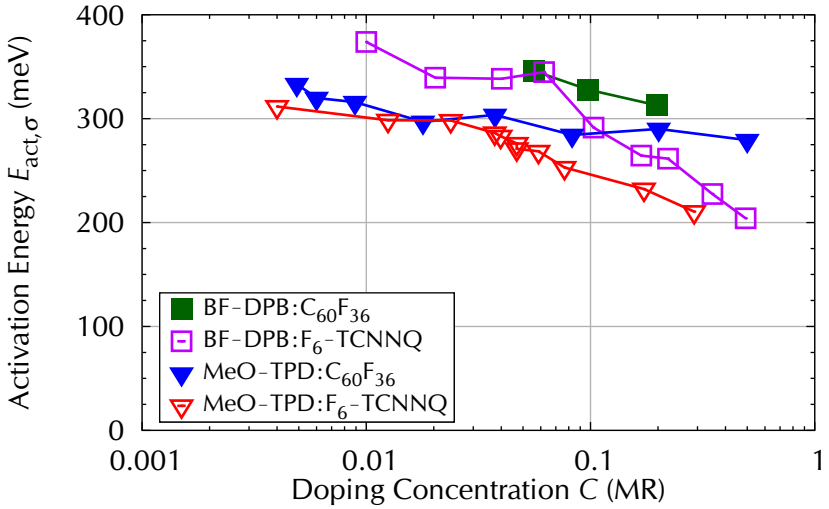

Figure 6.3: *Activation energy of the conductivity $E_{act,\sigma}$, derived from the temperature dependence of the conductivity $\sigma(T)$ displayed in figure 6.2, calculated using equation (2.25) on page 16 for samples of MeO-TPD (triangles) and BF-DPB (squares) doped by F_6-TCNNQ (empty symbols) and $C_{60}F_{36}$ (filled symbols).*

Samples of MeO-TPD doped by F_6-TCNNQ yield their largest value of $E_{act,\sigma} = 312\,\text{meV}$ for the lowest used doping concentration of $C = 0.004\,\text{MR}$. This value is reduced to $E_{act,\sigma} = 211\,\text{meV}$ at $C = 0.290\,\text{MR}$, corresponding to a linearly fitted reduction of 56 meV per order of magnitude of C.

Doping MeO-TPD by $C_{60}F_{36}$ instead, a value of $E_{act,\sigma} = 333\,\text{meV}$ at the lowest doping concentration of 0.005 MR is reduced to $E_{act,\sigma} = 279\,\text{meV}$ at 0.500 MR. The slope of 23 meV per order of magnitude is approximately half the value found for the F_6-TCNNQ-doped samples.

For the combination of BF-DPB doped by F_6-TCNNQ, the largest $E_{act,\sigma} = 374\,\text{meV}$ of all p-doped samples is detected at $C = 0.010\,\text{MR}$. This material combination has the strongest change of $E_{act,\sigma}$ showing a lowering of 98 meV per order of magnitude of C, as also the lowest value of all p-doped samples is reached by this combination with $E_{act,\sigma} = 204\,\text{meV}$ at $C = 0.490\,\text{MR}$. At low doping concentrations, a smaller and at $C > 0.060\,\text{MR}$ a larger slope is found. The doping concentration of 0.060 MR is the same from where on a superlinear gain in conductivity with C is observed.

Doping BF-DPB by $C_{60}F_{36}$, the $E_{act,\sigma} = 346\,\text{meV}$ at $C = 0.056\,\text{MR}$ decreases to 313 meV at 0.200 MR, giving the highest values of all material combinations at the corresponding doping concentration. The slope of the decrease derived from the three samples is 60 meV per order of magnitude of C.

In conclusion, the samples of all four material combinations yield the same tendency of a linear reduction of $E_{act,\sigma}$ with increasing logarithm of C. The samples with MeO-TPD as host material have smaller values of $E_{act,\sigma}$ and smaller slopes compared to the BF-DPB samples, in agreement with BF-DPB having a larger IE. At low C the curves are parallel, whereas at high C for samples of BF-DPB a faster decrease of $E_{act,\sigma}$ is found.

Comparing the two dopants in each host material, similar values of $E_{\mathrm{act},\sigma}$ are observed for low doping concentrations of F_6-TCNNQ and $C_{60}F_{36}$. With increasing doping concentrations, the $E_{\mathrm{act},\sigma}$ are diverging and the values obtained for using $C_{60}F_{36}$ as dopant are higher compared to F_6-TCNNQ. At high C, similar values for each dopant in both hosts are derived, with the samples doped by F_6-TCNNQ approaching $E_{\mathrm{act},\sigma} = 200\,\mathrm{meV}$, being at least 80 meV lower than for the highest $C_{60}F_{36}$-doped samples. The larger $E_{\mathrm{act},\sigma}$ for $C_{60}F_{36}$ can be correlated to a thermal activation of dopant ionization. As discussed in section 6.1.1 the conductivities of $C_{60}F_{36}$-doped samples saturate at high C, indicating that the real EA of $C_{60}F_{36}$ is smaller than the IEs of both hosts, MeO-TPD and BF-DPB. In this case only a fraction of the $C_{60}F_{36}$ molecules will be ionized. By rising the temperature, the number of ionized dopants increases due to more thermal energy, leading to an increase of the density of free holes n_{h}, which contributes to a higher conductivity at higher T and thus raises $E_{\mathrm{act},\sigma}$. Additionally, a rise of n_{h} can also result in a gain of mobility[Ark05b,Ark05a], further increasing the conductivity and hence $E_{\mathrm{act},\sigma}$.

In comparison to the n-doped C_{60} samples, discussed in the previous chapters, it can be seen that the $E_{\mathrm{act},\sigma}$ of all p-doped samples are almost twice as high as the values derived for n-doped C_{60} samples at corresponding doping concentrations. The values measured are also higher than literature values for instance the $E_{\mathrm{act},\sigma}$ of VOPc[‡] p-doped by F_4-TCNQ range from 280 meV to 210 meV for low doping concentrations of $C = 0.002\,\mathrm{MR}$ to $0.020\,\mathrm{MR}$[Pfe98]. The larger $E_{\mathrm{act},\sigma}$ might be attributed to the amorphous hosts MeO-TPD and BF-DPB, since C_{60} as well as VOPc form polycrystalline layers. Similar to the findings for C_{60} using the air-stable n-dopants, AOB and DMBI-POH, an increase of $E_{\mathrm{act},\sigma}$ at large doping concentrations is not present.

6.2 Thermoelectric Measurements

6.2.1 Temperature Dependence of the Seebeck Coefficient

Thermoelectric investigations at different temperatures are performed along with the conductivity experiments, similar to the studies of the n-doped samples. The resulting Seebeck coefficients S at different temperatures are presented in figure 6.4 for all four material combinations. As expected, all values of S are positive in sign, thus holes are the dominating charge carrier species for all the p-doped samples. Electron conduction along the dopant molecules is not detected, not even for large doping concentrations. The observed values for S range from $100\,\mu\mathrm{V/K}$ to $1000\,\mu\mathrm{V/K}$ and a lowering of S with rising doping concentration is found. It was not possible to perform reliable Seebeck measurements on samples of BF-DPB doped by $C < 0.030\,\mathrm{MR}$ of $C_{60}F_{36}$, as the resulting conductivities were below the resolution limit of the setup, as discussed in section 3.1.5.

[‡]VOPc is vanadyl-phthalocyanine

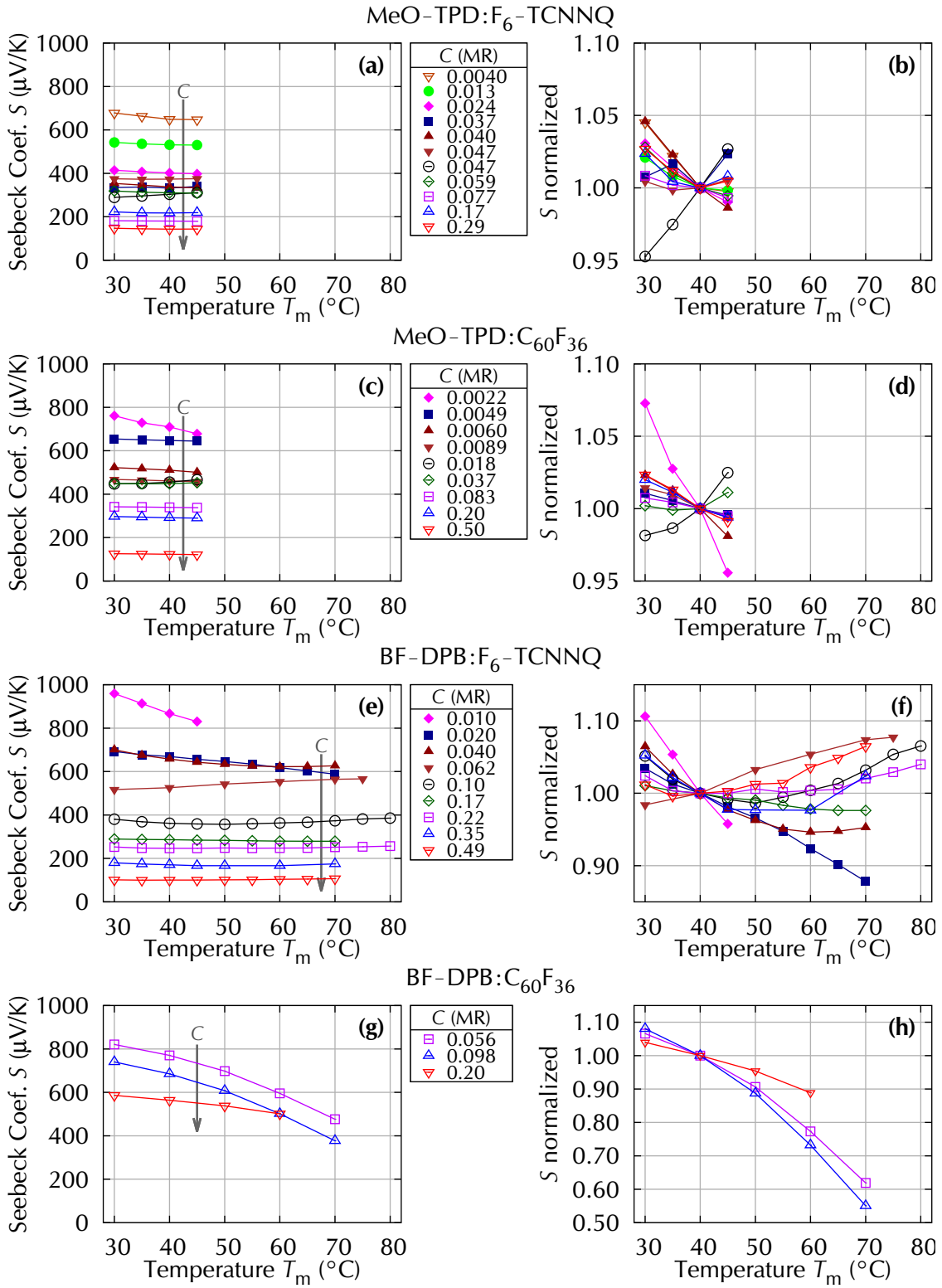

Figure 6.4: *Temperature dependence of the Seebeck coefficient S for four different material combinations, left: absolute values, right: normalized to the $T_m = 40\,°C$ measurements.*

The samples with MeO-TPD as host material have only been measured in the range of $T_m = 30\,°C$ to $45\,°C$, due to the low glass transition temperature of this material. Higher temperatures of up to $T_m = 80\,°C$ could be applied to the samples using BF-DPB as host. In order to investigate the influence of the temperature T_m, the relative changes of S, normalized to the value at $T_m = 40\,°C$, are depicted at the right hand side graphs in figure 6.4. A temperature of $40\,°C$ is chosen, as it is a device-relevant temperature and more stable to control than $T_m = 30\,°C$.

No clear trend of the temperature dependence of S can be derived from the data. In the range of $T_m = 30\,°C$ to $45\,°C$ most samples vary by about $\pm 5\,\%$. This effect is much smaller than the influence a variation of the doping concentration has. The three samples of BF-DPB doped by $C_{60}F_{36}$ dramatically decrease in S at elevated temperatures. This tendency is not present in the data of the other material combinations and is opposite to the results for n-doped C_{60} samples, where a gain of S with temperature is found, as discussed in sections 4.2.1 and 5.2.1. As a decreasing S is correlated to an increasing density of free holes, the data of BF-DPB doped by $C_{60}F_{36}$ supports the theory of $C_{60}F_{36}$ having a lower EA than the IEs of both hosts. Higher thermal energy allows to overcome the energetic difference and hence ionization of more and more dopants.

6.2.2 Relation of Seebeck Coefficient to Doping Concentration

Comparing the Seebeck coefficients at one temperature of $T_m = 40\,°C$ for different doping concentrations, a lowering of S with increasing C is found for all four material combinations, ranging from $867\,\mu V/K$ to $100\,\mu V/K$, as displayed in figure 6.5. Using equation (2.66) on page 28, the energetic difference E_S between the Fermi level E_F and the transport level E_{Tr} can be derived:

$$E_S = S \cdot e \cdot T \quad \text{with} \quad E_S := E_F - E_{Tr}\,. \tag{2.66}$$

E_S is given as the right hand axis in figure 6.5. Following the trend of S, the value of E_S decreases with increasing C for both dopants, which is correlated to a shift of the Fermi level E_F towards the transport level E_{Tr}. This finding is in agreement with the observations of the n-doped samples, where E_S drops with rising doping concentration. No saturation is visible in the data and the samples of all four material combinations yield an almost linear relation of S and E_S to the logarithm of C.

The series of MeO-TPD doped by F_6-TCNNQ starts at $C = 0.004\,MR$ with $E_S = 203\,meV$. This value is reduced to $E_S = 45\,meV$ at $C = 0.290\,MR$, corresponding to a linear slope of 88 meV per order of magnitude of C.

Doping MeO-TPD by $C_{60}F_{36}$ instead, a deviation from a linear relation is present between $C = 0.006\,MR$ and $0.018\,MR$. Overall the slope is determined to $E_S = 67\,meV$ per order of magnitude of C and therefore somewhat lower than for the use of F_6-TCNNQ as dopant.

In case of BF-DPB doped by F_6-TCNNQ, the values for E_S at low C are larger than observed for MeO-TPD as host material. At $C > 0.100\,MR$ a reasonable agreement is

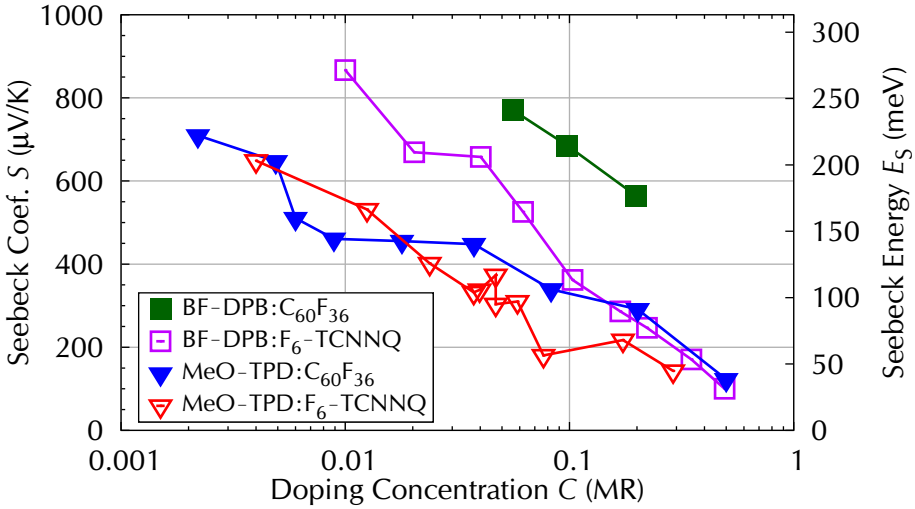

Figure 6.5: *Seebeck coefficient S and derived Seebeck energy E_S at $T_m = 40\,°C$ for samples of MeO-TPD (triangles) and BF-DPB (squares) doped by F_6-TCNNQ (empty symbols) and $C_{60}F_{36}$ (filled symbols).*

found. The overall linear slope is 142 meV per order of magnitude, being the highest of all four material combinations.

For the three reliably measurable samples of BF-DPB doped by large concentrations of $C_{60}F_{36}$, the highest values of all four material combinations in the corresponding C-regime are measured, with a maximum of $E_S = 241\,\text{meV}$ at $C = 0.056\,\text{MR}$. Here the slope is 118 meV per order of magnitude of C.

In conclusion, the samples of all four material combinations yield the same trend of a linear reduction of S and E_S with increasing logarithm of C. Comparing the hosts, samples of BF-DPB have larger values of S and E_S and stronger slopes compared to samples of MeO-TPD. The larger values are in agreement with BF-DPB having a larger IE than MeO-TPD, making electron transfer to the dopant less probable and therefore generating a lower density of free holes at the same doping concentration for each dopant. This results in a greater energetic difference between Fermi level and transport level and thus a larger value of S and E_S, particularly for doping by $C_{60}F_{36}$. The strong slope of S and thus E_S observed for BF-DPB as host is attributed to filling of the tail states of the host's density of states that leads to a rapid shift of E_F. At high doping concentrations of F_6-TCNNQ, a reduced slope is found, comparable to the samples of MeO-TPD.

Concerning the dopants, F_6-TCNNQ leads to a lower value of S and E_S and to a larger slope with C than $C_{60}F_{36}$. The lower values of S and E_S indicate a higher doping efficiency of F_6-TCNNQ compared to $C_{60}F_{36}$. This finding supports the above proposed theory of F_6-TCNNQ having a larger EA than $C_{60}F_{36}$, contrary to the literature values.

Comparing the results to the n-doped C_{60} samples of the previous chapters, larger values of S and E_S are detected for the p-doped samples at low doping concentrations. This can be understood from the fact that the amorphous hosts investigated in this

chapter are expected to have broader densities of states compared to the polycrystalline C_{60}. A broader host's *DOS* leads to a larger fraction of host molecules having a larger IE than the EA of the dopant and hence doping these molecules is less probable. Consequently, the density of free holes is lower which results in a larger S and E_S.

6.2.3 Comparison of Seebeck Energy and Activation Energy

In figure 6.6, E_S is compared to the previously discussed activation energy of the conductivity $E_{act,\sigma}$, for the four different material combinations. All samples show an E_S that is approximately 100 meV lower than $E_{act,\sigma}$. Such a large difference is not observed for the n-doped samples discussed in the previous chapters. In case of C_{60} n-doped by the air-sensitive dopants $Cr_2(hpp)_4$ and $W_2(hpp)_4$, a difference of only 25 meV to 75 meV is found at $C > 0.100$ MR. That observation is attributed to a disturbance of the morphology by the large number of dopant molecules and hence a decreasing mobility with increasing C, as discussed in section 4.2.3.

In order to investigate the difference of E_S and $E_{act,\sigma}$ more closely, this quantity is plotted in figure 6.7. Three of the four material combinations are in good agreement, only the three samples of BF-DPB doped by $C_{60}F_{36}$ show a difference that is smaller by $\approx$ 50 meV. The calculated differences range from 100 meV to 200 meV with one

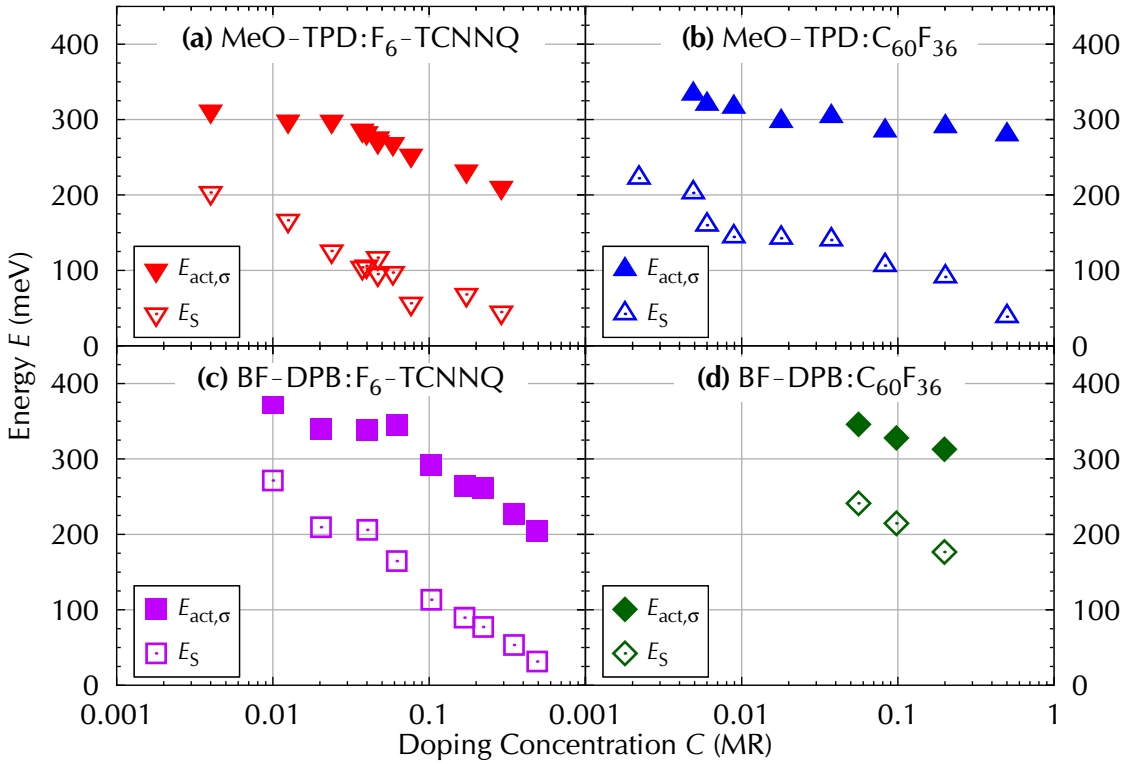

Figure 6.6: *Comparison of Seebeck energy E_S and activation energy of the conductivity $E_{act,\sigma}$ for four different material combinations. E_S is probed at $T_m = 40\,°C$, $E_{act,\sigma}$ is fitted from conductivity data presented in figure 6.2.*

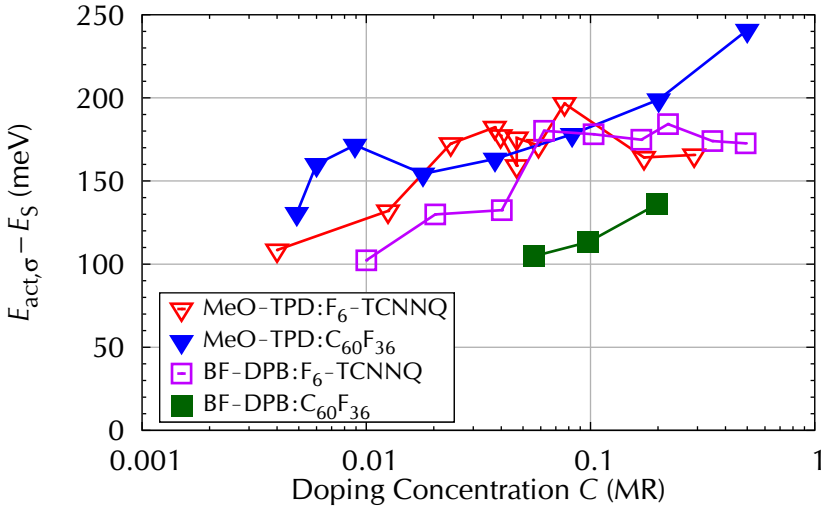

Figure 6.7: *Difference between activation energy of the conductivity $E_{act,\sigma}$ and Seebeck energy E_S for samples of MeO-TPD (triangles) and BF-DPB (squares) doped by F_6-TCNNQ (empty symbols) and $C_{60}F_{36}$ (filled symbols).*

value as high as 241 meV. All material combinations yield a rising difference with C at low C. Doping both hosts by $C > 0.050$ MR of F_6-TCNNQ, the difference between E_S and $E_{act,\sigma}$ is found to be constant at a similar value around 175 meV. This suggests that for all these samples the mobility has the same dependence on the temperature, compare equation (2.72) on page 32.

Samples doped by $C_{60}F_{36}$ show a further increasing difference at larger C, due to a faster decreasing E_S than $E_{act,\sigma}$ at these doping concentrations. The slower drop of $E_{act,\sigma}$ with C at high C of $C_{60}F_{36}$ is attributed to thermal activation of dopants, due to the expected low EA of $C_{60}F_{36}$ in respect with the IEs of the hosts as discussed in section 6.1.2. This model is supported by the temperature-dependent Seebeck experiments on the samples of BF-DPB doped by $C_{60}F_{36}$, where a strong reduction of S with increasing T at high C is observed, compare figure 6.4 (h).

6.3 Degradation

In this section, the effect of elevated temperatures on p-doped layers is studied by conductivity investigations. Three samples of different material combinations are investigated. In order to compare the data, the conductivity of each sample is normalized to the value at $T = 25\,°C$, and depicted in figure 6.8. The conductivity is measured twice with a delay of 30 minutes to 1 hour for most temperatures, which allows for detection of sample degradation. As reported in section 6.1.2 for all samples at low T, an increase of σ with T is visible.

The sample of MeO-TPD doped by F_6-TCNNQ (at $C = 0.040$ MR) shows a slight degradation starting at $T = 65\,°C$. A single measurement at $T = 80\,°C$ yields a maximum of

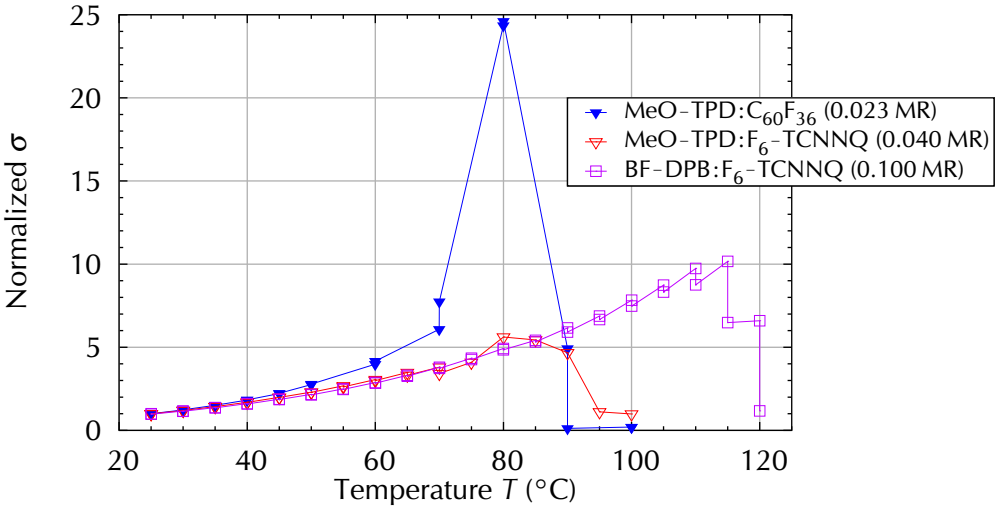

Figure 6.8: *Degradation induced by heating for three different material combinations. The conductivity is normalized to the value at $T = 25\,°C$.*

σ, followed by a rapid decrease. The degradation is attributed to the glass transition of MeO-TPD ($T_g = 67\,°C$[The98]).

Doping MeO-TPD by $C_{60}F_{36}$ (at $C = 0.023\,MR$) a different tendency is found. Between $T = 70\,°C$ and $80\,°C$ a sudden gain of σ by a factor of more than 3 is observed. 37 minutes later, at the same temperature, σ changes only by 1 %, so no degradation is visible at $T = 80\,°C$. At $T = 90\,°C$ the sample is degrading rapidly. This data indicates that the presence of $C_{60}F_{36}$ might shift the glass transition temperature of MeO-TPD upwards. Furthermore, it seems evident that thermal annealing raises the doping efficiency of $C_{60}F_{36}$ in MeO-TPD. As $C_{60}F_{36}$ has been reported[Mao13] to thermally decompose at $T = 120\,°C$[‡], it is possible that in MeO-TPD the dopant decomposes as well. This could lead to a donation of strongly electronegative flour atoms to the host that would work as additional p-dopants and strongly increase the density of free holes.

Using BF-DPB as host and F_6-TCNNQ as dopant (at $C = 0.100\,MR$), a higher thermal stability is found. Starting at $T = 65\,°C$ a slow degradation of σ is observed, but up to $T = 100\,°C$ the effect is much lower than the gain due to the rising temperature. At $T \geq 115\,°C$ a strong degradation is present.

No degradation is studied for BF-DPB doped by $C_{60}F_{36}$.

[‡]on indium tin oxide (ITO) substrates

6.4 Conclusion

Comparing the host materials when using the same dopant, the samples of MeO-TPD show higher conductivities than samples of BF-DPB, often by more than one order of magnitude. This trend is particularly interesting, as for both materials a similar OFET-mobility has been measured. Hence, the larger conductivity for MeO-TPD is attributed to a larger density of free holes due to the lower ionization energy compared to BF-DPB. The activation energy of the conductivity is lower for MeO-TPD samples compared to BF-DPB, but the difference decreases with increasing doping concentration. A similar tendency is observed by the Seebeck investigations, showing that the Seebeck coefficients and hence E_S are larger for BF-DPB, again with a decreasing difference with increasing doping concentration. These larger values obtained for BF-DPB are in agreement with it having the larger IE, making electron transfer to the dopant less probable and therefore leading to a lower density of free holes compared to MeO-TPD. The strong slope of S and hence E_S, observed for BF-DPB as host is attributed to filling of tail states of the density of states. Finally, it is evident that BF-DPB has a higher thermal stability than MeO-TPD, which degrades already at $T = 80\,°C$.

Comparing the dopants in the same host material, higher conductivities are obtained for using the lighter F_6-TCNNQ than for $C_{60}F_{36}$. This trend shows that F_6-TCNNQ has a larger EA than $C_{60}F_{36}$, opposite to the estimated literature values[Tie12,Mee11]. For F_6-TCNNQ, an EA larger and for $C_{60}F_{36}$ an EA lower than 5.2 eV is expected, as the IE of BF-DPB is 5.23 eV and only the former is able to dope it well. The activation energies of the conductivity suggest a thermally induced ionization for large concentrations of $C_{60}F_{36}$, leading to higher density of free holes at elevated temperatures. Seebeck measurements yield that in MeO-TPD, both dopants result in similar S and hence E_S. At large C, samples of F_6-TCNNQ yield somewhat lower values compared to $C_{60}F_{36}$. In samples of BF-DPB doped by $C_{60}F_{36}$ much larger S are found compared to doping by F_6-TCNNQ. This suggests that $C_{60}F_{36}$ generates a lower density of free holes in BF-DPB, in agreement with its above discussed expected low EA. Temperature-dependent Seebeck studies show that for this material combination at elevated temperatures the resulting values of S strongly decrease, supporting the model of thermal induced dopant ionization.

Most material combinations yield a strongly superlinear increase in conductivity with doping concentration, opposite to the n-doping experiments of the previous chapters, where mostly linear relations are found. Here, only for the combination of doping MeO-TPD by $C_{60}F_{36}$ in the medium doping regime a linear relation is observed. In general, the host BF-DPB and the dopant F_6-TCNNQ lead to stronger slopes than the other materials. While samples using $C_{60}F_{36}$ yield a reduced slope at elevated doping concentrations, samples doped by F_6-TCNNQ continue to show strongly increasing conductivities. Seebeck studies of samples doped by F_6-TCNNQ show a rapid drop of the Seebeck coefficient in the medium doping regime indicating an increasing doping efficiency. The comparison of conductivity and Seebeck investigations of samples of MeO-TPD doped by $C_{60}F_{36}$ indicate that the decreasing slope of $\sigma(C)$ at elevated C is most likely due to a reduction of the mobility, since the Seebeck coefficient and hence

the density of free holes is not saturating. This reduction is attributed to a disturbance of the layer morphology by the heavy dopant molecules. Analogously, the decreasing σ-slope of samples of BF-DPB highly doped by $C_{60}F_{36}$ is explained.

Overall, for devices the combination of the more stable host BF-DPB with the stronger dopant F_6-TCNNQ is advised. In a future work the higher fluorinated compound $C_{60}F_{48}$ should be investigated, since it has been reported to have a larger EA than $C_{60}F_{36}$ [Liu97] due to the increased amount of electron attracting fluorine atoms and has been shown to be electrically stable even upon twofold ionization [Jin94].

Chapter 7

Pentacene p-Doped by F_4-TCNQ

After studying two amorphous organic hole transporters in the previous chapter, the high mobility prototypical polycrystalline organic material pentacene is investigated in the following. F_4-TCNQ is chosen as p-dopant, since it has almost the same size and weight as pentacene and is expected to neatly integrate into pentacene layers at low doping concentrations. Theoretical studies predict an increasing doping efficiency with doping concentration for this material combination, which is experimentally tested in this chapter.

The combination of pentacene doped by F_4-TCNQ has been studied earlier by several groups and techniques. AFM surface scans have shown that layers of pentacene can be grown highly crystalline and that at very low doping concentration, F_4-TCNQ does not disturb the molecular order of pentacene [Ha09]. Increasing the doping concentration, the crystallite size has been found to decrease and rough surface structures have been reported [Kle12a]. Details about the materials are summarized in the materials section 3.2.

Theoretical studies on this model system of pentacene doped by F_4-TCNQ, with similar-sized dopant and host, suggest [Mit12b] that for organic semiconductors, a certain threshold doping concentration exists, below which doping does not increase the conductivity. This threshold is attributed to electron–hole attraction hindering the charge pair dissociation. Increasing the doping concentration C, the potential landscape of the ionization energy IE is expected to be altered such that percolation pathways for dissociation are generated. Hence, the doping efficiency is expected to increase with C. To test this model, conductivity and Seebeck investigations are performed.

7.1 Conductivity Changes after Preparation

In an analogous way to the previously investigated materials, the change of conductivity of freshly produced 30 nm thick layers over time is investigated before reporting on the observed conductivities. As for most sets of materials, the conductivity of each sample is continuously probed in-situ for 1 hour at a fixed temperature of $T = 25\,^{\circ}\mathrm{C}$, as discussed in detail in section 4.1.1. A strong reduction of conductivity σ over time is detected for most samples of pentacene doped by F_4-TCNQ. To quantify the change in conductivity, the data are fitted according to equation (4.2) on page 53 and

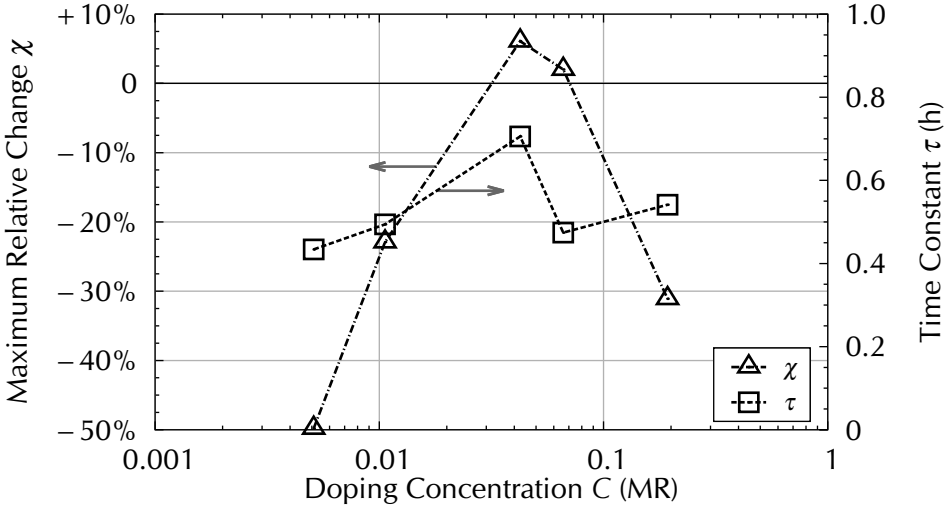

Figure 7.1: *Conductivity change during the first hour after sample preparation for pentacene doped by F_4-TCNQ. Fitting parameters, according to equation (4.2) on page 53.*

a good agreement with the fit function is found for most samples. The resulting fitting parameters are presented in figure 7.1.

The strongest reduction is determined for the lowest doped sample, resulting in a fitted maximal relative change χ of $-50\,\%$ of the initial value of the conductivity. Samples of higher doping concentrations show smaller decreases and two samples ($C = 0.043$ MR and 0.066 MR) even a slightly increasing conductivity over time. The highest doped sample of $C = 0.193$ MR shows again a strong reduction.

The time constant τ scatters around 30 min for all samples, being comparable to the results for C_{60} n-doped by DMBI-POH (compare figure 5.2 on page 74).

7.2 Relation of Conductivity to Doping Concentration

Measured directly after sample fabrication at $T = 25\,°C$, the detected conductivities are in the range of $\sigma = 5.8{\cdot}10^{-3}\,S/cm$ to $3.7{\cdot}10^{-2}\,S/cm$, and a sublinear (slope < 1.0) increasing with doping concentration up to 0.080 MR, followed by a decrease at higher C is found, as shown by the full circles in figure 7.2. The sublinear rise of $\sigma(C)$ suggests a reducing charge carrier mobility with increasing doping concentration and hence a compensation to the gain of density of free holes induced by the dopants. This decrease of the mobility is attributed to a disturbance of the polycrystalline morphology of pentacene by the rising number of dopants, as reported in literature [Kle12a].

As described in the previous section, the in-situ conductivity strongly changed after sample fabrication. To reach stable measurement conditions, the samples were thermally annealed for 1 hour at $T = 70\,°C$ prior to further investigations. Afterwards,

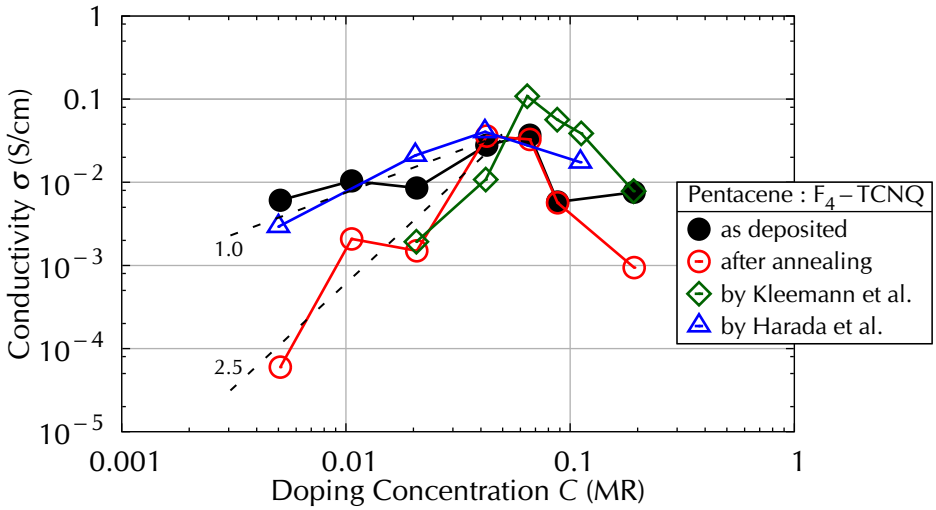

Figure 7.2: *As-prepared conductivity vs. doping concentration of layers of pentacene doped by F_4-TCNQ, probed at $T = 25\,°C$, directly after sample preparation (full circles) and after thermal annealing (open circles). Literature values taken from Harada et al. [Har10] and Kleemann et al. [Kle12a] are added for comparison. Dashed lines are linear fits with slopes 1.0 and 2.5.*

the conductivities are measured again and found to be constant over time, thus the heating seems to accelerate and saturate the effect responsible for the change of the conductivity over time. The values are displayed by the open circles in figure 7.2. It can be seen that the heat treatment changes the room temperature conductivity in the same direction as the trend of the continuous investigations after sample preparation indicated. The conductivity of the lowest doped sample drops by two orders of magnitude, whereas samples of higher doping concentrations show less reduction. Only the conductivity of the sample of $C = 0.043\,\mathrm{MR}$ increased slightly after heating. Two samples with higher doping concentrations show almost constant conductivities and the highest doped sample decreased by almost one order of magnitude, in agreement with the tendency of the continuous measurements directly after sample fabrication.

After thermal annealing, the conductivity has a strong C-dependency in the low to medium doping regime. A strongly superlinear rise with a slope around 2.5 in this double-logarithmic plot is found for the four lowest doped samples, as indicated by the dashed line in figure 7.2. Similar slopes are determined for MeO-TPD and BF-DPB p-doped by $C_{60}F_{36}$ in section 6.1.1, but at large doping concentrations. The strong change of the conductivity directly after fabrication as well as after thermal annealing is either attributed to changes of the mobility or to changes of the density of free holes, for example by diffusion and agglomerating or re-evaporation of the light diffusive dopant F_4-TCNQ, having a sublimation temperature in the range of $T_{\mathrm{dep}} = 100\,^{\circ}\mathrm{C}$. As this effect has a C-dependency, it might be responsible for the superlinear rise of $\sigma(C)$ as well. The changes of the conductivity are smallest for samples of doping concentrations between $C = 0.043\,\mathrm{MR}$ and $0.066\,\mathrm{MR}$, indicating that F_4-TCNQ is best integrated into the layer of pentacene in this range of doping concentration.

Interestingly, the conductivity values as well as their slope prior to annealing are in good agreement with investigations published by Harada et al. [Har10], whereas after heating they agree to experiments by Kleemann et al. [Kle12a]. Both sets of data are shown in figure 7.2, with the authors' kind permissions. Harada et al. have reported[‡] that they observed a decreasing conductivity after sample processing as well. They decided to measure conductivity and Seebeck coefficient as quickly as possible, instead of performing a thermal annealing step as done here. This explains why their conductivity data are in agreement with the above discussed measurements prior to heat treatment. Kleemann et al. on the other hand used samples that where in contact with air for 30 minutes after fabrication. Thus, this suggests that air-exposure has a similar influence on the conductivity of these samples than thermal treatment. It is possible that the light and volatile F_4-TCNQ molecules desorb from the layer upon contact with air or during heating in vacuum.

Both studies have presented C-dependent OFET-mobility measurements in addition to conductivity studies and reported a similar trend of a slowly decreasing OFET-mobility at low C, followed by a significant decrease at $C > 0.050\,\mathrm{MR}$. Hence, the drop of σ at high C detected in all four experiments and shown in figure 7.2, is explained by a decreasing mobility. Due to very narrow contact distances and thus high fields in an OFET geometry, it is expected that the density of free holes is strongly enhanced and

[‡]Personal correspondence with the author.

hence compensates for dopant induced traps. Thus, in conductivity geometry a different tendency of the mobility, especially for low doping concentrations, is expected.

7.3 Comparison of Seebeck Energy and Activation Energy

Temperature-dependent conductivity investigations in the range of $T = 25\,°C$ to $70\,°C$ on this material system allow to derive an activation energy of the conductivity $E_{act,\sigma}$ for each sample, using equation (2.25) on page 16. The derived $E_{act,\sigma}$ is depicted in figure 7.3 and found to strongly vary with doping concentration, with a maximum of $E_{act,\sigma} = 357\,meV$ at $C = 0.011\,MR$. The obtained trend of $E_{act,\sigma}(C)$ is almost inverse to the tendency of the $\sigma(C)$ after thermal annealing. Samples of high σ show low values of $E_{act,\sigma}$ and vice versa, in agreement with the data presented in the previous chapters and only the lowest doped sample deviating.

Besides conductivity investigations, Seebeck measurements at $T_m = 40\,°C$ (after thermal annealing) are performed on this material system as well, allowing to derive the energetic difference E_S between Fermi level E_F and transport level E_{Tr}. E_S is positive for all samples, as expected for p-doped layers and the values are presented in figure 7.3 where they are compared to $E_{act,\sigma}$. The highly doped samples yield a slowly decreasing $E_S(C)$, in the range of $E_S = 103\,meV$ to $73\,meV$, whereas for the lowest doped sample the Seebeck measurement was not successful. This rather small E_S at low C indicates a high doping efficiency of F_4-TCNQ in pentacene. Another explanation for the low E_S is that intrinsic pentacene has been reported to have an extremely narrow density of states DOS with a Gaussian width in the range of only $\sigma_G = 70\,meV$ [Yog11]. Such a narrow DOS requires a small E_S to generate free charges.

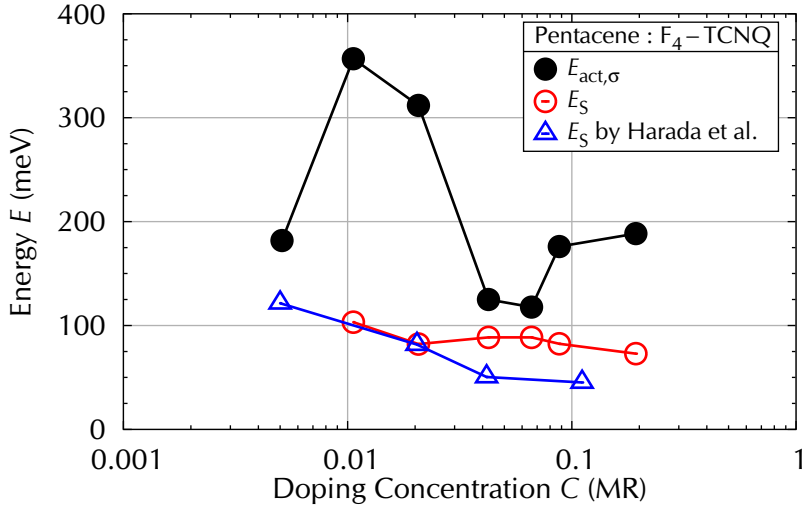

Figure 7.3: *Comparing activation energy of the conductivity $E_{act,\sigma}$ and Seebeck energy E_S. $E_{act,\sigma}$ is fitted from conductivity data of $T = 25\,°C$ to $70\,°C$, E_S is measured at $T_m = 40\,°C$. Literature values for E_S taken with kind permission from Harada [Har10] are added for comparison.*

Upon doping, the width of the *DOS* and hence E_S are expected to rise due to molecular disorder. This effect is not visible in the data and might be compensated by the increasing doping concentration, resulting in an almost constant E_S.

The differences between E_S and $E_{act,\sigma}$ for most samples are attributed to a thermal activation of the mobility, as discussed in section 4.2.3. This contribution is strongest for the sample of $C = 0.011\,\mathrm{MR}$ and decreasing with C. As in the same C-regime, a superlinear rise of $\sigma(C)$ is observed and E_S is almost constant, the decreasing thermal activation of the mobility seems to be correlated to a mobility rise in this regime of C.

Harada et al.[Har10] have performed Seebeck measurements on pentacene doped by F_4-TCNQ as well, but at lower $T_m = 24\,^\circ\mathrm{C}$ and without thermal annealing the samples. Their data are included in figure 7.3. An almost identical value of E_S is measured at $C = 0.020\,\mathrm{MR}$ in both setups: Harada reported $E_S = 81.7\,\mathrm{meV}$ ($S = 275.0\,\mu\mathrm{V/K}$ at $T_m = 24\,^\circ\mathrm{C}$), compared to $E_S = 82.2\,\mathrm{meV}$ ($S = 262.5\,\mu\mathrm{V/K}$ at $T_m = 40\,^\circ\mathrm{C}$) measured in our setup. At higher doping concentrations, the two experiments differ, with Harada's values being lower. The deviation of the two experiments is attributed to the fact that Harada did not anneal the samples prior to Seebeck investigations, as discussed above. Thus, this deviation is an indication for heating or air-exposure of highly F_4-TCNQ-doped pentacene samples reducing the density of free holes, most probably by the agglomeration or re-evaporation of the diffusive F_4-TCNQ molecules. At low doping concentrations, where the two Seebeck measurements are in agreement, the density of free holes seems not to be affected by thermal annealing and therefore the different conductivities are attributed to changes in the mobility induced by morphological changes in the layer and accelerated by the heat treatment. Re-evaporation of dopants is not likely to be present in the data at low C, since this would correspond to a shift of E_S to smaller doping concentrations, flattening the curve even more.

7.4 Conclusion

The strong reduction of the in-situ conductivity over time, which could be accelerated and saturated by heat treatment, is attributed to morphological changes in the layer, reducing the mobility. A decreasing conductivity at high doping concentrations is in agreement with a strongly reduced OFET-mobility reported in literature[Har10,Kle12a]. The rather small E_S at low doping concentrations indicates a high doping efficiency of F_4-TCNQ in pentacene and/or a narrow density of states. At higher doping concentrations the E_S is found to be almost constant, but larger than obtained for highly n-doped C_{60} samples, which is attributed to a broadening of the density of states, partly compensated by the increasing doping concentration. A comparison with literature values of unannealed samples suggests that at $C > 0.020\,\mathrm{MR}$ during thermal treatment, re-evaporation of the light and diffusive dopant molecules occurs.

Neither the presence of a threshold doping concentration for the generation of free charge carriers nor indications for an increasing doping efficiency upon rising doping concentration, as predicted by Mityashin et al.[Mit12b], are observed by the measurements. Rather high conductivities directly after sample fabrication, showing only a

moderate increase with C, even contradict this model. Seebeck measurements do not show indications for an increasing doping efficiency with C, which would be correlated to a more rapid decrease of E_S. It is possible that the predicted phenomena are concealed by morphological effects or that they occur at lower doping concentrations.

Chapter 8

Estimating the Doping Efficiency and the Mobility

Following four experimental chapters, a theoretical model for deriving trends for the density of free charge carriers, the doping efficiency as well as the charge carrier mobility from conductivity and Seebeck data is developed and is first applied to data of n- and later to p-doped samples. In section 8.1, a lower limit for the charge carrier mobility is derived from conductivity measurements. Afterwards, in section 8.2 a similar estimation is performed for the density of free charge carriers and the doping efficiency. Supporting these findings by Seebeck data, the physically allowed position of the transport level is narrowed down in section 8.3. This leads in section 8.4 to the assumption of a constant transport level for all n-doped samples, allowing to derive absolute values for the above mentioned parameters of each sample. Finally, in section 8.5 the developed model is applied to data of p-doped samples. This chapter is finalized by a conclusion in section 8.6.

8.1 Lower Limit of the Mobility

In this first section a lower limit for the charge carrier mobility μ_{LL} is derived from conductivity measurements. Assuming a C-independent and constant doping efficiency η_{dop}, the density of free charge carriers $n_{\mathrm{e/h}}$ directly follows the trend of the density of dopant molecules n_{D} for varying doping concentration, illustrated in figure 8.1, and can be calculated by equation (2.45) on page 23:

$$n_{\mathrm{e/h}} = \eta_{\mathrm{dop}} \cdot n_{\mathrm{D}} = \eta_{\mathrm{dop}} \cdot n_{\mathrm{Mol}} \cdot \frac{C}{1+C} \,. \tag{8.1}$$

This calculated value of $n_{\mathrm{e/h}}$ can be correlated to the charge carrier mobility $\mu_{\mathrm{e/h}}$ for a measured conductivity σ as

$$\mu_{\mathrm{e/h}} = \frac{\sigma}{e \cdot n_{\mathrm{e/h}}} \tag{8.2}$$

$$\Rightarrow \mu_{\mathrm{e/h}} = \frac{\sigma}{e \cdot \eta_{\mathrm{dop}} \cdot n_{\mathrm{Mol}}} \cdot \frac{1+C}{C} \,. \tag{8.3}$$

Above equations show that for a given (measured) conductivity, the estimated mobility is inversely proportional to the estimated $n_{\mathrm{e/h}}$ and thus the η_{dop}. Consequently, by measuring σ and assuming the maximum possible doping efficiency of $\eta_{\mathrm{dop}} = 100\,\%$, meaning each dopant molecule is ionized and provides one free charge carrier, the lower limit of the mobility μ_{LL} can be derived:

$$\mu_{\mathrm{LL}} = \frac{\sigma}{e \cdot 100\,\% \cdot n_{\mathrm{Mol}}} \cdot \frac{1+C}{C} \,. \tag{8.4}$$

In figure 8.2, this calculation is performed for the n-doped C_{60} samples presented in chapters 4 and 5, using four different n-dopants. Here, the conductivity measured

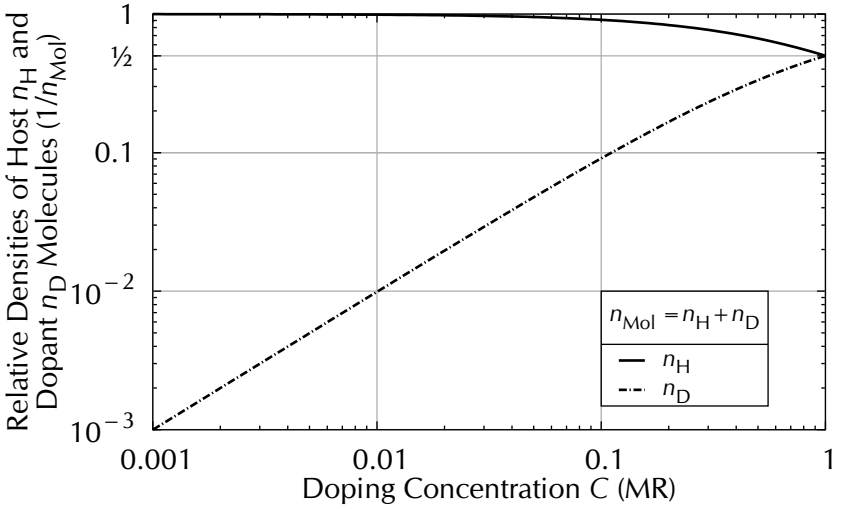

Figure 8.1: *Influence of doping concentration C on densities of host n_H and dopant n_D molecules, calculated via equations (2.43) on page 23. Values given as a fraction of the total density of molecules $n_{Mol} = n_H + n_D$.*

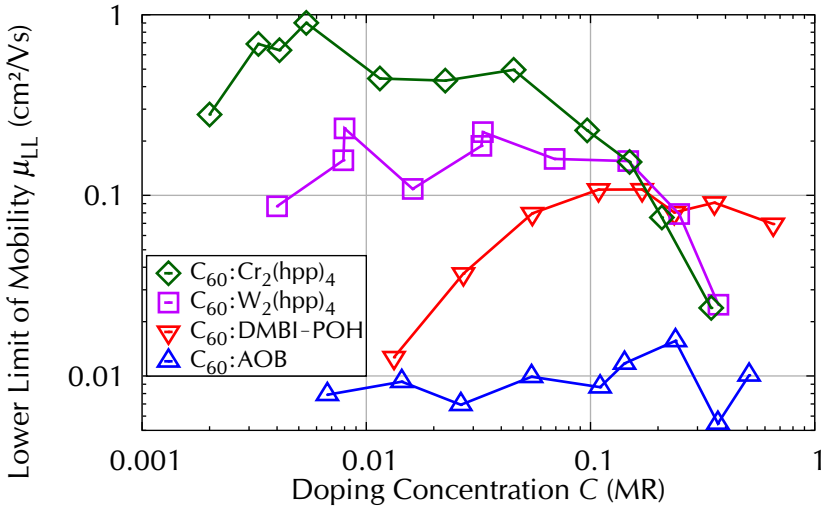

Figure 8.2: *Lower limit of the charge carrier mobility μ_{LL} for n-doped C_{60}, calculated by equation (8.4) using measured conductivity data, probed at $T = 40\,°C$.*

at a temperature of $T = 40\,°C$ (after thermal annealing) is used, as this data will later be compared to Seebeck studies performed at $T_m = 40\,°C$. The lower limit of the mobility μ_{LL} is found to be highest for the dopant $Cr_2(hpp)_4$ with a maximum of $\mu_{LL} = 0.90\,cm^2/Vs$ for $C = 0.005\,MR$. Record values of the mobility of undoped C_{60} layers in the order of $\mu = 5\,cm^2/Vs$ are found in the literature[Ita06]‡. At doping concentrations of $C < 0.045\,MR$, μ_{LL} is rather constant for $Cr_2(hpp)_4$ with values in the range of $\mu_{LL} = 0.50\,cm^2/Vs$, whereas at higher C the μ_{LL} drops significantly. A similar trend is found for the second air-sensitive dopant $W_2(hpp)_4$. Below $C = 0.150\,MR$, almost constant values in the range of $\mu_{LL} = 0.15\,cm^2/Vs$ are derived, followed by a drop for higher doping concentrations. This drop of the μ_{LL} suggests a disturbance of the morphology by the large amount of heavy dopants in the layer and hence a reduction of the real mobility.

A different relation is found for the lighter air-stable dopants, AOB and DMBI-POH. The samples doped by AOB yield an almost constant lower limit of the charge carrier mobility in the order of only $\mu_{LL} = 9{\cdot}10^{-3}\,cm^2/Vs$. Samples doped by DMBI-POH have a μ_{LL} that is as small as for AOB for the lowest C, but strongly increasing with C. A saturation value around of $\mu_{LL} = 0.1\,cm^2/Vs$ is observed, being even higher than for the air-sensitive dopants at these doping concentrations.

Figure 8.2 shows that the materials which yield a linear relation of $\sigma(C)$ at low doping concentrations (compare figure 5.4 on page 76) have a C-independent μ_{LL}. It is expected that for low doping concentrations the mobility is the same for each dopant, therefore the different and almost constant values of the μ_{LL} indicate different doping efficiencies of the dopants, which is addressed in the next section. As the conductivities of samples of C_{60} doped by DMBI-POH increases superlinearly with doping concentration, this effect can most probably be attributed to an increasing η_{dop} with C for this dopant, as discussed in section 5.1.2. From this simple model it cannot be

‡measured in an OFET geometry on a monolayer of pentacene

distinguished whether the observed decrease or saturation of the μ_{LL} at high C for $Cr_2(hpp)_4$, $W_2(hpp)_4$ and DMBI-POH are correlated to trends of the real mobility or a decreasing η_{dop}.

8.2 Lower Limit of the Doping Efficiency

Besides estimates for the lower limit of the mobility by assuming $\eta_{dop} = 100\,\%$, as done in the previous section, the opposite approach can be performed by assuming a constant mobility. If the highest measured literature value for the mobility μ_{UL} of the host material is chosen, a lower limit of the density of free charge carriers $n_{e/h,LL}$ and doping efficiency $\eta_{dop,LL}$ can be derived:

$$n_{e/h,LL} = \frac{\sigma}{e \cdot \mu_{UL}} \tag{8.5}$$

$$\eta_{dop,LL} = \frac{\sigma}{e \cdot \mu_{UL} \cdot n_{Mol}} \cdot \frac{1+C}{C} \,. \tag{8.6}$$

As the real mobility in the used sample geometry is expected to be lower than this record value μ_{UL} and furthermore is expected to be negatively affected by the introduction of dopant molecules disturbing the morphology, the real values of $n_{e/h}$ and η_{dop} must be larger than $n_{e/h,LL}$ and $\eta_{dop,LL}$ to fulfill equation (8.3).

In case of C_{60}, the maximum reported value is in the order of $\mu = 5\,{}^{cm^2}/_{Vs}$ [Ita06], measured in an OFET geometry. This value can be interpreted as an upper limit μ_{UL}, because OFET experiments usually overestimate the charge carrier mobility in comparison to conductivity measurements, as discussed in section 4.2.3. In an OFET geometry the free charge carriers are generated by the field induced by the gate voltage and their number typically is much larger than values achieved by doping. As the mobility of an organic semiconductor usually increases with charge carrier density, OFET channel mobilities are generally larger than the mobilities in the bulk material and hence in the conductivity geometry.

The lower limit of the density of free charge carriers $n_{e,LL}$ is calculated for the n-doped C_{60} samples discussed in chapters 4 and 5, again using the conductivity measured at a temperature of $T = 40\,°C$. The results are depicted in figure 8.3 (a) and found to be largest for samples doped by $Cr_2(hpp)_4$ and lowest for AOB, as expected from the estimates for μ_{LL} in the previous section. All material combinations show an increase of $n_{e,LL}$ with doping concentration, with a saturation and a decrease observed for high concentrations of the two air-sensitive dopants, $Cr_2(hpp)_4$ and $W_2(hpp)_4$. If this decrease in $n_{e,LL}$ is present in the real values of n_e as well, and not an artifact produced by the assumption of a constant mobility, the reason most probably is agglomeration and thus shielding of dopants. The highest $n_{e,LL}$ close to $10^{19}\,cm^{-3}$ are obtained for C_{60} highly doped by DMBI-POH, $Cr_2(hpp)_4$ or $W_2(hpp)_4$, whereas for AOB the largest value is one order of magnitude lower. These obtained values have to be seen in relation to the density of molecules of C_{60} of $n_{Mol,C_{60}} = 1.36{\cdot}10^{21}\,cm^{-3}$ calculated via equation (2.40) using the material parameters from table 3.2 on page 50.

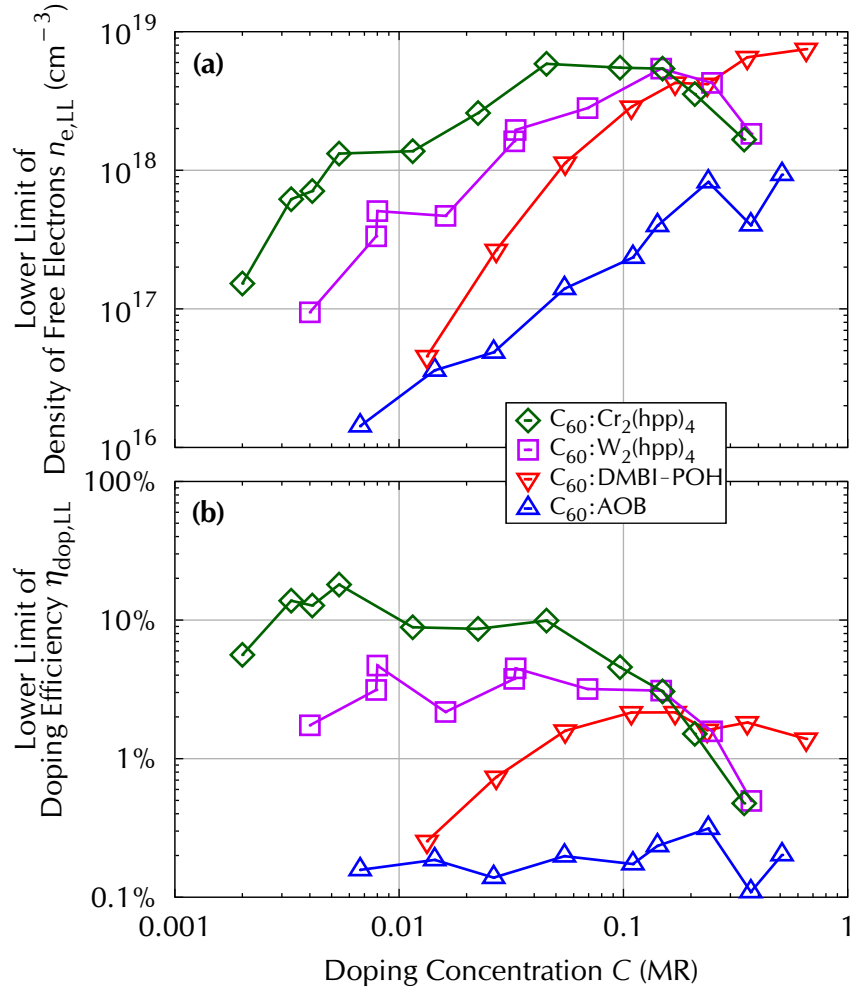

Figure 8.3: *Lower limits of (a) density of free electrons $n_{e,LL}$ and (b) doping efficiency $\eta_{dop,LL}$ for n-doped C_{60}, calculated by assuming a constant mobility set to the record value for intrinsic C_{60} of $\mu = 5\,cm^2/Vs$ [Ita06] and using measured conductivity data, probed at $T = 40\,°C$.*

Knowing $n_{e,LL}$, the lower limit of the doping efficiency $\eta_{dop,LL}$ for each sample is calculated using equation (8.6) and the results are presented in figure 8.3 (b). As mobility and doping efficiency are inversely proportional, the trends of the curves for $\eta_{dop,LL}$ correspond to the trends of the lower limits of the mobilities μ_{LL}, presented in figure 8.2. C_{60} doped by $Cr_2(hpp)_4$ leads to a maximum value of $\eta_{dop,LL} = 18\,\%$ at $C = 0.005\,MR$ and an almost constant $\eta_{dop,LL} \approx 10\,\%$ up to $C = 0.045\,MR$, followed by a decrease. Samples comprising $W_2(hpp)_4$ yield efficiencies around $\eta_{dop,LL} = 3\,\%$ and a drop at $C > 0.147\,MR$. AOB-doped samples have the lowest $\eta_{dop,LL}$ of around $\eta_{dop,LL} = 0.2\,\%$ and DMBI-POH samples start at a similar value, rising by a factor of 10 to a saturation around $\eta_{dop,LL} = 2\,\%$ at high doping concentrations. The gain in $\eta_{dop,LL}$ for low C of DMBI-POH samples is most probably correlated to an increasing real η_{dop} in this range, as it is not unlikely that only for one dopant the mobility of C_{60} is rising with the doping concentration.

At low doping concentrations, the real mobilities of all four material combinations are

expected to be least affected by the dopants and are consequently similar. Therefore, the calculated $\eta_{\mathrm{dop,LL}}$ at low C can be directly compared and should be correlated to the real doping efficiency η_{dop} by the same constant factor for all four combinations. This factor is given by the ratio of the used record mobility of $\mu = 5\,\mathrm{cm^2/Vs}$ and the real value of the bulk material in this sample geometry. Hence, at low doping concentration the real doping efficiency η_{dop} of $Cr_2(hpp)_4$ is approximately 3 times higher than for $W_2(hpp)_4$ and around 15 times larger than for both air-stable compounds.

8.3 Conclusions from Seebeck Measurements

The density of free charge carriers $n_{\mathrm{e/h}}$ is correlated to the density of dopant molecules n_{D} via the doping efficiency η_{dop}, see equation (8.1). On the other hand, $n_{\mathrm{e/h}}$ can be calculated by solving the integral of the product of density of states $DOS(E)$ and Fermi-Dirac distribution function $f_{\mathrm{FD}}(E, E_{\mathrm{F}})$ over all energies, as demonstrated in equation (2.1) on page 6. Thus, for a known $DOS(E)$ and given η_{dop}, the position of the Fermi level E_{F} can be derived by shifting E_{F} until this condition is fulfilled:[‡]

$$n_{\mathrm{e/h}} = \eta_{\mathrm{dop}} \cdot n_{\mathrm{D}} = \int_{-\infty}^{\infty} DOS(E) \cdot f_{\mathrm{FD}}(E, E_{\mathrm{F}})\, dE\ . \tag{8.7}$$

Using a Gaussian density of states and setting its maximum to $E_{\mathrm{G}} = 0$ this becomes:

$$n_{\mathrm{e/h}} = \eta_{\mathrm{dop}} \cdot n_{\mathrm{D}} = \int_{-\infty}^{\infty} \frac{n_{\mathrm{H}}}{\sqrt{2\pi}\,\sigma_{\mathrm{G}}} \exp\left(-\frac{E^2}{2\sigma_{\mathrm{G}}^2}\right) \cdot \frac{1}{1+\exp\left(\frac{E-E_{\mathrm{F}}}{k_{\mathrm{B}}T}\right)}\, dE\ . \tag{8.8}$$

With n_{H} and n_{D} being the densities of host and dopant molecules that can be calculated from the doping concentration C via equations (2.41) and (2.42). Iterative numerical calculations allow to derive E_{F} for varying C and η_{dop}, which is plotted in figure 8.4 for n-doping using a C-independent DOS of width $\sigma_{\mathrm{G}} = 100\,\mathrm{meV}$ (sketched in figure 8.4) and setting $T = 40\,^{\circ}\mathrm{C}$. As the doping efficiency cannot exceed $\eta_{\mathrm{dop}} = 100\,\%$, only values above the solid line corresponding to the E_{F} at $\eta_{\mathrm{dop}} = 100\,\%$ are physically allowed. It can be seen that with increasing C the E_{F} reaches densely populated regions of the DOS, when assuming a constant η_{dop}.

The approach presented above of deriving the position of E_{F} for a given doping efficiency η_{dop} is now combined with the data of the Seebeck studies to calculate the absolute position of the transport level E_{Tr}. Via Seebeck investigations the energy difference E_{S} between E_{F} and E_{Tr} at a certain doping concentration is derived, which is subtracted from a calculated E_{F} for a given η_{dop} at the same C, yielding the position of E_{Tr}:

$$E_{\mathrm{Tr}} = E_{\mathrm{F}} - E_{\mathrm{S}}\ . \tag{2.65}$$

[‡]Here, for holes $f_{\mathrm{FD}}(E)$ instead of $1 - f_{\mathrm{FD}}(E)$ is used as well, as for p-conduction the corresponding DOS is switched from LUMO to HOMO.

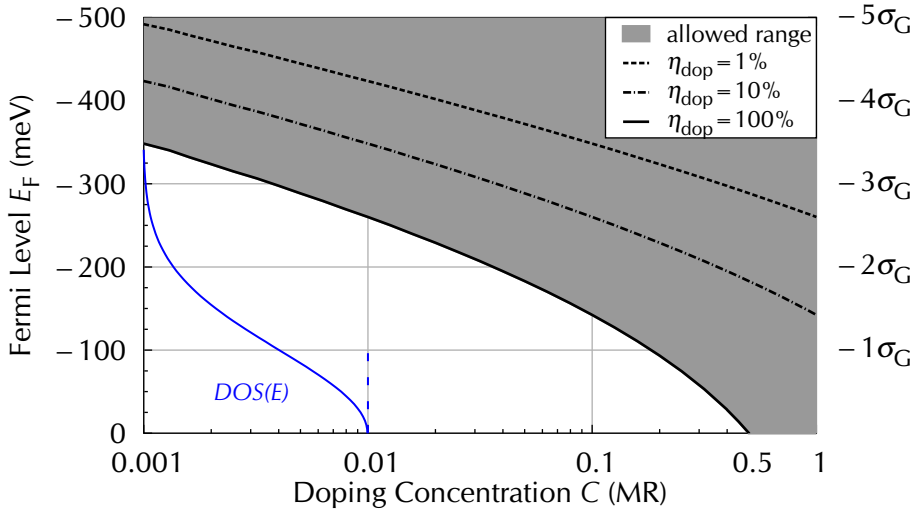

Figure 8.4: *Calculated Fermi level position $E_F(C)$ for different doping efficiencies η_{dop} using equation (8.8) for a Gaussian DOS with $\sigma_G = 100\,meV$ and $T = 40\,°C$. Only values in the gray area are physically allowed with $\eta_{dop} \leq 100\,\%$.*

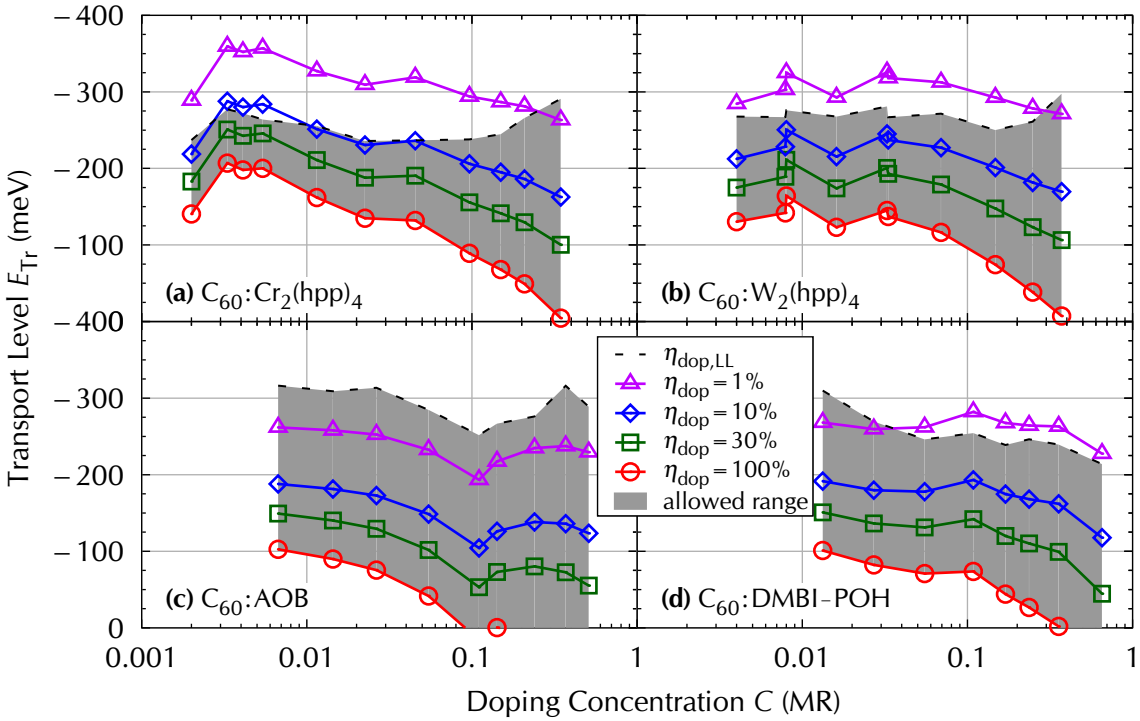

Figure 8.5: *Calculated transport level position E_{Tr} with respect to the maximum of the Gaussian density of states for measured E_S and varying doping concentration and η_{dop} for n-doped C_{60} samples. Parameters used: $\sigma_G = 100\,meV$ and $T = 40\,°C$. The gray area corresponds to the physically allowed range between lower and upper limit of the doping efficiency.*

Figure 8.5 shows the resulting E_{Tr} for the data of the studied n-doped C_{60} layers. In this calculation the width of the Gaussian *DOS* is set to $\sigma_G = 100\,\text{meV}$ for all C, which is chosen to be somewhat higher than the reported $\sigma_G = 88\,\text{meV}$ [Fis10] for undoped C_{60} to compensate the influence of doping that is expected to broaden the *DOS*. As the doping efficiency is required to be greater than the above derived lower limit $\eta_{dop,LL}$ and cannot exceed $\eta_{dop} = 100\,\%$, only a certain region of E_{Tr} is allowed, marked by the filled areas in figure 8.5. This physically possible region is for most samples between $-300\,\text{meV}$ and $-100\,\text{meV}$ with respect to the maximum of the Gaussian density of states. It is narrowest for $Cr_2(hpp)_4$, due to the large value obtained for $\eta_{dop,LL}$.

8.4 Assuming a Constant Transport Level

As derived in the last section, for most of the investigated n-doped samples the physically allowed transport level is in the range of $E_{Tr} = -300\,\text{meV}$ to $-100\,\text{meV}$ with respect to the maximum of the Gaussian density of states, when above mentioned parameters and assumptions are used. This suggests as a further approximation the assumption of a constant transport level for all samples and doping concentrations. A value of $E_{Tr} = -225\,\text{meV}$ is chosen, as this value is in the allowed regime for almost all samples, indicated by the gray area in figure 8.5.

Subtracting this fixed $E_{Tr} = -225\,\text{meV}$ from the calculated $E_F(C)$ for different η_{dop}, as plotted in figure 8.4, similar graphs can be drawn. These curves are compared to the measured Seebeck data in figure 8.6. It can be seen that under this assumption the Seebeck results of C_{60} doped by $C < 0.100\,\text{MR}$ of $W_2(hpp)_4$ or DMBI-POH follow the

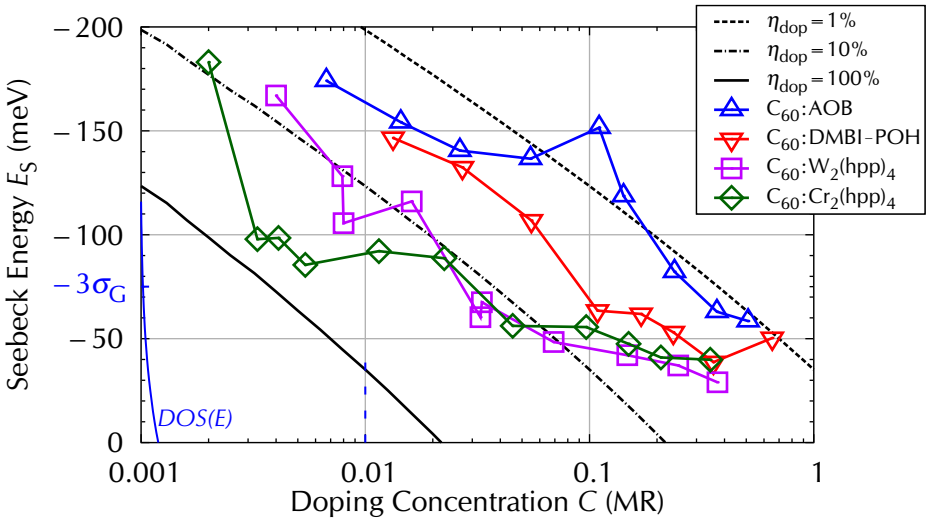

Figure 8.6: *Measured Seebeck energy E_S for n-doped C_{60} compared to calculated $E_S(C)$ for constant transport level $E_{Tr} = -225\,meV$ at different doping efficiencies η_{dop}. Calculations performed analogously to figure 8.4 and subtracting E_{Tr}. Only values above the solid black line corresponding to $\eta_{dop} = 100\,\%$ are physically allowed. The DOS is sketched using the same scale as in figure 8.4.*

trend of a constant doping efficiency, whereas at larger C the E_S tends towards lower η_{dop}. The samples doped by $Cr_2(hpp)_4$ and AOB show deviations from the tendency of a constant η_{dop}.

Using this fixed $E_{Tr} = -225\,meV$, the corresponding density of free electrons n_e is calculated for each sample by solving the above discussed integral (8.8) of the product of density of states DOS and Fermi distribution f_{FD}. Thereby, the measured E_S is used to calculate the Fermi level $E_F = E_{Tr} + E_S$. The results are presented in figure 8.7 (a).

For all four material combinations, the calculated n_e increases with C until at high C a saturation is observed. Samples of both air-sensitive dopants, $Cr_2(hpp)_4$ and $W_2(hpp)_4$, saturate around $n_e = 10^{19}\,cm^{-3}$ for doping concentrations $C \geq 0.040\,MR$. The same n_e is reached by DMBI-POH samples, but at higher C, with the highest doped sample ($C = 0.650\,MR$) showing a decrease by a factor of almost 1.5. AOB-doped samples saturate around lower $n_e = 5{\cdot}10^{18}\,cm^{-3}$ for $C > 0.100\,MR$. These values have to be seen in relation to the density of molecules of C_{60} of $n_{Mol,C_{60}} = 1.36{\cdot}10^{21}\,cm^{-3}$ as discussed above. Overall these trends seem to be more realistic than those derived with the assumption of constant mobility, compare figure 8.3 on page 119 (a), where a decrease of the lower limit of the density of free electrons $n_{e,LL}$ is found at high doping concentration for both air-sensitive dopants, $Cr_2(hpp)_4$ and $W_2(hpp)_4$ as well.

Knowing n_e for a given C, the doping efficiency η_{dop} can be derived, which is depicted in figure 8.7 (b). A maximum of $\eta_{dop} = 62\,\%$ is found for the sample of $C = 0.0033\,MR$ of $Cr_2(hpp)_4$, which suggests that lower values of E_{Tr} might not be realistic, as these would result in an even larger value of η_{dop}. Larger values of E_{Tr} on the other hand would lead to a violation of the derived lower limit $\eta_{dop,LL}$. Hence, $E_{Tr} = -225\,meV$ seems to be a good compromise. The doping efficiencies of $Cr_2(hpp)_4$ and $W_2(hpp)_4$ samples decrease with doping concentration and both series are in very good agreement for $C \geq 0.040\,MR$. AOB-doped samples show a similar trend but at lower values, whereas η_{dop} is almost constant for the samples doped by DMBI-POH.

Combining the derived values of the density of free electrons n_e and the detected conductivity at $T = 40\,°C$, the mobility μ is calculated from equation (8.2) and presented in figure 8.7 (c). The calculated μ is rather high, in agreement with the lower limit μ_{LL}, derived in section 8.1. Both air-sensitive dopants, $Cr_2(hpp)_4$ and $W_2(hpp)_4$, show an almost constant mobility at low and medium C, followed by a decrease at high C that might be attributed to changes in the morphology as discussed in chapter 4. Most of the mobilities derived for $W_2(hpp)_4$ samples are lower than those for $Cr_2(hpp)_4$. This can be interpreted as $W_2(hpp)_4$, with its extremely small ionization energy and thus strong tendency towards ionization, resulting in a reduction of the charge carrier mobility. The samples doped by the air-stable dopants, AOB and DMBI-POH, show low mobilities at low doping concentration and an increase in the medium doping regime. For AOB-doped samples, a decrease at high C is observed, whereas for DMBI-POH the mobility rises further, up to a value above the expected limit of $\mu = 5\,cm^2/Vs$. This is due to a derived η_{dop} below $\eta_{dop,LL}$, suggesting a smaller value of E_{Tr} for this sample.

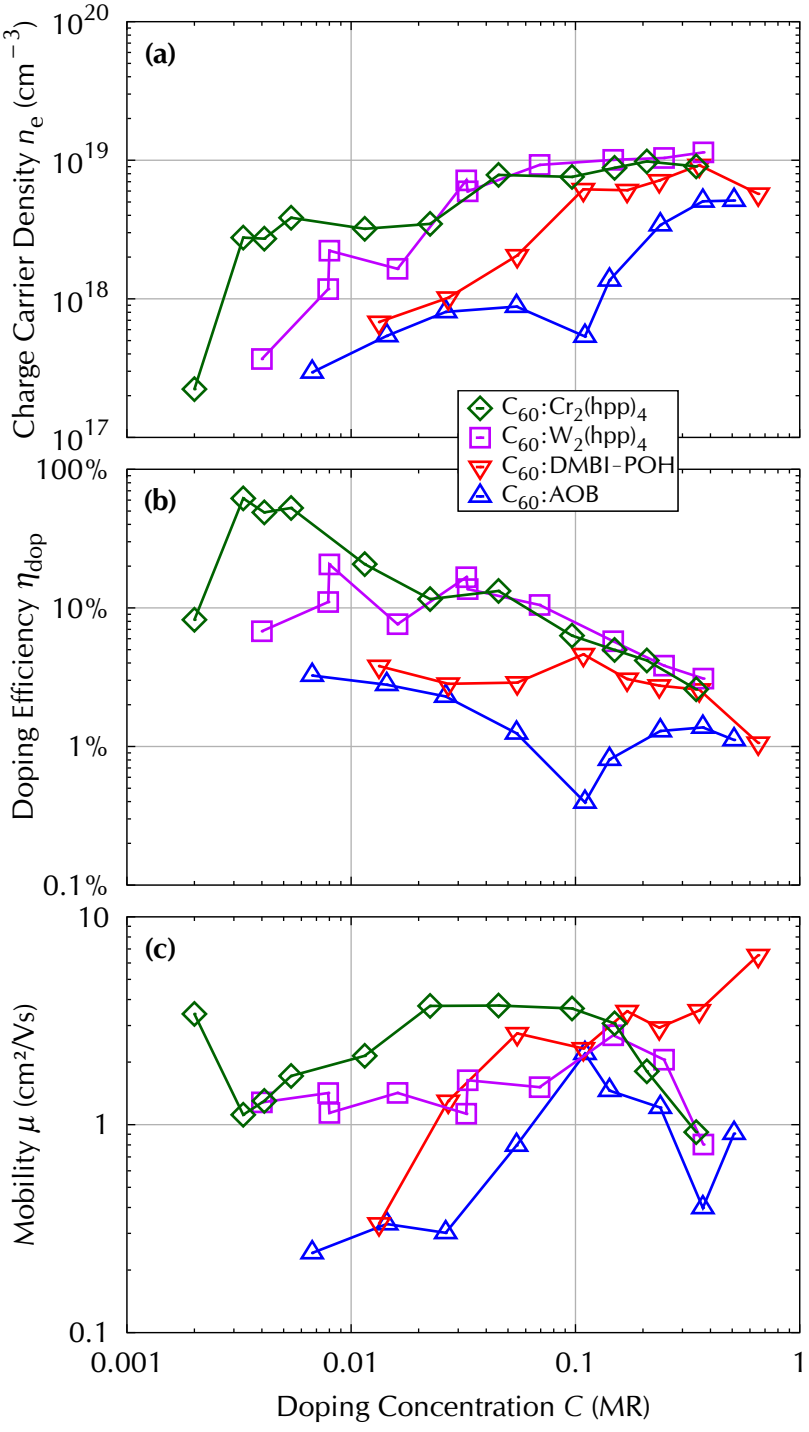

Figure 8.7: *Calculated values of (a) charge carrier density n_e, (b) doping efficiency η_{dop} and (c) mobility μ, for assuming a constant $E_{Tr} = -225\,meV$, using $\sigma_G = 100\,meV$ and n-doped C_{60} data measured at $T = 40\,°C$.*

Overall, the results derived from this rather drastic assumption of a constant transport level E_{Tr} for all samples seem reasonable, as both, the values and the trends are in the expected range. In general, it is expected that E_{Tr}, which is defined by equation (2.62) on page 27 as the energy weighted by the differential conductivity,

$$E_{\mathrm{Tr}} = \frac{1}{\sigma} \int_{-\infty}^{+\infty} E\ \sigma'(E)\ dE \tag{2.62}$$

shifts upon increasing doping concentration towards the maximum of the Gaussian density of states, as the maximum of the differential conductivity $\sigma'(E)$ is expected to shift in this direction. This would result in an upward shift of the trend of n_{e} with C and thus η_{dop}, whereas the tendency observed for μ would be shifted downwards. Modeling this trend would require detailed knowledge on the energetic distribution of the mobility $\mu(E)$ contributing to the differential conductivity $\sigma'(E)$. Furthermore, the density of states might be broadened upon doping due to disturbance of the layer morphology by the dopants.

8.5 Applying the Models to p-Doped Data

After developing and testing these models with n-doped data, in this section, similar calculations are performed for p-doped layers. The data of the dopants F_6-TCNNQ and $C_{60}F_{36}$ in the hosts MeO-TPD and BF-DPB studied in chapter 6 is chosen, as it allows for a comprehensive study. First, the lower limits of the mobilities μ_{LL} are derived from the conductivity data at $T = 40\,^{\circ}\mathrm{C}$ by setting the doping efficiency to the maximum of $\eta_{\mathrm{dop}} = 100\,\%$, as discussed in section 8.1 and the results are depicted in figure 8.8 (a). In both hosts high doping concentrations of F_6-TCNNQ lead to an almost steady gain of μ_{LL} with C, approaching the measured mobilities in OFET geometry (compare section 3.2.1) of $\mu = 2.3{\cdot}10^{-5}\,\mathrm{cm^2/Vs}$ for MeO-TPD and $\mu = 5.7{\cdot}10^{-5}\,\mathrm{cm^2/Vs}$ for BF-DPB, as indicated by the dashed lines in the figure. The μ_{LL} of the two highest doped samples of MeO-TPD even exceeds the measured μ, which is surprising, since OFET studies usually overestimate the mobility due to the high density of free charge carriers generated by the high applied fields, as discussed in section 8.2. This is an indication for the n_{h} of highly doped samples being even higher than the n_{h} generated in the OFET channel region. A similar trend is observed if BF-DPB is doped by F_6-TCNNQ, but up to the highest investigate C, the μ_{LL} is still below the μ of undoped BF-DPB, which is higher than for MeO-TPD. Employing $C_{60}F_{36}$ as dopant yields smaller values of the μ_{LL} in both hosts, with a saturation at high C.

In the following, an estimated upper limit of $\mu_{\mathrm{UL}} = 10^{-4}\,\mathrm{cm^2/Vs}$, being larger than all calculated μ_{LL} values, is used to estimate the lower limits of the density of free holes $n_{\mathrm{h,LL}}$ as well as for the doping efficiencies $\eta_{\mathrm{dop,LL}}$, as discussed in section 8.2. The $n_{\mathrm{h,LL}}$ (depicted in figure 8.8 (b)) rises steadily with C for each material combination, reaching values above $n_{\mathrm{h,LL}} = 10^{20}\,\mathrm{cm^{-3}}$ for both hosts when highly p-doped by F_6-TCNNQ. Such a large $n_{\mathrm{h,LL}}$, being relatively close to the total density of molecules

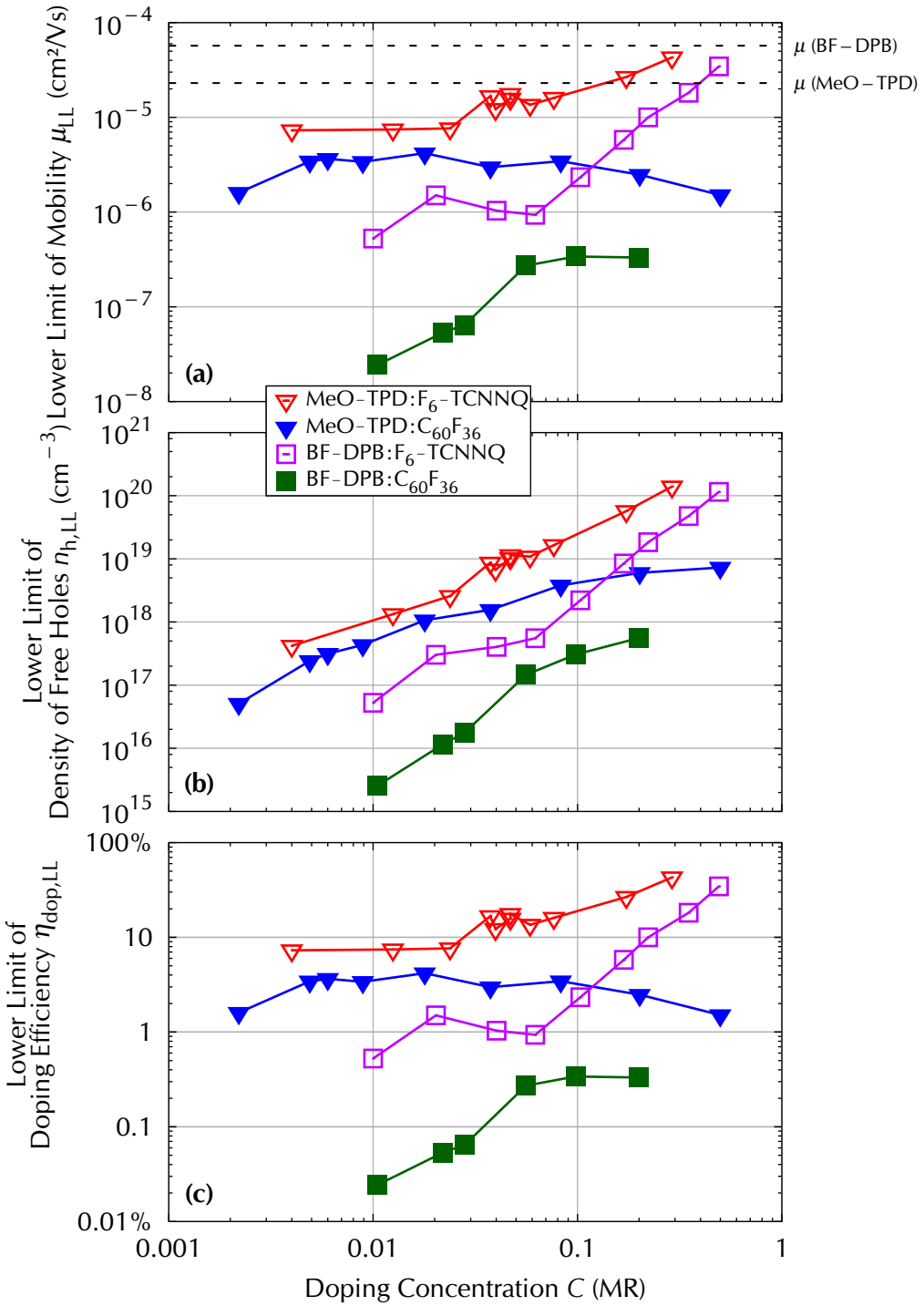

Figure 8.8: *Lower limits of (a) mobility μ_{LL}, (b) density of free holes $n_{h,LL}$ and (c) doping efficiency $\eta_{dop,LL}$ for p-doped samples, calculated via equations (8.4), (8.5) and (8.6) from measured conductivity data probed at $T = 40\,°C$. For $n_{h,LL}$ and $\eta_{dop,LL}$, an upper limit for the mobility is assumed to $\mu_{UL} = 10^{-4}\,cm^2/Vs$, being greater than the OFET-measured mobility of the intrinsic hosts, indicated by the dashed lines in (a).*

$n_{\mathrm{Mol}} = 1.45{\cdot}10^{21}\,\mathrm{cm}^{-3}$ and $1.01{\cdot}10^{21}\,\mathrm{cm}^{-3}$ for MeO-TPD and BF-DPB, respectively, indicate that the assumed $\mu_{\mathrm{UL}} = 10^{-4}\,\mathrm{cm}^2/\mathrm{Vs}$ might still be too low. Using $C_{60}F_{36}$, the highest observed value is one order of magnitude lower in MeO-TPD and even two orders of magnitude lower in BF-DPB.

The lower limits of the doping efficiencies (presented in figure 8.8 (c)) are almost constant for $C < 0.100\,\mathrm{MR}$ of three material combinations, excluding BF-DPB doped by $C_{60}F_{36}$. The highest $\eta_{\mathrm{dop,LL}}$ are derived for samples of MeO-TPD doped by F_6-TCNNQ, followed by samples of $C_{60}F_{36}$ in the same host and finally BF-DPB doped by F_6-TCNNQ. Using BF-DPB and $C_{60}F_{36}$, the smallest $\eta_{\mathrm{dop,LL}}$ are found, but an increase with C is present. Doping both hosts by F_6-TCNNQ, the $\eta_{\mathrm{dop,LL}}$ is constant at low C but raises strongly at elevated C, whereas for $C_{60}F_{36}$ no gain at high C is observed.

Assuming the real mobilities in the low doping regime not being affected by doping and being comparable for the similar structured hosts, the trends of the real η_{dop} follow the tendencies of the $\eta_{\mathrm{dop,LL}}$ in this C-regime, being almost constant for most material combinations. Their relative positions can than be used to derive the relation of the real η_{dop} of the different materials. Doping MeO-TPD by F_6-TCNNQ is hence 2 to 3 times more efficient than using $C_{60}F_{36}$ and approximately 7 times more efficient than the doping of BF-DPB by F_6-TCNNQ, whereas BF-DPB highly doped by $C_{60}F_{36}$ saturates at a η_{dop} approximately 20 times lower.

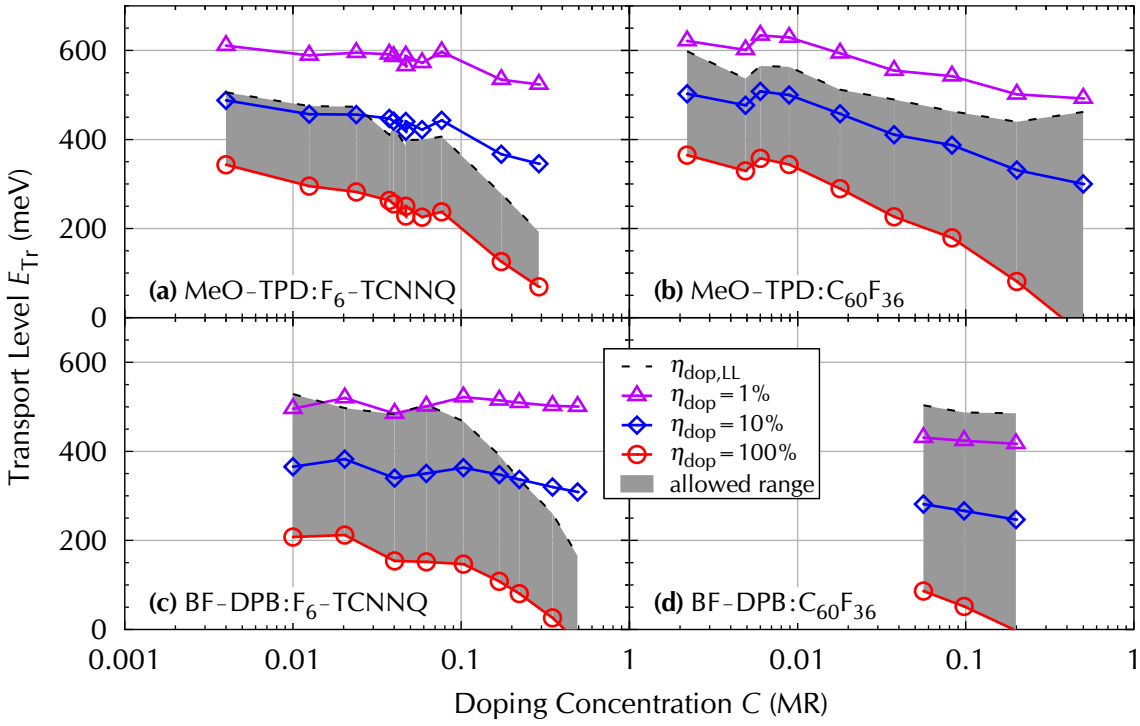

Figure 8.9: *Calculated transport level position E_{Tr} with respect to the maximum of the Gaussian density of states for measured E_S and varying doping concentration and η_{dop} for p-doped samples. Parameters used: $\sigma_G = 200\,meV$ and $T_m = 40\,°C$. The gray area corresponds to the physically allowed regime between lower and upper limit of the doping efficiency.*

As performed in section 8.3 for C_{60}, Seebeck data can be used to derive information about the transport level E_{Tr}. Since the two host materials used for the p-doping are expected to form amorphous layers, as discussed in section 3.2, the density of states is expected to be broader. For simplicity, a value of $\sigma_{\mathrm{G}} = 200\,\mathrm{meV}$, twice as wide as for C_{60} is assumed to calculate the position of the E_{Tr} from measured Seebeck data for varying η_{dop}. The results are presented in figure 8.9. As before, the gray areas indicate the physically allowed regime between lower and upper limit of the doping efficiency. This regime is narrowest for MeO-TPD doped by F_6-TCNNQ and widest for the low conducting samples of BF-DPB doped by $C_{60}F_{36}$. Following the trend of the superlinearly rising $\sigma(C)$ for highly F_6-TCNNQ-doped samples, the $\eta_{\mathrm{dop,LL}}$ strongly limits the allowed regime of E_{Tr} for these samples. While a constant E_{Tr} for all the n-doped samples is assumed in section 8.4, this assumption is not possible for the p-doped samples analyzed in this section due to the strongly limited E_{Tr} for the F_6-TCNNQ samples. Hence, knowledge of the shift of E_{Tr} upon doping is required to calculate the mobility, the density of free holes and the doping efficiency for these p-doped samples.

8.6 Conclusion

The rather simple models presented here are powerful tools for deriving lower limits of the important parameters charge carrier mobility, density of free charge carriers and doping efficiency from conductivity data of doped layers. These give an insight to the trends of the corresponding real values and allow to compare the relative values for different material combinations. Even without knowledge of the energetic dependency of the macroscopic mobility $\mu(E)$, it is possible to narrow down the physically possible regime for the transport level by combining Seebeck and conductivity studies.

For the n-doped samples, the rather drastic assumption of a constant transport level position for all samples is used, which turned out to yield quite reasonable trends for density of free electrons, doping efficiency and mobility. This assumption however is not possible for the p-doped samples since the lower limit of the doping efficiency strongly reduces the allowed region of the transport level.

A more sophisticated model would require profound knowledge of the shape of the density of states and the energetic distribution of the mobility, as well as of the influence of doping on these, which are pathways for future studies.

Chapter 9

Summary and Outlook

9.1 Summary

Experimental

First, an existing setup was fundamentally improved and several possible sources of errors or interferences were eliminated. Software access to all devices allowed for better control of deposition rates as well as for monitoring and logging during sample fabrication process, supporting diagnostics. Furthermore, the computer control make automation and remote control of measurements possible, enabling for longer measurement time and more stable temperature control without electrical disturbances by people operating the setup. The enhanced accuracy and reproducibility of the measurements are the basis for the data presented in this thesis.

n-Doping

The high electron mobility material C_{60} was chosen as host for five different n-dopants ($Cr_2(hpp)_4$, $W_2(hpp)_4$, AOB, DMBI-POH and *o*-MeO-DMBI-I), to study and compare the doping mechanism of these compounds. Each dopant was able to dope C_{60}, tuning the conductivity by several orders of magnitude through varying the doping concentration. Probing the conductivity directly after sample fabrication, changes over time were detected, which could be accelerated and saturated by thermal annealing the samples prior to further measurements, to ensure stable measurement conditions. Rather large conductivities were achieved, with four of the five dopants reaching $\sigma > 1\,{}^{S}/_{cm}$ and a record of $\sigma = 10.9\,{}^{S}/_{cm}$ using *o*-MeO-DMBI-I. At low doping concentrations, the air-sensitive compounds $Cr_2(hpp)_4$ and $W_2(hpp)_4$ were superior, but

showed a drop at high doping concentrations, which is attributed to a decreasing mobility. Thus, both air-stable DMBI derivatives, DMBI-POH and *o*-MeO-DMBI-I reached greater conductivities at elevated doping concentrations. Thereby, it is proven that the easier to handle air-stable precursor n-dopants have the potential to replace air-sensitive dopants in future devices. While most n-dopants showed a linear relation of conductivity to doping concentration, the DMBI derivatives resulted in a superlinear relation. AOB yielded several orders of magnitude lower conductivities directly after sample fabrication than the other dopants. Thermal annealing all samples reduced this difference significantly, but the samples of AOB stayed one order of magnitude below the values achieved for the other dopants, indicating a rather large ionization energy of the active dopant compound of AOB. The conductivity rose with temperature, indicating a temperature-activated hopping transport with an activation energy of the conductivity that lowers upon doping.

Thermoelectric studies yielded a decreasing value of the Seebeck coefficient upon doping, indicating a shift of the Fermi level towards the transport level and thus an increasing density of free electrons with raising doping concentration. For most materials, at high doping concentrations the difference between the two energy levels saturated at $E_S < 2\,k_B T$. A deviation between the activation energy of the conductivity and the E_S, observed for all AOB samples, as well as for highly doped samples of $Cr_2(hpp)_4$ and $W_2(hpp)_4$, was attributed to a thermal activation of the charge carrier mobility.

AFM probing yielded a correlation between surface roughness and doping concentration, but highly doped samples of $Cr_2(hpp)_4$ and $W_2(hpp)_4$ showed smooth layers, which was interpreted as an artifact due to measurement in air.

The study of the degradation by air-exposure of a C_{60} sample doped by the air-sensitive dopant $W_2(hpp)_4$, proved that a post-exposure vacuum and heat treatment can restore a large fraction of the initial conductivity, which allows for device processing steps under ambient conditions, greatly enhancing device fabrication possibilities.

p-Doping

Investigations of p-doped samples using two hosts (MeO-TPD and BF-DPB) and two dopants (F_6-TCNNQ and $C_{60}F_{36}$) were performed to study the influence of the molecular energy levels on the doping effect.

Comparing the hosts MeO-TPD and BF-DPB of similar structure and OFET-mobility, the expected trend was verified, as MeO-TPD with smaller ionization energy leads to a higher conductivity along with a lower Seebeck coefficient at each doping concentration.

The dopants F_6-TCNNQ and $C_{60}F_{36}$ on the other hand, revealed a different picture, since doping by F_6-TCNNQ was more efficient despite the estimated literature value of its electron affinity being lower. It was concluded that the estimated literature values

are incorrect and that the real electron affinity of $C_{60}F_{36}$ is most likely smaller than 5.2 eV, whereas the real electron affinity of F_6-TCNNQ is larger.

A superlinearly rising conductivity with doping concentration was observed for most material combinations, opposite to the n-doping experiments, where mostly a linear relation was found. No saturation of this tendency was visible for samples doped by F_6-TCNNQ and an increasing doping efficiency with doping concentration was postulated. For the heavier $C_{60}F_{36}$, a smaller conductivity slope at elevated doping concentration was explained by a disturbance of the morphology and hence a reduction of the mobility.

Similar to the n-doped samples, the conductivity rose with temperature and again an activation energy of the conductivity $E_{\mathrm{act},\sigma}$ was derived that decreased upon doping. This energy, however, was found to be much larger for the p-doped samples and comparing it to Seebeck investigations the difference was attributed to a strong thermal activation of the mobility.

Concluding, for device application, the use of the thermally more robust BF-DPB as host and the more efficient dopant F_6-TCNNQ is suggested.

Investigating the model system of the polycrystalline pentacene p-doped by the similar-sized F_4-TCNQ, much larger conductivities compared to the amorphous hosts MeO-TPD and BF-DPB were measured and attributed to a higher mobility. Directly after sample deposition, a strong reduction of the in-situ conductivity over time was detected, which could be accelerated and saturated by heat treatment and was attributed to morphological changes in the layer, reducing the mobility. This effect explained the difference between published studies on this material system. However, neither the presence of a threshold doping concentration for the generation of free charge carriers nor indications for an increasing doping efficiency with doping concentration, as theoretically predicted for this material system, were observed in the experiments. It is possible that these phenomena were concealed by morphological effects or that they occur at lower doping concentrations.

Estimating the Doping Efficiency and the Mobility

Finally, a model was developed that allows to derive lower limits for the charge carrier mobility, the density of free charge carriers as well as the doping efficiency from a conductivity measurement. Combining the derived lower limit of the doping efficiency with Seebeck data, the energetic position of the transport level could be narrowed down. In case of the n-doped C_{60} samples the rather drastic assumption of a constant transport level for all material combinations and doping concentrations yielded quite reasonable results for the derived densities of free electrons, doping efficiencies as well as charge carrier mobilities.

9.2 Outlook

Further Improvements of the Setup

Several further improvement of the setup may be worth considering in the future. Firstly, the replacement of the water-cooling by an electrically driven and remotely controllable cooling system. These rather expensive systems can provide liquid solvents at temperatures down to $-50\,°C$ and would greatly enhance the measurement range. Cooling is preferred over heating, since at elevated temperatures the morphology might change or the molecules might even decompose or re-evaporated from the sample. As conductivity measurements do not require as stable temperature control as Seebeck experiments, conductivity studies on doped samples could be performed using liquid nitrogen cooling at the existing setup, as mentioned in section 3.1.1. Secondly, the temperature gradient required for Seebeck investigations could be generated by a Peltier element instead of two individually heated copper blocks [Per08], which should result in an even more stable temperature gradient during Seebeck measurements. Thirdly, in-situ mounting the sample via a transfer system without opening the chamber to air would greatly enhance sample fabrication speed, by preventing contamination and re-evacuation of the chamber. This could furthermore allow for the measurement of samples fabricated in other labs, if they are encapsulated during transport to prevent degradation in air. Finally, full automation of the rate control during co-deposition of host and dopant materials may be worth considering.

Short-Term Studies

It would be interesting to study the influence of much lower and even higher doping concentrations. Lower concentrations would require a modified setup, for example by introducing a shutter above the dopant source, reducing the material flow. An optimized sample geometry for conductivity studies with a high contact length to distance ratio could even allow measuring intrinsic conductivities. Higher concentrations on the other hand are cost-intensive, since the dopants are usually rather expensive, but especially for the p-dopant F_6-TCNNQ, such a study would be interesting, since no saturation of the superlinearly rising conductivity with doping concentration was observed so far. Furthermore, it would be fascinating to try whether host and dopant switch roles at $C > 1.0\,\mathrm{MR}$, which would be visible in a sign change of the Seebeck coefficient.

Further studies of the influence of air-exposure and post-exposure heat and vacuum treatment on doped layers would be of great interest for device fabrication issues. Additionally, the influence of the doping concentration on the thermal stability of the layers could be of interest.

The n-dopants studied should be tested in a series of hosts of smaller electron affinities to check their doping capability. *o*-MeO-DMBI-I, which did not deploy its full doping capability in a vacuum chamber of lower base pressure, should be tried in

different setups. Modifications of the chemical structure of the promising novel air-stable precursor n-dopant class of DMBI derivatives should be studied in more detail, since it might reveal further insight of the doping mechanism.

Medium-Term Studies

The higher fluorinated compound $C_{60}F_{48}$ might be a better choice than the investigated $C_{60}F_{36}$, since its electron affinity is reported to be larger [Liu97].

The materials investigated in this work should be employed in devices to study the influence of conductivity and Seebeck coefficient on device performance. First tests in electron and hole transporting layers of photovoltaic cells where successful, but so far insufficient data were collected to compare the materials.

The origin for the change in conductivity over time observed for many samples directly after sample deposition should be investigated further, for example by performing similar measurements in a vacuum chamber of lower base pressure or by encapsulating the films shortly after fabrication to identify whether it is an artifact of contamination or an internal effect.

Applying p- and n-doping on the same host allows fabrication of p-n-junctions, being the building block for most electronic devices. First p-n-junctions of ZnPc by employing $C_{60}F_{36}$ and $W_2(hpp)_4$ were promising [Bur13].

In the presented setup, nitrogen cooling could be used to study the temperature dependence of the conductivity in more detail. First conductivity studies were successful, but the temperature control was too unstable for Seebeck investigations.

Long-Term Studies

A model describing the energetic dependency of the microscopic mobility would be of great use, since combined with Seebeck data this knowledge would allow for determination of the positions of transport level and Fermi level.

The influence of doping on the morphology is another interesting topic, since the morphology strongly influences the mobility and consequently the conductivity. Morphological analysis of the molecular arrangement could be investigated by techniques like X-ray diffraction or refraction in addition to AFM surface probing.

The optical properties of doped layers are of interest as well, since in optoelectronic devices parasitic light absorption hinders device performance.

Studying the same material system by several techniques could greatly enhance the scientific output compared to single experiments. For example, impedance spectroscopy could be used to derive the density of ionized dopants and thereby the doping efficiency. By the surface sensitive technique of ultraviolet photoelectron spectroscopy (UPS), the Fermi level position in p-doped layers could be determined. The

influence of temperature and doping concentration on the mobility might be obtained using Hall or time of flight (TOF) measurements. Combining this knowledge with a Seebeck and conductivity study should provide a deep insight into the underlaying physics.

Bibliography

[Aka54] H. Akamatu, H. Inokuchi & Y. Matsunaga, *Electrical conductivity of the perylene-bromine complex*, Nature 173(4395), 168, 1954
http://dx.doi.org/10.1038/173168a0

[Aka08] K. Akaike, K. Kanai, H. Yoshida, J. Tsutsumi, T. Nishi, N. Sato, Y. Ouchi & K. Seki, *Ultraviolet photoelectron spectroscopy and inverse photoemission spectroscopy of [6,6]-phenyl-C_{61}-butyric acid methyl ester in gas and solid phases*, Journal of Applied Physics 104(2), 023710, 2008
http://dx.doi.org/10.1063/1.2957588

[Anc12] A. Anctil, C. W. Babbitt, R. P. Raffaelle & B. J. Landi, *Cumulative energy demand for small molecule and polymer photovoltaics*, Progress in Photovoltaics: Research and Applications 2012
http://dx.doi.org/10.1002/pip.2226

[Ark05a] V. Arkhipov, E. Emelianova, P. Heremans & H. Bässler, *Analytic model of carrier mobility in doped disordered organic semiconductors*, Physical Review B 72(23), 235202, 2005
http://dx.doi.org/10.1103/PhysRevB.72.235202

[Ark05b] V. Arkhipov, P. Heremans, E. Emelianova & H. Bässler, *Effect of doping on the density-of-states distribution and carrier hopping in disordered organic semiconductors*, Physical Review B 71(4), 045214, 2005
http://dx.doi.org/10.1103/PhysRevB.71.045214

[Arr84] S. A. Arrhenius, *Recherches sur la conductibilité galvanique des électrolytes*, Dissertation, Uppsala, 1884

[Bar09] A. B. Barron, R. Maleszka, P. G. Helliwell & G. E. Robinson, *Effects of cocaine on honey bee dance behaviour*, The Journal of Experimental Biology 212, 163, 2009
http://dx.doi.org/10.1242/jeb.025361

[Bäs82] H. Bässler, G. Schönherr, M. Abkowitz & D. Pai, *Hopping transport in prototypical organic glasses*, Physical Review B 26(6), 3105, 1982
http://dx.doi.org/10.1103/PhysRevB.26.3105

[Bey97] A. Beyer, *Seebeck-Effekt und thermisch aktivierte Leitfähigkeit dotierter organischer Farbstoffaufdampfschichten*, Diploma thesis, TU Dresden, 1997

[Blo98] J. Blochwitz, M. Pfeiffer, T. Fritz & K. Leo, *Low voltage organic light emitting diodes featuring doped phthalocyanine as hole transport material*, Applied Physics Letters 73(6), 729, 1998
http://dx.doi.org/10.1063/1.121982

[Blo01] J. Blochwitz, *Organic light-emitting diodes with doped charge transport layers*, Dissertation, TU Dresden, 2001

[Böh95] W. Böhm, *Untersuchung des Leitungsverhaltens sublimierter organischer Farbstoffschichten*, Dissertation, TU Dresden, 1995

[Bol63] B. Bolto, R. McNeill & D. Weiss, *Electronic conduction in polymers. III. Electronic properties of polypyrrole*, Australian Journal of Chemistry 16(6), 1090, 1963
http://dx.doi.org/10.1071/CH9631090

[Bur12] L. Burtone, D. Ray, K. Leo & M. Riede, *Impedance model of trap states for characterization of organic semiconductor devices*, Journal of Applied Physics 111(6), 064503, 2012
http://dx.doi.org/10.1063/1.3693545

[Bur13] L. Burtone, D. Ray, K. Leo & M. Riede, *An all-organic p/n homojunction diode*, in preparation 2013

[Cam10] J. Cami, J. Bernard-Salas, E. Peeters & S. E. Malek, *Detection of C_{60} and C_{70} in a young planetary nebula*, Science 329(5996), 1180, 2010
http://dx.doi.org/10.1126/science.1192035

[Cha06] C.-C. Chang, M.-T. Hsieh, J.-F. Chen, S.-W. Hwang & C. H. Chen, *Highly power efficient organic light-emitting diodes with a p-doping layer*, Applied Physics Letters 89(25), 253504, 2006
http://dx.doi.org/10.1063/1.2405856

[Cha08] C. Chan, W. Zhao, S. Barlow, S. R. Marder & A. Kahn, *Decamethylcobaltocene as an efficient n-dopant in organic electronic materials and devices*, Organic Electronics 9(5), 575, 2008
http://dx.doi.org/10.1016/j.orgel.2008.03.003

[Cha09] C. K. Chan & A. Kahn, *n-doping of pentacene by decamethylcobaltocene*, Applied Physics A 95(1), 7, 2009
http://dx.doi.org/10.1007/s00339-008-4997-x

[Col73] L. Coleman, M. Cohen, D. Sandman, F. Yamagishi, A. Garito & A. Heeger, *Superconducting fluctuations and the peierls instability in an organic solid*, Solid State Communications 12(11), 1125, 1973
http://dx.doi.org/10.1016/0038-1098(73)90127-0

[Cot02] F. A. Cotton, N. E. Gruhn, J. Gu, P. Huang, D. L. Lichtenberger, C. A. Murillo, L. O. Van Dorn & C. C. Wilkinson, *Closed-shell molecules that ionize more readily than cesium*, Science 298(5600), 1971, 2002
http://dx.doi.org/10.1126/science.1078721

[Cot03] F. A. Cotton, P. Huang, C. A. Murillo & X. Wang, *Synthesis and reactivity of a very strong reducing agent containing a quadruple bond: Structures of $W_2(hpp)_4$ and $W_2(hpp)_4Cl_2{\cdot}4CH_2Cl_2$*, Inorganic Chemistry Communications 6(2), 121, 2003
http://dx.doi.org/10.1016/S1387-7003(02)00701-3

[Cot05] F. A. Cotton, J. P. Donahue, D. L. Lichtenberger, C. A. Murillo & D. Villagrán, *Expeditious access to the most easily ionized closed-shell molecule, $W_2(hpp)_4$*, Journal of the American Chemical Society 127(31), 10808, 2005
http://dx.doi.org/10.1021/ja0535458

[Cou85] C. A. de Coulomb, *Premier mémoire sur l'électricité et le magnétisme*, Histoire de l'Académie Royale des Sciences p. 569, 1785
http://books.google.de/books?id=by5EAAAAcAAJ&pg=PA569

[Cur62] J. Curry & E. P. Cassidy, *Effect of halogens on the resistance of single crystals of copper phthalocyanine*, The Journal of Chemical Physics 37(9), 2154, 1962
http://dx.doi.org/10.1063/1.1733442

[Dem04] W. Demtröder, *Experimentalphysik 2: Elektrizität und Optik*, Springer-Lehrbuch (Springer), 3rd edn., 2004, ISBN 3-540-20210-2
http://dx.doi.org/10.1007/3-540-35146-9

[Dem09] W. Demtröder, *Experimentalphysik 3*, Springer-Lehrbuch (Springer), 3rd edn., 2009, ISBN 978-3-642-03910-2
http://dx.doi.org/10.1007/978-3-642-03911-9

[Dre04] J. Drechsel, B. Männig, D. Gebeyehu, M. Pfeiffer, K. Leo & H. Hoppe, *MIP-type organic solar cells incorporating phthalocyanine/fullerene mixed layers and doped wide-gap transport layers*, Organic Electronics 5(4), 175, 2004
http://dx.doi.org/10.1016/j.orgel.2003.11.005

[End92] R. Enderlein & A. Schenk, *Grundlagen der Halbleiterphysik* (Akademie-Verlag), 1992, ISBN 978-3055014000

[Fel08] A. Feltrin & A. Freundlich, *Material considerations for terawatt level deployment of photovoltaics*, Renewable Energy 33(2), 180, 2008
http://dx.doi.org/10.1016/j.renene.2007.05.024

[Fer26] E. Fermi, *Zur Quantelung des idealen einatomigen Gases*, Zeitschrift für Physik 36(11-12), 902, 1926
http://dx.doi.org/10.1007/BF01400221

[Fer73] J. Ferraris, D. O. Cowan, V. Walatka & J. H. Perlstein, *Electron transfer in a new highly conducting donor-acceptor complex*, Journal of the American

Chemical Society 95(3), 948, 1973
http://dx.doi.org/10.1021/ja00784a066

[Fis10] I. I. Fishchuk, a. K. Kadashchuk, J. Genoe, M. Ullah, H. Sitter, T. B. Singh, N. S. Sariciftci & H. Bässler, *Temperature dependence of the charge carrier mobility in disordered organic semiconductors at large carrier concentrations*, Physical Review B 81(4), 045202, 2010
http://dx.doi.org/10.1103/PhysRevB.81.045202

[Fis12] A. Fischer, R. Scholz, K. Leo & B. Lüssem, *An all C_{60} vertical transistor for high frequency and high current density applications*, Applied Physics Letters 101(21), 213303, 2012
http://dx.doi.org/10.1063/1.4767391

[Fra13] Fraunhofer ISE, *Aktuelle Fakten zur Photovoltaik in Deutschland*, PV Fakten 03, 2013
http://www.pv-fakten.de

[Fri71] H. Fritzsche, *A general expression for the thermoelectric power*, Solid State Communications 9(21), 1813, 1971
http://dx.doi.org/10.1016/0038-1098(71)90096-2

[Fuj94] S. Fujimori, K. Hoshimono & S. Fujita, *Variation of conductivity and activation energy in metal-doped and undoped C_{60} films under oxygen exposure*, Solid State Communications 89(5), 437, 1994
http://dx.doi.org/10.1016/0038-1098(94)90208-9

[Fuk06] H. Fukagawa, H. Yamane, T. Kataoka, S. Kera, M. Nakamura, K. Kudo & N. Ueno, *Origin of the highest occupied band position in pentacene films from ultraviolet photoelectron spectroscopy: hole stabilization versus band dispersion*, Physical Review B 73(24), 24, 2006
http://dx.doi.org/10.1103/PhysRevB.73.245310

[Gao01] W. Gao & A. Kahn, *Controlled p-doping of zinc phthalocyanine by coevaporation with tetrafluorotetracyanoquinodimethane: A direct and inverse photoemission study*, Applied Physics Letters 79(24), 4040, 2001
http://dx.doi.org/10.1063/1.1424067

[Gau01] O. Gaudin, R. B. Jackman, T.-P. Nguyen & P. Le Rendu, *Determination of traps in poly(p-phenylene vinylene) light emitting diodes by charge-based deep level transient spectroscopy*, Journal of Applied Physics 90(8), 4196, 2001
http://dx.doi.org/10.1063/1.1403669

[Geb55] T. Geballe & G. Hull, *Seebeck effect in silicon*, Physical Review 98(4), 940, 1955
http://dx.doi.org/10.1103/PhysRev.98.940

[Gre04] B. A. Gregg, S.-G. Chen & R. A. Cormier, *Coulomb forces and doping in organic semiconductors*, Chemistry of Materials 16(23), 4586, 2004
http://dx.doi.org/10.1021/cm049625c

[Gre13] M. A. Green, K. Emery, Y. Hishikawa, W. Warta & E. D. Dunlop, *Solar cell efficiency tables (version 41)*, Progress in Photovoltaics: Research and Applications 21(1), 1, 2013
http://dx.doi.org/10.1002/pip.2352

[Gro09] L. Gross, F. Mohn, N. Moll, P. Liljeroth & G. Meyer, *The chemical structure of a molecule resolved by atomic force microscopy*, Science 325(5944), 1110, 2009
http://dx.doi.org/10.1126/science.1176210

[Guo12] S. Guo, S. B. Kim, S. K. Mohapatra, Y. Qi, T. Sajoto, A. Kahn, S. R. Marder & S. Barlow, *n-doping of organic electronic materials using air-stable organometallics*, Advanced Materials 24(5), 699, 2012
http://dx.doi.org/10.1002/adma.201103238

[Ha09] S. Ha & A. Kahn, *Isolated molecular dopants in pentacene observed by scanning tunneling microscopy*, Physical Review B 80(19), 195410, 2009
http://dx.doi.org/10.1103/PhysRevB.80.195410

[Had91] R. C. Haddon, A. F. Hebard, M. J. Rosseinsky, D. W. Murphy, S. J. Duclos, K. B. Lyons, B. Miller, J. M. Rosamilia, R. M. Fleming, A. R. Kortan, S. H. Glarum, A. V. Makhija, A. J. Muller, R. H. Eick, S. M. Zahurak, R. Tycko, G. Dabbagh & F. A. Thiel, *Conducting films of C_{60} and C_{70} by alkali-metal doping*, Nature 350(6316), 320, 1991
http://dx.doi.org/10.1038/350320a0

[Hak06] H. Haken & H. C. Wolf, *Molekülphysik und Quantenchemie* (Springer), 5th edn., 2006, ISBN 978-3-540-30314-5
http://dx.doi.org/10.1007/3-540-30315-4

[Ham93] A. Hamed, Y. Sun, Y. Tao, R. Meng & P. Hor, *Effects of oxygen and illumination on the in situ conductivity of C_{60} thin films*, Physical Review B 47(16), 10873, 1993
http://dx.doi.org/10.1103/PhysRevB.47.10873

[Har07] K. Harada, F. Li, B. Männig, M. Pfeiffer & K. Leo, *Ionized impurity scattering in n-doped C_{60} thin films*, Applied Physics Letters 91(9), 92118, 2007
http://dx.doi.org/10.1063/1.2776355

[Har08] K. Harada, *Organic p-i-n homojunctions: fundamentals and applications*, Dissertation, TU Dresden, 2008

[Har10] K. Harada, M. Sumino, C. Adachi, S. Tanaka & K. Miyazaki, *Improved thermoelectric performance of organic thin-film elements utilizing a bilayer structure of pentacene and 2,3,5,6-tetrafluoro-7,7,8,8-tetracyanoquinodimethane (F_4-TCNQ)*, Applied Physics Letters 96(25), 253304, 2010
http://dx.doi.org/10.1063/1.3456394

[Has01] Y. Hashimoto, M. Hamagaki & T. Sakakibara, *Effect of ionization potential of hole transport layer on device characteristics of organic light emitting diode with oxygen plasma treated indium tin oxide*, Japanese Journal of Applied

Physics 40(1,7), 4720, 2001
http://dx.doi.org/10.1143/JJAP.40.4720

[He04a] G. He, M. Pfeiffer, K. Leo, M. Hofmann, J. Birnstock, R. Pudzich & J. Salbeck, *High-efficiency and low-voltage p-i-n electrophosphorescent organic light-emitting diodes with double-emission layers*, Applied Physics Letters 85(17), 3911, 2004
http://dx.doi.org/10.1063/1.1812378

[He04b] G. He, O. Schneider, D. Qin, X. Zhou, M. Pfeiffer & K. Leo, *Very high-efficiency and low voltage phosphorescent organic light-emitting diodes based on a p-i-n junction*, Journal of Applied Physics 95(10), 5773, 2004
http://dx.doi.org/10.1063/1.1702143

[Hel13] Heliatek GmbH, *Press Release*, 2013
http://www.heliatek.com/wp-content/uploads/2013/01/130116_PR_Heliatek_achieves_record_cell_effiency_for_OPV.pdf

[Her12] M. Hermenau, M. Riede & K. Leo, *Degradation of small-molecule-based OPV*, in *Stability and Degradation of Organic and Polymer Solar Cells*, edited by F. C. Krebs, chap. 5 (John Wiley & Sons, Ltd, Chichester, UK), 2012, ISBN 9781119952510
http://onlinelibrary.wiley.com/doi/10.1002/9781119942436.ch5/summary

[Ike10] H. Ikeda & F. Salleh, *Influence of heavy doping on Seebeck coefficient in silicon-on-insulator*, Applied Physics Letters 96(1), 012106, 2010
http://dx.doi.org/10.1063/1.3282783

[Ing89] M. Ingram, *Ionic conductivity and glass structure*, Philosophical Magazine Part B 60(6), 729, 1989
http://dx.doi.org/10.1080/13642818908209739

[ISI] *Web of Science, accessed 13.03.2013*
http://webofknowledge.com/?DestApp=WOS

[Ita06] K. Itaka, M. Yamashiro, J. Yamaguchi, M. Haemori, S. Yaginuma, Y. Matsumoto, M. Kondo & H. Koinuma, *High-mobility C_{60} field-effect transistors fabricated on molecular-wetting controlled substrates*, Advanced Materials 18(13), 1713, 2006
http://dx.doi.org/10.1002/adma.200502752

[Jér80] D. Jérome, A. Mazaud, M. Ribault & K. Bechgaard, *Superconductivity in a synthetic organic conductor (TMTSF)$_2$PF$_6$*, Journal de Physique Lettres 41(4), 95, 1980
http://dx.doi.org/10.1051/jphyslet:0198000410409500

[Jin94] C. Jin, R. L. Hettich, R. N. Compton, A. Tuinman, A. Derecskei-Kovacs, D. S. Marynick & B. I. Dunlap, *Attachment of two electrons to C60F48: coulomb barriers in doubly charged anions*, Physical Review Letters 73(21), 2821,

1994
http://dx.doi.org/10.1103/PhysRevLett.73.2821

[Kea60] D. R. Kearns, G. Tollin & M. Calvin, *Electrical properties of organic solids. II. Effects of added electron acceptor on metal-free phthalocyanine*, The Journal of Chemical Physics 32(4), 1020, 1960
http://dx.doi.org/10.1063/1.1730844

[Kit11] M. Kitamura & Y. Arakawa, *High current-gain cutoff frequencies above 10 MHz in n-channel C_{60} and p-channel pentacene thin-film transistors*, Japanese Journal of Applied Physics 50, 01BC01, 2011
http://dx.doi.org/10.1143/JJAP.50.01BC01

[Kle12a] H. Kleemann, C. Schünemann, A. A. Zakhidov, M. Riede, B. Lüssem & K. Leo, *Structural phase transition in pentacene caused by molecular doping and its effect on charge carrier mobility*, Organic Electronics 13(1), 58, 2012
http://dx.doi.org/10.1016/j.orgel.2011.09.027

[Kle12b] H. Kleemann, A. A. Zakhidov, M. Anderson, T. Menke, K. Leo & B. Lüssem, *Direct structuring of C_{60} thin film transistors by photo-lithography under ambient conditions*, Organic Electronics 13(3), 506, 2012
http://dx.doi.org/10.1016/j.orgel.2011.12.009

[Koe10] P. K. Koech, A. B. Padmaperuma, L. Wang, J. S. Swensen, E. Polikarpov, J. T. Darsell, J. E. Rainbolt & D. J. Gaspar, *Synthesis and application of 1,3,4,5,7,8-hexafluorotetracyanonaphthoquinodimethane (F6-TNAP): A conductivity dopant for organic light-emitting devices*, Chemistry of Materials 22(13), 3926, 2010
http://dx.doi.org/10.1021/cm1002737

[Kön99] R. Könenkamp, G. Priebe & B. Pietzak, *Carrier mobilities and influence of oxygen in C_{60} films*, Physical Review B 60(16), 11804, 1999
http://dx.doi.org/10.1103/PhysRevB.60.11804

[Kra11] D. Kraemer, B. Poudel, H.-P. Feng, J. C. Caylor, B. Yu, X. Yan, Y. Ma, X. Wang, D. Wang, A. Muto, K. McEnaney, M. Chiesa, Z. Ren & G. Chen, *High-performance flat-panel solar thermoelectric generators with high thermal concentration*, Nature Materials 10(7), 532, 2011
http://dx.doi.org/10.1038/nmat3013

[Kro85] H. W. Kroto, J. R. Heath, S. C. O'Brien, R. F. Curl & R. E. Smalley, *C_{60}: Buckminsterfullerene*, Nature 318(6042), 162, 1985
http://dx.doi.org/10.1038/318162a0

[Krö09] M. Kröger, S. Hamwi, J. Meyer, T. Riedl, W. Kowalsky & A. Kahn, *p-type doping of organic wide band gap materials by transition metal oxides: a case-study on molybdenum trioxide*, Organic Electronics 10(5), 932, 2009
http://dx.doi.org/10.1016/j.orgel.2009.05.007

[Leo13] K. Leo & M. Hummert, *Doping of organic semiconductors*, in *Handbook of Organic Materials for Optical and Optoelectronic Devices: Properties and Applications*, edited by O. Ostroverkhova (not published yet), 2013, ISBN 978 0 85709 265 6
http://www.woodheadpublishing.com/en/book.aspx?bookID=2494

[Li05] F. Li, *Novel dopants for n-type doping of electron transport materials: cationic dyes and their bases*, Dissertation, TU Dresden, 2005

[Li06] F. Li, M. Pfeiffer, A. Werner, K. Harada, K. Leo, N. Hayashi, K. Seki, X. Liu & X.-D. Dang, *Acridine orange base as a dopant for n doping of C_{60} thin films*, Journal of Applied Physics 100(2), 23716, 2006
http://dx.doi.org/10.1063/1.2219374

[Liu97] N. Liu, Yasunari Morio, F. Okino, H. Touhara, O. V. Boltalina & V. K. Pavlovich, *Electrochemical properties of $C_{60}F_{36}$*, Synthetic Metals 86, 2289, 1997
http://dx.doi.org/10.1016/S0379-6779(97)81130-7

[Loh23] W. Z. Lohrmann, *Beobachtungen von Sternschnuppen, angestellt zu Dresden vom 29 Aug. bis 1 Octob. 1823*, Annalen der Physik und der physikalischen Chemie 75(10), 215, 1823
http://dx.doi.org/10.1002/andp.18230751009

[Lüs12] B. Lüssem, M. Riede & K. Leo, *Doping of organic semiconductors*, in *Physics of organic semiconductors*, edited by W. Brütting & C. Adachi, chap. 14 (Wiley-VCH Verlag GmbH & Co. KGaA), 2nd edn., 2012, ISBN 9783527654949
http://doi.wiley.com/10.1002/9783527654949

[Lüs13] B. Lüssem, M. Riede & K. Leo, *Doping of organic semiconductors*, Physica Status Solidi A 210(1), 9, 2013
http://dx.doi.org/10.1002/pssa.201228310

[Mak01] T. L. Makarova, *Electrical and optical properties of pristine and polymerized fullerenes*, Semiconductors 35(3), 243, 2001
http://dx.doi.org/10.1134/1.1356145

[Män01] B. Männig, M. Pfeiffer, A. Nollau, X. Zhou, K. Leo & P. Simon, *Controlled p-type doping of polycrystalline and amorphous organic layers: self-consistent description of conductivity and field-effect mobility by a microscopic percolation model*, Physical Review B 64(19), 195208, 2001
http://dx.doi.org/10.1103/PhysRevB.64.195208

[Män04a] B. Männig, *Organische p-i-n Solarzellen*, Dissertation, TU Dresden, 2004

[Män04b] B. Männig, J. Drechsel, D. Gebeyehu, P. Simon, F. Kozlowski, A. Werner, F. Li, S. Grundmann, S. Sonntag, M. Koch, K. Leo, M. Pfeiffer, H. Hoppe, D. Meissner, N. Sariciftci, I. Riedel, V. Dyakonov & J. Parisi, *Organic p-i-n solar cells*, Applied Physics A 79(1), 1, 2004
http://dx.doi.org/10.1007/s00339-003-2494-9

[Mao13] H. Y. Mao, R. Wang, J. Q. Zhong, S. Zhong, J. D. Lin, X. Z. Wang, Z.-K. Chen & W. Chen, *High work function anode interfacial layer via mild temperature thermal decomposition of $C_{60}F_{36}$ thin film on ITO*, Journal of Materials Chemistry C 1(7), 1491, 2013
http://dx.doi.org/10.1039/C2TC00110A

[Mat07] T. Matsushima, M. Yahiro & C. Adachi, *Estimation of electron traps in C_{60} field-effect transistors by a thermally stimulated current technique*, Applied Physics Letters 91(10), 103505, 2007
http://dx.doi.org/10.1063/1.2779240

[Mat10] M. Matis, P. Rapta, V. Lukes, H. Hartmann & L. Dunsch, *Highly charged cations from N,N,N',N'-tetrakis(4-aminophenyl)benzidine and its N,N,N',N'-tetrakis(4-methoxyphenyl)-substituted homologue studied by thin-layer in situ electron spin resonance/UV-vis-NIR spectroelectrochemistry*, The Journal of Physical Chemistry B 114(13), 4451, 2010
http://dx.doi.org/10.1021/jp912213v

[May10] J. Mayer, K. Khairy & J. Howard, *Drawing an elephant with four complex parameters*, American Journal of Physics 78(6), 648, 2010
http://dx.doi.org/10.1119/1.3254017

[Mee11] R. Meerheim, S. Olthof, M. Hermenau, S. Scholz, A. Petrich, N. Tessler, O. Solomeshch, B. Lüssem, M. Riede & K. Leo, *Investigation of $C_{60}F_{36}$ as low-volatility p-dopant in organic optoelectronic devices*, Journal of Applied Physics 109(10), 103102, 2011
http://dx.doi.org/10.1063/1.3590142

[Mei11] J. Meiss, T. Menke, K. Leo, C. Uhrich, W.-M. Gnehr, S. Sonntag, M. Pfeiffer & M. Riede, *Highly efficient semitransparent tandem organic solar cells with complementary absorber materials*, Applied Physics Letters 99(4), 043301, 2011
http://dx.doi.org/10.1063/1.3610551

[Men12a] T. Menke, D. Ray, J. Meiss, K. Leo & M. Riede, *In-situ conductivity and Seebeck measurements of highly efficient n-dopants in fullerene C_{60}*, Applied Physics Letters 100(9), 093304, 2012
http://dx.doi.org/10.1063/1.3689778

[Men12b] T. Menke, P. Wei, D. Ray, H. Kleemann, B. D. Naab, Z. Bao, K. Leo & M. Riede, *A comparison of two air-stable molecular n-dopants for C_{60}*, Organic Electronics 13(12), 3319, 2012
http://dx.doi.org/10.1016/j.orgel.2012.09.024

[Mey09] J. Meyer, S. Hamwi, S. Schmale, T. Winkler, H.-H. Johannes, T. Riedl & W. Kowalsky, *A strategy towards p-type doping of organic materials with HOMO levels beyond 6 eV using tungsten oxide*, Journal of Materials Chemistry 19(6), 702, 2009
http://dx.doi.org/10.1039/b819485h

[Mil12] W. H. Mills & M. Mills, *The synthetical production of derivatives of dinaphthanthracene*, Journal of the Chemical Society, Transactions 101, 2194, 1912
http://dx.doi.org/10.1039/CT9120102194

[Mit12a] A. Mityashin, D. Cheyns, B. P. Rand & P. Heremans, *Understanding metal doping for organic electron transport layers*, Applied Physics Letters 100(5), 053305, 2012
http://dx.doi.org/10.1063/1.3681383

[Mit12b] A. Mityashin, Y. Olivier, T. Van Regemorter, C. Rolin, S. Verlaak, N. G. Martinelli, D. Beljonne, J. Cornil, J. Genoe & P. Heremans, *Unraveling the mechanism of molecular doping in organic semiconductors*, Advanced Materials 24(12), 1535, 2012
http://dx.doi.org/10.1002/adma.201104269

[Moh08] P. J. Mohr, B. N. Taylor & D. B. Newell, *CODATA recommended values of the fundamental physical constants: 2006*, Reviews of Modern Physics 80(2), 633, 2008
http://dx.doi.org/10.1103/RevModPhys.80.633

[Mur07] A. R. Murphy & J. M. J. Fréchet, *Organic semiconducting oligomers for use in thin film transistors*, Chemical reviews 107(4), 1066, 2007
http://dx.doi.org/10.1021/cr0501386

[Nol00] A. Nollau, M. Pfeiffer, T. Fritz & K. Leo, *Controlled n-type doping of a molecular organic semiconductor: naphthalenetetracarboxylic dianhydride (NTCDA) doped with bis(ethylenedithio)-tetrathiafulvalene (BEDT-TTF)*, Journal of Applied Physics 87(9), 4340, 2000
http://dx.doi.org/10.1063/1.373413

[Nol02] A. Nollau, *Investigation of the doping process in organic molecular thin films*, Dissertation, TU Dresden, 2002

[Nor00] B. Nordén & E. Krutmeijer, *The Nobel Prize in Chemistry 2000: conductive polymers*, Kungliga Vetenskapsakademien 2000

[Ohm27] G. S. Ohm, *Die galvanische Kette, mathematisch bearbeitet* (Riemann, Berlin), 1827
http://www2.ohm-hochschule.de/bib/textarchiv/Ohm.Die_galvanische_Kette.pdf

[Olt09] S. Olthof, W. Tress, R. Meerheim, B. Lüssem & K. Leo, *Photoelectron spectroscopy study of systematically varied doping concentrations in an organic semiconductor layer using a molecular p-dopant*, Journal of Applied Physics 106(10), 103711, 2009
http://dx.doi.org/10.1063/1.3259436

[Olt10] S. Olthof, *Photoelectron spectroscopy on doped organic semiconductors and related interfaces*, Dissertation, TU Dresden, 2010

[Olt12] S. Olthof, S. Mehraeen, S. K. Mohapatra, S. Barlow, V. Coropceanu, J.-L. Brédas, S. R. Marder & A. Kahn, *Ultralow doping in organic semiconductors: evidence of trap filling*, Physical Review Letters 109(17), 176601, 2012
http://dx.doi.org/10.1103/PhysRevLett.109.176601

[Osa70] E. Osawa, *Superaromaticity*, Kagaku 25, 854, 1970

[Osa93] E. Osawa, H. W. Kroto, P. W. Fowler & E. Wasserman, *The evolution of the football structure for the C_{60} molecule: a retrospective*, Philosophical Transactions of the Royal Society A: Mathematical, Physical and Engineering Sciences 343(1667), 1, 1993
http://dx.doi.org/10.1098/rsta.1993.0035

[OW] *orgworld.de, accessed 13.03.2013*
http://www.orgworld.de

[Par08] T. J. Park, S. Y. Kim, W. S. Jeon, J. J. Park, R. Pode, J. Jang & J. H. Kwon, *Electrical characterization of n- and n-doped hole and electron only organic devices*, Journal of Nanoscience and Nanotechnology 8(10), 5606, 2008
http://dx.doi.org/10.1166/jnn.2008.1434

[Pau25] W. Pauli, *Über den Zusammenhang des Abschlusses der Elektronengruppen im Atom mit der Komplexstruktur der Spektren*, Zeitschrift für Physik 31(1), 765, 1925
http://dx.doi.org/10.1007/BF02980631

[Pei93] H. Peimo, X. Yabo, Z. Xuejia, Z. Xinbin & L. Wenzhou, *Electrical conductivity studies of a pure C_{60} single crystal*, Journal of Physics: Condensed Matter 5(37), 7013, 1993
http://dx.doi.org/10.1088/0953-8984/5/37/019

[Pel34] J. C. A. Peltier, *Nouvelles expériences sur la caloricité des courants électrique*, Annales de Physique et Chimie 56, 1834

[Per08] K. P. Pernstich, B. Rossner & B. Batlogg, *Field-effect-modulated Seebeck coefficient in organic semiconductors*, Nature Materials 7(4), 321, 2008
http://dx.doi.org/10.1038/nmat2120

[Pfe98] M. Pfeiffer, A. Beyer, T. Fritz & K. Leo, *Controlled doping of phthalocyanine layers by cosublimation with acceptor molecules: a systematic Seebeck and conductivity study*, Applied Physics Letters 73(22), 3202, 1998
http://dx.doi.org/10.1063/1.122718

[Pfe99] M. Pfeiffer, *Controlled doping of organic vacuum deposited dye layers: basics and applications*, Dissertation, TU Dresden, 1999

[Pfe03] M. Pfeiffer, *Doped organic semiconductors: physics and application in light emitting diodes*, Organic Electronics 4(2-3), 89, 2003
http://dx.doi.org/10.1016/j.orgel.2003.08.004

[Plö99] B. Plönnings, *Elektrische und strukturelle Charakterisierung dotierter FSAS*, Diploma thesis, TU Dresden, 1999

[Pop99] M. Pope & C. E. Swenberg, *Electronic processes in organic crystals and polymers* (Oxford University Press), 2nd edn., 1999, ISBN 978-0195129632

[Ram90] M. Ramsey, D. Steinmüller & F. Netzer, *Explicit evidence for bipolaron formation: Cs-doped biphenyl*, Physical Review B 42(9), 5902, 1990
http://dx.doi.org/10.1103/PhysRevB.42.5902

[Rei09] S. Reineke, F. Lindner, G. Schwartz, N. Seidler, K. Walzer, B. Lüssem & K. Leo, *White organic light-emitting diodes with fluorescent tube efficiency*, Nature 459(7244), 234, 2009
http://dx.doi.org/10.1038/nature08003

[Rie11a] M. Riede, B. Lüssem & K. Leo, *Organic Semiconductors*, in *Comprehensive Semiconductor Science and Technology*, edited by P. Bhattacharya, R. Fornari & H. Kamimura, chap. 4.13, pp. 448–507 (Elsevier Science), 2011, ISBN 978-0-444-53153-7
http://dx.doi.org/10.1016/B978-0-44-453153-7.00123-1

[Rie11b] M. Riede, C. Uhrich, J. Widmer, R. Timmreck, D. Wynands, G. Schwartz, W.-M. Gnehr, D. Hildebrandt, A. Weiss, J. Hwang, S. Sundarraj, P. Erk, M. Pfeiffer & K. Leo, *Efficient organic tandem solar cells based on small molecules*, Advanced Functional Materials 21(16), 3019, 2011
http://dx.doi.org/10.1002/adfm.201002760

[Sal12] I. Salzmann, G. Heimel, S. Duhm, M. Oehzelt, P. Pingel, B. George, A. Schnegg, K. Lips, R.-P. Blum, A. Vollmer & N. Koch, *Intermolecular hybridization governs molecular electrical doping*, Physical Review Letters 108(3), 035502, 2012
http://dx.doi.org/10.1103/PhysRevLett.108.035502

[Sch26] E. Schrödinger, *An undulatory theory of the mechanics of atoms and molecules*, Physical Review 28(6), 1049, 1926
http://dx.doi.org/10.1103/PhysRev.28.1049

[Sch03] R. Schmechel, *Hopping transport in doped organic semiconductors: A theoretical approach and its application to p-doped zinc-phthalocyanine*, Journal of Applied Physics 93(8), 4653, 2003
http://dx.doi.org/10.1063/1.1560571

[Sch04] R. Schmechel & H. von Seggern, *Electronic traps in organic transport layers*, Physica Status Solidi A 201(6), 1215, 2004
http://dx.doi.org/10.1002/pssa.200404343

[Sch05] M. Schwoerer & H. C. Wolf, *Organische Molekulare Festkörper: Einführung in die Physik von π-Systemen* (Wiley-VCH), 2005
http://www.wiley-vch.de/publish/en/books/bySubjectPH00/ISBN3-527-40539-9/

[Sch12] C. Schünemann, D. Wynands, L. Wilde, M. Hein, S. Pfützner, C. Elschner, K.-J. Eichhorn, K. Leo & M. Riede, *Phase separation analysis of bulk heterojunctions in small-molecule organic solar cells using zinc-phthalocyanine and*

C_{60}, Physical Review B 85(24), 245314, 2012
http://dx.doi.org/10.1103/PhysRevB.85.245314

[Sch13] S. Schubert, Y. H. Kim, T. Menke, A. Fischer, R. Timmreck, L. Müller-Meskamp & K. Leo, *Highly doped Fullerene C_{60} thin films as transparent stand alone top electrode for organic solar cells*, submitted to Organic Electronics 2013

[See23] T. J. Seebeck, *Magnetische Polarisation der Metalle und Erze durch Temperatur-Differenz*, Abhandlungen der Königlichen Preußischen Akademie der Wissenschaften zu Berlin 1, 1823
http://bibliothek.bbaw.de/bbaw/bibliothek-digital/digitalequellen/schriften/anzeige?band=07-abh/18221823

[Sel91] H. Selig, C. Lifshitz, T. Peres, J. E. Fischer, A. R. McGhie, W. J. Romanow, J. P. McCauley & A. B. Smith, *Fluorinated fullerenes*, Journal of the American Chemical Society 113(14), 5475, 1991
http://dx.doi.org/10.1021/ja00014a061

[Shi81] T. B. Shimony & J. S. Ishay, *Thermoelectric (Seebeck) effect of the cuticle of social wasps*, Journal of Theoretical Biology 92(4), 497, 1981
http://dx.doi.org/10.1016/0022-5193(81)90262-9

[Sho50] W. Shockley, *Electrons and Holes in Semiconductors* (D. Van Nostrand), 1950, ISBN 978-0442075934

[Ste06] S. Steudel, K. Myny, S. De Vusser, J. Genoe & P. Heremans, *Patterning of organic thin film transistors by oxygen plasma etch*, Applied Physics Letters 89(18), 183503, 2006
http://dx.doi.org/10.1063/1.2374679

[Sue04] K. Suemori, T. Miyata, M. Hiramoto & M. Yokoyama, *Enhanced photovoltaic performance in fullerene:phthalocyanine codeposited films deposited on heated substrate*, Japanese Journal of Applied Physics 43(8A), L1014, 2004
http://dx.doi.org/10.1143/JJAP.43.L1014

[Sze81] S. M. Sze, *Physics of Semiconductor Devices* (Wiley & Sons Australia, Limited, John), 3rd edn., 1981, ISBN 0-471-05661-8

[Tes09] N. Tessler, Y. Preezant, N. Rappaport & Y. Roichman, *Charge transport in disordered organic materials and its relevance to thin-film devices: a tutorial review*, Advanced Materials 21(27), 2741, 2009
http://dx.doi.org/10.1002/adma.200803541

[The98] M. Thelakkat, R. Fink, F. Haubner & H.-W. Schmidt, *Synthesis and properties of novel hole transport materials for electroluminescent devices*, Macromolecular Symposia 125(1), 157, 1998
http://dx.doi.org/10.1002/masy.19981250114

[Thu11] F. Thuselt, *Physik der Halbleiterbauelemente* (Springer, Berlin, Heidelberg), 2nd edn., 2011, ISBN 978-3-642-20031-1
http://dx.doi.org/10.1007/978-3-642-20032-8

[Tie12] M. Tietze, L. Burtone, M. Riede, B. Lüssem & K. Leo, *Fermi level shift and doping efficiency in p-doped small molecule organic semiconductors: a photoelectron spectroscopy and theoretical study*, Physical Review B 86(3), 035320, 2012
http://dx.doi.org/10.1103/PhysRevB.86.035320

[Tie13] M. L. Tietze, F. Wölzl, T. Menke, A. Fischer, M. Riede, K. Leo & B. Lüssem, *Self-passivation of molecular n-type doping during air exposure using a highly efficient air-instable dopant*, Physica Status Solidi A 2013
http://dx.doi.org/10.1002/pssa.201330049

[Tro11] A. Troisi, *Charge transport in high mobility molecular semiconductors: classical models and new theories*, Chemical Society Reviews 40(5), 2347, 2011
http://dx.doi.org/10.1039/c0cs00198h

[Tse10] L. Tsetseris & S. Pantelides, *Oxygen and water-related impurities in C_{60} crystals: a density-functional theory study*, Physical Review B 82(4), 045201, 2010
http://dx.doi.org/10.1103/PhysRevB.82.045201

[Tyc91] R. Tycko, R. C. Haddon, G. Dabbagh, S. H. Glarum, D. C. Douglass & A. M. Mujsce, *Solid-state magnetic resonance spectroscopy of fullerenes*, The Journal of Physical Chemistry 95(2), 518, 1991
http://dx.doi.org/10.1021/j100155a006

[Uch08] K. Uchida, S. Takahashi, K. Harii, J. Ieda, W. Koshibae, K. Ando, S. Maekawa & E. Saitoh, *Observation of the spin Seebeck effect*, Nature 455(7214), 778, 2008
http://dx.doi.org/10.1038/nature07321

[Upp74] D. Upper, *The unsuccessful self-treatment of a case of writer's block*, Journal of Applied Behavior Analysis 7(3), 497, 1974
http://dx.doi.org/10.1901/jaba.1974.7-497a

[Vät96] C. Väterlein, B. Ziegler, W. Gebauer, H. Neureiter, M. Stoldt, M. Weaver, P. Bäuerle, M. Sokolowski, D. Bradley & E. Umbach, *Electrical conductivity and oxygen doping of vapour-deposited oligothiophene films*, Synthetic Metals 76(1-3), 133, 1996
http://dx.doi.org/10.1016/0379-6779(95)03436-N

[Vis98] M. C. J. M. Vissenberg, *Theory of the field-effect mobility in amorphous organic transistors*, Physical Review B 57(20), 12964, 1998
http://dx.doi.org/10.1103/PhysRevB.57.12964

[Waa73] J. D. van der Waals, *Over de Continuiteit van den Gas-en Vloeistoftoestand*, Dissertation, Leiden, 1873
http://www.scs.illinois.edu/~mainzv/exhibit/vanderwaals.htm

[Wag07] M. WAGNER, *Simulation of thermoelectric devices*, Dissertation, TU Wien, 2007
http://www.iue.tuwien.ac.at/phd/mwagner/

[Wal07] K. WALZER, B. MÄNNIG, M. PFEIFFER & K. LEO, *Highly efficient organic devices based on electrically doped transport layers*, Chemical Reviews 107(4), 1233, 2007
http://dx.doi.org/10.1021/cr050156n

[Wei10] P. WEI, J. H. OH, G. DONG & Z. BAO, *Use of a 1H-benzoimidazole derivative as an n-type dopant and to enable air-stable solution-processed n-channel organic thin-film transistors*, Journal of the American Chemical Society 132(26), 8852, 2010
http://dx.doi.org/10.1021/ja103173m

[Wei12] P. WEI, T. MENKE, B. D. NAAB, K. LEO, M. RIEDE & Z. BAO, *2-(2-methoxyphenyl)-1,3-dimethyl-1H-benzoimidazol-3-ium Iodide as a new air-stable n-type dopant for vacuum processed organic semiconductor thin films*, Journal of the American Chemical Society 134(9), 3999, 2012
http://dx.doi.org/10.1021/ja211382x

[Wel09] P. WELLMANN, *Lebensdauer und Stabilität elektrisch dotierter OLEDs*, Dissertation, TU Dresden, 2009

[Wer03a] A. WERNER, *n-type doping of organic thin films using a novel class of dopants*, Dissertation, TU Dresden, 2003

[Wer03b] A. WERNER, F. LI, K. HARADA, M. PFEIFFER, T. FRITZ & K. LEO, *Pyronin B as a donor for n-type doping of organic thin films*, Applied Physics Letters 82(25), 4495, 2003
http://dx.doi.org/10.1063/1.1583872

[Wer05] A. WERNER, O. KÜHL, S. GESSLER, K. HARADA, H. HARTMANN, A. GRÜSSING, M. LIMMERT & A. LUX, *Patent: Use of metal complexes as n-dopants for organic semiconductors and production thereof including their ligands*, 2005
http://www.freepatentsonline.com/WO2005086251.html

[Whe75] R. C. WHELAND & E. L. MARTIN, *Synthesis of substituted 7,7,8,8-tetracyanoquinodimethanes*, The Journal of Organic Chemistry 40(21), 3101, 1975
http://dx.doi.org/10.1021/jo00909a019

[Wid12] J. R. WIDAWSKY, P. DARANCET, J. B. NEATON & L. VENKATARAMAN, *Simultaneous determination of conductance and thermopower of single molecule junctions*, Nano Letters 12(1), 354, 2012
http://dx.doi.org/10.1021/nl203634m

[Yam79] Y. YAMAMOTO, K. YOSHINO & Y. INUISHI, *Electrical properties of phthalocyanine-halogen complexes*, Journal of the Physical Society of Japan 47(6), 1887, 1979
http://dx.doi.org/10.1143/JPSJ.47.1887

[Yog11] S. Yogev, E. Halpern, R. Matsubara, M. Nakamura & Y. Rosenwaks, *Direct measurement of density of states in pentacene thin film transistors*, Physical Review B 84(16), 165124, 2011
http://dx.doi.org/10.1103/PhysRevB.84.165124

[Yos12] H. Yoshida, *Near-ultraviolet inverse photoemission spectroscopy using ultra-low energy electrons*, Chemical Physics Letters 539-540, 180, 2012
http://dx.doi.org/10.1016/j.cplett.2012.04.058

[Zha09] W. Zhao & A. Kahn, *Charge transfer at n-doped organic-organic heterojunctions*, Journal of Applied Physics 105(12), 123711, 2009
http://dx.doi.org/10.1063/1.3153962

List of Tables

List of Figures

Acknowledgments / Danksagung

Nun möchte ich mich bei all den Leuten bedanken, die diese Arbeit auf die ein oder andere Art unterstützt haben. Zuallererst danke ich meinem Doktorvater Professor Dr. Karl Leo für die Möglichkeit, diese Dissertation anzufertigen und dafür, daß er das Institut für Angewandte Photophysik zu dem gemacht hat, was es heute ist.
Professorin Dr. Elizabeth von Hauff danke ich für die bereitwillige Begutachtung dieser Arbeit.

Besonderer Dank gebührt meinem Gruppenleiter Moritz Riede, der die durch Konversion von Frustration in Motivation diese Arbeit stets unterstützte. Hoch anzurechnen ist ihm auch, daß er das Ringen um Projektmittel weitestgehend von den Schultern seiner osol-Gruppe fern hielt. Dies, kombiniert mit seiner Affinität für technische Details, bescherte ihm viele 36h Tage, was ihn aber trotzdem nicht davon abhielt, Zeit für das Korrekturlesen von Arbeiten und Veröffentlichungen zu finden.

I thank Debu, Debdutta Ray, who claimed that my early state data were making sense after all and supported this work by many fruitful discussions and numerous private lessons in semiconductor physics, as well as troubleshooting the setup and proofreading this manuscript.
Mein zweiter wichtiger Diskussionspartner und Ideenfundus Hans Kleemann saß praktischerweise im selben Büro wie Debu, was zu einem erheblichen Schokikonsum führte, der nur noch von seinem eigenen Kaffeedurchsatz getoppt wurde. Ihm danke ich auch für das Schleifen meines Schreibstils. Ohne Debu und Hans hätte diese Arbeit sicher nicht diese Form erreicht.

I enjoyed the fruitful cooperation with Professor Zhenan Bao's group of Stanford University on the dmbi n-dopants and was glad for the chance to meet Zhenan Bao, Peng Wei and Benjamin Naab in person.
Ebenfalls danke ich der Novaled AG und insbesondere Jan Blochwitz-Nimoth für die Bereitstellung der n-Dotanden.

Das Handwerk des Dotierens durch Koverdampfung lernte ich maßgeblich von Selina Olthof, die auch upf-Messungen beisteuerte und mit der ich den Interkontinentalvideoabend erfunden habe. Ich bitte um Verzeihung dafür, daß ich dich in der Danksagung der ersten Veröffentlichung vergessen habe.

Meinem alten Weggefährten Jan Meiß danke ich dafür, daß er mich für das iapp rekrutierte, diverse Teilnahmen an Teamlaufveranstaltungen organisierte und eine Papervorlage mit Grundstruktur und Mietzekatzen entwarf.

Viel Spaß hatte ich mit meinem langjährigen Bürokollegen Johannes Widmer, dessen angenehme Art einen steten Ruhepol bildete. Ich genoss die unzähligen technischen Diskussionen und freute mich über kritische Korrekturen der Grundlagenkapitel. Seine vorbildliche Denkweise und sein Engagement beeindruckten mich immer wieder.

Einige Leute haben freundlicherweise Messungen für diese Arbeit beigesteuert. Da wären upf-Messungen von Selina Olthof und Max Tietze, ofet-Messungen von Moritz Hein und Jens Jankowski, sowie Fabrikation und Vermessung von organischen Solarzellen (die es leider nicht in diese Arbeit geschafft haben) durch Bernhard Siegmund, Jens Jankowski, Caroline Walde und Ralph Dannroth. Für die Anleitung und Fehlersuche bei afm-Messungen danke ich Lars Müller-Meskamp, Sarah Röttinger sowie Tobias Mönch. Hans Kleemann und Kentaro Harada stellten freundlicherweise ihre Daten für das Pentacen Kapitel zur Verfügung. Ken danke ich außerdem für die Übergabe des Messaufbaus und insbesondere der Vorführung der japanischen Lösung für die Stickstoffkühlung. Axel Fischer, Max Tietze und Florian Wölzl danke ich für die gute Zusammenarbeit im Frankensteinprojekt. Andreas Wendel präparierte Grundkontakte auf alle in dieser Arbeit verwendeten Substrate in Massenproduktion und ersparte mir dadurch viel Zeit.

Professor Dr. Horst Hartmann, Markus Hummert, Roland Gresser und Alexander Hoyer danke ich für die Diskussionen über die chemischen Strukturen der Dotanden sowie Auffrischung meiner Chemiekenntnisse. Gerne diskutierte ich auch mit Max Tietze, Matthias Schober, Janine Fischer, Johannes Widmer und Paul Pahner über physikalische Modelle und freute mich über Anmerkungen zu meinen Veröffentlichungsentwürfen von Björn Lüssem, Martin Pfeiffer und Jan Blochwitz-Nimoth.
Über Fragen der zukünftigen Energieversorgung habe ich mich gerne mit Carsten Knoll, Christoph Schünemann, Johannes Widmer, Jan Meiß und Wolfgang Tress ausgetauscht.

Für technische Hilfe bei der Erweiterung des Messaufbaus danke ich Carsten Wolf (Rat und Tat sowie Ölpestbekämpfung), Sven Kunze , Daniel Dietrich und Daniel Kasemann, sowie Carsten Knoll und Philipp Latzel für Tipps zur Pythonprogrammierung. Ferner den ufo-Piloten für das Nachsehen Christiane Falkenberg, Selina Olthof, Christian Körner, David Wynands, Felix Holzmüller, Franz Selzer und Toni Müller. Sowie Magdalene Menke für die Bereitstellung der Lampe für die Beleuchtung der aob-Proben während der Präparation. Auch dem unbekannten Opensource Softwareentwickler sei an dieser Stelle gedankt, da ich seine Produkte gern und viel genutzt habe, z.B. Linux, Latex, Perl, Python, Gnuplot, LibreOffice, Inkscape und Gimp.

Beosnedrer Dnak gehübrt acuh den Ferudnen, die biem Ausmrezen der Tpipfheler gehlofen haebn.

Veelen Dank an all de bannig veelen Lüd, de mi in jede Lag wiegerholpen hebbt. Alleen har ick dat nich so öllig tosamen kreegen. Ik denk girn trück an:

- de fründliche Ümgang mit de Lü in de Schrievstuv: Johannes Widmer, Melanie Lorenz-Rothe, Roman Forker, Björn Lüssem und Christian Wagner (mit seinem beeindruckenden Schreibtischchaos)
- de gaude Tosamenholt in de Warkstäh: Benjamin Röttig, Danny Jenner, Daniel Kasemann, Jan Förster, Sylvio Schubert und Tobias Günther
- dan veelen Spaß mit de Nahbers vun uns Schrievstuv: Christoph Schünemann, Debdutta Ray, Hans Kleemann, Jörg Alex, Lorenzo Burtone und Philipp Siebeneicher
- de Ünnerkunft in de Middagsstunn in mien tweite Schrievstuv: Hannah Ziehlke, Jan Meiß, Steffen Pfützner, Maik Langner, Robert Brückner, Daniel Kasemann und Johannes Haase.
  Eten un drinken hölt Liev un Seel tosamen
- dat scheune ut feuern tau Konferenzen in de wiege Welt mit: Caroline Murawski, Christian Körner, Christian Uhrich, Gregor Schwartz, Hans Kleemann, Lars Müller-Meskamp, Lorenzo Burtone, Marion Wrackmeyer, Merve Anderson, Michael Machala und Tobias Schwab

- Sport mit de Kollegen, Hol di fuchtig un risch as dull as du kanns: Jan Meiß, Steffen Pfützner, René Kullock, Nico Seidler, Robert Brückner, Tobias Schwab, Phil Goldberg, Moritz Riede (Laufen, Triathlon), Christiane Falkenberg, Christoph Schünemann, Janine Fischer, Hans Kleemann (Akrobatik), Hannah Ziehlke (Fit im Büro), Felix Holzmüller, Matthias Schober sowie Hans-Georg von Ribbeck und Roland Greffer (sportliches Radeln und so)
- dat Rümvriemeln in veele scheune Bastelstund'n: Christiane Falkenberg, Daniel Kasemann, Hans Kleemann, Johannes Widmer und Selina Olthof
- un nich to vergeten, de leiben Lü, de ik reinweg noch nich upschreben hev: Alexander Kittner, André Döring, André Merten (Projektberichte), Annette Petrich (Hilfe im Chemielabor), Chris Elschner, Christoph Sachse, Ellen Siebert-Henze, Hannes Klumbies, Ines Rabelo de Moraes, Marek Rölke, Marieta Levichkova, Martin Hermenau, Rico Meerheim, Rico Schüppel, Ronny Timmreck, Ruben Seifert, Simone Hofmann, Steef Corvers, Stefan Auschill, Till Hoheisel und Tina Träger sowie den leider hier vergessenen Mitgliedern der osol-Gruppe für die gute Zusammenarbeit.

Näm de Kollegen müch ick aber ok miene Familie, Franca un Frünn Dank seggen. Sei hebt mi mit veel Pläsier und Tauspruch über de ganze Tied ünnerstützt. Franca dank ick besünners för de Nahhülp in Saaken Work-Life-Balance. Ick dank miene Frünn för de Aflenkungen mid Tühnkrom un Spijöks, wenn dat in de Warkstäh nich so an loopen weu as dacht oder wenn bi dat Schrieven de Faden afreten weu.

Veelen herzlichen Dank dörfür, dat weu ne gaude Tied!

Erklärung

Diese Dissertation wurde am Institut für Angewandte Physik/Photophysik der Fakultät Mathematik und Naturwissenschaften an der Technischen Universität Dresden unter wissenschaftlicher Betreuung von Prof. Dr. Karl Leo angefertigt.

Hiermit versichere ich, dass ich die vorliegende Arbeit ohne unzulässige Hilfe Dritter und ohne Benutzung anderer als der angegebenen Hilfsmittel angefertigt habe; die aus fremden Quellen direkt oder indirekt übernommenen Gedanken sind als solche kenntlich gemacht. Die Arbeit wurde bisher weder im Inland noch im Ausland in gleicher oder ähnlicher Form einer anderen Prüfungsbehörde vorgelegt.

Weiterhin versichere ich, dass keine früheren Promotionsverfahren stattgefunden haben.

Ich erkenne die Promotionsordnung der Fakultät Mathematik und Naturwissenschaften an der Technischen Universität Dresden vom 23.02.2011 an.

Torben Menke

Dresden, den 26. März 2013